2015

Study on Sulfur Cathode Materials for High Performance Lithium/Sulfur Batteries

Xin Liang
University of Wollongong

UNIVERSITY OF WOLLONGONG

Institute for Superconducting and Electronic Materials

(ISEM)

Study on Sulfur Cathode Materials for High Performance Lithium/Sulfur Batteries

Xin Liang

This thesis is presented as part of the requirements for the Award of the

Degree of Doctor of Philosophy

of the University of Wollongong

September 6, 2015

Declaration

I, Xin Liang, declare that this thesis, submitted in fulfilment of the requirements for the award of Doctor of Philosophy, in the Institute for Superconducting and Electronic Materials, Faculty of Engineering, University of Wollongong, is wholly original work unless otherwise referenced or acknowledged. This thesis has not been submitted for qualifications at any other academic institution.

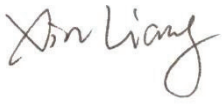

Xin Liang

September 6, 2015

Dedication

To my family who stand by me all the time.

Abstract

Rechargeable lithium/sulfur batteries have attracted significant attention due to their high theoretical specific capacity, high power density and low cost. Nevertheless, sulfur is very much an electrically insulating material, which leads to poor electrochemical accessibility and low utilization of the sulfur in the electrode. The polysulfide anions which are formed as the reaction intermediates are highly soluble in the organic electrolyte solvent, which results in low active material utilization, low coulombic efficiency and short cycle life of the sulfur electrode. Many approaches have been investigated for improving the performances of the sulfur cathode, such as synthesizing sulfur/carbon and sulfur/conducting polymer composites, adding adsorption additives into the electrodes, modification of the electrolyte, etc. Much attention has been paid to recent advances in the sulfur cathodes. In my doctoral work, honeycomb-like sulfur was synthesized via a soft template strategy for lithium/sulfur battery cathode, which has shown improved electrochemical performance compared to commercial sulfur particles. Another polypyrrole@sulfur@polypyrrole (PPy@S@PPy) composite with half-split tubular structure was prepared by the oxidative chemical polymerization method together with the chemical precipitation method. Moreover, the spray pyrolysis method was applied to synthesize a porous sulfur/dual-carbon composite with improved electrochemical performance, which shows great potential for the commercialization of lithium/sulfur batteries. Finally, an active carbon/nano-sulfur/polypyrrole composite with host-container architecture was prepared by the spray precipitation method and a subsequent oxidative chemical polymerization method for lithium/sulfur battery cathode. Further details are as follows:

Sulfur particles with honeycomb-like morphology were prepared via a cooperative self-assembly process. The cells with the honeycomb-like sulfur electrode retained a reversible discharge capacity higher than 650 mAh g^{-1} for 50 cycles, while the discharge

capacity of the commercial sulfur electrode was 200 mAh g^{-1}. Moreover, the honeycomb morphology is stable and can be maintained during cycling.

Polypyrrole@sulfur@polypyrrole (PPy@S@PPy) composite with a novel three-layer-three-dimensional (3D)-structure, which consists of an external polypyrrole coating layer, an intermediate sulfur filling layer, and an internal polypyrrole split-half-tube conducting matrix layer, has been synthesized by the oxidative chemical polymerization method and the chemical precipitation method in this PhD thesis work. Due to this unique three-layer-structure, the PPy@S@PPy composite cathode retained a discharge capacity of 554 mAh g^{-1} after 50 cycles, which represents 68.8% retention of the initial discharge specific capacity. It is concluded that the unique three-layer-structure played an essential role in improving the performance of the lithium/sulfur batteries. Moreover, the effects of $LiNO_3$ additive in the electrolyte on the coulombic efficiency are discussed to further confirm the containment function of the external layer of polypyrrole in the PPy@S@PPy composite, which is evidence that the external layer of polypyrrole can effectively confine the dissolved polysulfides.

Ternary composites with porous sulfur/dual-carbon architectures have been synthesized by a single-step spray-pyrolysis/sublimation technique, which is an industry-oriented method that features continuous fabrication of products with highly developed porous structures without the need for any further treatments. A double suspension of commercial sulfur and carbon scaffolding particles was dispersed in ethanol/water solution and sprayed at 180ºC using a spray pyrolysis system. In the resultant composites, the sulfur particles were subjected to an ultra-short sublimation process, leading to the development of a highly porous surface, and were meanwhile coated with amorphous carbon, obtained through the pyrolysis of the ethanol, which acts as an adhesive interface to bind together the porous sulfur with the scaffolding

carbon particles, to form a ternary composite architecture. This material has an effective conducting-carbon/sulfur-based matrix and interconnected open pores to reduce the diffusion paths of lithium ions, buffer the sulfur volumetric expansion, and absorb electrolyte and polysulfides. Due to the unique chemistry and the structure, the composites show stable cycling performance for 200 cycles and good rate capability of 520 mAh g^{-1} at 2 C. This advanced spray-pyrolysis/sublimation method is easy to scale up and shows great potential for commercialization of lithium/sulfur batteries.

Active-carbon – nano-sulfur – polypyrrole composite with host-container architecture was prepared by the spray precipitation method and subsequent chemical polymerization. In this architecture, the active carbon acts as a host to adsorb sulfur in its pore spaces, and the polypyrrole layer works not only as a container to improve the conductivity of the electrode and prevent the diffusion of dissolved polysulfide, but is also an active material that contributes extra capacity to the sulfur cathode in the lithium/sulfur batteries. Moreover, an interlayer consisting of a flexible film of single-walled carbon nanotubes was inserted between the cathode and the separator, where it significantly improves the rate capability of the active-carbon – nano-sulfur – polypyrrole composite cathode in the lithium/sulfur batteries. The as-prepared composite was applied in lithium/sulfur batteries, where it presents much better electrochemical performance than sulfur cathode and active-carbon – nano-sulfur composite cathode.

Acknowledgements

First of all, I would like to express my deepest appreciation to my supervisors, A/Prof. Jiazhao Wang, Dr. Kosta Konstantinov and Prof. Huakun Liu, for their academic supervision and guidance, constant support and encouragement, and invaluable advice during my PhD study in Wollongong. I also would like to thank Prof. Chunhua Chen who provided me with supervision and support during my visit to the University of Science and Technology of China (USTC). Many thanks go to Dr. Tania Silver as well, who always critically read every manuscript during my Ph.D study.

Financial support provided by an Australian Research Council (ARC) Linkage Project (LP100100802) and industry partner PT Nipress TbK is gratefully acknowledged. I also would like to thank the University of Wollongong as sponsor of the University Postgraduate Award and the International Postgraduate Tuition Award.

Moreover, I would like to thank the staff members and technicians at ISEM for their kind assistance, including Dr. Germanas Peleckis (XRD), Dr. David Wexler (TEM), Dr. Kosta Konstantinov (BET, TGA/DTA), Mr. Darren Attard (SEM), Mr. Tony Romeo (SEM, EDS), Mrs. Crystal Login, Mrs. Narelle Badger, Ms. Joanne George (OH&S), Mr. Robert Morgan, Mr. Mathew Davis, and Mrs. Candace Gabelish.

Many thanks to Mr. Mohammad Rejaul Kaiser, Dr. Dan Li, Dr. Yi Shi, Dr. Yunxiao Wang, Dr. Zhijia Zhang, Dr. Jiantie Xu, Mr. Yuede Pan, Mr. Jun Wang, Ms. Lili Liu, Ms. Weijie Li, Ms. Xuanwen Gao, Ms. Li Li, Ms. Sha Li, Mr. Wenbin Luo, Dr. Chao Zhong, Dr. Lin Lu, and other students and staff in ISEM, as well as Prof. Mingang Zhang in Taiyuan University of Science and Technology and Dr. Xiaohang Ma, Mr. Bangkun Zou, Dr. Linchao Zhang, Mrs. Miaomiao Deng, Mr. Xin Sun, Dr. Jianwu Wen, Dr. Chuxiong Ding, Mr. Yong Zang and other students and staff in USTC, for their kind help and valuable advice.

Finally, I would like to express my deepest appreciation and love to my parents, my husband, my son and my brother, who are stand by me and support me all the time.

Table of Contents

Nomenclature

List of Abbreviations

Abbreviation	Full name
3D	Three-dimensional
a.u.	Arbitrary unit
BET	Brunauer-Emmett-Teller
CNT	Carbon nanotube
CV	Cyclic voltammetry
DTA	Differential thermal analysis
EDS	Energy dispersive X-ray spectroscopy
EIS	Electrochemical impedance spectroscopy
EVs	Electric vehicles
FESEM	Field-emission scanning electron microscopy
HEVs	Hybrid electric vehicles
GO	Graphene oxide
HRTEM	High-resolution transmission electron microscopy
LIBs	Lithium-ion batteries
MWCNT	Multi-walled carbon nanotube
NMP	1-methyl-2-pyrrolidinone
PPy	Polypyrrole
PTS Na	Sodium p-toluenesulphonate
PVDF	Polyvinylidene fluoride
SAED	Selected area electron diffraction
SDBS	sodium dodecyl benzene sulphonate

SEI	Solid electrolyte interphase
SEM	Scanning electron microscopy
SWCNT	Single-walled carbon nanotube
TEM	Transmission electron microscopy
TGA	Thermogravimetric analysis
XRD	X-ray diffraction

List of Symbols

Symbol	Name	Unit
2θ	Detection angle in XRD	°/Degree
C-rate	Charge or discharge rate	$mA\ g^{-1}$
m	Active material weight	G
P	Relative pressure	Pa
P_0	Saturation pressure	Pa
S_{BET}	Specific BET surface area	$m^2\ g^{-1}$
SE	Specific energy	$Wh\ kg^{-1}$
SP	Specific power	$W\ kg^{-1}$
T	Temperature	K or °C
t	Time	h or s
λ	X-ray wavelength	Å

List of Organizations

Abbreviation	Full name
AIIM	Australian Institute for Innovative Materials

EMC	Electron Microscopy Centre
ISEM	Institute for Superconducting and Electronic Materials
UOW	University of Wollongong
USTC	University of Science and Technology of China

List of Figures

List of Tables

Chapter 1. Introduction

1.1. General background and motivation

Clean and efficient energy storage devices are in high demand due to the limited global energy supply, environmental pollution, and the increasing consumption of energy worldwide. Among all the energy storage devices, the lithium ion battery is one of the most important groups since the first lithium ion battery was introduced in 1991. This is becuase of their relatively high specific capcity, high energy density and superior electrochemical performance [3]. Lithium ion batteries have been widely used in portable devices, such as mobile phones, cameras and laptops. They are also of crucial importance for laboratory equipment, portable instruments, industrial control remote control, and even spaceships. Nevertheless, due to the limited specific capacity of the current cathode materials in the conventional lithium ion batteries, it is impossible to meet the requirements of the electric vehicles that will characterize the transport market of the future, even if the current lithium ion batteries are fully developed and reach the theoretical capacity of their current cathode materials. Thus, it is necessary to explore and develop next-generation energy storage devices. Since lithium /sulfur batterie was first investigated in the 1940s, they have attracted considerable attention. Especially from the point of view of the high demands of electric vehicles, lithium/sulfur batteries are considered to be a promising next-generation energy device along with lithium/air batteries. This is because sulfur has the highest theoretical specific capcity among all the known solid cathode materials [26-30], and a very high energy density as well [14, 31-37]. In addition, sulfur is abundant in nature, low-cost, and non-toxic[38-42]. Nevertheless, the fabrication and commercialization of lithium/sulfur batteries have encountered a number of challenges [9, 43, 44, 45-49]. Firstly, sulfur is very much an electrically insulating material. Secondly, the densities of S and Li_2S are different. Thirdly, the polysulfide anions are highly soluble in the organic electrolyte solvent. The last but not the

least, the sulfur-based cathode materials are difficult to be prepared in large scale. These reasons lead to low active material utilization, low coulombic efficiency, short cycle life of the sulfur electrode, and difficulty of the commercialization of lithium/sulfur batteries.

1.2. Objectives of the research

In order to overcome the challenges mentioned above, this doctoral research plans to achieve four main objectives as following:

The first objective is the improvement of the conductivity of sulfur cathode. Sulfur is very much an electrically insulating material, thus in order to operate the lithium/sulfur battery, the conductivity of the sulfur cathode must be enhanced. The formation of porous structure and adding conducting agents are the two approaches. The porous structure increases the contact surface area between the sulfur and the carbon black, which increases the conductivity of the electrode; and the porous structured electrode has a faster charge transfer process, and thus the electrochemical kinetics of the porous sulfur with porous additive electrode are improved in rechargeable lithium batteries [50]. In this PhD thesis work, the porous sulfur and porous sulfur-based composites have been synthesized for enhancement of the conductivity of the sulfur cathodes. To introduce conductive agents into the sulfur by synthesizing composites of sulfur/conductive agents is the second method to increase the conductivity of sulfur cathode. The conducting agents include mesoporous carbon, multiwalled carbon nanotubes, carbon fibre, reduced graphene oxide, carbon black [1, 5, 8, 10-15, 31, 32, 34, 35, 51-60], and conducting polymers [18, 19, 27, 33, 61-64]. In this doctoral work, I have applied active carbon, graphite, MWCNTs, carbon black, and polypyrrole (PPy) to prepare sulfur/carbon and sulfur/PPy composite as cathode materials in lithium/sulfur batteries.

The buffer of the volume expansion of the cathode is the second objective of this doctoral work. As the differences on densities of S and Li_2S, during the charge and discharge

processes, the active materials in cathode are easily pulverised because of the volume expansion. This objective can be achieved by the existence of pores in materials and conducting polymer coating. The porous structure can provide sufficient space for the volume change between S and Li_2S. In this thesis work, porous sulfur and porous sufur – carbon composites have been prepared for buffering the volumetric expansion of the cathode. Moreover, conducting polymers are soft and self-healing, which provides a solution to problems related to volume expansion and material pulverization. In this thesis work, PPy has been applied to synthesize the S@PPy composite and PPy@S@PPy composite to buffer the volume expansion of the cathode.

The third objective is to trap the diffusion of dissolved polysulfides. The diffusion of the dissolved polysulfides can lead to "shuttle effect", which results in low active material utilization, low coulombic efficiency and short cycle life of the sulfur electrode in lithium/sulfur batteries. The dissolved polysulfide anions can be prevented from diffusion to the Li anode by five approaches. (1) Porous structure can absorb the soluble lithium polysulfides formed during discharge, and reduce the dissolution of the active materials into the electrolyte in some extent. In this doctoral thesis, the designs of the honeycomb-like sulfur and active-carbon – nano-sulfur – polypyrrole composite are also for this purpose. (2) The conducting polymer coating can effectively trap the diffusion of the dissolved polysulfides. In this thesis work, PPy works as a container in PPy@S@PPy composite to prevent the diffusion of polysulfides. (3) Inserting an interlayer between the separator and the cathode can serve as an excellent matrix to retain and accommodate dissolved intermediate polysulfides. In this doctoral work, a SWCNT flexible paper was applied as an interlayer to contain the diffusion of polysulfide ions. (4) The electrolyte with high viscosity can reduce the diffusion speed of the polysulfides in some extent. In this thesis work, I have employed PEGDME 500 and DOL/DME (1:1) as the electrolytes for lithium/sulfur batteries. (5) The

fixing charging capacity method can prohibit the formation of the long chain polysulfides, which is the responsible for the capacity decay. In this doctoral work, I also applied this new charging method to improve the cycling performance of the as-prepared sulfur-based cathode in lithium/sulfur batteries.

The fourth objective is the production of sulfur cathode materials continuously in large scale. In my doctoral work, a scalable and continuous-production spray-pyrolysis/sublimation method developed and applied to produce the porous sulfur/dual-carbon composites, which shows great potential for the commercialization of lithium/sulfur batteries.

In summary, the research effort in this doctoral work has been put into sulfur cathode materials for lithium/sulfur batteries. It can be described in terms of the following directions: (1) modify the pure sulfur with special morphology; (2) introduce various carbon sources to synthesize sulfur/carbon composites; (3) apply polypryrrole to prepare sulfur/PPy composite; (4) employ different synthesis methods to form various morphologies, (5) try different electrolytes for lithium/sulfur batteries; (6) apply the new charging method to improve the cycling performance of the lithium/sulfur batteries; and (7) insert a flexible film of SWCNTs as an interlayer to provent the diffusion of the dissolved polysulfide ions during charge/discharge processes of lithium/sulfur batteries.

1.3. Thesis structure

A brief overview of this doctoral thesis is outlined as follows:

Chapter 1 simply introduces the general background, major problems, and some approaches for improving the electrochemical performance of lithium/sulfur batteries, explains the objectives of the study, and gives an outline of the thesis.

Chapter 2 presents a literature review on lithium/sulfur batteries, including a basic

introduction to lithium/sulfur batteries, the challenges to be faced for commercializing lithium/sulfur batteries and the approaches to overcome the challenges.

Chapter 3 presents the chemicals and methods used to synthesize honeycomb-like pure sulfur, polypyrrole@sulfur@polypyrrolecomposite, sulfur@polypyrrole composite, porous sulfur/graphite composites and sulfur-carbon, and sulfur-conducting polymer composite materials. This chapter also briefly introduces the instrumental analysis techniques used to characterize the electrode materials, including X-ray diffraction (XRD) , thermogravimetric analysis (TGA), Raman spectroscopy, scanning electron microscopy (SEM), field emission scanning electron microscopy (FESEM), transmission electron microscopy (TEM), energy dispersive X-ray spectroscopy (EDS), Brunauer-Emmet-Teller (BET) surface area measurements, and electrochemical measurements, including cyclic voltammetry (CV), galvanostatic charge-discharge cycling, and electrochemical impedance spectroscopy (EIS).

Chapter 4 investigates the porous morphology of pure sulfur for improving the electrochemical properties of lithium/sulfur batteries. The cooperative self-assembly process is introduced and applied to the synthesis of pure sulfur with porous structure, while sodium dodecyl benzene sulphonate (SDBS) is used as a soft template. The mechanism for the synthesis of the honeycomb like sulfur particles is explained. The effects of the concentration of SDBS are studied,. Finally, the electrochemical performance of the as-prepared pure honey-comb-like sulfur is tested and showed siginificantly improvement compared with commercial sulfur and the as-prepared sulfur without porous structures.

Chapter 5 investigates conducting polymers to modify sulfur cathode for lithium/sulfur batteries. A polypyrrole@sulfur@polypyrrole composite (PPy@S@PPy composite) with a novel three-layer-three-dimensional (3D) structure is proposed by not only loading sulfur on PPy, but also by coating PPy on sulfur. The composite is synthesized by the

oxidative chemical polymerization and chemical precipitation methods. In order to analyze the function of this novel three-layer-structure of the PPy@S@PPy composite, a sulfur@polypyrrole composite (S@PPy composite) with the same components as the prepared PPy@S@PPy composite, but without three-layer-structure, was synthesized for comparison. First, the preparation process is introduced, and then XRD patterns, Raman spectra, and TGA are employed to confirm the components of these two synthesized composites. The morphology of the composites is investigated by TEM and SEM, which confirms the unique split-half-tube structure. This unique split-half-tube structure has many advantages, such as having higher surface area and improving the amount of sulfur loading, leading to a thin and uniform coating layer of sulfur. Next, the conductivity, capacity, reversibility, and rate capability of the composite cathodes are investigated by electrochemical testing, which confirms the improvements in the electrochemical performance due to this novel structure. Finally, the effects of $LiNO_3$ additive in the electrolyte on coulombic efficiency are tested, which further identifies the existence of the external layer of PPy in the PPy@S@PPy composite and confirms the containment function of the external layer of PPy toward trapping the dissolved polysulfides.

Chapter 6 presents a cost-effective industrially oriented approach, an advanced *in-situ* spray-pyrolysis/sublimation method, to continuously produce a porous sulfur/dual-carbon ternary composite with graphite, carbon black, and multi-walled carbon nanotube (CNT) scaffolding particles as cathode materials for lithium/sulfur batteries. A series of experiments were carried out to find the best experimental parameters, such as temperature, solvent, and scaffolding carbon type. Graphite is found to be the best form of carbon for this spray-pyrolysis/sublimation system. The bridging graphite can be bound to porous sulfur by an adhesive interface of amorphous carbon to form an interparticle conductive matrix. Moreover, the pores on sulfur

formed from sulfur sublimation and the interconnected open pores from the matrix increase the contact area with Super-P and electrolyte, decrease the transport pathways for both electrons and lithium ions, and confine the soluble lithium polysulfides, as well as providing sufficient space to accommodate sulfur volumetric expansion during charge and discharge processes. Due to this unique chemistry and structure, the porous sulfur/dual-carbon composites with graphite present attractive cycling performance and good high rate capability. The new charging method, which involves fixing the charging capacity, is also applied to improve the cycling performance of the as-prepared porous sulfur/dual-carbon composites. The scalable and continuous-production spray-pyrolysis/sublimation method that has been developed and the novel architecture of the porous sulfur/dual-carbon composites prepared for the first time in this work show great potential for the commercialization of lithium/sulfur batteries.

In Chapter 7, the active-carbon – nano-sulfur – polypyrrole composite with host-container architecture was prepared, where the active carbon acts as a host to adsorb sulfur in its pore spaces and the polypyrrole layer works as a container to protect the sulfur from diffusion of the dissolved polysulfide ions in lithium/sulfur batteries. Then, the interlayer of single-walled carbon nanotube flexible film was inserted between the cathode and the separator, where it could significantly improve the rate capability of the composite cathode in lithium/sulfur batteries. The new charging method is also applied to improve the cycling performance of the as-prepared composites as well. As a result, the as-prepared active-carbon – nano-sulfur – polypyrrole composite was applied in lithium/sulfur batteries, which presented much better electrochemical performance than sulfur cathode and active-carbon - nano-sulfur composite cathode.

In Chapter 8, the general conclusions are summarized and recommendations for further research work based on this doctoral work are discussed as well.

References are listed after Chapter 8, followed by publications and awards received during the period of my PhD study.

Chapter 2. Literature review

2.1. Berief introduction to lithium / sulfur batteries

Due to limited global energy supplies, environmental pollution, and the increasing consumption of the energy worldwide, clean and efficient energy storage devices are in high demand, especially for electric vehicles (EVs) and hybrid electric vehicles (HEVs)[3, 25, 65-67]. As shown in Figure 2.1, the existing Li ion cells have a specific energy of up to 200 Wh kg^{-1}, which is not high enough for 200+ mile range EVs[68]. Thus, the rechargeable lithium/sulfur battery has attracted significant attention due to its high theoretical specific capacity of 1675 mAh g^{-1}, which is the highest value among all known solid cathode materials[52, 56, 69-80]. In comparison with conventional lithium ion batteries, Li/S batteries also have higher energy density at a lower cost. The theoretical power density of a Li/S battery can reach as high as 2500 Wh kg^{-1} or 2800 Wh L^{-1}, based on weight or volume, assuming complete reaction to Li_2S[25, 67, 81-86], as is shown in Figure 2.2. Moreover, sulfur is abundant in nature, as it is the seventeenth richest element in the Earth's crust, and it is also inexpensive and nontoxic[87-96].

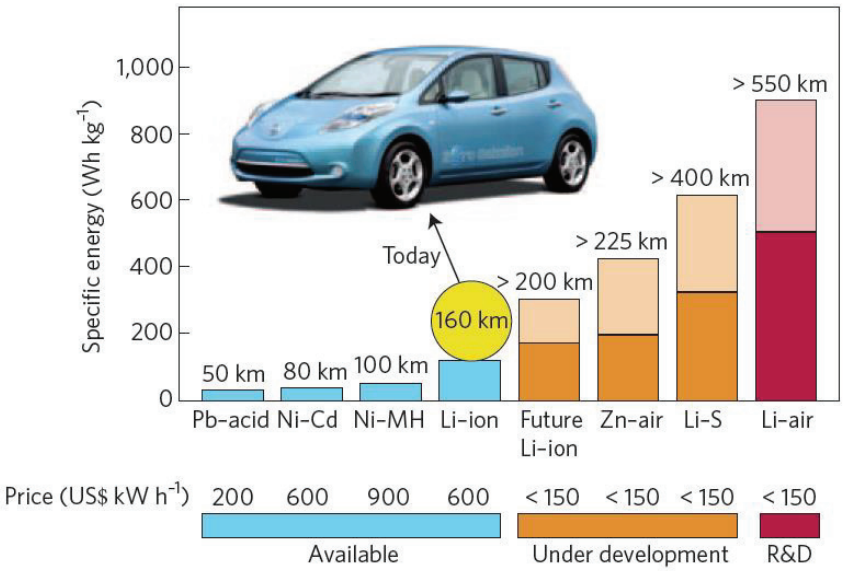

Figure 2.1 Practical specific energies, estimated driving distances and pack prices of some

rechargeable batteries [1].

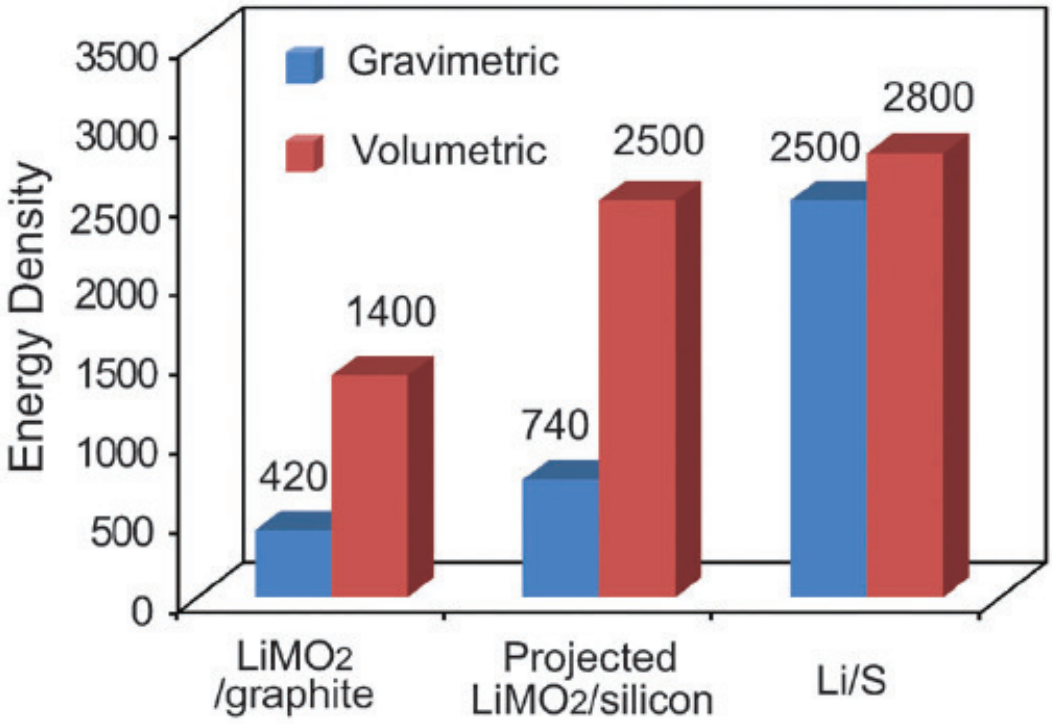

Figure 2.2 The theoretical energy density of three rechargeable battery systems based on active materials only. The units of gravimetric and volumetric energy density are Wh kg^{-1} and Wh L^{-1}, respectively. M= $Ni_{1/3}Mn_{1/3}Co_{1/3}$ [2].

Sulfur was first applied as a cathode electrode material by Herbet and Ulam in 1962. As shown in Figure 2.3, a typical lithium/sulfur battery contains six main parts: the anode, electrolyte, cathode, separator, binder, and current collector. The details are shown as follows:

(1) Anode: Li metal

(2) Electrolyte: lithium salt+organic solvent

(3) Cathode: S (composite)+carbon black

(4) Separator : Celgard

(5) Binder: PVDF

(6) Current collector: Al

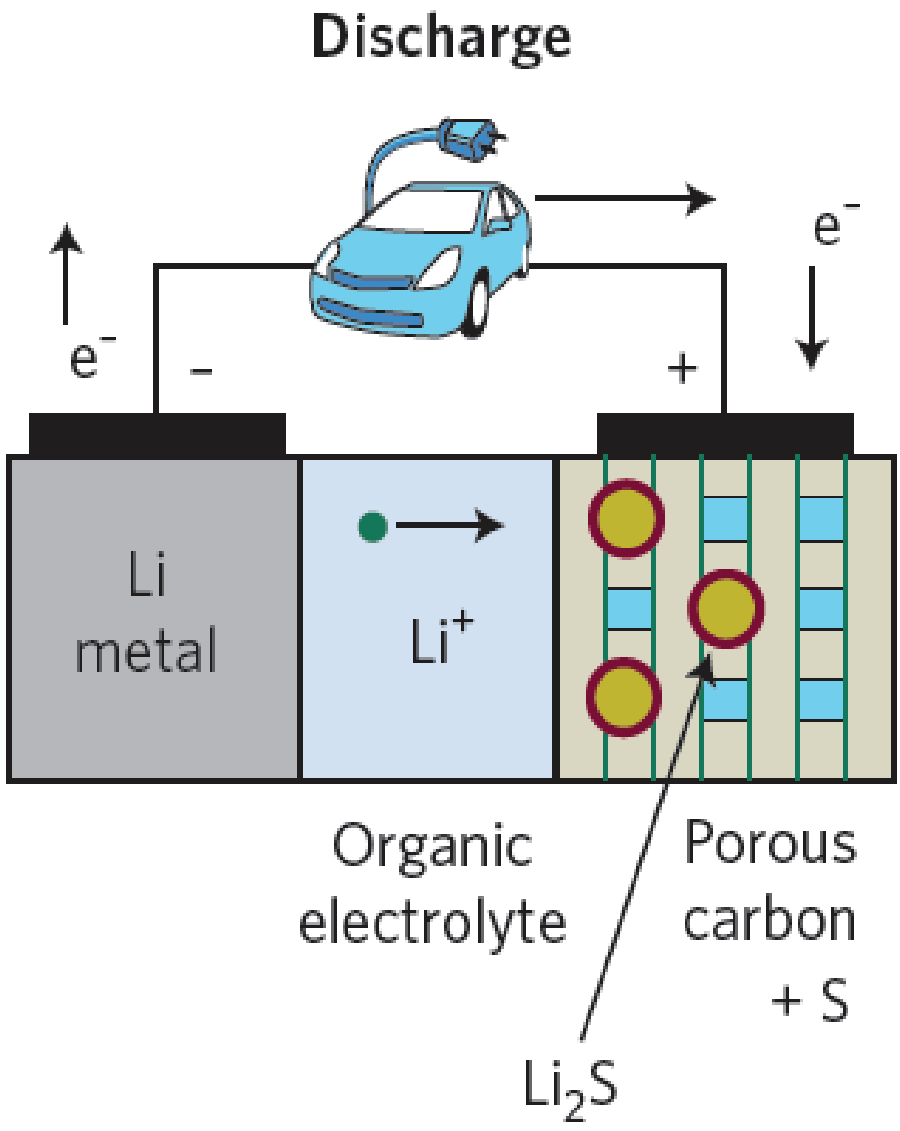

Figure 2.3 Schematic illustration of Li/S cell[3].

In a Li/S cell, the overall reaction during discharge can be described as:

Cathode reaction: S_8+ 16 Li+16e^- → 8 Li_2S; Anode reaction: 16 Li → 16Li^+ + 16e^- . Its average voltage is 2.15 V[97].

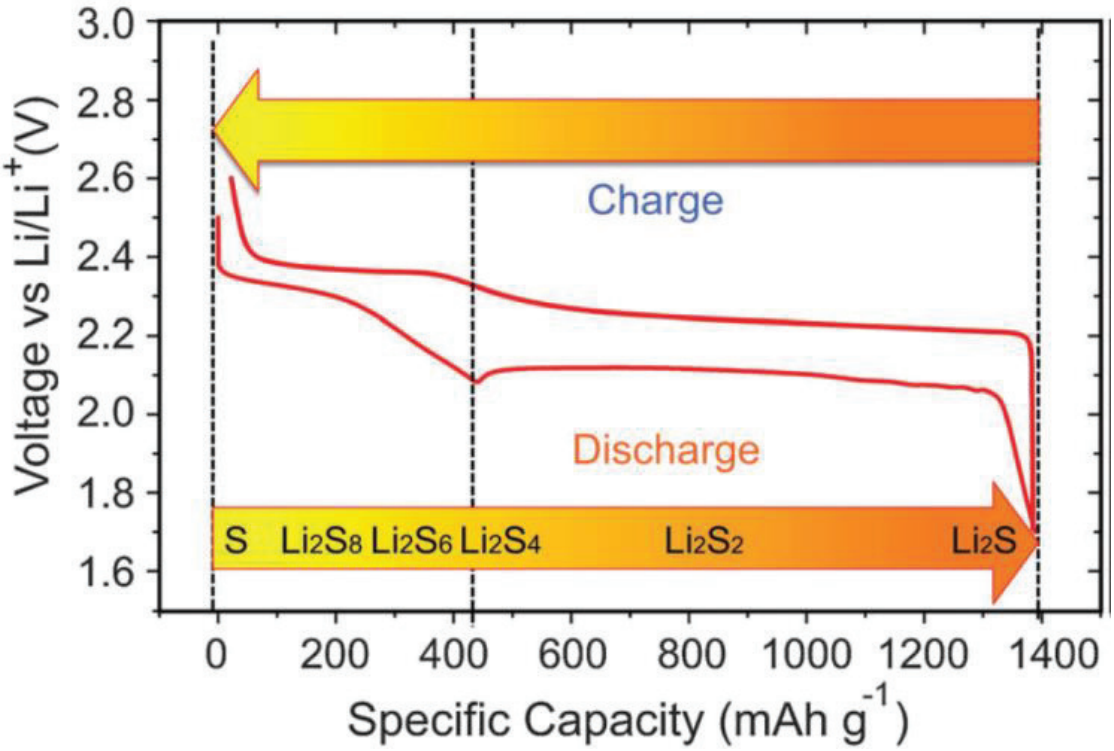

Figure 2.4 Voltage profile and chemistry of the sulfur cathode in the organic electrolyte in lithium/sulfur batteries[4].

Figure. 2.4 shows a typical discharge and charge voltage profile for the first cycle of a Li/S cell. Based on the phase changes of the sulfur species, the discharge process can be divided into five reduction regions:

Step (2.1): A solid-liquid two-phase reduction from elemental sulfur to Li_2S_8. In this region, the thus-formed Li_2S_8 dissolves into the liquid electrolyte to become a liquid cathode.

$$S_8 + 2e^- \rightarrow S_8^{2-} \qquad (2.1)$$

Step (2.2): A liquid-liquid single-phase reduction from the dissolved Li_2S_8 to a low-order lithium polysulfide (Li_2S_6).

$$S_8^{2-} + 2\,e^- \rightarrow S_6^{2-} \qquad (2.2)$$

Step (2.3): Li_2S_6 is further reduced to low-order lithium polysulfide (Li_2S_4).

$$S_6^{2-} + 2e^- \rightarrow S_4^{2-} \qquad (2.3)$$

Step (2.4): A liquid-solid two-phase reduction from the dissolved low-order lithium polysulfide Li_2S_4 to insoluble Li_2S_2.

$$S_4^{2-} + 4Li^+ + 2e^- \rightarrow 2Li_2S_2 \qquad (2.4)$$

Step (2.5):A solid-solid reduction from insoluble Li_2S_2 to Li_2S.

$$Li_2S_2 + 2Li^+ + 2e^- \rightarrow 2Li_2S \qquad (2.5)$$

It needs to be pointed out that these five steps are the simplified situation. In fact, the polysulfide anions coexist in the solution through a series of chemical equilibria, due to the similar Gibbs free-energy (ΔG^0), which is shown in Table 2.1.

Table 2.1 Thermodynamic data of various PS anions (S_n^{2-}) formed in aqueous solution[25].

S_n^{2-} with	$n = 2$	$n = 3$	$n = 4$	$n = 5$	$n = 6$	$n = 7$	$n = 8$
ΔG^0, kJ mol^{-1}	77.4 ± 1.3	71.1 ± 0.7	67.1 ± 0.1	66.0 ± 0.1	67.4 ± 0.1	70.7 ± 0.3	74.9 ± 0.5
ΔH^0, kJ mol^{-1}	13.0	6.6 ± 0.1	9.0 ± 0.1	9.6 ± 0.1	13.3 ± 0.1	16.5 ± 0.1	23.8 ± 0.2
S^0, kJ mol^{-1} K^{-1}	−22	9 ± 4	63 ± 1	100 ± 2	139 ± 1	171 ± 4	213 ± 8

In summary, the first three steps correspond to the higher plateau at 2.15-2.4 V in the voltage profile (Figure 2.3). During the last two steps, the insoluble Li_2S_2 and Li_2S are formed and precipitated at the cathode. The last two steps form the lower voltage plateau at 1.9-2.1 V, which contributes to the major capacity of a lithium/sulfur battery.

2.2. Challenges of lithium / sulfur batteries

In spite of their considerable advantages, the fabrication of lithium/ sulfur batteries encounters a number of challenges, including the sulfur cathode, the electrolyte, and the lithium anode.

2.2.1 Sulfur Cathode

First, sulfur is a highly electrically insulating material[82, 98-103], which leads to poor electrochemical accessibility and low utilization of the sulfur in the electrode. Second, Li_2S is the reduction product of S, which is also electronically and ionically insulating[104-107]. Once a thin Li_2S layer completely covers the whole electrode, further lithiation will be largely

impeded, and the voltage decreases rapidly. Thus, complete conversion of sulfur to Li_2S is very difficult. This is the reason why most reports show the discharge capacity to be less than 80% of the theoretical limit. Third, the polysulfide anions which are formed as the reaction intermediates are highly soluble in the organic electrolyte solvent[106]. These soluble species can be reduced to Li_2S at the lithium anode surface, passivating the anode and leading to both material loss and an increase in impedance. Moreover, the dissolution and precipitation process alters the morphology of the cathode in each cycle, which induces strain inside the electrode and degrades the cycle life[93, 108-110]. The dissolution of polysulfides also results in the so-called "shuttle effect", where long chain polysulfides diffuse to the surface of the lithium anode and are reduced to short chain polysulfides[111-127]. The short chain polysulfides can then move back to the cathode and be oxidized to long chain polysulfides. This parasitic process takes place continuously, creating an internal ''shuttle'' phenomenon, the mechanism of which is shown in Figure 2.5. On Li anode, the dissolved polysulfide (PS) can be electrochemically and chemically reduced, as described by Eqs. (2.6) and (2.7), respectively:

$$(n\text{-}1)\ Li_2S_n + 2Li^+ + 2e^- \rightarrow nLi_2S_{n-1} \qquad \text{Electrochemical reduction} \qquad (2.6)$$

$$(n\text{-}1)\ Li_2S_n + 2Li \rightarrow nLi_2S_{n-1} \qquad \text{Chemical redox reaction} \qquad (2.7)$$

These parasitic reactions cause such problems as (1) consuming the active sulfur species, (2) corroding the Li anode, and (3) polarizing the Li anode once the insoluble Li_2S and Li_2S_2 are formed and deposited on the Li surface. This shuttle phenomenon results in low active material utilization, low coulombic efficiency and short cycle life of the sulfur electrode [9, 43].

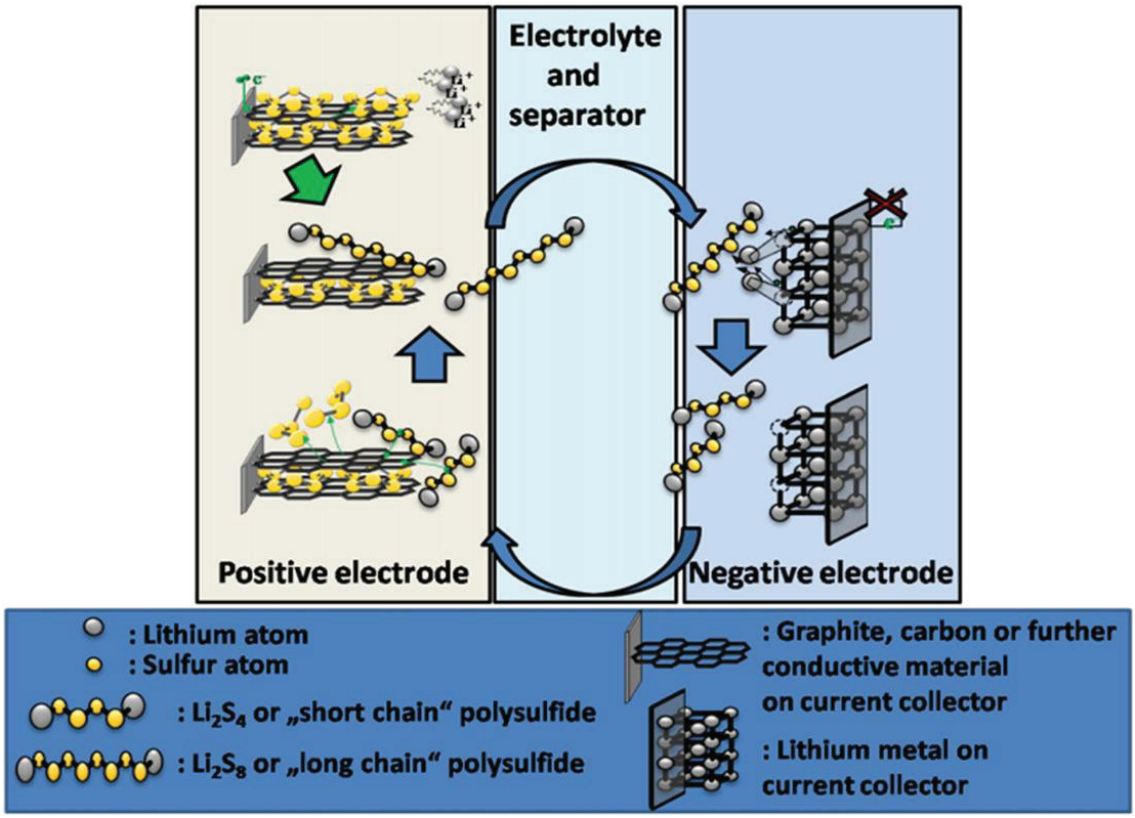

Figure 2.5. Polysulfide shuttle mechanism in lithium/sulfur batteries[5].

Moreover, the volume changes of the sulfur cathode during the charge and discharge processes are also a big problem that needs to be faced. The density of sulfur is 2.07 g cm^{-1}, while the the density of Li_2S is only 1.66 g cm^{-1}. Thus, reduction from sulfur to Li_2S will lead to volume expansion as large as 80%, which results in pulverization of the active materials and fast capacity decay[128].

2.2.2 Electrolyte

Polysulfide anions are extremely reactive, and they are well known to react with most of the common electrolyte solvents, such as esters, carbonates, and phosphates. As a result, suitable electrolyte solvents for lithium/ sulfur batteries are very limited. The ideal electrolyte solvent for lithium/ sulfur batteries should meet the following requirements: (1) be chemically stable against polysulfide anions, polysulfide anionic radicals and lithium anode; (2) has high polysulfide solubility; (3) has low viscosity in polysulfide solution. Based on

recent research, suitable electrolyte solvents for lithium/sulfur batteries are limited to the linear and cyclic ethers, such as poly (ethylene glycol) dimethyl ether (M_n=500)[33], Tetraethylene glycol dimethyl ether[8], 1,2-dimethyl ether (DME) and 1,3-dioxolane (DOL)[7, 10, 11, 13, 14, 53, 56, 62, 129, 130]. As the lithium polysulfides can react with most of the conventional lithium salts, such as $LiPF_6$, $LiBF_4$, lithium bisoxalatoborate (LiBOB), and lithium difluoro(oxalato)borate ($LiBF_2C_2O_4$), the choice of lithium salt is also very limited[131]. So far, only $LiSO_3CF_3$[130]and $LiN(SO_2CF_3)_2$ [54, 132]have been used as the lithium salt in electrolyte for lithium/sulfur batteries.

2.2.3 Lithium anode

Dendritic lithium is usually a big safety issue in the lithium cell system, but in lithium/sulfur batteries, it is not so severe. The dissolved polysulfide can "chemically dissolve" the lithium dendrites due to the high surface area of the lithium dendrites. Moreover, the Li_2S and Li_2S_2 produced during the reaction between the polysulfide and the dendritic lithium can form dense surface layers, which will slow down or even fully inhibit further reaction between the polysulfide and the lithium[66]. As a result, the main problem with the lithium anode is not the safety issue, but rather the low coulombic efficiency, the capacity fading, and the rough/loose morphology of the lithium plating.

2.3. Methods to overcome the challenges

Many approaches have been investigated for improving the performances of the Li/S battery, such as synthesizing sulfur/carbon composite and sulfur/conducting polymer composites [8, 33, 133-152], adding adsorption additives such as Al_2O_3 and TiO_2 to the cathodes [2, 17, 65, 76, 153-157], introducing a proctective film for the lithium anode[158], modification of the electrolyte[159], and applying the new capacity limited charging technique to improve the cycling performance.

2.3.1 Modification of the sulfur cathode

2.3.1.1 Synthesis of carbon-sulfur composite

Carbon has played an important role in the cathode of lithium/sulfur batteries, not only because of its high electronic conductivity, but also due to its very good polysulfide absorbent properties [1, 4, 35, 43, 51, 133, 137, 160-175]. The conductive carbon can provide sites for the reactions of sulfur and polysulfides. It can also trap the polysulfide species. There are four methods reported for the synthesis of carbon-sulfur composites. The first one is the melt-diffusion method [6, 8, 9, 16, 32, 53], which involves heating sulfur to near 160 ºC and then impregnating the melting sulfur into the pores of the carbon. The second one is the solution method, dissolving sulfur in a solvent such as carbon disulphide (CS_2), toluene, o-xylene, or dimethyl sulfoxide (DMSO), followed by adding porous carbon into the solution to absorb the dissolved sulfur [7, 12, 13, 176]. The third method is the chemical precipitation method, depositing sulfur into carbon by decomposition of thiosulfate in acid [11, 54]. The reaction equation is as follows:

$$S_2O_3^{2-} + 2H^+ \rightarrow S\downarrow + SO_2\uparrow + H_2O. \quad (2.8)$$

The fourth method involves subliming sulfur into the carbon source [5].

2.3.1.1.1. Porous carbon-sulfur composite

Many scientists have tried to synthesize porous carbon-sulfur composites to enhance the electrochemical performance of sulfur cathode[177-181].

The Linda F. Nazar group reported spherical ordered mesoporous carbon nanoparticles/sulfur cathode for lithium/sulfur batteries synthesized by the melt-diffusion method. Figure 2.6 presents SEM and TEM images of the spherical ordered mesoporous carbon nanoparticles/sulfur composite. The composite shows a high reversible charge capacity of up to 1200 mAh g^{-1} and good cycling stability [6].

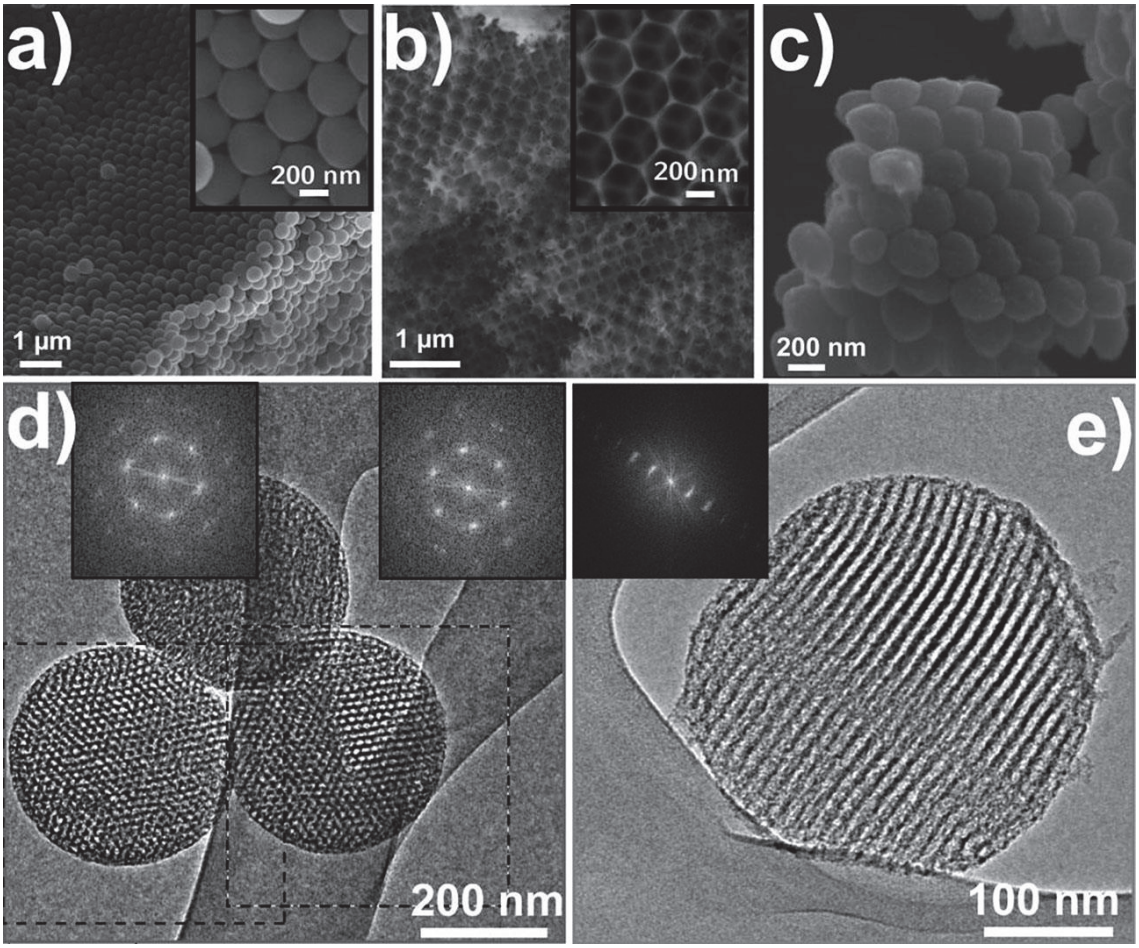

Figure 2.6 SEM images of: (a) poly(methyl methacrylate) (PMMA) spheres with ordered close packing; (b) Silica inverse opal structure; (c) Octylmethoxycinnamate (OMC) spheres ordered in opal structure. (d, e) TEM images of spherical OMC nanoparticles (inset: fast Fourier transforms (FFT) of the indicated squares) [6].

Hierarchically structured sulfur/carbon nanocomposite material has been reported to improve the cyclability and the utilization of sulfur in lithium/sulfur batteries by Chengdu Liang and his co-workers, as shown in Figure 2.7. [7] In that work, the initial discharge capacity of the cells could be as high as 1584 mAh g^{-1}.

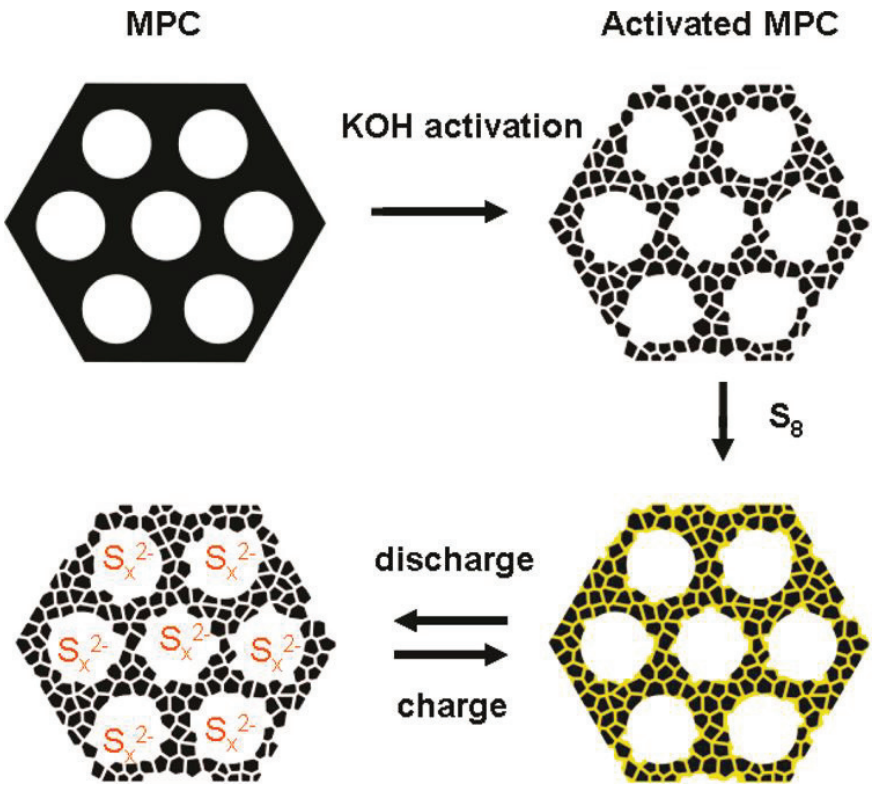

Figure 2.7 Illustration of the preparation of sulfur-carbon composite [7].

As shown in Figure 2.8, Chaofeng Zhang et al. synthesized a new sulfur-carbon nanocomposite by confining the sulfur in double-shelled hollow carbon spheres for lithium/sulfur batteries. Figure 2.9 demonstrates that the as-prepared sulfur-carbon nanocomposite has superior electrochemical performance with high specific capacity, and excellent cycling stability and rate capability [8].

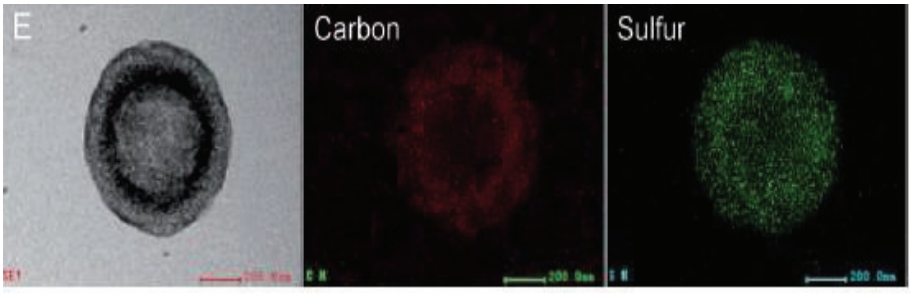

Figure 2.8 TEM image and corresponding elemental mapping of a prepared single double shelled hollow carbon – sulfur sphere (DHCS-S) [8].

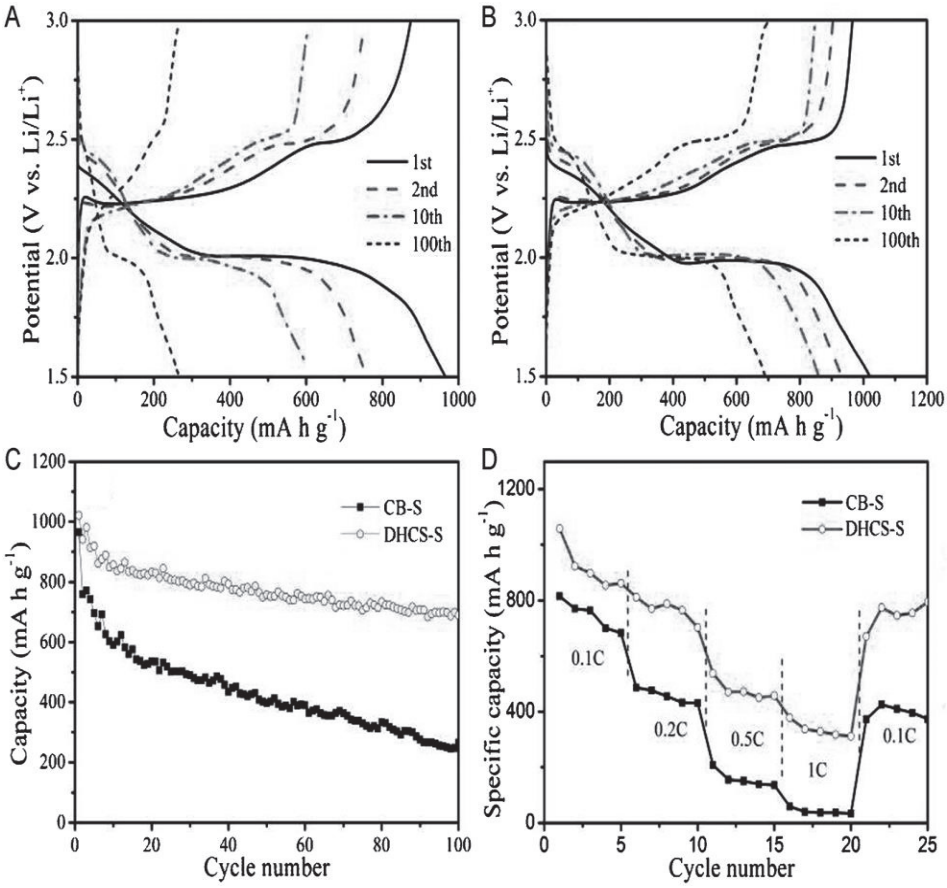

Figure 2.9 Discharge/charge profiles for selected cycles of: (A) carbon-black – sulfur (CB-S) and (B) double-shelled hollow carbon spheres-sulfur (DHCS-S) electrodes, (C) cycling performance of CB-S and DHCS-S , (D) rate capabilities of the CB-S and DHCS-S [8].

Moreover, one type of sulfur-carbon sphere composite was reported to enhance the long-term stability of sulfur cathode for a high energy lithium-sulfur battery system, as is shown in Figure 2.10 [9]. It is claimed that the sulfur–carbon sphere composite with 42 wt% sulfur presents the large reversible capacity of about 650 mAh g^{-1} after 500 cycles at current density of 400 mA g^{-1}. It is concluded that the long-term electrochemical stability of sulfur cathode can be enhanced significantly by encapsulating sulfur into the narrow micropores of the carbon spheres.

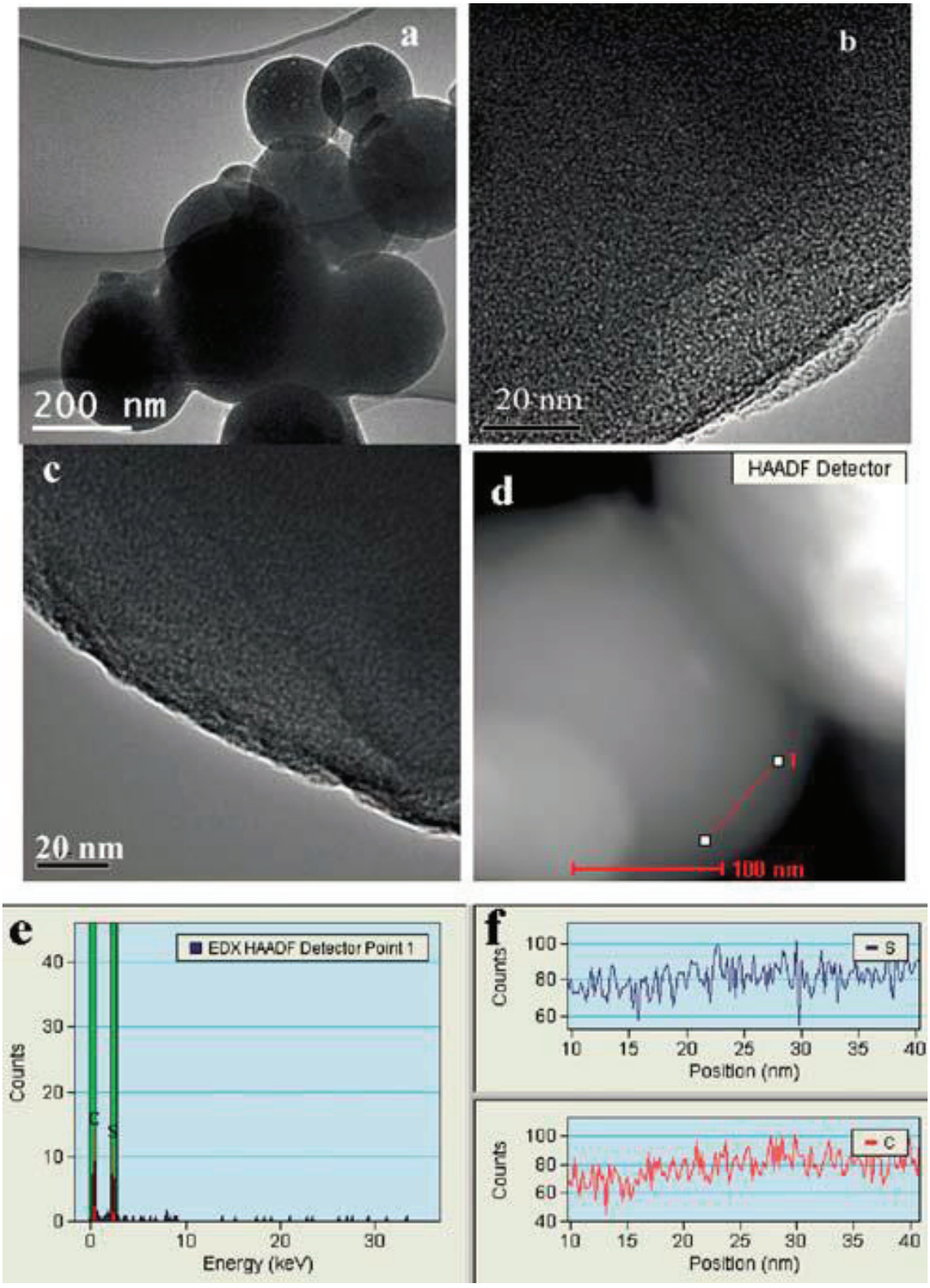

Figure 2.10 (a) and (b)TEM images of carbon spheres at different magnification; (c) the sulfur–carbon sphere composite with 42 wt% sulfur; (d) high angle annular dark field – scanning TEM (HAADF-STEM) image; (e) energy dispersive X-ray spectroscopy (EDX)

spectrum; and (f) corresponding line-scanning of sulfur and carbon elements across a selected area (red line in d) of the sulfur–carbon sphere composite with 42 wt% sulfur.[9]

2.3.1.1.2. CNT-sulfur composite

Carbon nanotube (CNT) is one type of useful conducting agent that has been considered to improve the conductivity of sulfur cathode and to confine the dissolved polysulfides to some extent[182].

Zhou et al. reported the template-directed synthesis of sulfur-carbon nanotubes for lithium/sulfur batteries, and the structure of their S-CNT cathode is shown in Figure 2.11. The discharge capacity of sulfur in this electrode was 712 mA h g^{-1} (23 wt% S) and 520 mA h g^{-1} (50 wt% S) at a high current density (6 A g^{-1}). These results demonstrate the great potential of this sulfur-CNT cathode for Li-S batteries with fast charge–discharge performance and long life [10].

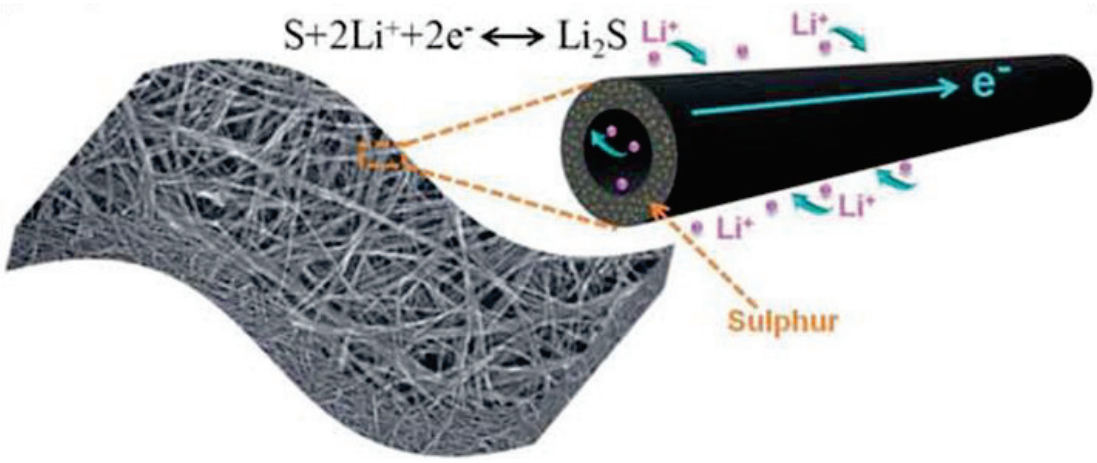

Figure 2.11 Schematic diagram of S-CNT cathode [10].

Self-weaving sulfur-multiwalled (MW) CNT composite cathodes with high-rate cyclability have been reported by Manthiram's group [11]. The composite was synthesized by an *in-situ* sulfur deposition method, as shown in Figure 2.12. The SEM images and EDS mapping of the self-weaving sulfur – MWCNT composite are presented in Figure 2.13. The

composite cathode exhibits high capacities of 1352 mAh g^{-1} at the 1 C rate and 1012 mAh g^{-1} at the 4 C rate. While the highly conductive MWCNTs improve the active material utilization at high rates, the absorption capability of the cathode framework localizes the electrolyte and suppresses the migration of soluble polysulfides. The design and facile synthesis of this cathode enhance the feasibility of practical high-rate Li–S batteries.

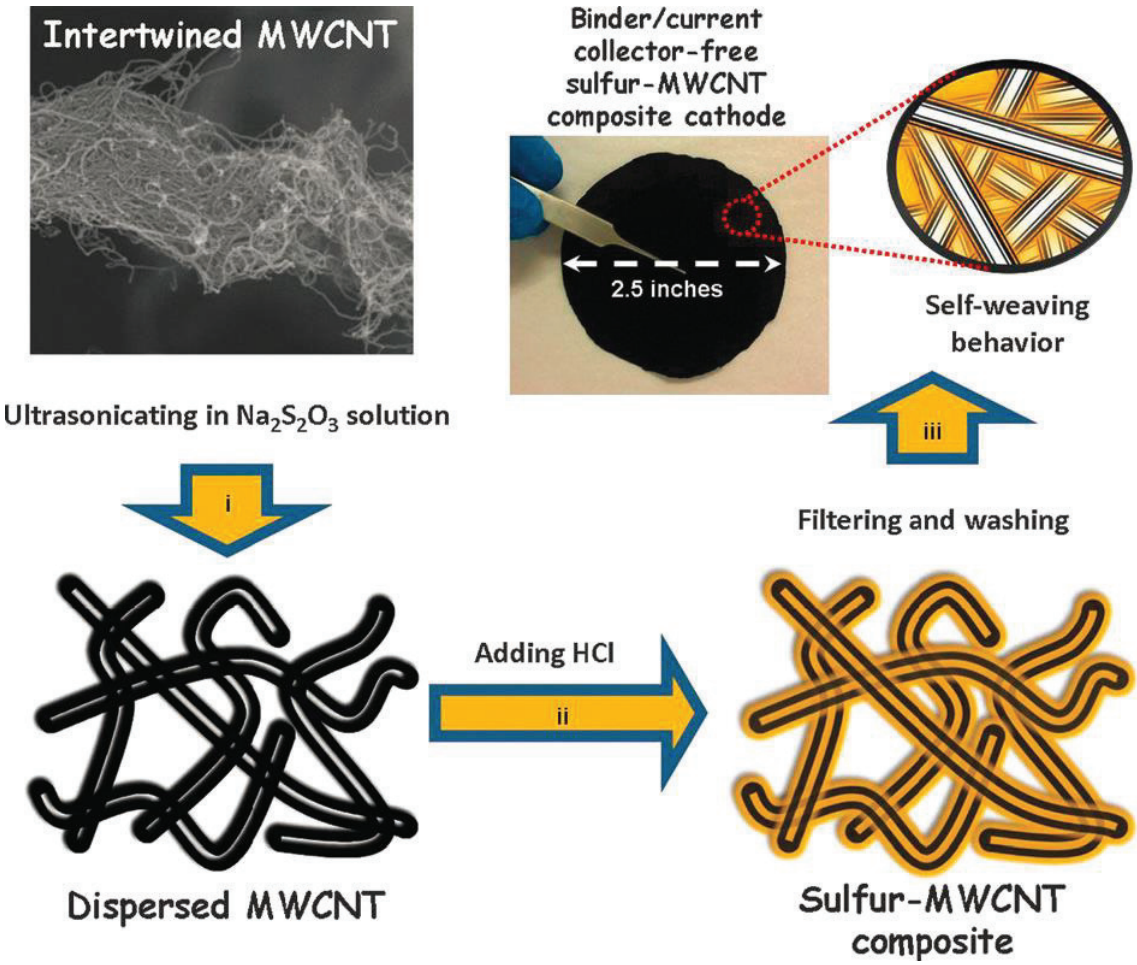

Figure 2.12 Schematic illustration of the three-step fabrication process for a self-weaving sulfur–MWCNT composite cathodes: (i) dispersion of MWCNTs, (ii) sulfur nucleation (yellow) onto MWCNTs, and (iii) vacuum filtration, washing, and then drying [11].

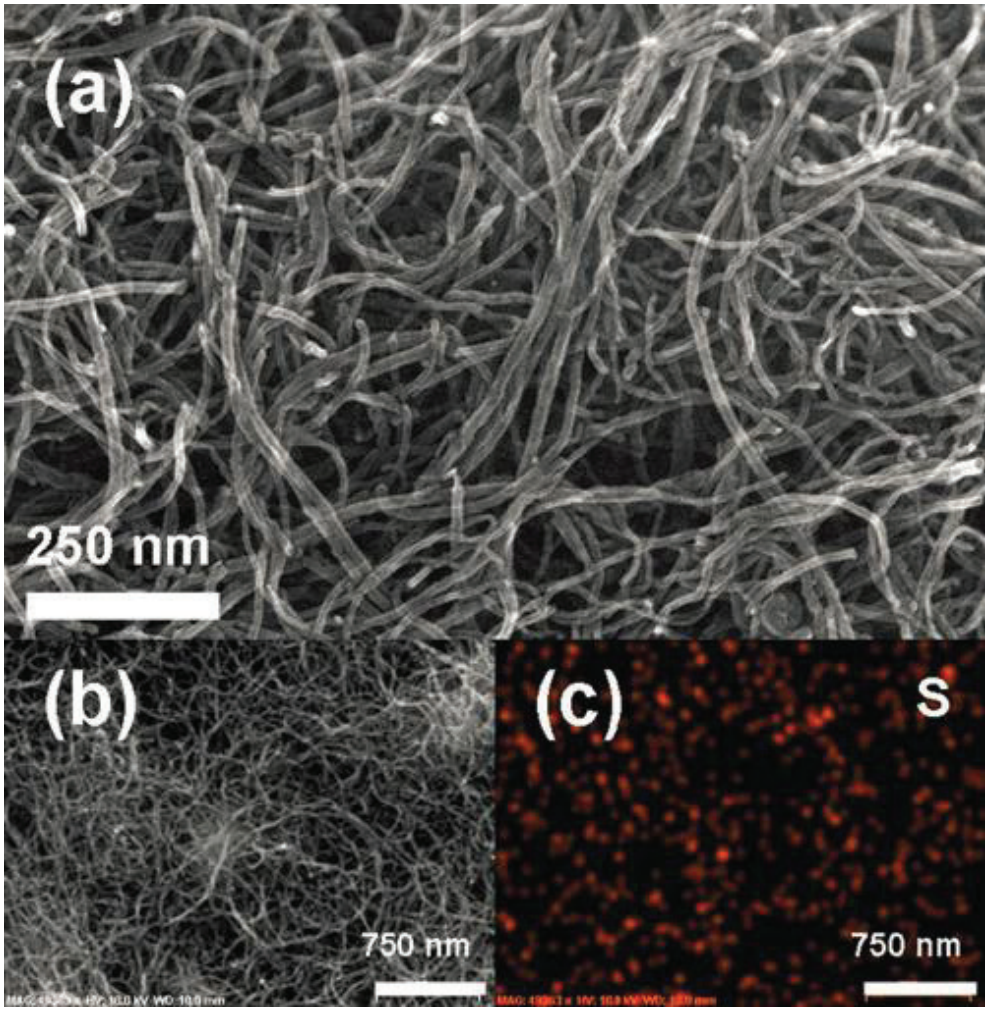

Figure 2.13 (a) High-resolution SEM image of MWCNTs in the S-CNT-A cathode, (b) SEM image of the S–CNT–A cathode sample, and (c) elemental sulfur distribution in (b) [11].

M. Hagen prepared binder-free CNT cathodes containing the highest total percentage of sulfur (90%) in the electrode to be reported so far [5]. SEM images of the CNT electrodes sulphurized through different techniques are presented from different points of view and at different magnifications in Figure 2.14. It is reported that the sulphur mass per cm^2 electrode can be more than three times as high as in regular slurry-based sulphur electrodes, thus doubling the volumetric energy density.

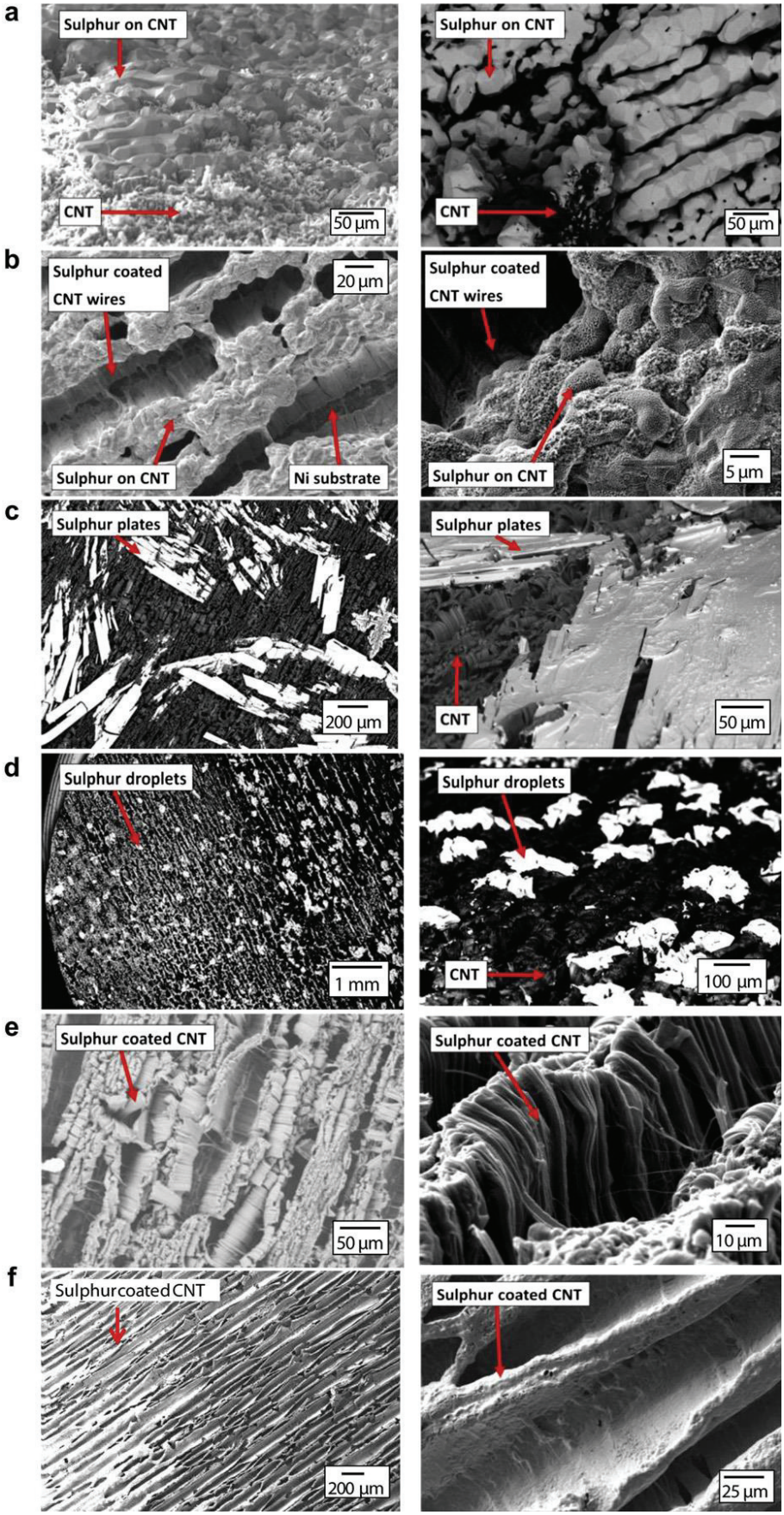

Figure 2.14 SEM images of: (a) vaporization of sulfur with subsequent condensation on CNT

surface; (b) Sulfur powder melted on CNT at 120 °C; (c) hot toluol + S solution (80 °C) deposited on RT CNT-electrode; (d) RT toluol + S solution deposited on room temperature (RT) CNT-electrode; (e) hot toluol + S solution (80 °C) deposited on hot CNT-electrode; and (f) RT toluol + S solution deposited on hot CNT-electrode [5].

2.3.1.1.3. CNF-sulfur composite

High-performance of a hollow carbon nanofiber (CNF)-encapsulated sulfur cathode (shown in Figure 2.15) for lithium sulfur batteries has been reported by Yi Cui's group [12]. A high specific capacity of about 730 mAh/g was observed at the C/5 rate after 150 cycles of charge/discharge. Later, his group also reported the amphiphilic surface modification of the hollow carbon nanofibers leading to improved cycle life of lithium sulfur batteries [13]. The modified sulfur cathode shows excellent cycling performance with specific capacity close to 1180 mAh/g at the C/5 current rate. Capacity retention of 80% is achieved over 300 cycles at C/2 in Figure 2.16.

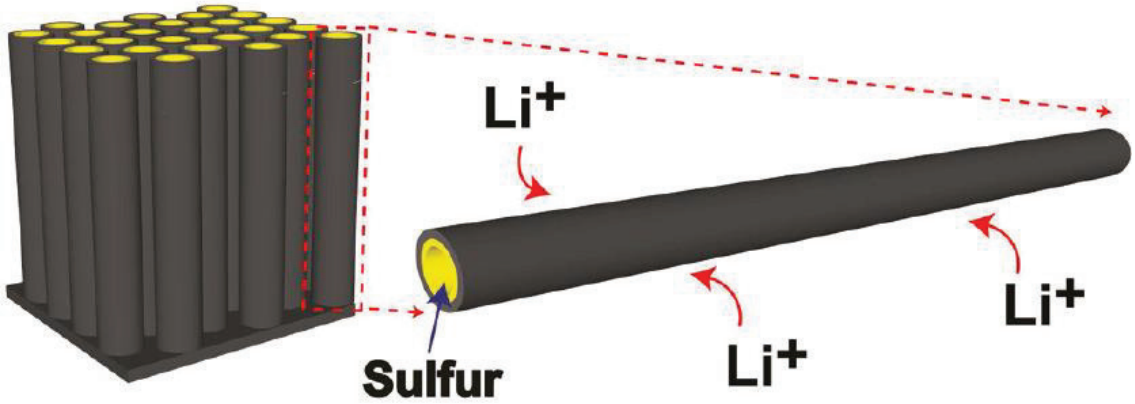

Figure 2.15 Schematic illustration of the design and fabrication process for hollow carbon nanofibers/sulfur composite structure [12].

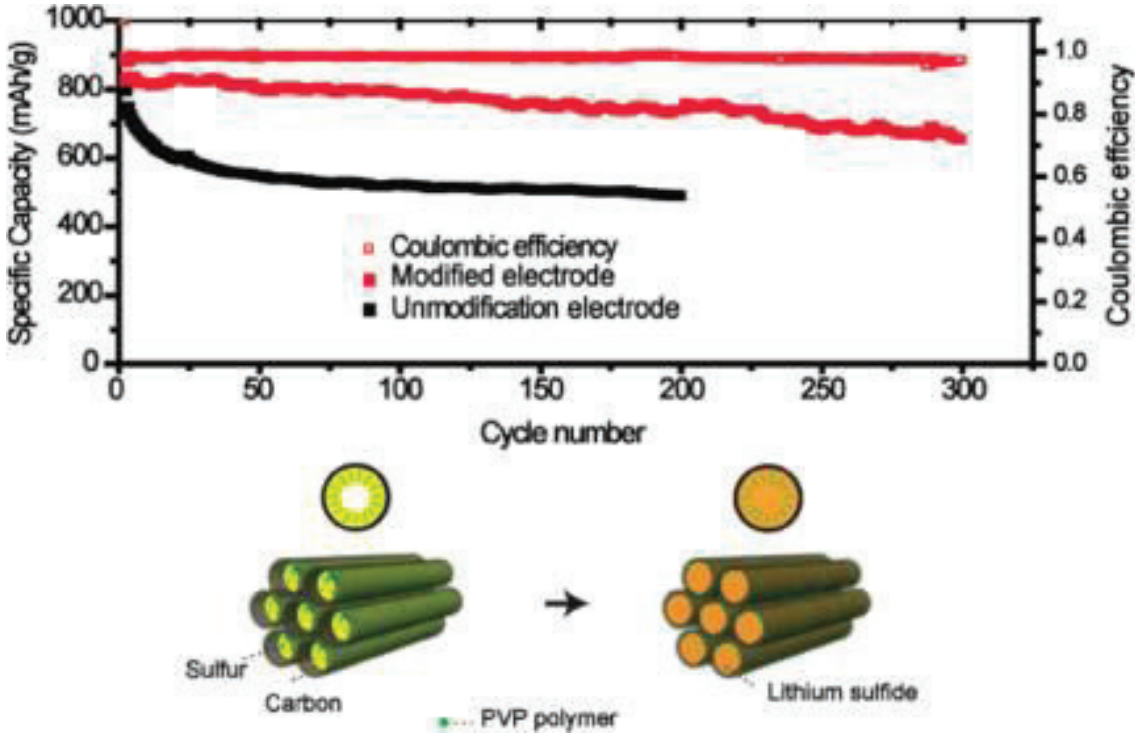

Figure 2.16 Cycling performance of the electrodes with and without polyviylpyrrolidone (PVP) modification at C/2; and schematic diagrams of the polymer modified sulfur cathode before (left) and after discharge (right) [13].

2.3.1.1.4. Graphene (oxide)-sulfur composite

Graphene is a single layer of carbon atoms tightly packed into a two-dimensional (2D) honeycomb sp^2 carbon lattice, which has attracted a great deal of attention in recent years because of its intriguing properties, such as high thermal conductivity, superior mechanical properties, and unusual electronic properties. The surface area of graphene is 2630 m^2 g^{-1}, which is hugely favourable for energy storage applications. Graphene is conductive and easy to functionalize with other molecules [183] .

Recently, graphene and reduced graphene oxide (RGO) have been used in Li–S cells as a conductive support and S immobilizer [31, 34, 57-60, 132, 184-188]. An RGO – thermally expanded graphene (TG) – S nanocomposite with an outstanding high-rate performance for lithium–sulfur batteries was reported by Yi Shi's group[14]. A schematic illustration of the

RGO–TG–S nanocomposite for improving cathode performance is shown in Figure 2.17. A reversible capacity of approximately 667 mAh g^{-1} was observed after 200 cycles at the high rate of 1.6 A g^{-1} (0.95 C).

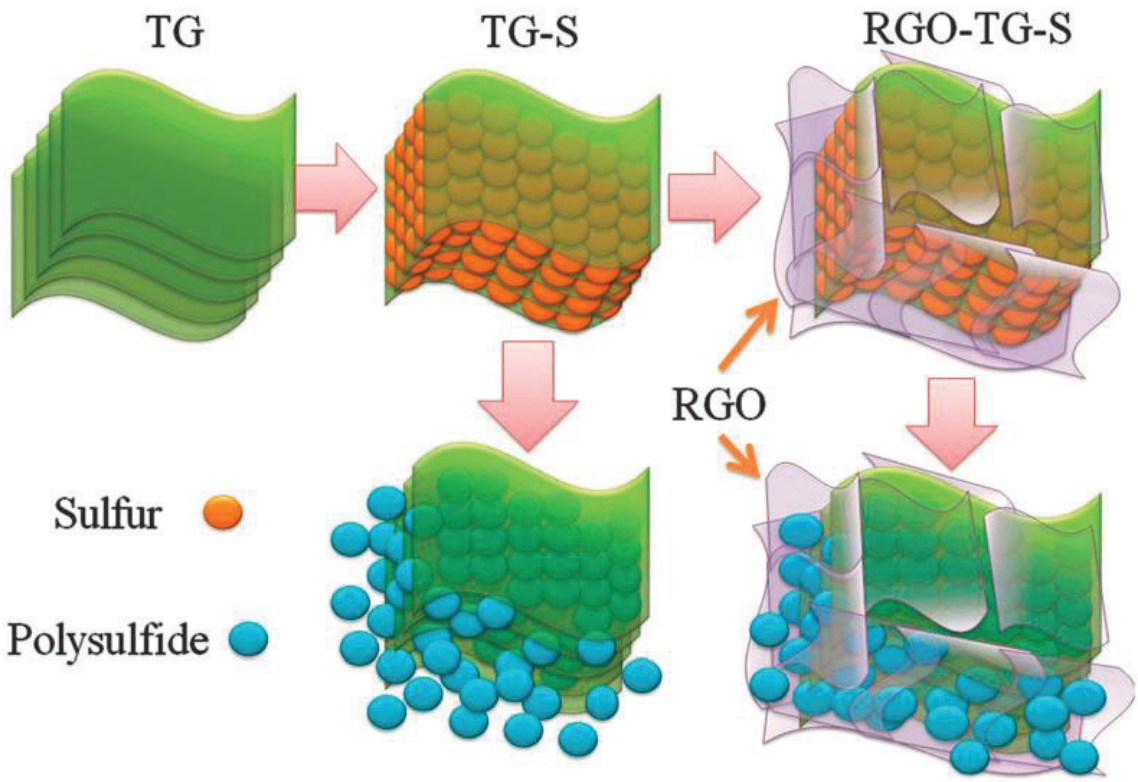

Figure 2.17 Schematic illustration of the RGO–TG–S nanocomposite for improving cathode performance in lithium/sulfur batteries. [14].

A sulfur-impregnated graphene composite with a one-step synthesis was demonstrated by Min-Sik Park et al.[15]. A schematic illustration of the heterogeneous crystal growth mechanism of S particles in the interior space between randomly dispersed graphene sheets by precipitation method is presented in Figure 2.18. FESEM images and TEM images of the S-impregnated graphene composite are shown in Figure 2.19, which demonstrates that the sulfur particles are very well impregnated into the graphene. The initial discharge capacity is as high as 1237 mA h g^{-1} during the first cycle, and good cyclic retention of 67% capacity after 50 cycles is attained in the voltage range of 1.8–2.6 V vs. Li/Li^{+}. It is proved that the sulfur-impregnated graphene composite is a superior cathode material, owing to its

advantages of confining the active sulfur, preventing the dissolution of soluble polysulfides, and providing sufficient electrical conduction.

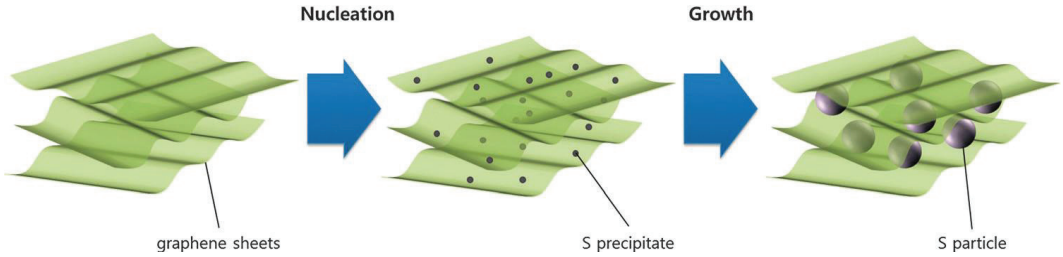

Figure 2.18 Schematic illustration of the heterogeneous crystal growth mechanism of sulfur particles in the interior space between randomly dispersed graphene sheets by the precipitation method [15].

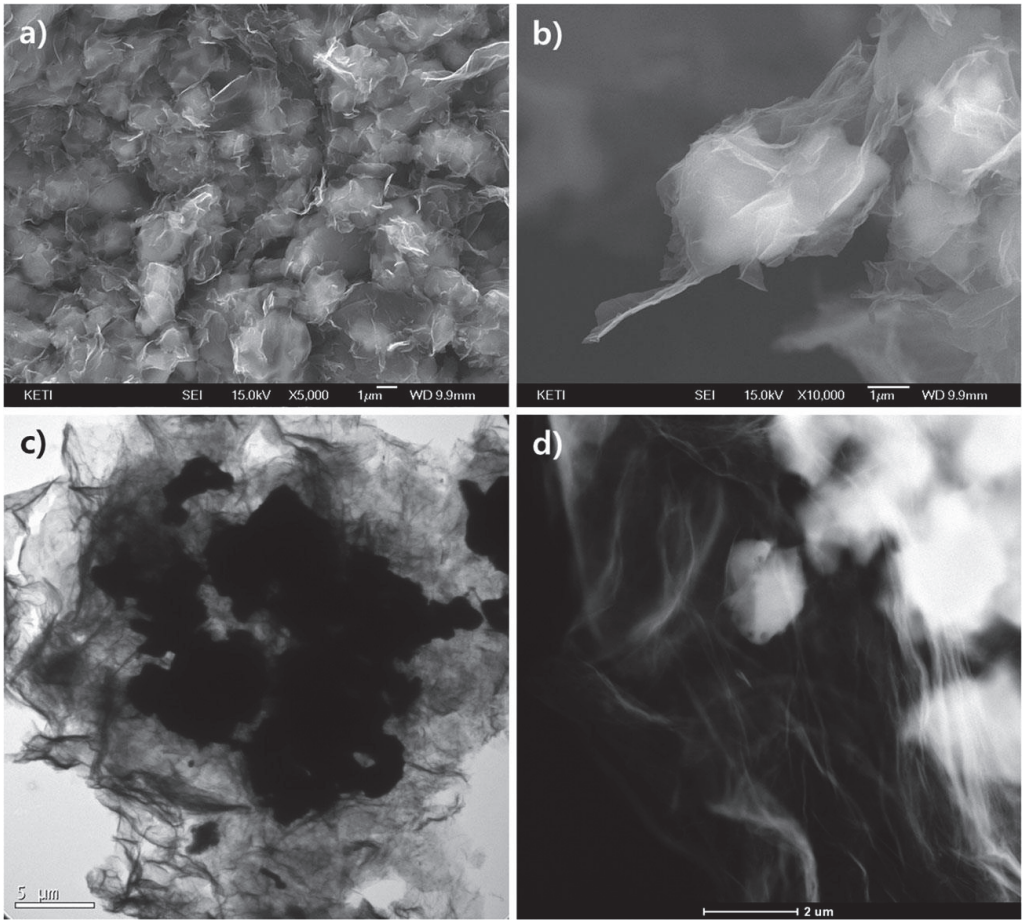

Figure 2.19 (a) and (b) FESEM images of S-impregnated graphene composite at different magnifications; (c) and (d) TEM image of the S-impregnated graphene composite [15].

Ding et al. reported an efficient strategy to confine active sulfur in chemically tailored graphene nanosheets, which were prepared via modified chemical activation of hydrothermal reduced graphene oxide hydrogels [16]. As shown in Figure 2.20, sulfur was uniformly confined in the nanopores of activated graphene nanosheets (AGNs). The sulfur was uniformly constrained and generated intimate electrical contact with the AGN framework, and the nanopores, acting as "micro-reactors" for the electrochemical reactions, were able to trap the polysulfide species and accommodate the volume expansion, leading to high specific capacity and excellent cycling stability.

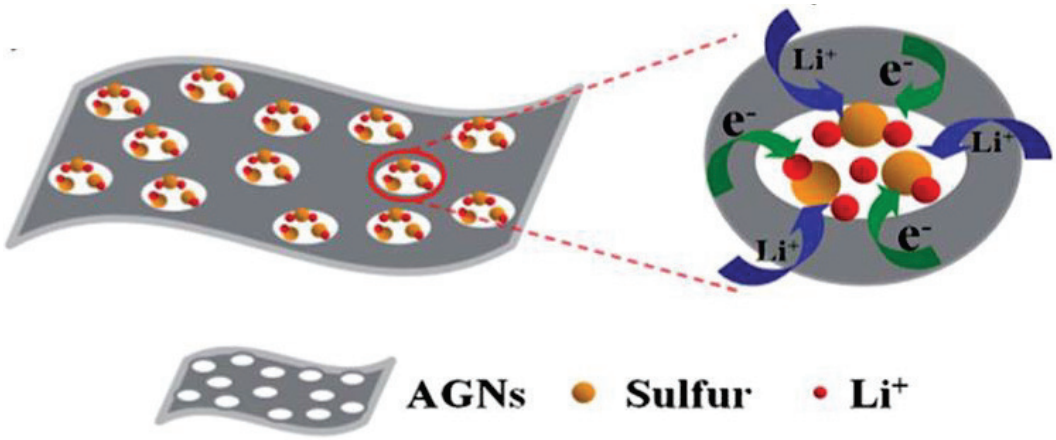

Figure 2.20 Schematic illustration of the AGNs/S composites to confine the diffusion of polysulfide species [16].

2.3.1.2. Synthesis of metal-oxide – sulfur composite

In order to trap the dissolved polysulfides in the cathode, many reseachers have tried to introduce metal oxide into the sulfur cathode of lithium/sulfur batteries, such as Al_2O_3 and TiO_2 [2, 17, 65, 129].

2.3.1.2.1. Al_2O_3-sulfur composite

Y. J. Choi demonstrated that a sulfur electrode containing nano-Al_2O_3 particles showed good cycling performance and higher discharge capacity of 660 mAh g^{-1} compared to sulfur electrode without nano Al_2O_3 [129]. It is therefore concluded that the addition of

nanosized Al_2O_3 particles has a beneficial effect towards preventing the dissolution of lithium polysulfides in liquid electrolyte.

2.3.1.2.2. TiO_2-sulfur composite

Linda F. Nazar's group reported that a cell containing TiO_2 with a 5 nm pore diameter exhibited 37% greater discharge capacity retention after 100 cycles than a cell without the titania additive [2]. The discharge capacity of the cell still remained above 750 mAh g^{-1} after 200 cycles, as shown in Figure 2.21.

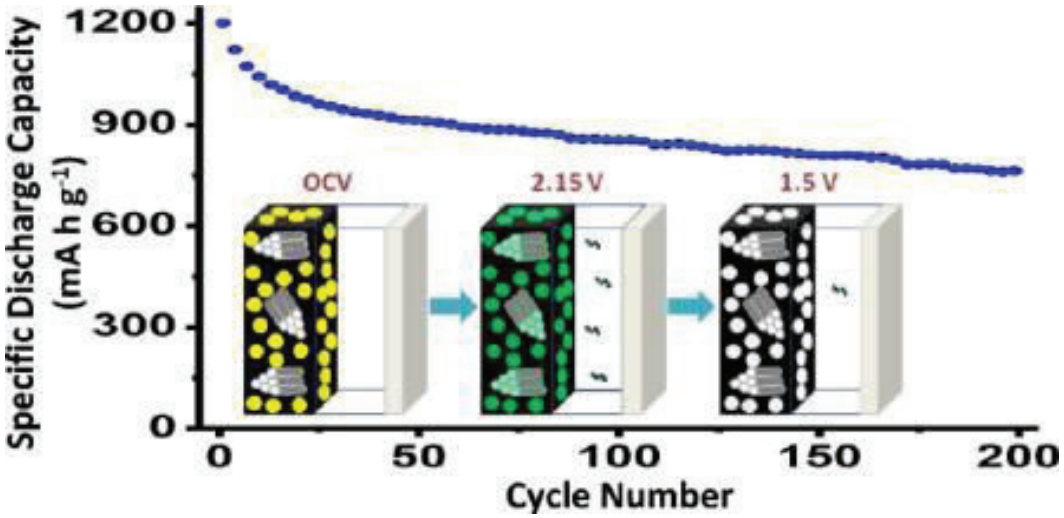

Figure 2.21 Schematic illustration of the concept of polysulfide reservoirs vs. no reservoirs and the cycling performance of silica colloid monolith (SCM)/S-α-TiO_2 [2].

Yi Cui's group demonstrated the design of a sulfur–TiO_2 yolk–shell nanoarchitecture with internal void space to accommodate the volume expansion of sulfur, resulting in an intact TiO_2 shell to minimize polysulfide dissolution [17]. The working mechanisms of the bare sulfur particles and the yolk–shell TiO_2-S are shown in Figure 2.22. The bare sulfur particles undergo large volumetric expansion and polysulfide dissolution upon lithiation, as presented in Figure 2.22(a). The core–shell morphology provides a protective coating, but as shown in Figure 2.22(b), cracking of the shell will take place upon volume expansion of sulfur during lithiation, resulting in polysulfide dissolution as well. In Figure 2.21(c), the yolk–shell

morphology provides internal void space to accommodate the volume expansion of sulfur during lithiation, leading to a structurally intact shell for effective trapping of polysulfides. As a result, an initial specific capacity of 1,030 mAh g^{-1} at 0.5 C and coulombic efficiency of 98.4% over 1,000 cycles are achieved. Most importantly, the capacity decay after 1,000 cycles is as small as 0.033% per cycle, which represents the best performance for long-cycle lithium–sulfur batteries so far.

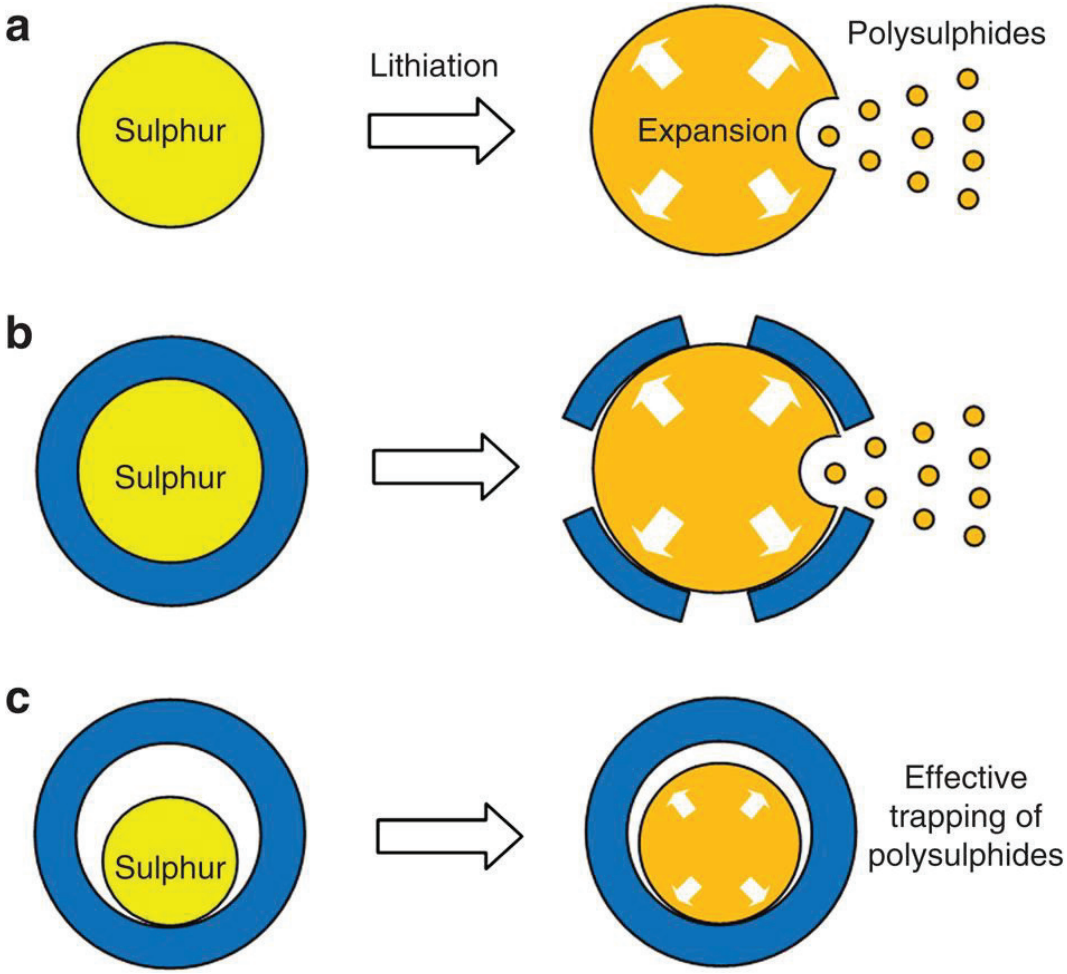

Figure 2.22 Schematic illustration of the working mechanism of bare sulfur particles and yolk–shell TiO_2-S particles [17].

2.3.1.3 Synthesis of conducting polymer-sulfur composite

As conducting polymers have a chain-like structure and rich functional groups, they can facilitate chemical trapping of polysulfides[189-191]. Thus, a conducting polymer can

maintain good physical confinement in a similar manner to carbon. Moreover, the mechanical properties of polymers allow for better accommodation of volume expansion than pure carbon coatings[192, 193]. These merits mean that conducting polymers offer exciting opportunities for designing sulfur cathodes with superior performance. Last but not least, conducting polymers are soluble or dispersible in various solvents, which makes the preparation of polymer-sulfur composites easier, especially by the wet chemical method. Because the melting point of sulfur is only 115 ℃, the reaction temperature should be no higher than 100 ℃ during the synthesis in the wet chemical method. [194-196].

J. Wang et al. prepared a novel conducing sulfur-polypyrrole composite by the chemical polymerization method for lithium/sulfur batteries [33]. The nanosize polypyrrole particles were uniformly coated on the surfaces of the sulfur particles, which significantly enhanced the discharge capacity and the cycling life of the cells. This is the first time that PPy was introduced into the lithium/sulfur battery system to improve the performance of sulfur cathodes.

Yongzhu Fu and Arumugam Manthiram reported that a mixed ionic−electronic conductor (MIEC) composed of polypyrrole (PPy) synthesized with poly(2-acrylamido-2-methyl-1 propanesulfonic acid) (PAAMPSA) was explored as an additive in sulfur cathodes for rechargeable lithium−sulfur (Li−S) batteries[62]. The composite shows enhanced electrochemical performance, which retains a capacity of > 600 mA h g^{-1} at low rates and 500 mA h g^{-1} at 1 C after 50 cycles. They also synthesized a sulfur−polypyrrole composite consisting of orthorhombic bipyramidal sulfur particles (63.3 wt %) coated with a polypyrrole nanolayer by a low cost, scalable, environmentally benign process and investigated it as a cathode material for lithium/sulfur batteries[18]. As shown in Figure 2.23, the well-shaped orthorhombic bipyramidal sulfur particles are coated very uniformly by a polypyrrole nano-layer, resulting in better electrochemical stability, cyclability, and rate

capability than pristine sulfur, because the polypyrrole coating works as a conductive matrix for electron transfer and prevents lithium polysulfide dissolution at the same time.

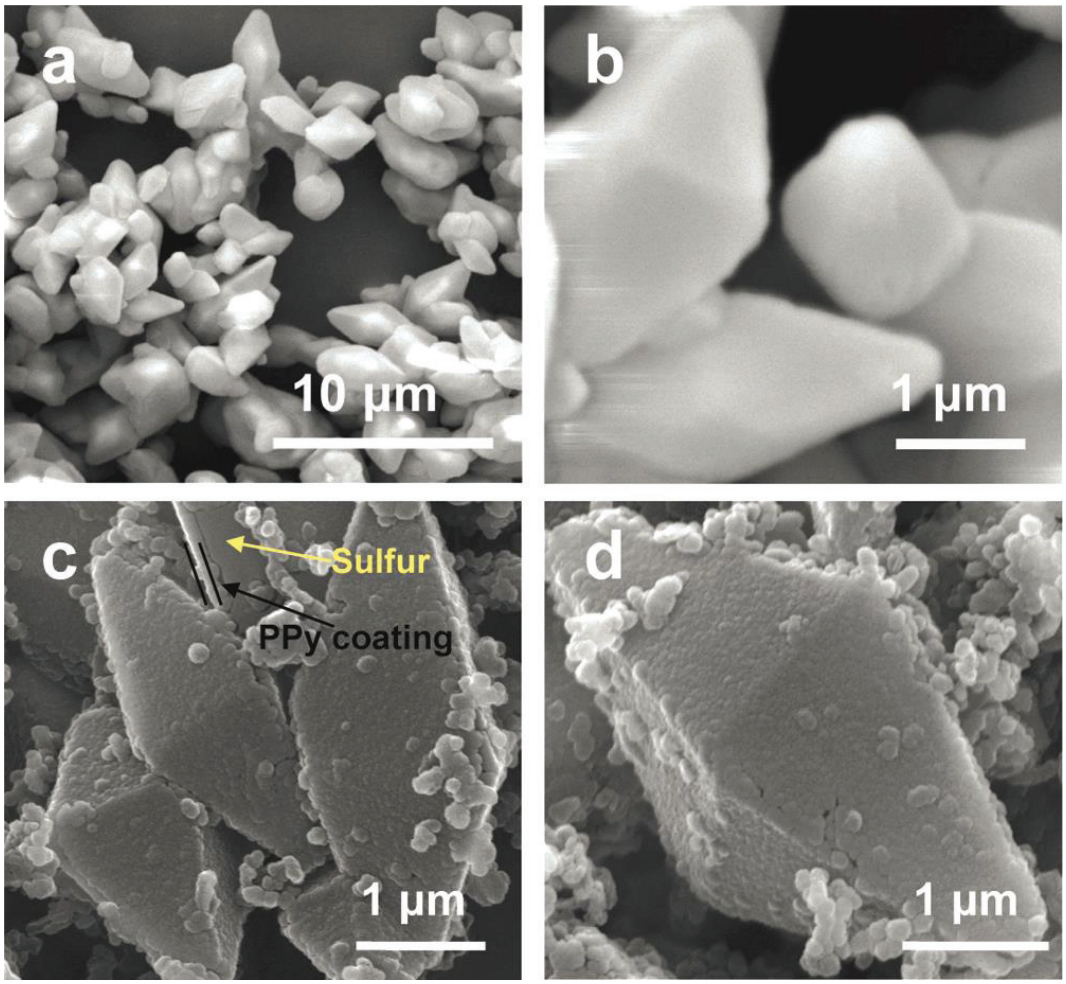

Figure 2.23 SEM images of: (a) the bipyramidal sulfur particles, (b) magnified sulfur particles, (c) sulfur−polypyrrole (S−PPy) composite with bipyramidal shape, and (d) a single S−PPy composite particle [18].

Yi Cui's group reported that coating the conducting polymer poly(3,4-ethylenedioxythiophene) polystyrene sulfonate (PEDOT:PSS) on the surfaces of mesoporous carbon/sulfur particles can effectively trap the polysulfides, minimizing the dissolution of polysulfides and the loss of the active mass in the cathode [19]. Figure 2.24 shows a schematic illustration of PEDOT:PSS-coated CMK-3/sulfur composite with improved cathode performance. On comparing Figure 2.24(a) and (b), it is found that with the conductive

polymer coating layer, the polysulfides could be confined within the carbon matrix. Lithium ions and electrons can move through this polymer layer. As a result, the initial discharge capacity reached 1140 mAh/g. And the discharge capacity was still over 600 mAh/g at the 150th cycle. In prolonged cycling, the capacity retention increased from ~60%/100 cycles to ~85%/100 cycles. Coulombic efficiency also increased from 93% to 97%. The cycle life and coulombic efficiency were markedly improved by coating with the conducting polymer PEDOT:PSS.

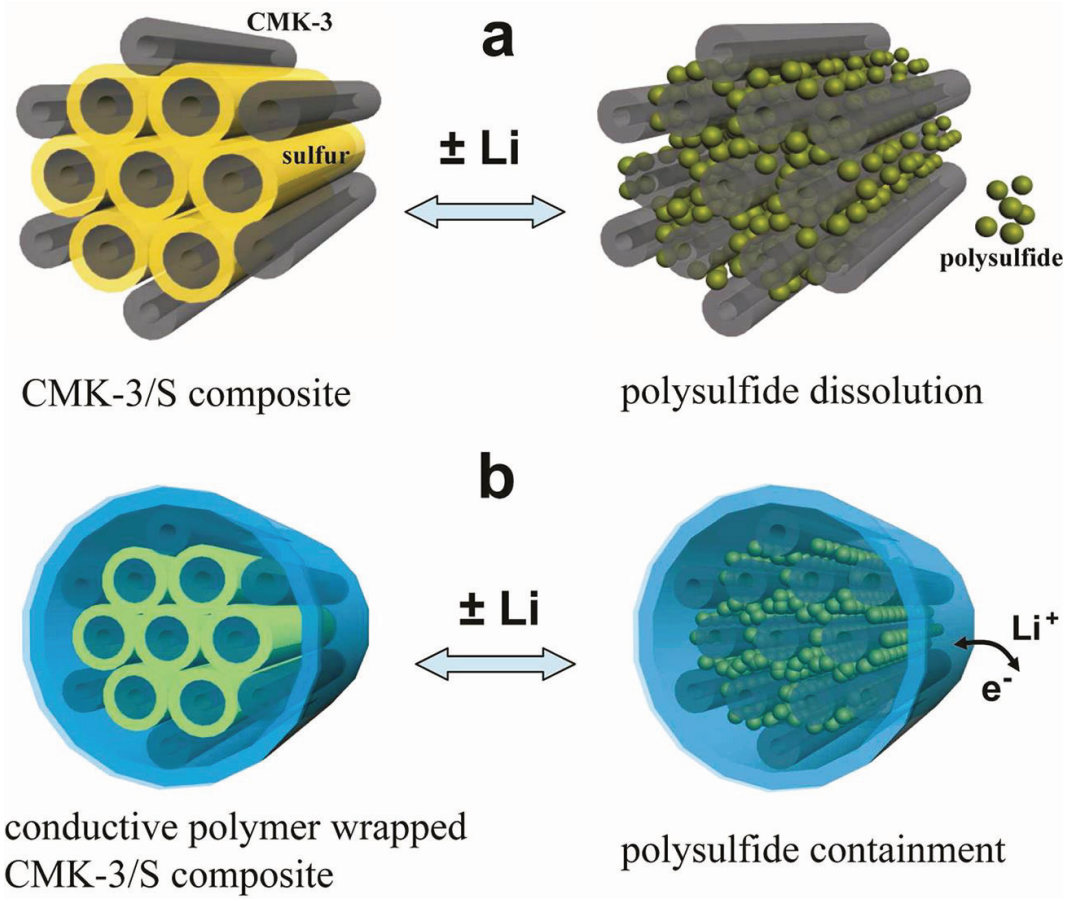

Figure 2.24 Schematic illustration of the polysulfide containment of the PEDOT:PSS coating layer on CMK-3/sulfur composite. (a) In CMK-3/S particles, polysulfides diffuse out of the carbon matrix during lithiation/ delithiation. (b) With a conductive polymer coating layer, polysulfides could be confined within the carbon matrix, while lithium ions and electrons can move through this polymer layer [19].

A novel vulcanized polyaniline (PANI) nanotube (NT)/sulfur composite was synthesized by Lifen Xiao et Al. via an *in-situ* vulcanization process. Figure 2.25 presents a schematic illustration of the construction and discharge/charge process of the sulfur polyaniline nanotube/sulfur (SPANI-NT/S) composite. Its SEM and TEM images are shown in Figure 2.26. Due to the protection of polyaniline, the electrode could retain a discharge capacity of 837 mAh g^{-1} after 100 cycles at the 0.1 C rate and manifested 76% capacity retention up to 500 cycles at the 1 C rate.

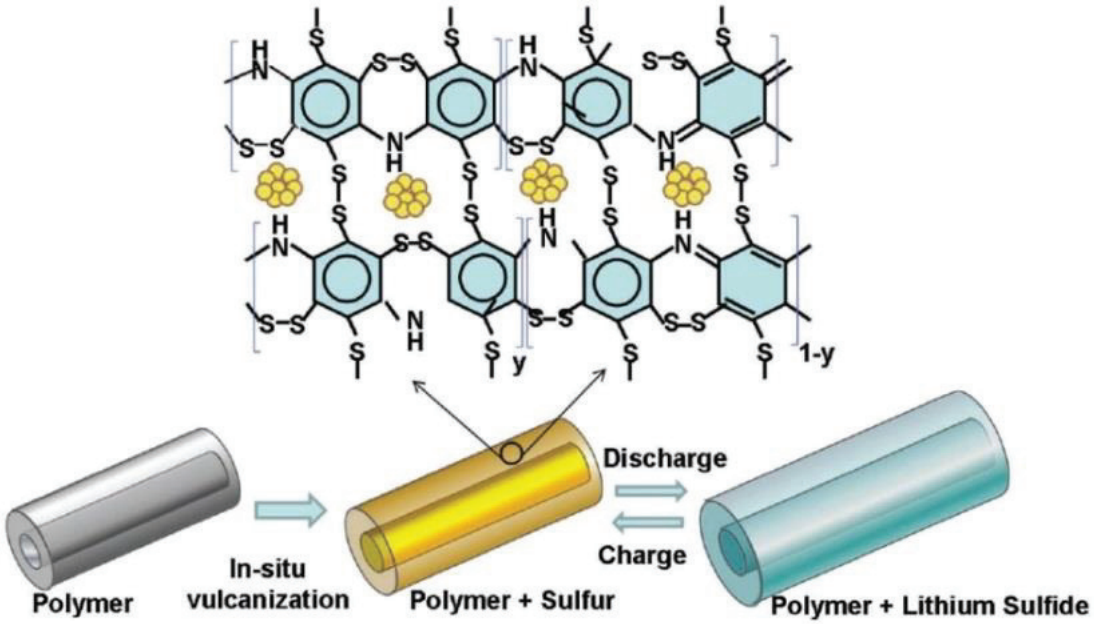

Figure 2.25 Schematic illustration of the construction and discharge/charge process of the SPANI-NT/S composite [20].

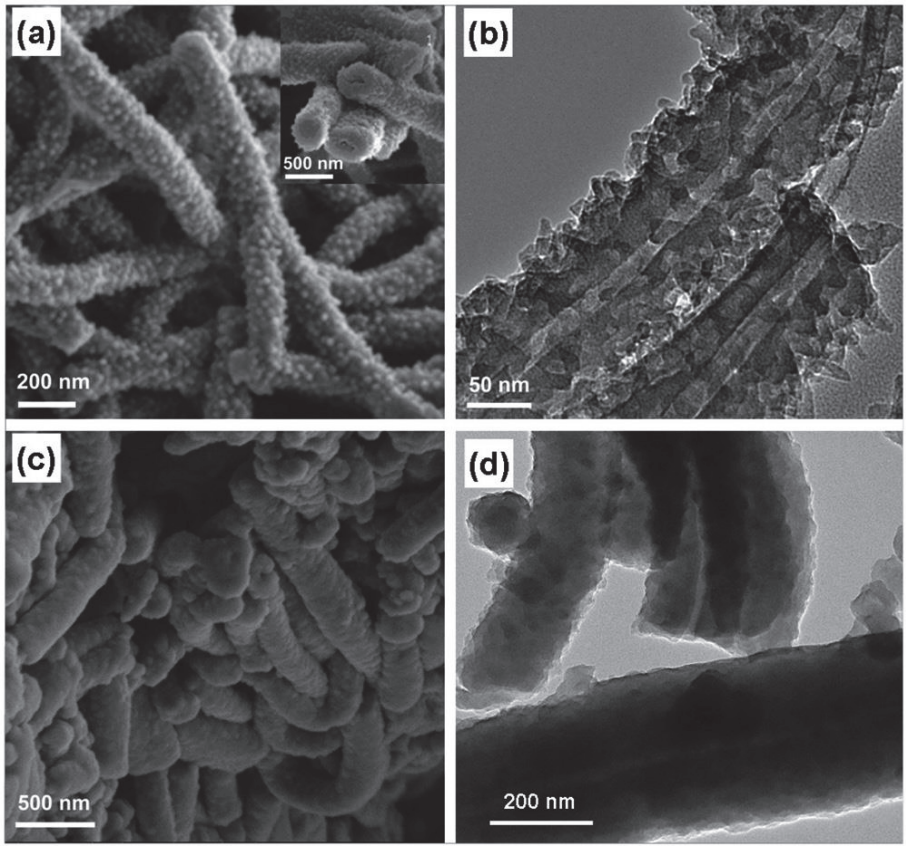

Figure 2.26 (a) SEM and (b) TEM images of the neat PANI-NT; (c) SEM and (d) TEM images of the SPANI-NT/S composite [20].

2.3.2 Modification of the electrolyte

Electrolyte has been attracted significant attention as it played an important role on improving the performance of the lithium/sulfur batteries. Many approaches have investigated to modify the electrolyte for lithium/sulfur batteries.

One is to introduce ionic liquid into the electrolyte[197]. Liwen Ji et al. used the ionic liquid lithium bis(fluorosulfonyl)imide (LiFSI) in 1-butyl-1-methylpyrrolidinium bis(trifluoromethanesulfonyl)imide ($PYR_{14}TFSI$) to modify poly(ethylene glycol) dimethyl ether (PEGDME) electrolyte for lithium/sulfur batteries with graphene oxide/sulfur as cathode [198]. The ionic liquid ($PYR_{14}TFSI$) can significantly reduce the viscosity and improve the ionic conductivity of the PEGDME. The lithium/sulfur cells demonstrated a high

reversible capacity of 950-1400 mA h g^{-1}, and stable cycling for more than 50 deep cycles at 0.1 C (1 C = 1675 mA g^{-1}).

Another approach is to use lithium nitrate ($LiNO_3$) as an additive [199]. Many studies have demonstrated its effect towards improving the performance of lithium/sulfur batteries, especially by enhancing the coulombic efficiency. Although the detailed chemical reactions of $LiNO_3$ inside the battery are not fully understood, it has been suggested that the oxidizing additive forms a stable passivation layer (Li_xNO_y and Li_xSO_y) on the lithium metal surface. This passivation layer can effectively slow down the reduction of polysulfide species at the lithium surface, resulting in higher Coulombic efficiency close to 98–99%. It is clear that the passivation film not only protects the lithium anode from chemical reaction with polysulfides, but also prevents polysulfides from undergoing electrochemical reduction on the lithium anode surface. The equations are shown as follows:

$(x\text{-}y)Li_2S_x + 2yLi \rightarrow xLi_2S_{x-y}$ chemical reduction (2.9)

$(x\text{-}y)Li_2S_x + 2yLi^+ + 2ye^- \rightarrow xLi_2S_{x-y}$ electrochemical reduction (2.10).

Sheng S. Zhang and Jeffrey A. Read reported that the $LiNO_3$ additive can dramatically improve the cell's coulombic efficiency [200]. Xiao Liang et al. demonstrated that a lithium/sulfur battery with 0.4 M $LiNO_3$ modified electrolyte showed improved cycling performance with coulombic efficiency above 95% and highly stable reversible discharge capacity of 527 mAh g^{-1} after 50 cycles [201].

2.3.3 The modification of lithium anode

It is well known that the dendrite deposition of Li metal is a major safety problem in the lithium metal battery system. In lithium/sulfur batteries, this problem is not so serious as in other lithium metal batteries, due to the dissolved polysulfides in the electrolyte. The dissolved polysulfides will diffuse to the lithium anode and react with the lithium dendrites on the lithium anode, preventing the growth of the lithium dendrites, which can now be called

"chemically dissolved lithium dendrites". Although the the lithium dendrite problem is not very serious, the lithium anode suffers from low coulombic efficiency because of the polysulfide redox shuttle. Therefore, the lithium anode needs to be modified. As this doctoral thesis is mainly about the modification o of sulfur cathode, here, I only briefly introduce several main approaches to protecting the lithium anode: (1) pre-passivation of lithium by using some sort of reactive chemical to form a stable passivation layer[202]; (2) employing Li-B alloy anode to replace pure lithium[203]; (3) applying a physical barrier layer; (4) using gel polymer electrolyte instead the liquid electrolyte [25]; and (5) preparing a hybrid anode to protect the lithium anode. As shown in Figure 2.27, Liu's group designed a Li-S battery using electrically connected graphite and lithium metal as a hybrid anode to control undesirable surface reactions on the lithium relating to the polysulfide shuttle phenomenon [21].

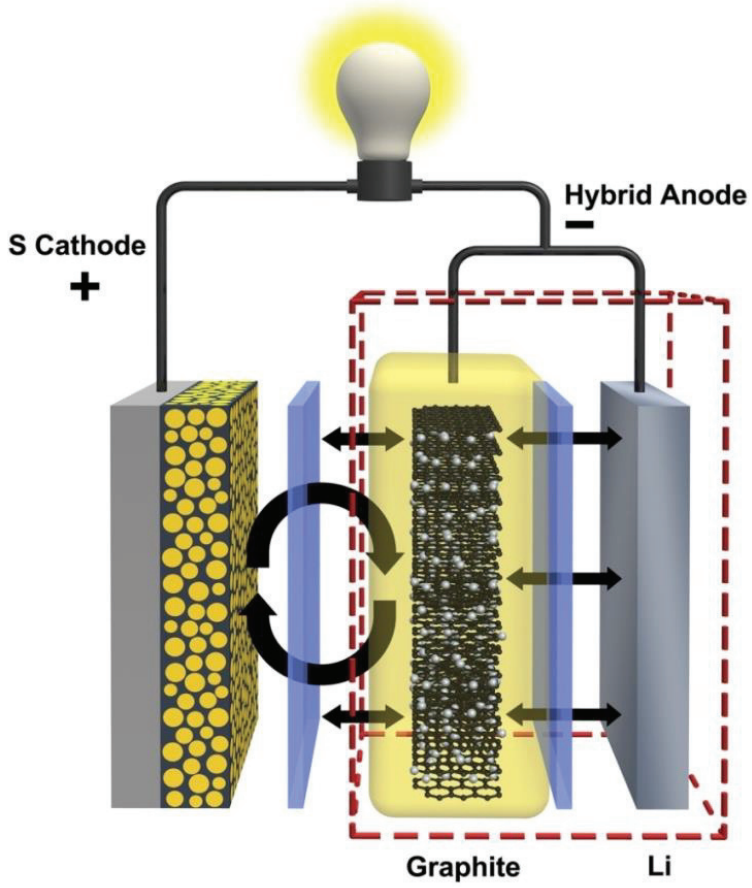

Figure 2.27 Illustration of a lithium/sulfur battery with a hybrid anode consisting of

electrically connected graphite and lithium metal [21].

2.3.4 Inserting an interlayer between the separator and the cathode

Optimized design of the cell is also critically important for improving the electrochemical performance of the lithium/sulfur batteries[204-210]. Recently, Manthiram's group reported a novel Li-S cell configuration method that involved the insertion of a microporous carbon interlayer of MWCNTs between the separator and the regular sulfur electrode [211]. As shown in Figure 2.28, the conductive MWCNT interlayer could not only improve the electrical contact with the sulfur, but also enabled the flow of Li^+ ions while serving as an excellent matrix to retain and accommodate dissolved intermediate polysulfides, leading to excellent cyclability, long cycle life, and high coulombic efficiency.

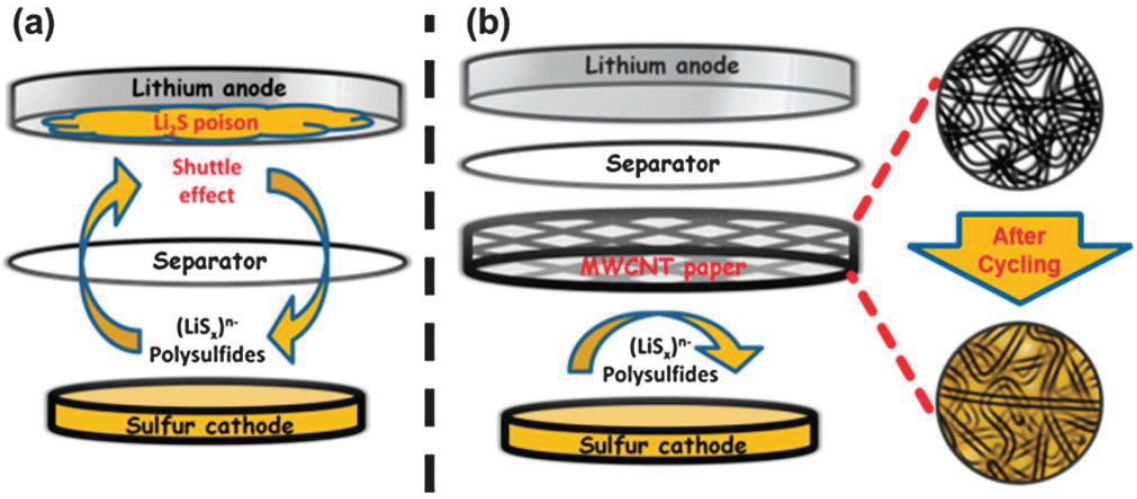

Figure 2.28 Schematic cell configuration of rechargeable Li–S batteries: (a) traditional configuration, and (b) new configuration with the MWCNT interlayer [22].

2.3.5 New charging method

It is well known that the diffusion of the dissolved polysulfide ions is the main reason for the capacity decay in lithium sulfur batteries. Thus, it is important to discover the reason behind the capacity fading. Manthiram's group [212] suggested that the long chain polysulfides (Li_2S_8 and Li_2S_6) which form during the first plateau of the discharge curve are responsible

for capacity fading. As shown in Figure 2.28, the long-chain polysulphides dissolve in the electrolyte, diminish the reaction rate, and also intensify the shuttle phenomenon, which leads to huge capacity fading. To prevent the formation of longer chain polysulfides, Manthiram's group applied a new charging method, whereby the batteries were charged up to a fixed capacity rather than within the conventional voltage window, so that the first plateau could not be formed. Then the charged cell discharged. It is found that with this new charging technique, it is possible to achieve very high capacity retention.

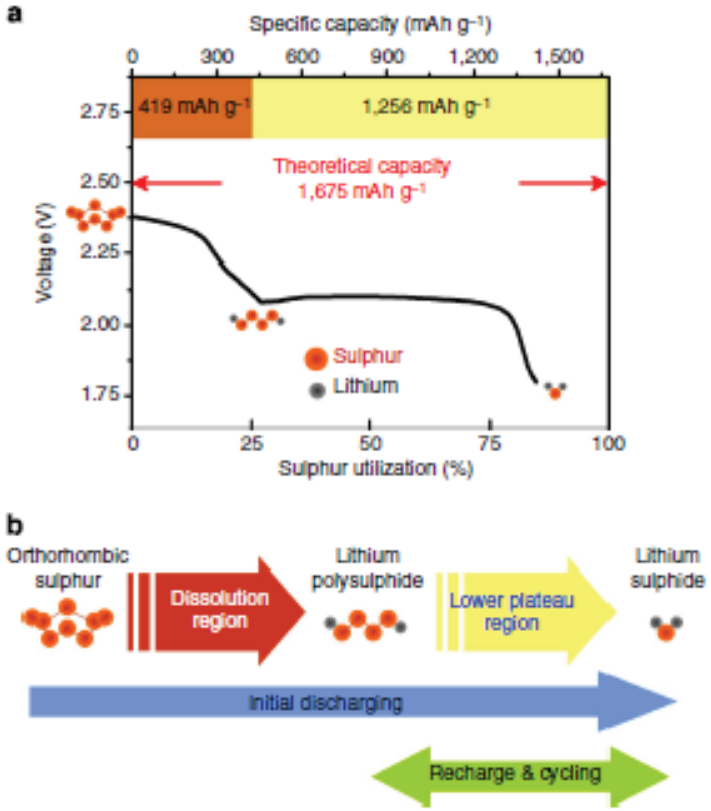

Figure 2.29 Recharge strategy for prolonging the cycle life of Li-S batteries: (a) Typical discharge profile of the Li-S battery. (b) Strategic approach to recharging Li-S batteries. [23].

In conclusion, the lithium sulfur battery is the most promising candidate for the next generation of energy storage systems. It has the highest theoretical capacity among all the known solid cathode materials and very high energy density, as well as being low-cost and non-toxic. Although the lithium/sulfur batteries still have a number of challenges to

overcome, many approaches have been reported to effectively improve the electrochemical performance. There is still a long and bright way to go to exploit the potentialities of lithium/sulfur batteries.

Chapter 3. Experiments

3.1. Overview

In this doctoral work, the logical framework of the experimental routes is illustrated in Figure 3.1. Firstly, pure sulfur or sulfur-conducting-agent composites were synthesized by the self-template strategy, the spray/pyroylysis/sublimation method, or the spray precipitation method. Then, a series of physical characterization techniques were used to observe and confirm the properties of the as-prepared samples, including X-ray diffraction (XRD), scanning electron microscopy/transmission electron microscopy/energy dispersive X-ray spectroscopy (SEM/TEM/EDS), thermogravimetric analysis (TGA), Raman spectroscopy, and the Brunauer-Emmett-Teller (BET) surface area analysis technique. After that, the as-prepared samples were used to prepare electrodes and assemble cells for lithium/sulfur batteries. Finally, the corresponding electrochemical performances of the lithium/sulfur batteries were tested, involving tests of cycling performance, rate capability, charge-dischage profiles, cyclic voltammetry (CV), and electrochemical impedance spectroscopy (EIS).

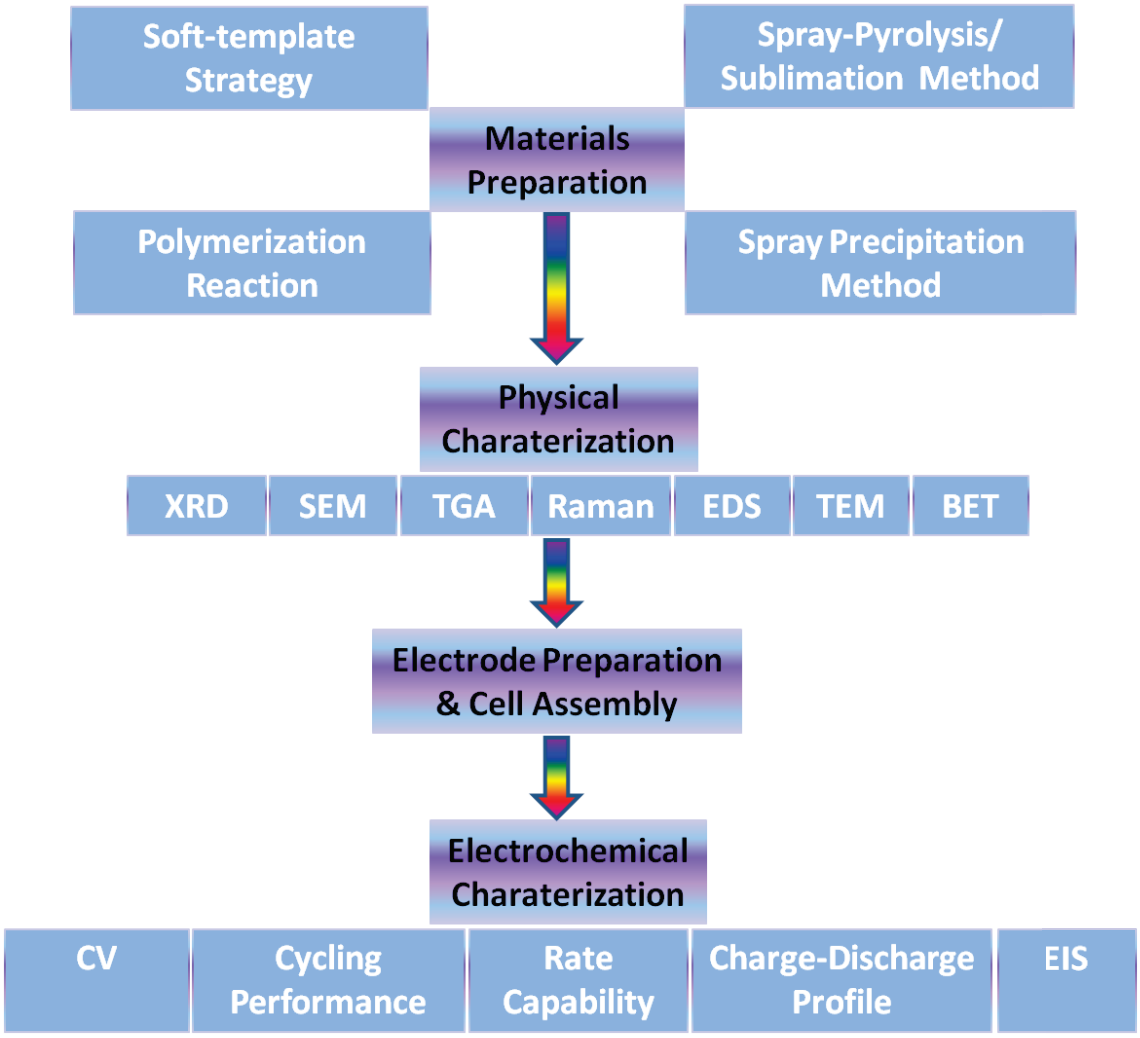

Figure 3.1 Outline of experimental procedures and techniques used in this thesis.

3.2. Chemicals and materials

The chemicals and materials used in this thesis for synthesis, characterization, and electrochemical tests are summarized in Table 3.1.

Table 3.1. Chemicals and materials for synthesis, characterization, and electrochemical tests.

Materials/Chemicals	Formula	Purity (%)	Supplier
1,3-dioxolane	$C_3H_6O_2$	99	Sigma Aldrich

			Australia
1-methyl-2-pyrrolidinone (NMP)	C_5H_9NO	99.5	Sigma Aldrich Australia
Acetone	CH_3COCH_3	99	Sigma Aldrich Australia
Activated Carbon	C	99	Sigma Aldrich Australia
Aluminium foil	Al	N/A	China
Ammonium persulfate	$(NH_4)_2S_2O_8$	>98	Sigma Aldrich Australia
Carbon black	C	N/A	Timcal Belgium
Cetyltrimethylammonium bromide	$(C_{16}H_{33})N(CH_3)_3Br$	99	Sigma Aldrich Australia
CR2032 type coin cells	N/A	N/A	China
Ethanol	C_2H_5OH	Reagent	Q-store, Australia
Graphite	C	N/A	Sigma Aldrich Australia

Hydrochloric acid	HCl	36.5	Sigma Aldrich Australia
Hydrogen peroxide	H_2O_2	30	Sigma Aldrich Australia
Iron (III) chloride	$FeCl_3$	97	Sigma Aldrich Australia
Lithium bis(trifluoromethanesulfonyl)imide	$CF_3SO_2NLiSO_2CF_3$	N/A	Sigma Aldrich Australia
Lithium metal	Li	99.9	Sigma Aldrich Australia
Multi-walled carbon nanotubes (CNTs)	C	99	Shen Zhen Nanotech Port.
Nano-graphite carbon	C	99	Sigma Aldrich Australia
Oxalic acid	$H_2C_2O_4$	99	Sigma Aldrich Australia
Poly(ethylene glycolo dimethyl ether 500 (PEGDME 500)	$CH_3O(CH_2CH_2O)_nCH_3$	N/A	Sigma Aldrich Australia

Polypropylene separator	$(C_3H_6)_n$	Celgard 2500	Hoechst Celanese Corporation USA
Polyvinylidene difluoride (PVDF)	$(CH_2CF_2)_n$	N/A	Sigma Aldrich Australia
Pure ethanol	C_2H_5OH	99.95% absolute	Sigma Aldrich Australia
Pyrrole	C_4H_5N	98	Sigma Aldrich Australia
Sodium dodecyl benzene sulphonate	$C_{18}H_{29}NaO_3S$	99	Sigma Aldrich Australia
Sodium nitrate	$NaNO_3$	99	Sigma Aldrich Australia
Sodium thiosulphate	$Na_2S_2O_3$	99	Sigma Aldrich Australia
Sodium p-toluenesulfonate	$CH_3C_6H_4SO_3Na$	95	Aldrich
Sulfur	S	99.5+	Sigma Aldrich Australia
Triton X-100	$C_{34}H_{62}O_{11}$	99	Sigma Aldrich

3.3. Materials preparation

The preparation methods applied in this doctoral work include the soft-template strategy, the polymerization reaction, the spray-pyrolysis/sublimation method, and the spray precipitation method. All the methods are briefly described below.

3.3.1. Soft-template strategy

A template is a kind of organic structure or inorganic structure where an inorganic material nucleates and grows in a "skin-tight" fashion. After removal of the templating structure, the geometric and electronic characteristics of the templating structure are replicated in the material. There are two main kinds of templates: one is the hard templates, such as porous silica, polystyrene, and colloidal silica spheres. The other is the soft templates, such as surfactant. The soft-template strategy is widely applied in the synthesis of materials with unique morphologies, especially the mesoporous structures, in the fields of surface science, nanotechnology, energy, and the environment[213]. During the preparation of the mesoporous materials, the organic surfactant molecules play a decisive role in generating porosity within the building blocks and thus working as templates or structure directing agents.

In my PhD thesis work, sodium dodecyl benzene sulphonate (SDBS) was choosen as a soft template for the synthesis of porous sulfur particles. SDBS is an excellent soft template to form porous structures. As shown in Figure 3.2, the structure of SDBS in aqueous solution can easily take on different forms, responding to the concentration of SDBS (C_{SDBS}) and the concentration of salt (C_{salt}) in the solution[213]. When the concentration of SDBS is appropriate, SDBS prefers to form spherical micelles, which are essential to form a porous morphology. The mechanism of the pore formation is shown in Figure 3.3. First, after dropping $H_2C_2O_4$ solution into $Na_2S_2O_3$ and SDBS solution, the SDBS lamellar micelles are transformed to spherical micelles as the concentrations of SDBS and salt decrease. At the same time, the

sulfur starts to precipitate. Thus, cooperative self-assembly occurs between the sulfur and the SDBS spherical micelles. Then, many more sulfur particles are produced, resulting in further condensation. Secondly, after adding a large amount of H_2O into the above solution, the SDBS spherical micelles break, and the SDBS is removed. The sulfur particles with porous honeycomb-like structure are then finally obtained.

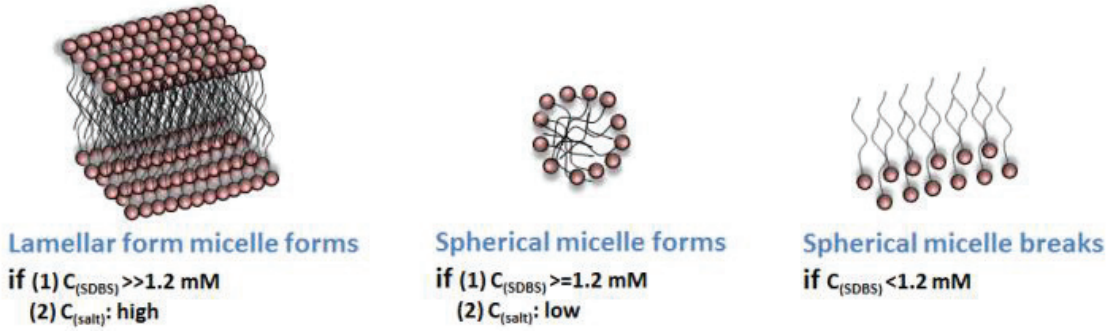

Figure 3.2 Different types of SDBS structure in aqueous solution.

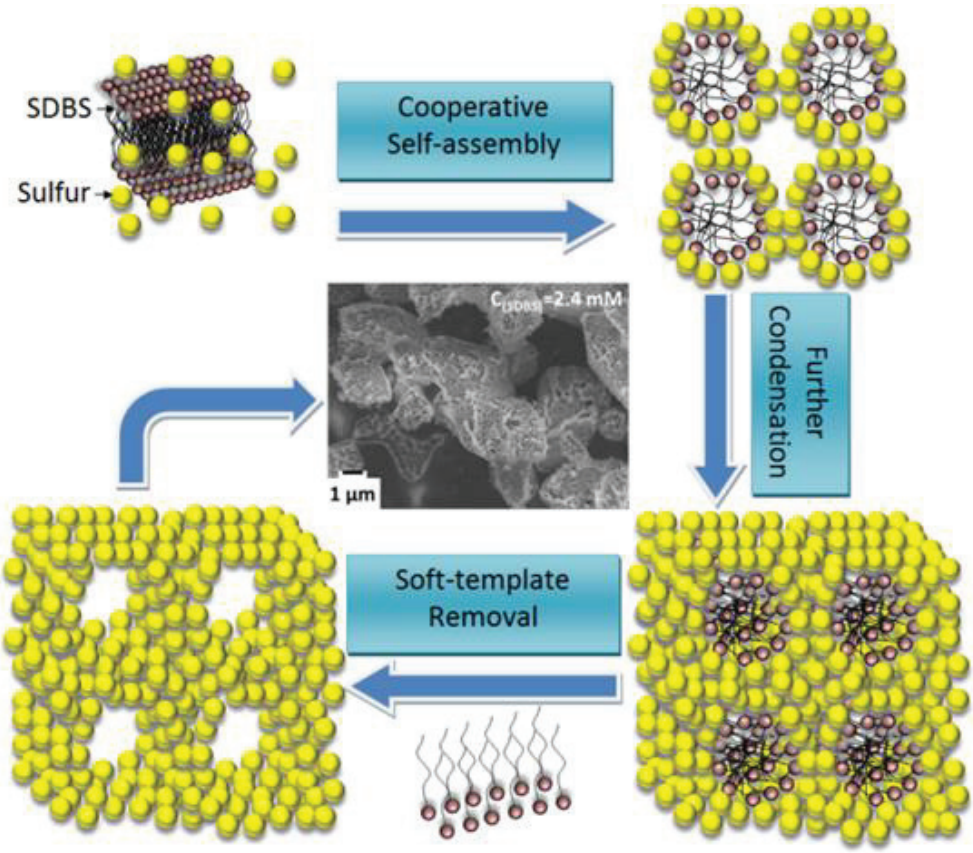

Figure 3.3 Mechanism of the synthesis of the honeycomb like sulfur particles.

In summary, the advanced features of the soft-template method include: (1) low operating temperature; (2) easy preparation process control; (3) mesoporous morphologies by controlled synthesis.

3.3.2. Polymerization reaction

Polymerization reaction is a process of reacting monomer molecules together in a chemical reaction to form polymer chains or three-dimensional networks. [214] In general, there are two kinds of polymer. The polymers consisting of repeated long chains or structure of the same monomer unit (Eq. 3.1) are referred to as "homopolymers", while the polymers consist of more than one molecule are referred to as copolymers (Eq. 3.2).

Homopolymers: $A + A + A ... \rightarrow AAA ...$ (3.1)

Copolymers: $A + B + A ... \rightarrow ABA$ (3.2)

There are two basic ways to form polymers: (1) linking small molecules together, and (2) combining two molecules (of the same type or different types) with the elimination of a stable small molecule such as water. [215] [216]

In this doctoral thesis work, polypyrrole PPy, one kind of conducting polymer, was applied as a conducting agent to prepare S@PPy composite, PPy@S@PPy composite and active-carbon – nano-sulfur – polypyrrole composite for Li/S batteries. Two kinds of morphologies of PPy have been synthesized, split-half-tubes and cauliflower, respectively. The PPy split-half-tubes were synthesised by the oxidative chemical polymerization method. Liquid pyrrole monomers and sodium p-toluenesulfonate (PTS Na) as a dopant were dispersed in a cetyltrimethylammonium bromide (CTAB) aqueous surfactant solution. Then, an oxidizing agent, ammonium persulfate aqueous solution, was gradually added into the above mixture to initiate the polymerization. All solutions were precooled to 0-5 ˚C, and the polymerization in the final mixture went on at 0-5 ˚C for 12 h. After reaction, the precipitates were filtrated and washed with deionized water and ethanol, then dried in a vacuum oven at

60 ˚C for 12 h. Finally, a black powder was obtained. The cauliflower PPy was prepared on the surface of the S@PPy composite and the surface of active-carbon – nano-sulfur composite by an optimized chemical polymerization method using pyrrole monomer, sodium p-toluenesulphonate (PTS Na) as the dopant, and $FeCl_3$ as the oxidant.

3.3.3. Spray-pyrolysis/sublimation method

The spray-pyrolysis/sublimation method is a modified spray-pyrolysis method for preparing sulfur based materials. The spray-pyrolysis method, in which we have established expertise [217-219], is a well-known proven industry-oriented technique, which can produce high performance cathode or anode active materials for lithium ion batteries or supercapacitors with highly developed porous structures rapidly and continuously, but without the need for any further treatments such as washing or grinding. This method has been widely and successfully used for synthesizing carbon-coated composite electrode materials for lithium ion batteries, which have shown significant improvement in their electrochemical performance over their counterparts made by other methods [218, 220, 221]. The conventional spray-pyrolysis technique that has been explored for producing carbon-sulfur composite materials for lithium/sulfur batteries is denoted as the “spray-pyrolysis/sublimation technique”. During the spray-pyrolysis/sublimation process, there is pyrolisation of the organic solvent or other organic chemicals as well as the sublimation of sulfur. The spray-pyrolysis/sublimation method is a promising method for synthesizing porous sulfur/carbon composites. Figure 3.4 presents a photograph of the device used in this doctoral thesis work for preparing porous sulfur/dual-carbon composite by the spray-pyrolysis/sublimation method, while Figure 3.5 presents a schematic diagram of spray-pyrolysis/sublimation device, which includes three main parts: the solution transfer unit, the reaction unit, and the sample collection unit. During the experiments, the solution, which

was kept under stirring, was first transferred to the furnace via a nozzle by a peristaltic pump and the carrier gas. The furnace is the reaction unit, with a 2 m SiO_2 tube inside. Finally, the as-prepared samples were collected in a jar by the extractor pump.

Figure 3.4 Photograph of the spray-pyrolysis/sublimation device used in this doctoral thesis work.

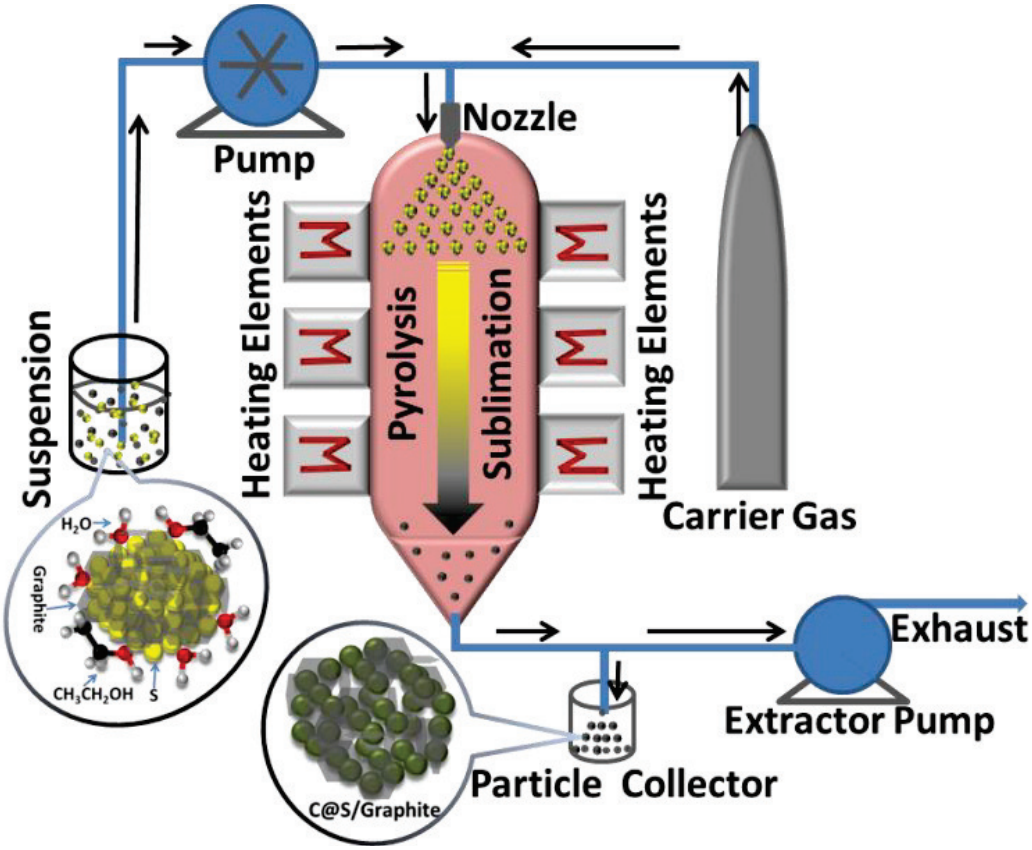

Figure 3.5 Schematic diagram of spray-pyrolysis/sublimation device.

3.3.4 Spray precipitation method

The spray precipitation method is an advanced chemical precipitation method, which has played a significant role in the fabrication of high-surface-area materials [222, 223]. The spray precipitation method is known as a simple, single-step, and industry-oriented method. In the spray precipitation method, a nozzle is applied to reduce the size of the droplets of the reactants, and then nanomaterials are obtained. Figure 3.6 shows a comparison of the drop precipitation method and the spray precipitation method, where a sulfur with very fine particle size has been prepared. The possible reaction mechanism can be explained as follows: the atomized thiosulfate creates numerous nucleation sites where the surrounding nuclei inhibit the growth process of the sulfur and help to produce submicron-sized elemental sulfur particles with higher surface area compared to the drop precipitation methods.

Moreover, the higher number of nucleation sites helps to achieve a homogeneous distribution of sulfur particles [224].

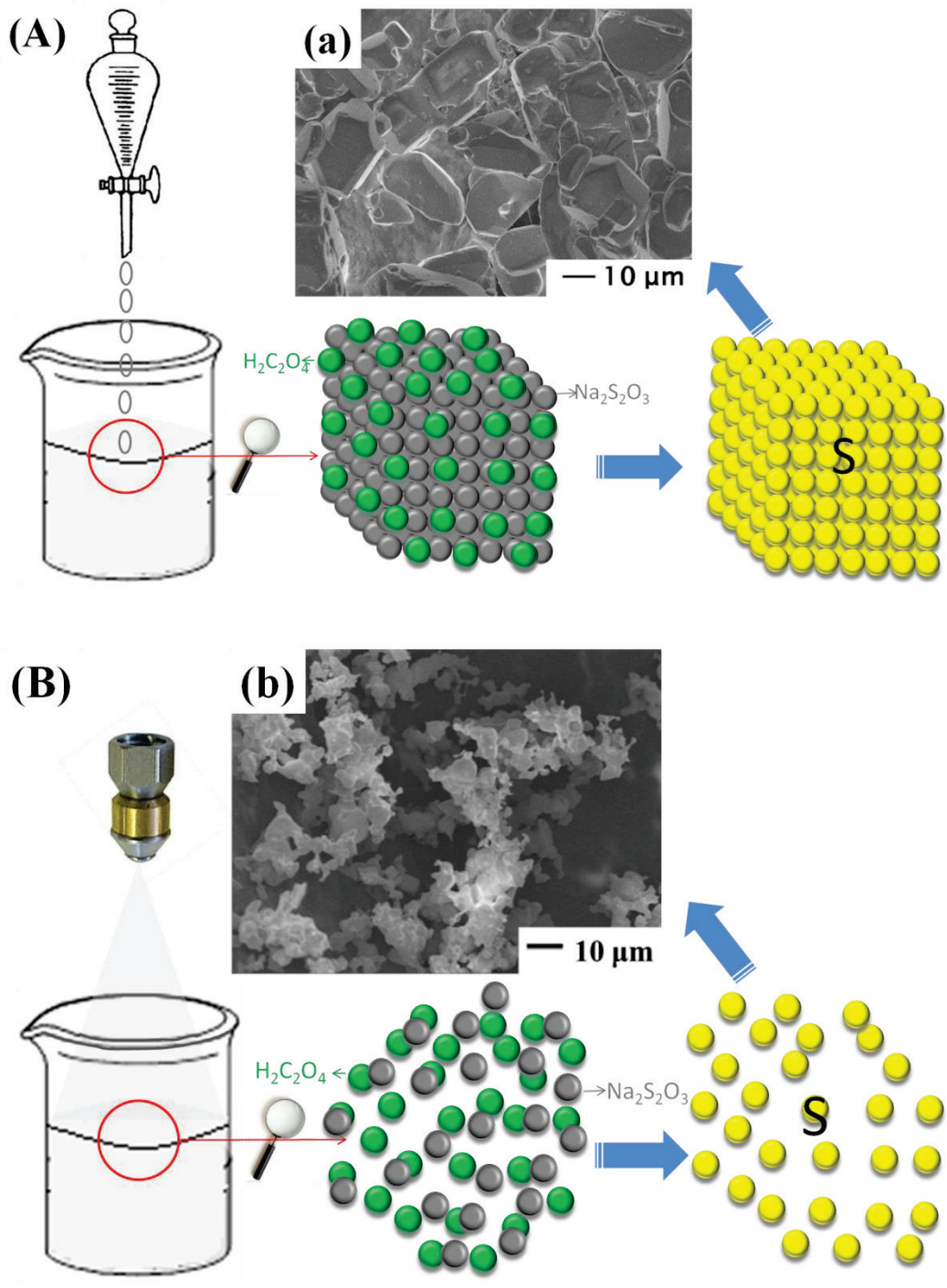

Figure 3.6 Schematic diagram showing the fabrication of (A) drop-precipitated sulfur; (B) spray-precipitated sulfur. FESEM image of (a) drop-precipitated sulfur, and (b) spray-precipitated sulfur.

3.4. Physical and chemical characterization techniques

The techniques for characterization of the as-prepared materials will be introduced in detail in the following sections.

3.4.1. X-ray diffraction

X-ray diffraction (XRD) is widely applied to detect the structural characterization of materials. X-rays are waves of electromagnetic radiation, and crystals are regular arrays of atoms. In this thesis, X-ray powder diffraction was conducted by a GBC MMA diffractometer in UOW. This XRD devices uses Cu Kα radiation, λ = 1.54056 Å.

3.4.2. Scanning electron microscopy and energy dispersive spectroscopy

A scanning electron microscope (SEM) is a microscope technique to produce images by scanning a sample with a focused beam of electrons. The interaction between electrons and the atoms in the sample can give out the information about the topography, composition, and other properties of the sample surface, such as electrical conductivity. The types of signals produced by a SEM include secondary electrons (SE), back-scattered electrons (BSE), characteristic X-rays, specimen currents under illumination, and transmitted electrons. All SEMs have the standard secondary electron detectors, but the other detectors for all possible signals are only installed together in a machine as options. The signals result from interactions of the electron beam with atoms at or near the surface of the sample. Due to the very narrow electron beam, the most common standard, secondary electron imaging (SEI) micrographs allow a large depth of field, so that a characteristic three-dimensional appearance of the surface structure of a sample can be obtained. The powder samples in this work were either dispersed in ethanol or directly loaded onto an aluminium holder using carbon conductive tape for SEM observation.

Energy-dispersive X-ray spectroscopy (EDS) is commenly used for the elemental

analysis or chemical characterization of materials, which is based on the investigation of an interaction between some source of X-ray excitation and the sample. As each element has a unique atomic structure, it allows unique set of peaks on its X-ray spectrum. In this thesis, the morphology, structure, and elemental mapping of the samples were detected with a field-emission scanning electron microscope (FESEM; JEOL 7500 in UOW).

3.4.3. Transmission electron microscopy

Transmission electron microscopy (TEM) is a microscopy technique to investigate the morphology, crystal structure, and electronic structure of the materials. In the TEM equipment, a beam of electrons is transmitted through an ultra-thin specimen, and the TEM image is formed from the interaction between electrons and the specimen when it passes through. In this thesis, the samples were dispersed in ethanol and then loaded onto a holey carbon support film on a copper grid, and the TEM images of the samples were collected by a JEOL 2011, 200 kV in UOW.

3.4.4. Thermogravimetric analysis

Thermogravimetric analysis (TGA) is a technique for analysis of the chemical changes or physical weight changes in materials with increasing temperature.[225] TGA can provide information on physical phenomena, such as vaporization, sublimation, absorption, and desorption, and also can provide information on chemical phenomena, such as chemisorption, dehydration, decomposition, and solid-gas reactions. In this doctoral work, TGA was used to determine the sulfur percentageand the carbon ratio in the composite materials. TGA was performed on a SETARAM Thermogravimetric Analyzer (France). The sample was placed in an alumina crucible with loading mass of 5-10 mg, depending on the density of the composite materials.

3.4.5. Raman spectroscopy

Raman spectroscopy is a spectroscopic technique to observe vibrational, rotational, and other low-frequency modes in a system, which can be employed to identify the component of materials[226]. In a Raman spectrometer, the energy shift of some laser photons, caused by the interaction between laser light and molecular vibrations, phonons, or other excitations, gives information on the phonon modes in the system. In this thesis, Raman spectra were recorded by a JOBIN Yvon Horiba Raman 57 Spectrometer model HR800 in UOW.

3.4.6. Brunauer-Emmett-Teller (BET) technique

The Brunauer-Emmett-Teller (BET) method has been widely used to measure the specific surface area and the pore size distribution of a material[227]. The BET surface areas of samples can be calculated based on the experimental points at a relative pressure of P/P_0 = 0.05 – 0.25, and the pore size distributions can be calculated by the Barrett-Joyner-Halenda (BJH) method based on the amount of nitrogen adsorbed at a relative pressure of P/P_0 = 0.99. In this doctoral work, nitrogen sorption was measured by a Quanta Chrome Nova 1000 in UOW in liquid nitrogen.

3.5. Electrochemical Measurements

3.5.1. Electrode preparation

For the preparation of the electrodes, a slurry consisting of a mixture of the electrode materials with conductive material (e.g. carbon black or Super P) and binder (e.g. polyvinylidene difluoride (PVDF) in N-methyl-2-pyrrolidone (NMP)) was prepared. The obtained slurry was coated onto the current collectors (aluminium foil), dried in a vacuum oven at 50°C for 24h, then pressed at moderate temperature and measured.

3.5.2. Battery assembly

Battery assembly was carried out in an Ar-filled glove box using CR2032-type coin cells. The stacking components of a CR2032 coin cell are shown in Figure 3.7. CR 2032 coin-type cells were assembled in the following orders: (1) the working electrode disc was placed at the positive cap followed by added 1-2 drops of electrolyte; (2) the separator was then evenly immersed in the electrolyte, and an extra 1-2 drops of electrolyte were dripped; (3) the lithium foil was placed onto the separator followed by the stainless steel spacer, spring, and negative cap; (4) finally, the coin cell is tightly sealed, and then rested for at least 12 hours before electrochemical testing.

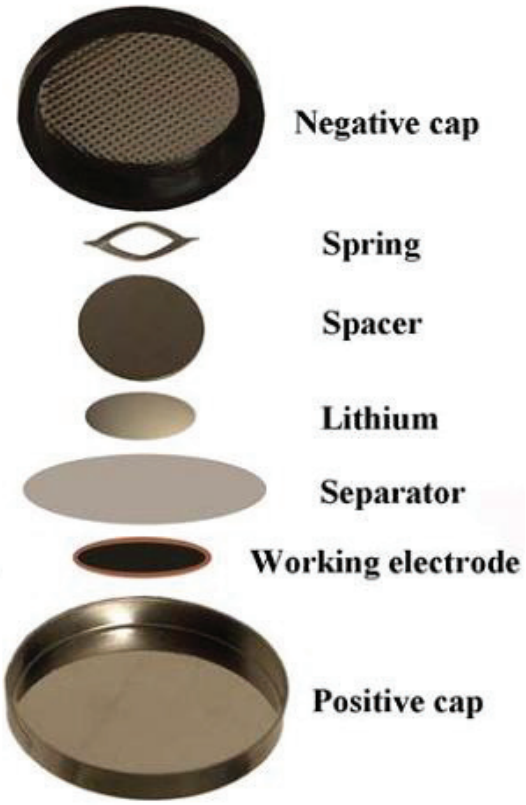

Figure 3.7 Stacking components of a CR2032 coin cell [24].

3.5.3. Electrochemical characterization

Electrochemical measurements were used to characterize the performance of the

electrodes in lithium/sulfur batteries and included cyclic voltammetry (CV), galvanostatic charge-discharge measurements, and electrochemical impedance spectroscopy (EIS).

3.5.3.1. Cyclic voltammetry

Cyclic voltammetry (CV) is widely used to study a variety of redox processes and for obtaining the stability of reaction products and determining the presence of intermediates in oxidation-reduction reactions in a coin cell, where a pairs of peaks are observed in both anodic and cathodic curves when a redox reaction occurs. CV is conducted by recording the response current when cycling the potential of a working electrode at a specified scan rate. In this doctoral work, the CV data were acquired on a Biologic VMP-3 electrochemical workstation in UOW.

3.5.3.2. Galvanostatic charge-discharge

The cycling performance, rate capability, and charge-discharge profile of the materials were investigated by galvanostatic charge-discharge tests, in which the cell is charged and discharged within a certain cut-off voltage range at a constant current. In this thesis, the 2032 coin cells were galvanostatically charged and discharged using an automatic Land® battery tester system in UOW.

3.5.3.3. Electrochemical impedance spectroscopy

Electrochemical Impedance Spectroscopy (EIS) is applied to test the inner resistance of a coin cell. In the impedance spectrum, the high-frequency semicircle is related to the kinetic processes, which indicates the charge transfer resistance and the double layer capacitance; the low-frequency linear tail reflects the solid-state diffusion of lithium ions into the bulk of the active materials. In this thesis, EIS data were collected on a Biologic VMP-3 electrochemical workstation in UOW.

Chapter 4. High Performance Pure Sulfur Honeycomb-like Architectures Synthesized by Cooperative Self-assembly Strategy for the Lithium/Sulfur Battery

4.1. Introduction

Clean and efficient energy storage devices are in high demand due to the limited global energy supply, environmental pollution, and the increasing consumption of energy[134, 228]. The rechargeable lithium/sulfur battery has attracted significant attention due to its high theoretical specific capacity and power density[14, 31-33, 198, 229]. Another advantage is that sulfur is abundant in nature, inexpensive and non-toxic[38].

In spite of these considerable advantages, the fabrication of lithium/ sulfur batteries encounters a number of challenges. Sulfur is a highly electrically insulating material, which leads to poor electrochemical accessibility and low utilization of the sulfur in the electrode. The polysulfide anions which are formed as the reaction intermediates are highly soluble in the organic electrolyte solvent, which results in low active material utilization, low coulombic efficiency, and short cycle life of the sulfur electrode[9, 43]. In order to successfully operate the lithium-sulfur battery, the elemental sulfur must be well combined with a strong adsorbent to construct a composite cathode[59, 133, 230, 231], so as to reduce the diffusion of lithium polysulfides into the electrolyte[2, 17, 65, 129]. The most promising adsorption agents for the Li/S battery are porous materials such as porous carbon[32, 133, 231, 232], with which porous structured sulfur-carbon composites are prepared by coating elemental sulfur on the surface of the porous carbon materials. The battery performance of these sulfur-carbon composites has shown significant improvement over elemental sulfur, as the porous structure has the following positive effects towards improving the electrochemical performance [50]: (1) the porous structure absorbs the soluble lithium polysulfides formed during discharge and reduces the dissolution of the active materials into the electrolyte; (2) the porous structure

increases the contact surface area between the sulfur and the carbon black, which increases the conductivity of the electrode; (3) the porous structure electrode has a faster charge transfer process, and thus the electrochemical kinetics of the porous sulfur – porous additive electrode is improved in rechargeable lithium batteries. The previously reported methods used for preparation of sulfur – porous additive composites are quite complicated, however, as well as being time-consuming, costly, not environmentally friendly, and difficult to scale up.

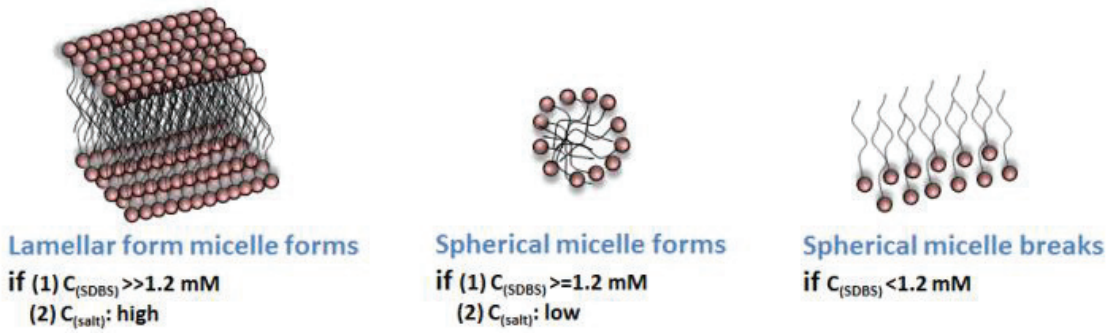

Figure 4.1 Different types of SDBS structure in aqueous solution.

It is therefore promising to try to synthesize pure sulfur with porous structure for Li/S batteries. In this study, the sulfur particles with honeycomb morphology were prepared via a cooperative self-assembly process, while sodium dodecyl benzene sulphonate (SDBS) was used as a soft template to form the porous structure. This method is simple, easily scaled up, and has low energy consumption. SDBS is an excellent soft template to form porous structures[213]. As shown in Figure 4.1, the structure of SDBS in aqueous solution can easily take on different forms, responding to the concentration of SDBS (C_{SDBS}) and the concentration of salt (C_{salt}) in the solution[213]. When the concentration of SDBS is appropriate, SDBS prefers to form spherical micelles, which are essential to form a porous morphology. Moreover, SDBS is a non-toxic, biodegradable, and environmentally friendly surfactant. In addition, SDBS is soluble and can be removed after the reaction by using distilled water. To

the best of the authors' knowledge, there has been no report on using this method to prepare honeycomb-like sulfur particles. It is believed that this method can provide useful guidance for producing high surface area sulfur for various applications, such as in chemical fertilizers, the pharmaceutical industry, the rubber and fibre industries, bioleaching processes, anti-microbial agents, insecticides, fumigants, etc. [233].

4.2. Experimental section

4.2.1. Materials:

Sodium thiosulphate ($Na_2S_2O_3$), oxalic acid ($H_2C_2O_4$), sulfur (S), and SDBS were all purchased from Sigma Aldrich (Australia). All the chemicals were used as received without any further purification.

4.2.2. Preparation of honeycomb-like sulfur:

Firstly, 3.60 g $H_2C_2O_4$ was dissolved in 250 mL distilled water at room temperature under vigorous stirring. Subsequently, 3.16 g $Na_2S_2O_3$ was also dissolved in 250 mL distilled water, and then 0.21 g SDBS was added and stirred vigorously. Afterwards, the $H_2C_2O_4$ solution was dropped into the $Na_2S_2O_3$ and SDBS solution within 20 minutes. After that, 30 minutes were allowed for the completion of the reaction under vigorous stirring. Then, over 500 mL distilled water was added into the solution. A light yellow powder was obtained after centrifuging. The light yellow powder was then dried in a vacuum oven at 45 °C for 24 hours after washing several times with distilled water and acetone.

For comparison, sulfur particles without pores were prepared following a similar procedure in the absence of SDBS.

4.2.3. Material characterization

The structure of the sulfur particles was characterized by X-ray diffraction (XRD) using a GBC MMA X-ray generator and diffractometer with Cu Kα radiation (λ = 1.5418 Å),

employing a scanning rate of 5°/min in the 2θ range from 10° to 70°. The morphology of the sulfur powder was investigated by field emission scanning electron microscope (FE-SEM; JEOL JSM-7500FA). The specific surface area of the powders was examined by gas sorption analysis using the Brunayer- Emmett-Teller method (Quanta Chrome Nova 1000).

4.2.4. Electrochemical measurements

The working electrodes were prepared by mixing 50 wt. % as-synthesized sulfur powder with 40 wt. % carbon black and 10 wt. % polyvinylidene fluoride (PVDF) binder in N-methyl-2-pyrrolidinone (NMP) solvent. The well-mixed slurry was tape-cast onto a sheet of aluminium foil substrates. The commercial sulfur was treated in the same way for comparison. The coated electrodes were dried in a vacuum oven at 45 °C for 48 h and then pressed. Subsequently, the electrodes were cut to a 1 × 1 cm^2 size. The loading weight of the active material is around 1 mg/ cm^2. 1 M lithium bistrifluoromethanesulfonamide (LiTFSI) in poly (ethylene glycol) dimethyl ether 500 (PEGDME 500) was used as electrolyte. 0.1 M $LiNO_3$ salt was used as an electrolyte additive. To compare the effect of the electrolyte, another electrolyte was also prepared, which is 1 mol/L lithium bistrifluoromethanesulfonamide (LiTFSI) in 1,3-Dioxolane(DOL) / 1,2-Dimethoxyethane (DME) (1 : 1 by volume) with 0.1 mol L-1 $LiNO_3$ as an additive. CR2032 coin cells were assembled in an Ar-filled glove box. Charge-discharge testing was carried out with a LAND battery test system at a current density of 50 mA g^{-1} with a voltage range of 1.5–3.0 V. Cyclic voltammetry (CV) and AC impedance measurements were performed using a Biologic VMP-3 Multichannel electrochemistry workstation at a scanning rate of 0.1 mV s^{-1} and a frequency range of 1 00 KHz - 0.01 Hz, respectively.

4.3. Results and discussions

The details of the synthesis processes are presented and the formation of the honeycomb-

like morphology of sulfur is explained in Figure 4.2. Solution A is 250 mL aqueous solution with 2.4 mM SDBS and 10 mM $Na_2S_2O_3$, while solution B is 250 mL distilled water with 40 mM $H_2C_2O_4$. In solution A, the concentration of SDBS is much higher than 1.2 mM, and the concentration of salt ($Na_2S_2O_3$) is also quite high, thus the SDBS prefers to form lamellar micelles. After dropping solution B into solution A, solution C was produced, which is 500 mL distilled water with 1.2 mM SDBS and 5 mM $Na_2S_2O_3$. As both the concentrations of SDBS and salt decrease, the SDBS lamellar micelles were transformed to spherical micelles which will form when the concentration of SDBS is equal or only a little bit higher than 1.2 mM and the concentration of salt ($Na_2S_2O_3$) is low. At the same time, the sulfur starts to precipitate. Thus, cooperative self-assembly occurs between the sulfur and the SDBS spherical micelles. Then, many more sulfur particles are produced, resulting in further condensation. Secondly, after adding a large amount of H_2O into solution C, the SDBS spherical micelles break because of the low concentration of SDBS and salt, and then the SDBS is removed. Finally, the sulfur particles with porous honeycomb-like structure are obtained.

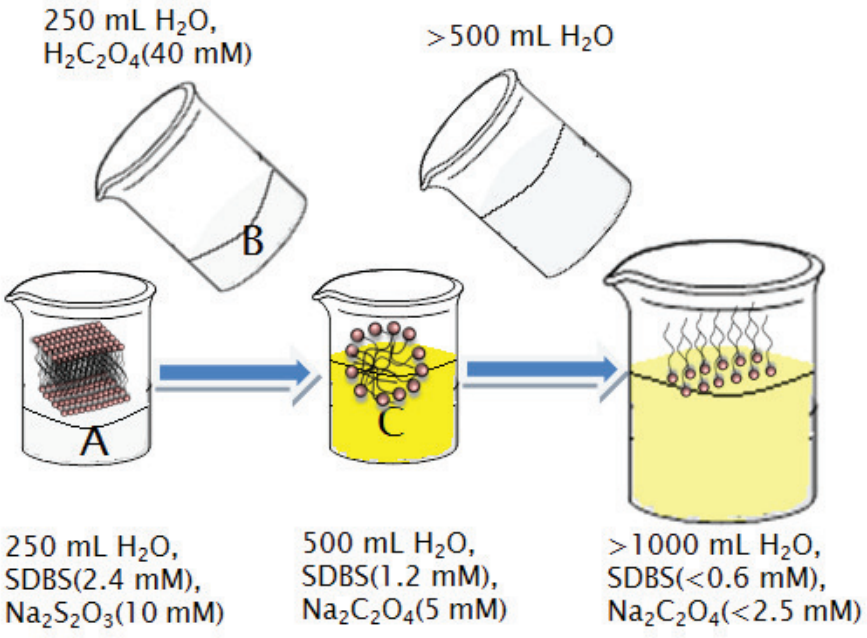

Figure 4.2 Details of the synthesis.

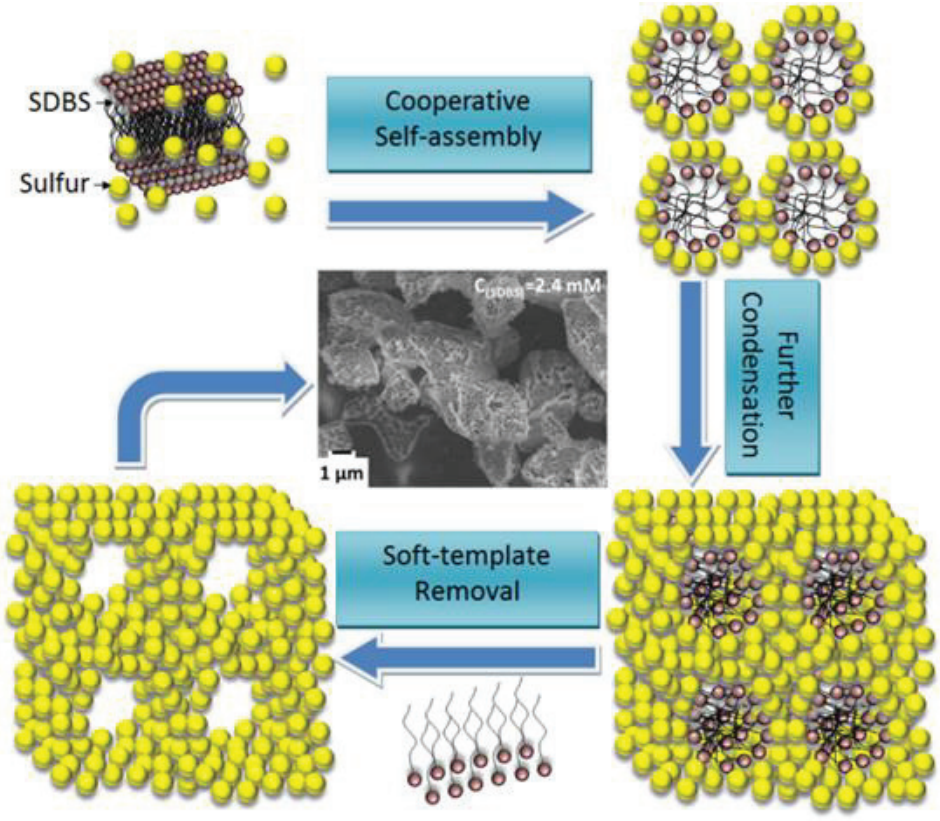

Figure 4.3 Mechanism of the synthesis of the honeycomb like sulfur particles.

The mechanism of the pore formation is shown in Figure 4.3. First, after dropping $H_2C_2O_4$ solution into $Na_2S_2O_3$ and SDBS solution, the SDBS lamellar micelles are transformed to spherical micelles as the concentrations of SDBS and salt decrease. At the same time, the sulfur starts to precipitate. Thus, cooperative self-assembly occurs between the sulfur and the SDBS spherical micelles. Then, many more sulfur particles are produced, resulting in further condensation. Secondly, after adding a large amount of H_2O into the above solution, the SDBS spherical micelles break, and the SDBS is removed. The sulfur particles with porous honeycomb-like structure are then finally obtained. Figure 4.4 (a) shows the XRD pattern of the prepared sulfur particles. The diffraction peaks can be indexed to the structure of space group Fddd (JCPDS No. 00-008-0247). Figure 4.4 (b) shows a field emission scanning electron microscope (FESEM) image of the as-prepared sulfur particles with SDBS. It is clear that the morphology is a porous, honeycomb like structure. Figure 4.4 (c) shows that the

sulfur particles without any pores are agglomerated when SDBS is absent. Thus, the SDBS is a critical factor for obtaining the porous sulfur particles. The FESEM image of the commercial sulfur powder in Figure 4.4 (d) shows that the commercial S particles have big particle size and smooth surfaces.

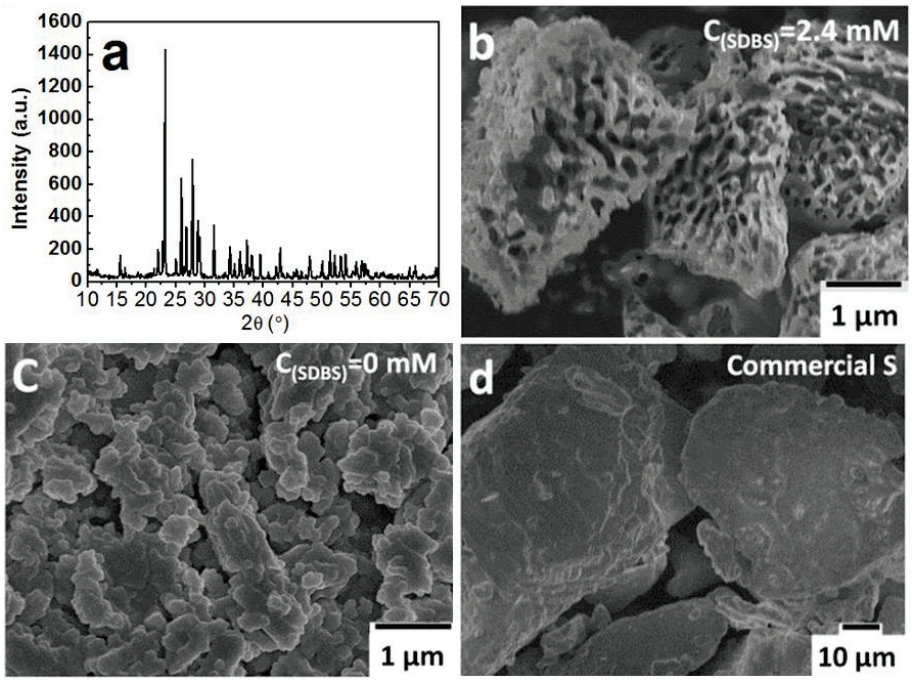

Figure 4.4 (a) XRD pattern of the sulphur particles; (b) FESEM image of as-prepared honeycomb-like sulfur made with SDBS at high magnification; (c) FESEM image of as-prepared sulfur particles without SDBS; (d) FESEM image of commercial sulfur particles.

The comparative experiments with different starting concentrations of SDBS were carried out. As shown in Table 4.1, there are four different starting concentrations of SDBS were applied, 4.8 mM, 2.4 mM, 1.2 mM and 0.6 mM respectively. After adding 250 mL 40 mM $H_2C_2O_4$ solution (solution B) into solution A, the concentrations of SDBS in solution C have reduced to 2.4 mM, 1.2 mM, 0.6 mM, 0.3 mM respectively. Figure 4.5 presents the relative FESEM images of the obtained sulfur particles in the comparison experiments. It is shown in Figure 4.5 (a) that there is not any porous structure of the sulfur particles can be observed when the start concentration of the SDBS is 4.8 mM. Because after adding solution B into

solution A, the concentration of SDBS reduced to 2.4 mM, thus during all the reaction, the concentration of SDBS is much higher than 1.2 mM, which is the critical micelle concentration of SDBS to form spherical micelles. The second condition was using 2.4 mM as the starting concentration of SDBS, after dropping solution B into solution A, the concentration of SDBS decreased to 1.2 mM, and has been kept for 30 mins. Thus, the cooperative self-assembly occurs between the sulfur and the SDBS spherical micelles. Figure 4.5(b) shows that honeycomb-like porous sulfur was obtained. In condition 3, the starting concentration of SDBS is 1.2 mM, so in solution A SDBS exists as spherical micelles, thus, a little amount precipitated sulfur can cooperative self-assemble with the spherical SDBS micelles at the very beginning of the reaction after adding solution B. That's why there some pores have been observed in Figure 4.5(c). In the fourth condition, 0.6mM was used as the starting concentration of SDBS, after the reaction, the final concentration of SDBS is only 0.3 mM, the concentration of SDBS is much lower than the critical micelle concentration of SDBS(1.2 mM). thus there is no spherical micelles exist during all the reaction progress, therefore the FESEM images of the obtained sulfur in Figure 4.5(d) shows no pores either. Based on the discussion above, it was found that the optimum starting concentration of SDBS was 2.4 mM.

Table 4.1 Parameters of the comparative experiments.

Conditions (Figures in Fig.4.5)	**Starting concentration of SDBS in solution A**	**Final concentration of SDBS in solution C**
1 (Fig. 4.5a)	4.8 mM	2.4 mM
2 (Fig. 4.5b)	2.4 mM	1.2 mM
3 (Fig. 4.5c)	1.2 mM	0.6 mM
4 (Fig. 4.5d)	0.6 mM	0.3 mM

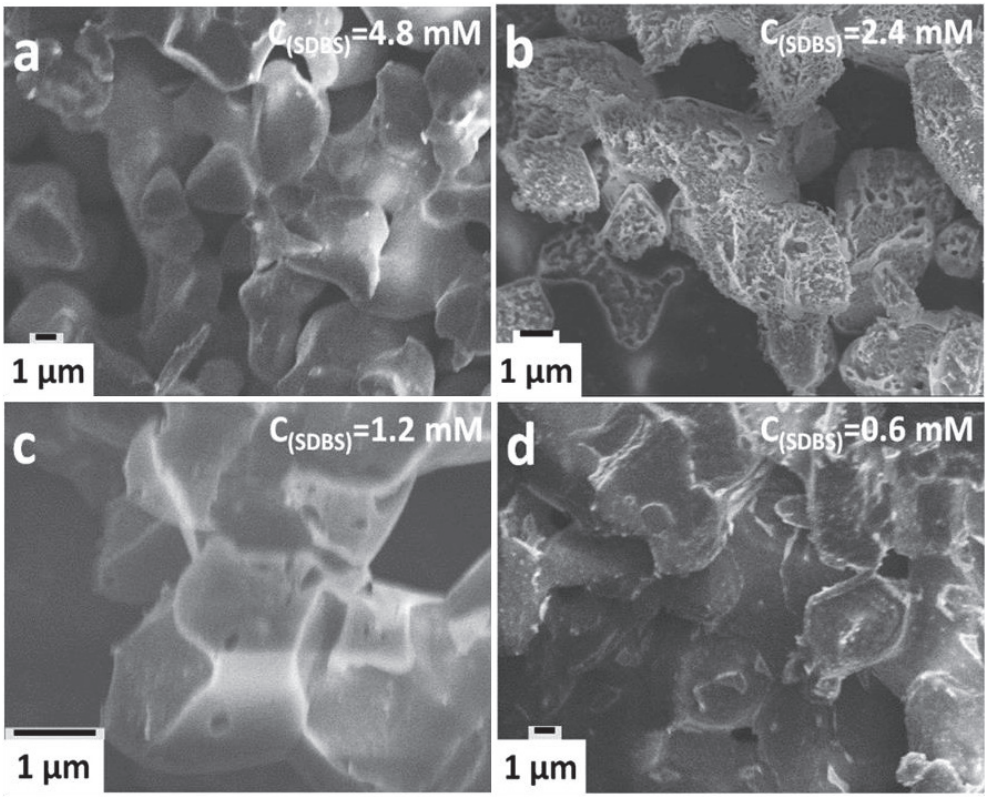

Figure 4.5 FESEM images of the as-prepared sulfur with different starting concentrations of SDBS: (a) 4.8 mM, (b) 2.4 mM, (c) 1.2 mM, (d) 0.6 mM.

The Brunauer-Emmett-Teller (BET) tests have shown that the specific surface area of the commercial sulfur powder is 0.2023 $m^2 g^{-1}$, whereas the specific surface area of the as-prepared honeycomb-like sulfur is 1.0990 $m^2 g^{-1}$, which is about 5 times higher than that of the commercial sulfur powder.

The electrochemical performances of the honeycomb-like sulfur and the commercial sulfur particles were investigated in the electrolyte of l M lithium bistrifluoromethanesulfonamide (LiTFSI) in poly (ethylene glycol) dimethyl ether 500 (PEGDME 500). Typical cyclic voltammograms (CV) of the porous sulfur electrode are shown in Figure 4.6 (a). In the first cycle, there are two main reduction peaks at around 2.4 and 1.8 V, and a small and broad peak near 2.1 V is also observed. The peak near 2.4 V corresponds to the reduction of elemental sulfur to higher-order lithium polysulfides (Li_2S_n, $n \geq 8$). The peak near 1.8 V can

be assigned to the reduction from polysulfides to Li_2S. The small and broad peak near 2.1 V is related to the reduction of higher order lithium polysulfides (Li_2S_8) to form lower-order lithium polysulfides, such as Li_2S_6 and Li_2S_4 [198], which are agreed well with the charge-discharge curve shown in Figure 4.7, in which the charge-discharge profiles are assigned to the two-step reaction of sulfur with lithium, a typical process in Li/S batteries. The charge and discharge potential values of the upper and lower plateaus are stabilized at approximately 2.5 and 2.27 V, and 2.44 and 1.97 V, respectively. Compared to the first cycle, the reduction peaks in the following cycles are shifted slightly to higher voltage because the electrochemical reaction during the first discharge process has to overcome the strong absorbing energy between the sulfur and the conductive matrix[27]. From the second cycle, the intensity of the two oxidation peaks increases with cycling, which indicates that the lithium ion insertion/extraction into sulfur is an activated process[4]. Figure 4.6 (b) shows the cycling performance of the honeycomb-like sulfur electrode in the electrolyte of 1 M LiTFSI in PEGDME 500. The potential range of 1.5–3.0 V was selected for the continuous charge–discharge cycling process. During the first 10 cycles, the specific discharge capacity of the honeycomb-like sulfur electrode increased from 696.9 mAh g^{-1} to 816.9 mAh g^{-1}. These results are in good agreement with the CV measurements because of the activation process due to the gradual penetration of the electrolyte into the porous electrode. The discharge specific capacity slightly decreased after 10 cycles. The cells retained a reversible discharge capacity higher than 650 mAh g^{-1} for 50 cycles, while the discharge capacity of the commercial sulfur is only about 200 mAh g^{-1}. It is interesting that the discharge capacity of the initial cycle of the as-prepared sulfur ($C_{(SDBS)}$=0 mM) electrode is as high as 1058 mAh $^{-1}$. It can be ascribed to the small particle size of the as-prepared sulfur ($C_{(SDBS)}$=0 mM) particles. The sulfur particle can be mixed very well with carbon black, thus the usage of the sulfur in the initial cycle is very high. But it is also very clearly that the capacity decay is dramatically

due to the non-porous structure. The cell with the honey-comb like Sulfur electrode presents improved cycling stability due to the following reasons mentioned in the introduction in relation to the sulfur – porous carbon composite: reduction of the dissolution of the active materials into the electrolyte, increased conductivity of the electrode, and improvement of the kinetics of the Li ion reaction with S.

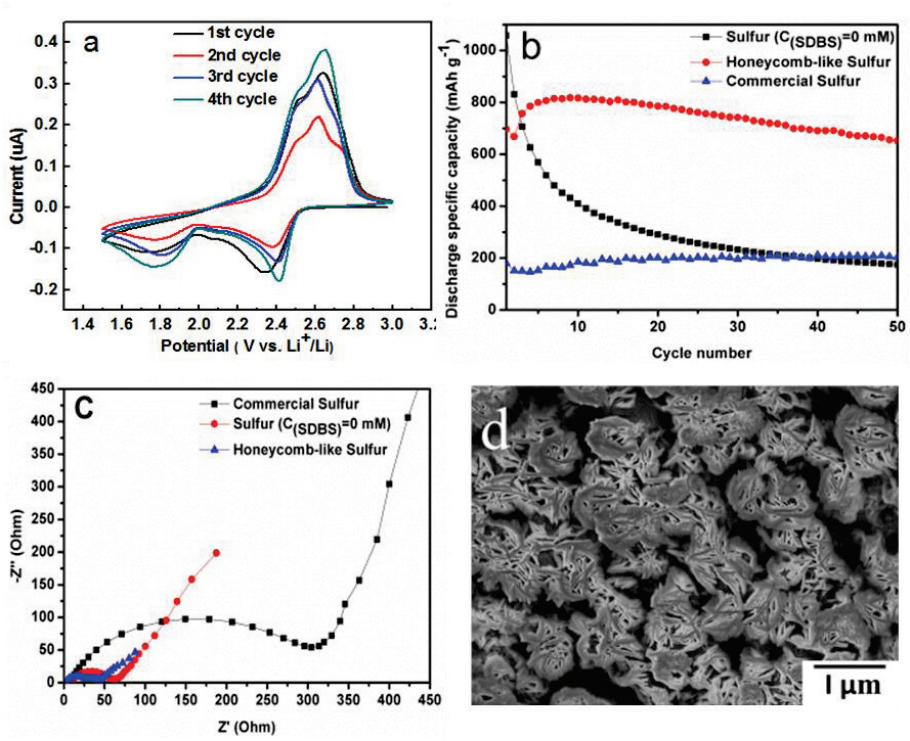

Figure 4.6 (a) Cyclic voltammograms for the first 4 cycles of the honeycomb-like sulfur electrode; (b) cycling performances of the honeycomb-like sulfur electrode, as-prepared sulfur ($C_{(SDBS)}$=0 mM) electrode and the commercial sulfur electrode; (c) impedance plots for the honeycomb-like sulfur electrode, as-prepared sulfur (C(SDBS)=0 mM) electrode and the commercial sulfur electrode; (d) FESEM image of the honeycomb-like sulfur electrode after 50 cycles.

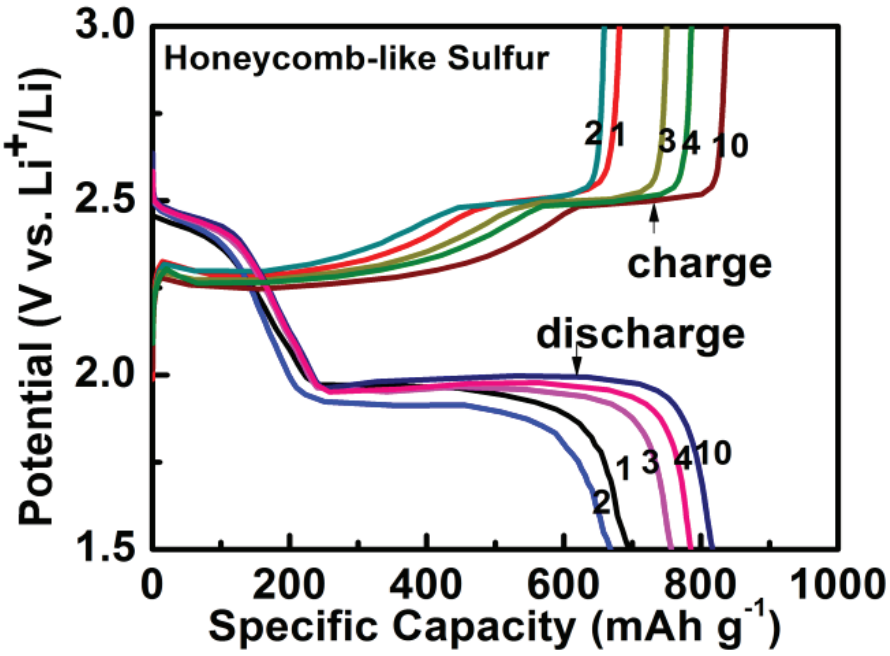

Figure 4.7 The charge/discharge profiles of the selected cycles of the honeycomb-like cathode.

In order to verify that the porous structure is responsible for the good performance of the Li/S cell, electrochemical impedance spectroscopy (EIS) measurements were carried out on the commercial Sulfur, as-prepared Sulfur ($C_{(SDBS)}$=0 mM) and honeycomb-like Sulfur electrodes after 5 cycles (Figure 4.6 (c)). The cell containing honeycomb-like Sulfur shows smaller charge-transfer resistance than the cell with as-prepared Sulfur ($C_{(SDBS)}$=0 mM) electrode and especially the cell with commercial S electrode. Thus, the electrochemical kinetics of the honeycomb-like sulfur has been improved in rechargeable lithium batteries. Figure 4.6 (d) shows the FESEM image of the honeycomb-like sulfur electrode after 50 cycles. It is clearly that the honeycomb morphology has maintained in the electrode film during cycling, which can be ascribed to the positive effects of the porous structure. Although sulfur has to be dissolved in to the electrolyte during the discharge progress, the pores in honeycomb-like sulfur can adsorb the dissolved polysulfides and trap the diffusion of the polysulfides, which is helpful for the honeycomb-like sulfur particles to keep their porous

morphology.

A comparison of the rate capability between the honeycomb-like sulfur electrode and the commercial sulfur electrode is shown in Figure 4.8. The discharge capacity of the honeycomb-like sulfur electrode decreases gradually as the current density is increased from 50 to 1600 mA g^{-1}, and then it recovers most of its original capacity when the current density is reduced back to 50 mA g^{-1}. After 25 cycles, its discharge capability can still reach 900 mAh g^{-1}. In contrast, the rate capability of the commercial sulfur electrode is very bad. When the current density rises to 1600 mA g^{-1}, the retained discharge capacity of the commercial sulfur electrode is only about 20 mAh g^{-1}.

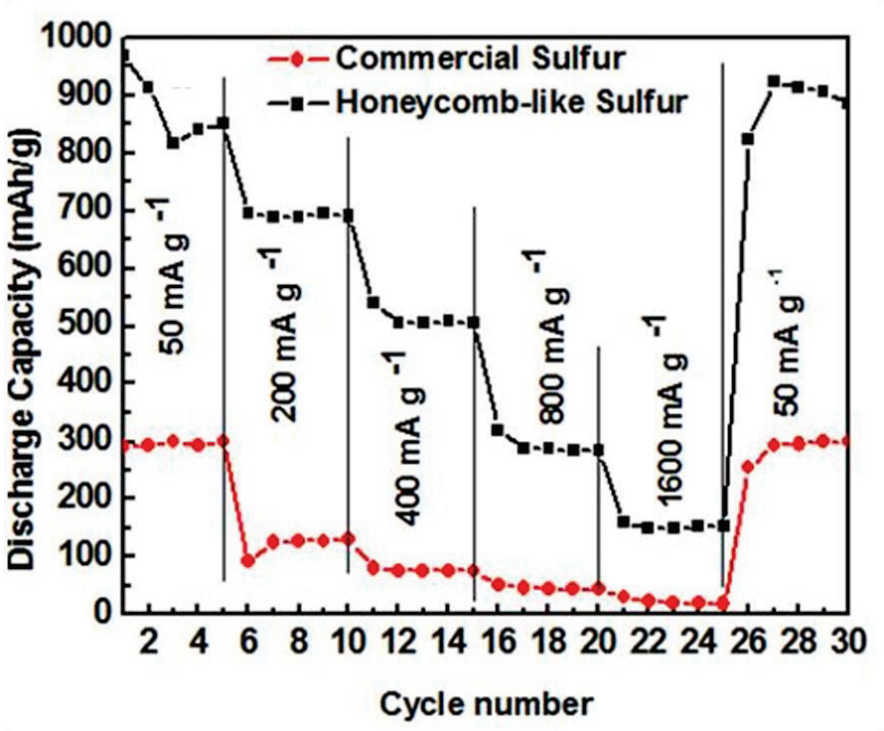

Figure 4.8 The rate capabilities of the honeycomb-like sulfur electrode and the commercial sulfur electrode.

It is well known that compare to PEGDME 500 solvent, 1,3-dioxolane (DOL) and 1,2-dimethoxyethane (DME) have good ionic conductivity and low viscosity which is essential to enhance the high rate capabilities[53, 67]. Thereby, in order to optimize the high rate

behaviour of the honeycomb-like sulfur cathode, 1 mol/L lithium bistrifluoromethanesulfonamide (LiTFSI) in a mixed solvent of 1,3-Dioxolane(DOL) / 1,2-Dimethoxyethane (DME) (1 : 1 by volume) with 0.1 mol L^{-1} $LiNO_3$ as an additive was used as electrolyte to test the rate capabilities of the honeycomb-like sulfur cathode as well. As shown in Figure 4.9, when the current densities are lower than 400 mA g^{-1}, the honeycomb-like sulfur cathode in the electrolyte with a mixed solvent of 1,3-Dioxolane(DOL)/1,2-Dimethoxyethane (DME) (1 : 1 by volume) shows lower capacities than in the electrolyte with solvent of PEGDME due to high solubility of polysulfides in DOL/DME. But when current densities are higher than 400 mA g^{-1}, the honeycomb-like sulfur cathode in the electrolyte with a mixed solvent of 1,3-Dioxolane(DOL)/1,2-Dimethoxyethane (DME) (1 : 1 by volume) presents much higher capacities than in the electrolyte with solvent of PEGDME. In addition, when the current density is increasing, the improvement becomes much obvious. Specifically, the capacities has been improved 140mAh g^{-1}at 800 mA $g^{-1}$and 250 mAh g^{-1}at 1600 mA g^{-1}. It further confirmed that the high-rate performance depends on the ion diffusion speed and the electronic conductivity of the electrolyte solvent. It can be concluded that the discharge capacity of the batteries depends on the balance between the ionic conductivity and the dissolution and diffusion of the polysulfide ions.There is a balance between the ionic conductivity and the dissolution and diffusion of the polysulfide ions. At lower current densities, the dissolution and diffusion of the polysulfide ions is the deciding factor for improving the electrochemical performance of lithium sulfur batteries. While, at high current densities the ionic conductivity plays the much more important roles on enhancing the capability of the sulfur cathode.

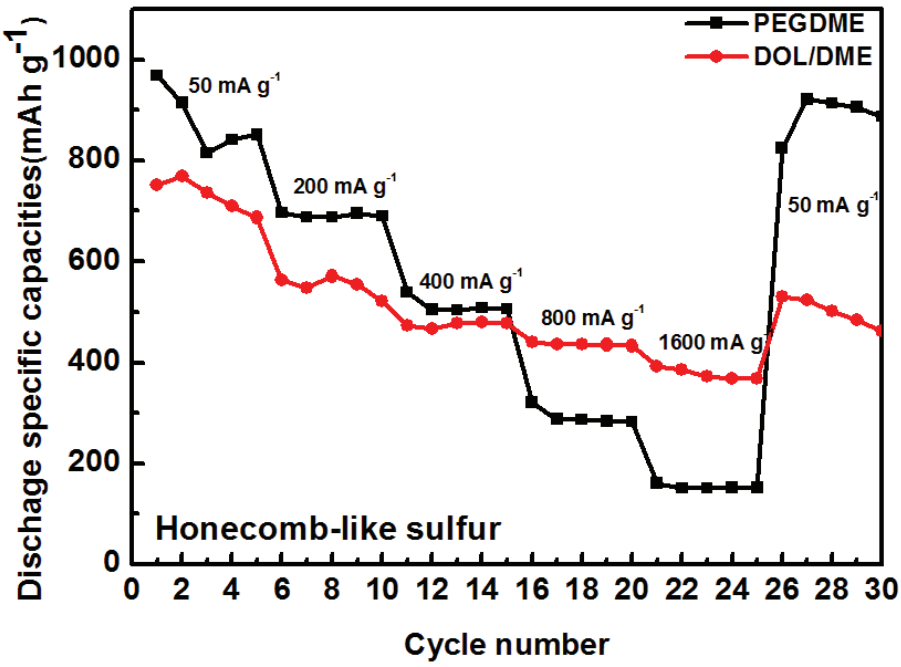

Figure 4.9 The rate capabilities of honeycomb-like sulfur electrode in PEGDME 500 and DOL/DME(1/1).

4.4. Conclusions

In summary, sulfur particles with honeycomb-like morphology were prepared via a cooperative self-assembly process. The batteries fabricated from the as-prepared honeycomb-like sulfur cathode without any extra adsorption additives show significantly improved electrochemical performance compared with the batteries using commercial sulfur powder and even the as-prepared sulfur without honeycomb-like morphology. The cells with the honeycomb-like sulfur electrode retained a reversible discharge capacity higher than 650 mAh g^{-1} for 50 cycles, while the discharge capacity of the commercial sulfur electrode was about 200 mAh g^{-1}. Moreover, the honeycomb morphology is stable and can be maintained during cycling.

Chapter 5. Split-half-tubular Polylyrrole@sulfur@polypyrrole Composite with a Novel Three-layer-3D Structure as Cathode for Lithium/Sulfur Batteries

5.1. Introduction

Due to limited global energy supplies, environmental pollution, and the increasing consumption of energy, green and efficient energy storage devices are in high demand in modern society[134, 228]. The lithium/sulfur battery is one of the most promising candidates, because the lithium/sulfur battery has the highest theoretical specific capacity of 1675 mAh g^{-1} among all the solid cathode lithium battery systems[26, 27]. It also has a very high specific energy density of 2500Wh kg^{-1} or 2800 Wh L^{-1}[14, 31-35]. In addition, sulfur is abundant in nature, low-cost, and non-toxic[38].

Nevertheless, the fabrication of lithium/sulfur batteries has encountered a number of challenges. Sulfur is very much an electrically insulating material, which leads to poor electrochemical accessibility and low utilization in the electrode. The polysulfide anions, which are formed as the reaction intermediates, are highly soluble in the organic electrolyte solvent. The diffusion of polysulfides to the lithium anode results in low active material utilization, low coulombic efficiency, and short cycle life of the sulfur electrode[9, 43]. In order to operate the lithium-sulfur battery, conductive agents should be introduced into the sulfur (by synthesizing composites of sulfur/conductive agents). It has been reported that mesoporous carbon, multiwalled carbon nanotubes, carbon fibre, reduced graphene oxide, and carbon black have all been applied to improve the electrochemical performance of the sulfur cathode in lithium/sulfur batteries[1, 5, 8, 10-15, 31, 32, 34, 35, 51-60]. Recently, in addition to the various types of carbon, conducting polymers have been investigated for lithium/sulfur batteries as well[18, 19, 27, 33, 61-64].

Compared with carbon, conducting polymer has many advantages for the lithium/sulfur battery system [25, 67]. First of all, the conducting polymer/sulfur composite

synthesis process is more feasible, because the synthesis only requires an in-situ one pot route below 100ºC, while the carbonization process usually requires very high temperature (above 600ºC), which is higher than the melting point of sulfur (115ºC). This makes synthesis of the carbon/sulfur composite by the in-situ one pot route very difficult. Moreover, conducting polymers have functional groups and unique chain structures, which can further confine the sulfur and the dissolved polysulfides by inter- and/or intra-chain bonding[20]. In addition, conducting polymers are soft and self-healing[205], which provides a solution to problems related to volume expansion and material pulverization. Finally, some polymers are electrochemically active, so that they contribute some capacity to the lithium/sulfur batteries by themselves[33].

Polyaniline, polyacrylonitrile,polypyrrole(PPy), poly(3,4-ethylenedioxythiophene) – poly(styrenesulfonate)and polythiophene have been successfully applied in lithium/sulfur batteries and are reported to significantly improve the performance of lithium/sulfur batteries[19, 64, 234-236]. Among these conducting polymers, PPy is a promising choice because the redox potential of PPy treated with lithium (2.5 V vs. Li/Li^+) is in the range of the redox potential of sulfur cathode in the lithium cell[64]. Therefore PPy not only acts as an electrically conducting agent, but also contributes to the capacity of the S cathode in the lithium/sulfur batteries. There are two major research directions in the investigation of PPy/sulfur cathode. One involves coating PPy on the surface of sulfur, while the other involves loading sulfur on the PPy. Coating with PPy is an efficient method to prevent polysulfide dissolution and to improve the conductivity between the composite particles. Wang et al. [33] first reported incorporating conductive polypyrrole into sulfur cathode. Nanosize polypyrrole particles were uniformly coated onto the surface of the sulfur powder, which significantly improved the electrical conductivity, the capacity, and the cycling durability in a lithium cell compared with the bare sulfur electrode. The Manthiram group[18] reported coating polypyrrole nano

layers on orthorhombic bipyramidal sulfur as a cathode material for lithium/sulfur batteries, which showed better electrochemical stability, cyclability, and rate capability than pristine sulfur. The role of PPy containment in preventing polysulfide dissolution was not fully discussed in these two papers, however. Furthermore, coating with PPy makes a limited contribution to improving the conductivity of the interior of the sulfur particles, which leads to the low utilization of the sulfur. In contrast, loading sulfur on a PPy conductive matrix is an efficient method to enhance the conductivity of the composite. Zhang et al. [61] loaded sulfur on branched PPy to make lithium/sulfur battery cathode, which showed improved electrochemical performance, although loading sulfur on the surface of the PPy raises the issue of the dissolution of polysulfides again. In order to obtain a thin and uniform coating layer of sulfur, the PPy conductive matrix should have high surface area. A special structure for the PPy matrix thus has to be prepared.

In order to combine the advantages of the two directions mentioned above, a Polypyrrole@Sulfur@Polypyrrole composite (PPy@S@PPy composite) with a novel three-layer-3D structure is proposed by not only loading sulfur on PPy but also coating PPy on sulfur. The composite is synthesized by the oxidative chemical polymerization method and chemical precipitation method, which has an external PPy coating layer, an intermediate sulfur filling layer and an internal PPy conducting matrix layer. In order to analyze the function of this novel three-layer-structure of the PPy@S@PPy composite, a Sulfur@Polypyrrole composite (S@PPy composite) with the same components as the prepared PPy@S@PPy composite but without three-layer-structure was synthesized for comparison. At first, the preparation process is introduced and then the XRD, Raman spectra and TGA are employed for the components confirmation for these two synthesized composites. The morphology of the composites is investigated by TEM and SEM, which confirms the unique split-half-tube structure. This unique split-half-tube structure has many

advantages, such as having higher surface area, improving the amount of sulfur loading and leading to a thin and uniform coating layer of sulfur. Next, the conductivity, capacity, reversibility and rate capability of the composite cathodes are valued by the electrochemical testing, which confirms the improvements of electrochemical performance due to this novel structure. At last, the effects of $LiNO_3$ additive in the electrolyte on coulombic efficiency are tested, which further identify the exist of the external layer of PPy in the PPy@S@PPy composite and confirm the containment function of the external layer of PPy for trapping the dissolved polysulfides.

5.2. Experimental section

5.2.1. Materials

Sodium thiosulphate ($Na_2S_2O_3$), oxalic acid ($H_2C_2O_4$), pyrrole monomer, sodium p-toluenesulphonate(PTS Na), $FeCl_3$, TX-100, cetyltrimethylammonium bromide (CTAB), ammonium persulfate, and sulfur(S) were all purchased from Sigma Aldrich (Australia). All the chemicals were used as received without any further purification.

5.2.2. Preparation process:

The preparation route for PPy@S@PPy composite is shown in Figure 5.1. There are three steps: firstly, PPy split-half-tubes were prepared by the oxidative chemical polymerization method; sulfur was then loaded on the surface of the PPy split-half-tubes via the chemical precipitation method to synthesize the S@PPy composite; and finally, an external PPy layer was coated on the surface of the S@PPy composite by the oxidative chemical polymerization method to obtain the PPy@S@PPy composite.

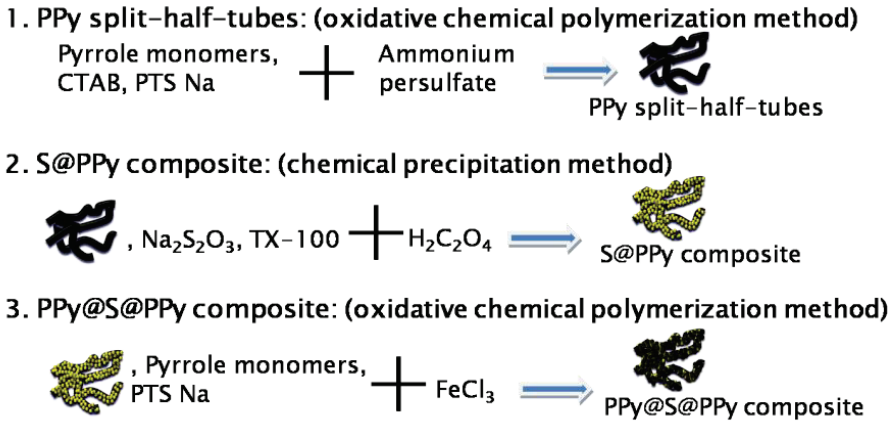

Figure 5.1 Preparation route for PPy@S@PPy composite.

5.2.2.1 Preparation of polypyrrole split-half-tubes:

Polypyrrole split-half-tubes were synthesized by the oxidative chemical polymerization method. 0.3 g liquid pyrrole monomers and 0.25 g sodium p-toluenesulfonate (PTS Na) as a dopant were dispersed in a 26 mM cetyltrimethylammonium bromide (CTAB) aqueous surfactant solution. Then, an oxidizing agent, ammonium persulfate (1 g) aqueous solution, was gradually added into the above mixture to initiate the polymerization. All solutions were precooled to 0-5 ˚C, and the polymerization in the final mixture went on at 0-5 ˚C for 12 h. After reaction, the precipitates were filtrated and washed with deionized water and ethanol, then dried in a vacuum oven at 60 ˚C for 12 h. Finally, a black powder was obtained.

5.2.2.2 Preparation of S@PPy composite as precursor (named S@PPy composite (precursor)):

Firstly, 32.10 mg of the obtained PPy split-half-tubes were added into 50 mL aqueous solution with 470 μL TX-100. After ultrasonication for 3 h, the obtained uniform suspension was transferred to a 1500 mL aqueous solution with 3 mmol $Na_2S_2O_3$. Then, 500 mL thiosulphate solution with 9 mmol $H_2C_2O_4$ was slowly dropped into the suspension under stirring. Sulfur was precipitated on the PPy split-half-tube network to form the S@PPy

precursor composite according to the following reaction: $Na_2S_2O_3 + H_2C_2O_4 \rightarrow Na_2C_2O_4 + SO_2\uparrow + S\downarrow + H_2O$. After reaction, the precipitates were filtrated and washed with deionized water and ethanol, then dried in a vacuum oven at 45 ºC for 36 h.

5.2.2.3 Preparation of PPy@S@PPy composite:

The polypyrrole layer was coated on the surface of the S@PPy composite by an optimized chemical polymerization method using pyrrole monomer, sodium p-toluenesulphonate (PTS Na) as the dopant, and $FeCl_3$ as the oxidant.

Preparation of Solution One: 57.88 mg sodium p-toluenesulfonate (PTS Na) was dispersed in 140 mL distilled water under stirring for 30 min with the temperature kept at 0-5 ºC. Then 60 μL liquid pyrrole monomer was added into the above solution under stirring for 30 min with the temperature kept at 0-5 ºC as well.

Preparation of Solution Two: 217.6 mg $FeCl_3$ was dissolved in 30 mL distilled water under stirring for 30 min with the temperature kept at 0-5 ºC.

Firstly, 400 μL TX-100 and 40 mg S@PPy precursor composite were dispersed in 35 mL Solution One with 15 μL liquid pyrrole monomers and 14.47 mg sodium p-toluenesulfonate (PTS Na) as dopant and kept under stirring for 1 h, with the temperature kept at 0-5 ºC. Then, 15 mL Solution Two with 108.8 mg $FeCl_3$ as an oxidizing agent was gradually dropped into the above mixture to initiate the polymerization. The mixture was stirred for 6 h and then aged for another 12 h. All the solutions were precooled to 0-5 ºC, and all the polymerization took place at 0-5 ºC. The resultant black aqueous solution was washed thoroughly with distilled water until free of $FeCl_3$. Finally, the black mass was dried at 45 ºC overnight under vacuum to yield PPy@S@PPy powder.

5.2.2.4 Preparation of S@PPy composite for comparison:

As well as the S@PPy precursor composite, another batch of S@PPy composite was also prepared for comparison. This S@PPy composite has the same ratio of sulfur to PPy as

in the PPy@S@PPy composite.

Firstly, 33.56 mg of the obtained PPy split-half-tubes were added into 50 mL aqueous solution with 470 μL TX-100. After ultrasonication for 3 h, the obtained uniform suspension was transferred to a 1500 mL aqueous solution with 2 mmol $Na_2S_2O_3$. Then, 500 mL thiosulphate solution with 6 mmol $H_2C_2O_4$ was slowly dropped into the suspension under stirring. Sulfur was precipitated on the PPy split-half-tube network to form S@PPy composite. After the reaction, the precipitate was filtrated and washed with deionized water and ethanol, then dried in a vacuum oven at 45 ºC for 36 h.

5.2.2.5 The mechanism of synthesis of two different morphologies of PPy (split-half tubes and cauliflower-like particles):

Both the surfactant and the oxidizing agent play key roles in controlling the morphology [85]. During the synthesis of internal PPy, CTAB was used as the surfactant, and ammonium persulfate was added as oxidizing agent. CTAB is a kind of long-chain cationic surfactant, which prefers to form a lamellar mesostructure by self-assembly. A lamellar structure is formed between the cations of the CTAB and the anions of the oxidizing agent ammonium persulfate in the aqueous solution, which is credited with leading to the growth of the ribbon-like polypyrrole. The formation of the split-half-tubular polypyrrole nanostructure is considered to be a result of rolling up the ribbon-like polypyrrole. For the preparation of external PPy, on the other hand, TX-100 was used, which is a kind of non-ionic surfactant. In this case, there is no soft template to form the lamellar structure. Thus, the typical cauliflower-like PPy was obtained.

5.2.2.6 Design synthesis steps:

1st step: To synthesize S@PPy composite (precursor) with the designed sulfur percentage of 74.9%.

In this experiment, 3 mmol $Na_2S_2O_3$ and 9 mmol $H_2C_2O_4$ were used, and according to the

reaction equation: $Na_2S_2O_3 + H_2C_2O_4 \rightarrow Na_2C_2O_4 + SO_2\uparrow + S\downarrow + H_2O$, 3 mmol sulfur is expected to be obtained. As 32.1 mg half-spilt tubes were added, the designed sulfur percentage should thus be: $(3\times32)/(3\times32+32.1)\times100\% = 74.9\%$. According to the TGA results, the real sulfur percentage is 73.6%. Thus, the real sulfur percentage is very close to the designed sulfur percentage.

2nd step: To synthesize PPy@S@PPy composite with the designed sulfur percentage of 62.0%.

In the S@PPy composite (precursor), the sulfur percentage is 73.6%, and thus the split-half tubular percentage is 100%–73.6% = 26.4%. 40 mg S@PPy composite (precursor) was used for the preparation, in which the amount of sulfur is $40 \times 73.6\% = 29.44$ mg, and the amount of split-half tubes is $40 \times 26.4\% = 10.56$ mg. As it is usually possible to obtain 1 mg PPy from 2 μL Py, 15 μL Py was added in the experiment, and thus about 7.5 mg PPy can be obtained. Then, the designed sulfur percentage in PPy@S@PPy composite is $29.44/(40.0+7.5) \times 100\% = 62.0\%$. The TGA results show that the real sulfur percentage in the PPy@S@PPy composite is 65.6%. The real sulfur percentage is a little bit higher than the designed value, but it is still acceptable for design of synthesis a kind of material by chemical reaction method.

3rd step: For comparison with PPy@S@PPy composite, to synthesize S@PPy composite with a designed sulfur percentage of 65.6%.

In this experiment, 2 mmol $Na_2S_2O_3$ and 6 mmol $H_2C_2O_4$ were used, according to the reaction equation: $Na_2S_2O_3 + H_2C_2O_4 \rightarrow Na_2C_2O_4 + SO_2\uparrow + S\downarrow + H_2O$, so 2 mmol sulfur is expected to be obtained. As 33.56 mg half-spilt tubes were added, the designed sulfur percentage should be: $(2\times32)/(2\times32+33.56) \times 100\% = 65.6\%$. According to the TGA results, the real sulfur percentage is 64.7%. Thus the real sulfur percentage is very close to the designed sulfur percentage.

There are three main points to realizing the controllable synthesis of the composite:

1. General principles for synthesis of PPy using Py: 2 μL Py → 1 mg PPy
2. Amounts of PTSNa and $FeCl_3$ (Mole Ratio): Py:PTSNa = 3:1, Py:$FeCl_3$ = 1:3
3. Accurately control the added amount of Py by preparing Solution One and Solution Two. Only ¼ Solution One and ½ Solution Two are used for the synthesis.

Table 5.1 Summary of the designed and calculated sulfur percentages of S@PPy composite and S@PPy composite (precursor).

Name	*Split-half PPy tubes*	*Sulfur Designed*	*S percentage*	
			Designed	*TGA Results*
S@PPy composite	*33.56 mg*	*2 mmol×32 g mol^{-1}*	*65.6%*	*64.7%*
S@PPy composite (precursor)	*32.1 mg*	*3 mmol×32 g mol^{-1}*	*74.9%*	*73.6%*

Table 5.2 Summary of the calculated sulfur percentages of PPy@S@PPy composite.

Name	*S from S@PPy composite (precursor)*	*PPy from S@PPy composite (precursor)*	*External layer PPy Designed*	*S percentage*	
				Designed	*TGA Results*
PPy@S@PPy composite	*29.44 mg*	*10.56 mg*	*7.5mg*	*62.0%*	*65.6%*

5.2.3. Physical Characterization:

The structures of the as-prepared sulfur, S@PPy composite, and PPy@S@PPy composite were characterized by X-ray diffraction (XRD) using a GBC MMA X-ray generator and diffractometer with Cu Kα radiation (λ = 1.5418 Å), employing a scanning rate of 5°min^{-1} in the 2θ range from 10° to 70°.Raman spectroscopy was conducted on a JOBIN YVON HR800 Confocal Raman system with 632.8 nm diode laser excitation on a 300 lines/mm grating at room temperature. Thermogravimetric analysis (TGA) was performed via a SETARAM Thermogravimetric Analyzer (France) in air to determine the changes in sample weight with increasing temperature and to estimate the amount of sulfur in the sample.

The morphology of the samples was obtained with a field-emission scanning electron microscope (FESEM; JEOL 7500, 5 kV). The specific surface area of the powders was examined by gas (ultra-high purity nitrogen) sorption analysis using the Brunauer-Emmett-Teller (BET) method (Quanta Chrome Nova 1000). Transmission electron microscope (TEM) images and EDS mapping results were also collected (JEOL 2011).

5.2.4. Electrochemical measurements:

The S@PPy composite cathode and PPy@S@PPy composite cathode slurries were made by mixing 70 wt. % composite with 20 wt. % carbon black and 10 wt. % polyvinylidenefluoride (PVDF) binder in N-methyl-2-pyrrolidinone (NMP) solvent. The slurries were spread onto aluminum foil substrates. The coated electrodes were dried in a vacuum oven at 50 ºC for 24 h and then pressed. Subsequently, the electrodes were cut into a 1×1 cm^2 size. A conventional organic solvent electrolyte consisting of 1 $molL^{-1}$ lithium bis(trifluoromethane) sulfonamide (LiTFSI) in poly (ethylene glycol) dimethyl ether 500 (PEGDME 500) was used with 0.1 mol L^{-1} $LiNO_3$ as an additive. To compare the effect of the electrolyte, another electrolyte was also prepared, which was 1 $molL^{-1}$LiTFSI in 1,3-dioxolane (DOL) / 1,2-dimethoxyethane (DME) (1:1 by volume) with 0.1 $molL^{-1}$ $LiNO_3$ as an additive.CR 2032 type coin cells were assembled in an Ar-filled glove box. Charge-discharge testing was carried out with a LAND battery test system at a current density of 50 mA g^{-1} within the voltage range of 1.5–3.0 V. Cyclic voltammetry (CV) and AC impedance measurements were performed using a Biologic VMP-3 Multichannel electrochemistry workstation at a scanning rate of 0.1 mV s^{-1} and over a frequency range of 1 00 kHz - 0.01 Hz, respectively.

5.3. Results and Discussion

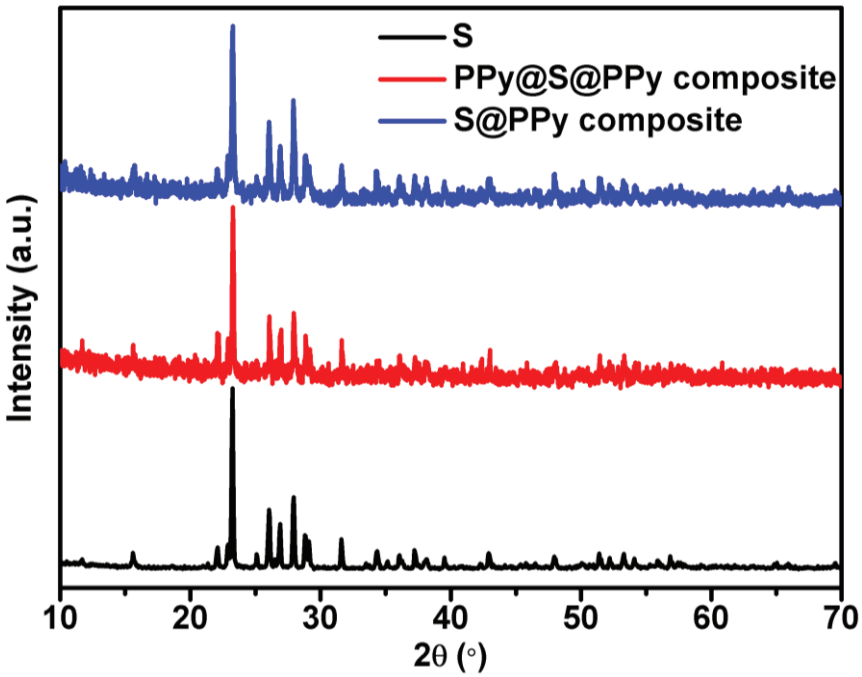

Figure 5.2 X-ray diffraction patterns of S, S@PPy composite, and PPy@S@PPy composite.

Figure 5.2 presents the X-ray diffraction (XRD) patterns of the commercial sulfur, S@PPy composite, and PPy@S@PPy composite. The diffraction peaks of the three samples match very well with the standard diffraction lines of sulfur (PDF card No. 00-001-0478), which can be indexed to the orthorhombic phase with space group Fddd. This indicates that no phase transformation of sulfur occurs during the in-situ chemical polypyrrole coating process.

The Raman spectra of bare S, S@PPy composite, and PPy@S@PPy composite are shown in Figure 5.3, which were obtained with 632.8 nm diode laser excitation at room temperature. The Raman spectrum of S displays three main peaks below 500 cm^{-1}, while the peaks in the Raman spectrum of PPy are located between 800 and 1700 cm^{-1}, which are identified as the characteristic peaks of C=C backbone stretching of PPy at 1580 cm^{-1}, C-H in-plane deformation at 1050 cm^{-1} and 1080 cm^{-1}, C-H out-of-plane bending of oxidized PPy at 930 cm^{-1}, N-H in-plane bending at 1240 cm^{-1}, and the ring-stretching mode of PPy at 1320

cm^{-1} and 1380 cm^{-1}, respectively[237]. The Raman spectra of S@PPy composite and PPy@S@PPy composite show not only the three characteristic peaks of sulfur below 500 cm^{-1}, but also the typical peaks of PPy between 800 and 1700 cm^{-1}. This confirms that the S@PPy composite and PPy@S@PPy composite contain both elemental sulfur and PPy.

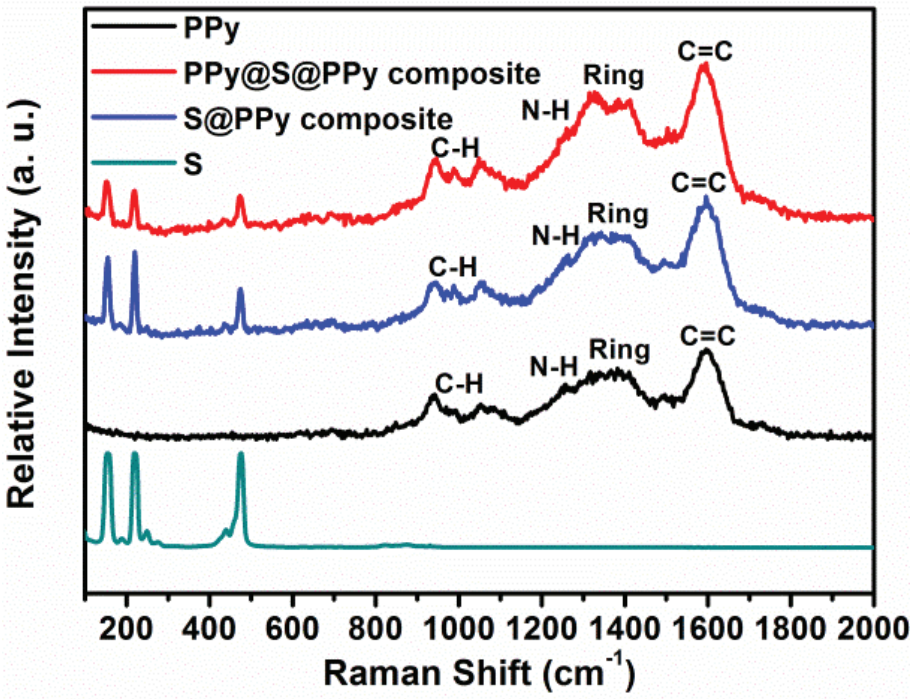

Figure 5.3 Raman spectra of S, PPy, S@PPy composite, and PPy@S@PPy composite.

To quantify the amount of the sulfur in the as-prepared S@PPy composite and the PPy@S@PPy composite, TGA analysis was carried out in air, with heating from 50ºC to 800 ºC at the rate of 5 ºC min^{-1}. As shown in Figure 5.4, the commercial sulfur shows a weight loss starting at around 115 ºC, which is the melting point of the elemental sulfur, and it was burned completely at around 230 ºC. PPy starts to be oxidised at around 220 ºC. For the S@PPy composite and PPy@S@PPy composite, sulfur is burned off at the first weight loss stage, followed by the decomposition of PPy at the second weight loss stage[18]. Thus, the S@PPy composite contains 64.7 wt% sulfur and 35.3wt% polypyrrole, while the PPy@S@PPy composite is composed of 65.6 wt% sulfur and 34.4 wt% polypyrrole. As shown in Figure 5.5, the S@PPy precursor composite is composed of 73.6 wt% sulfur and

26.4 wt% polypyrrole, so it can be calculated that the PPy@S@PPy composite contains 10.9% external PPy layer, 65.6% sulfur, and 23.5% inner PPy split-half-tubes. Therefore, the S@PPy composite and PPy@S@PPy composite have nearly the same components, but with different structures. Thus, it can be concluded that all the differences in the performance between the S@PPy composite and PPy@S@PPy composite are only related to the structure.

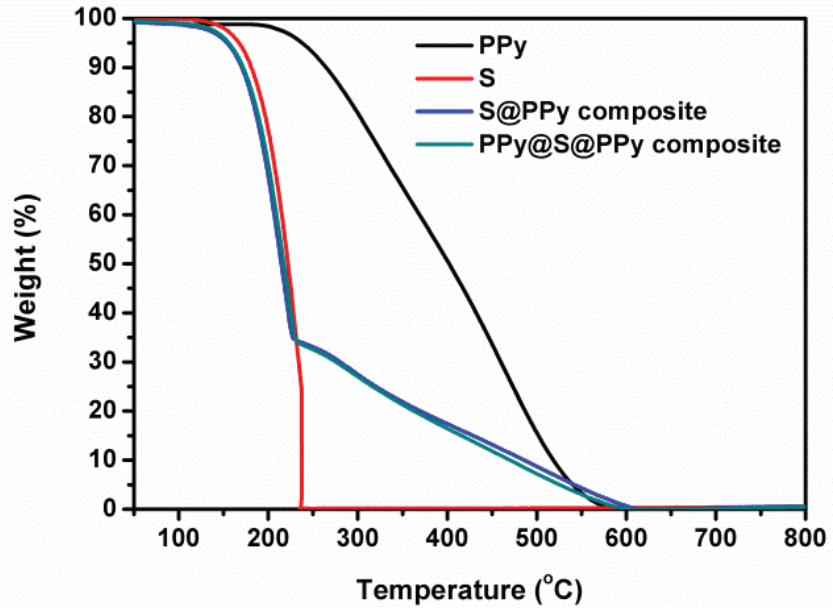

Figure 5.4 TGA curves of S, PPy, S@PPy composite, and PPy@S@PPy composite.

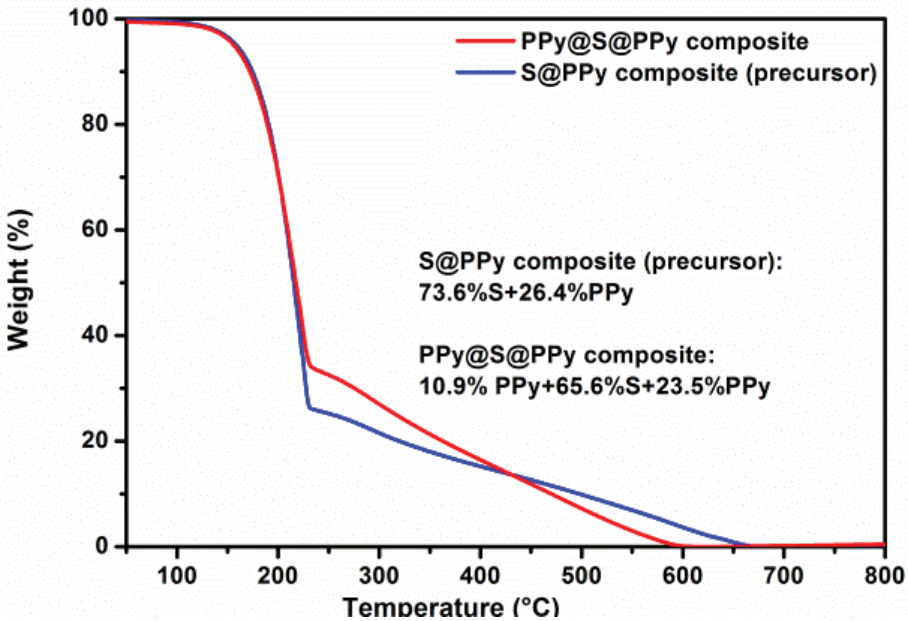

Figure 5.5 TGA curves of: S@PPy composite (precursor) and PPy@S@PPy composite.

The morphology of the as-prepared PPy was investigated by transmission electron microscopy (TEM), as shown in Figure 5.6. In Figure 5.6 (a), the morphology of the as-prepared PPy features split-half-tubes, with diameters around 70-100 nm. It is interesting that the surfaces of these split-half-tubes are not smooth, which can also be seen in Figure 5.6 (b-d). It is clear that a great many PPy particles grow in a line to form the split-half-tubular structure, as shown in Figure 5.6 (d). This unique split-half-tube structure has many advantages in comparison with previous reports, such as having higher surface area, improving the amount of sulfur loading, and facilitating a thin and uniform coating layer of sulfur. The BET surface area of whole tubular PPy is 17.0 m^2 g^{-1} in Ref.[238], and the sulfur loading is 30% and 50%. In this work, on the other hand, the surface area of the split-half-tubular PPy is 57.4 m^2g^{-1}, and the sulfur loading can be as high as 64.7% and 73.6%. The contact between the surfaces of the split-half-tubular PPy and sulfur will be increased compared with the whole tubular structure, and therefore, the conductivity will be increased.

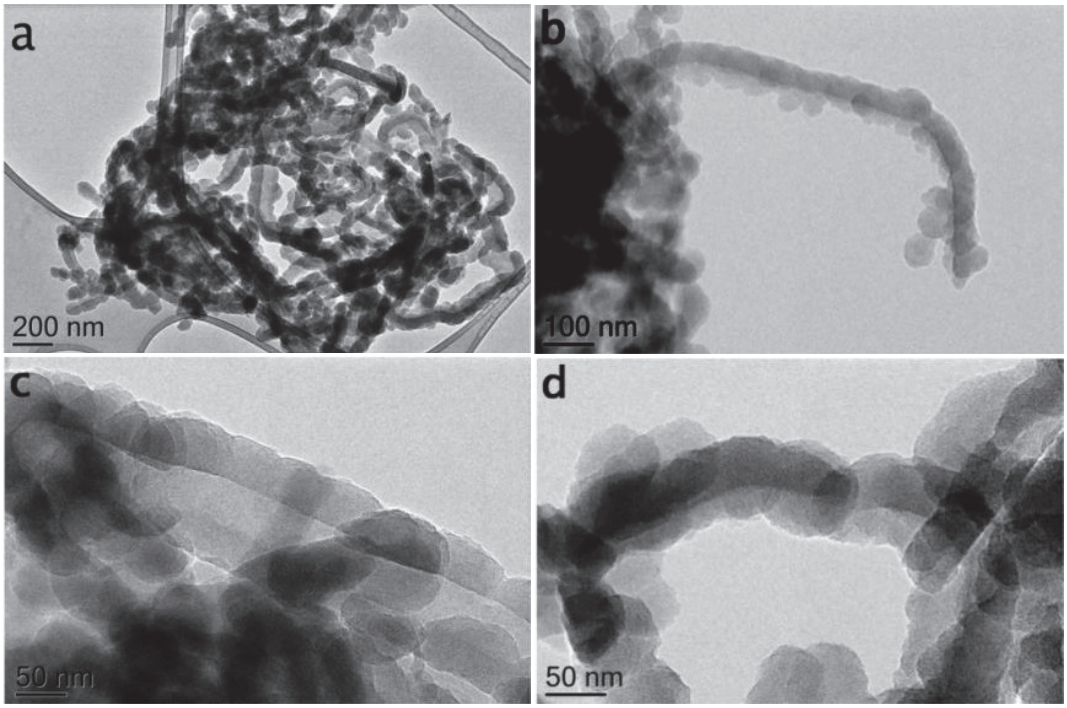

Figure 5.6 TEM images of PPy: (a) panoramic view at low magnification; (b) side view at high magnification; (c) front view at high magnification; (d) back view at high magnification.

The morphology of the as-prepared S@PPy composite and PPy@S@PPy composite was investigated by field-emission scanning electron microscopy (FESEM), as shown in Figure 5.7. The images of the as-prepared S@PPy composite and PPy@S@PPy composite reveal that the morphology of these two composites has kept the split-half-tube structure, with around 100-150 nm tube width, as shown in Figure 5.7(a, b). Figure 5.8 is a TEM image (secondary electron imaging mode) of the PPy@S@PPy composite. It is shown that the morphology of the external layer of PPy is typical cauliflower-like particles. TEM images of the PPy@S@PPy composite are also presented in Figure 5.9 at different magnifications and from different viewpoints. The images reveal that the morphology of the PPy@S@PPy composite has kept the split-half-tube structure with around 100 nm - 150 nm tube width. The surface has also become much smoother than in the as-prepared PPy split-half-tubes. The morphology of the S@PPy composite precursor for preparation of PPy@S@PPy composite is also presented in Figure 5.10. It is clearly shown that the morphology has kept the split-half-tube structure with rough surfaces.

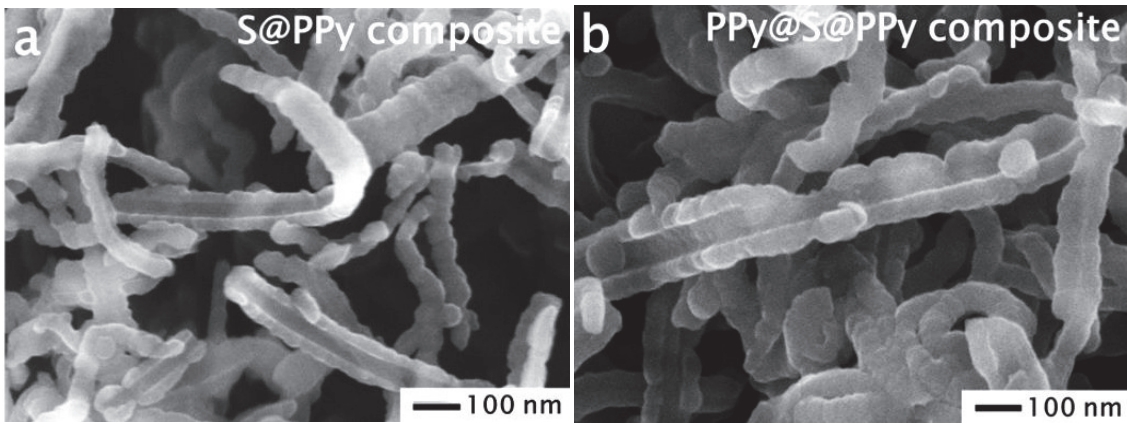

Figure 5.7 FESEM images of (a) S@PPy composite, (b) PPy@S@PPy composite.

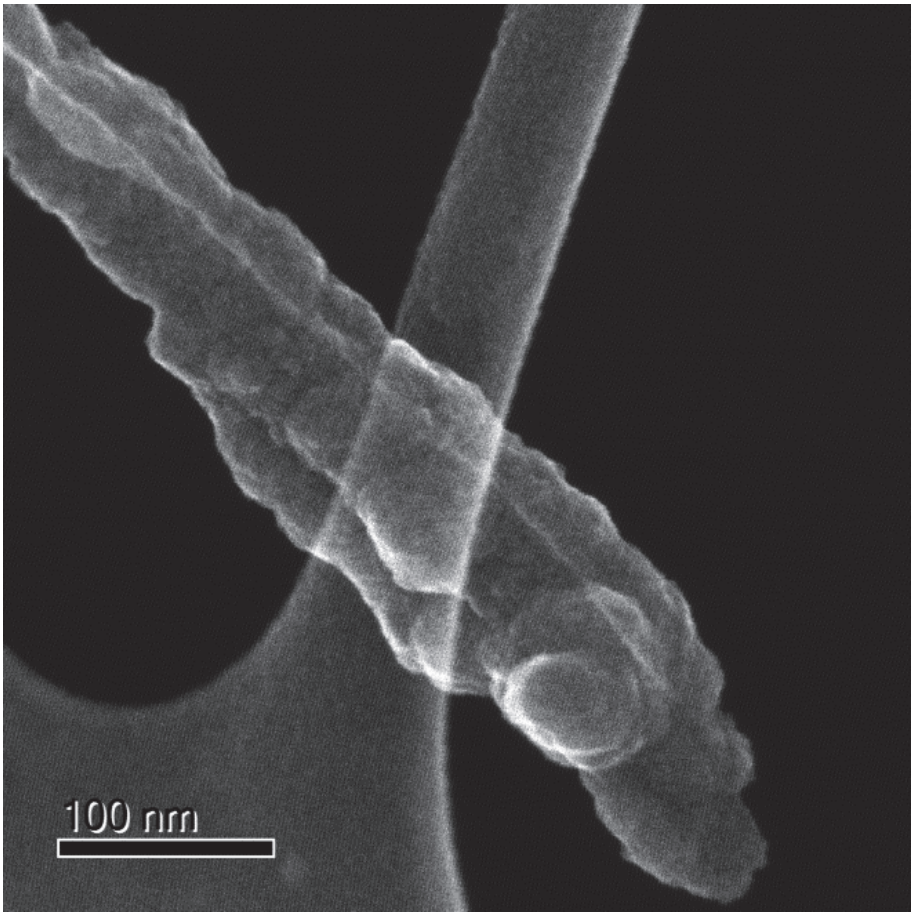

Figure 5.8 TEM image (secondary electron imaging mode) of the PPy@S@PPy composite

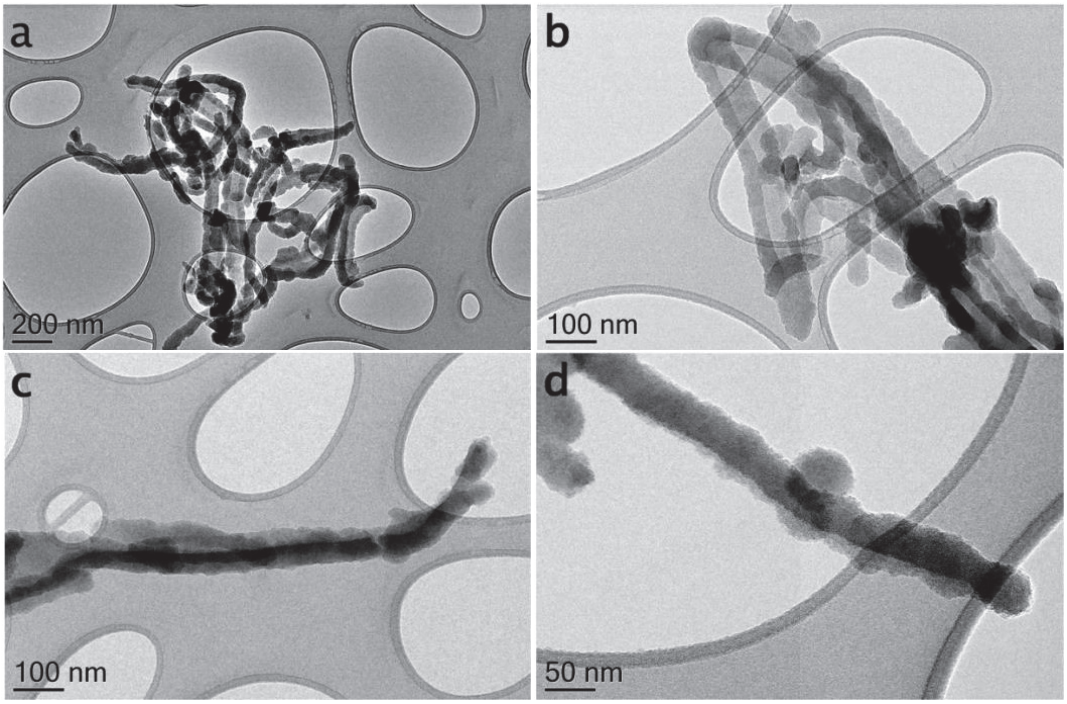

Figure 5.9 TEM images of PPy@S@PPy composite at different magnifications and from

different viewpoints.

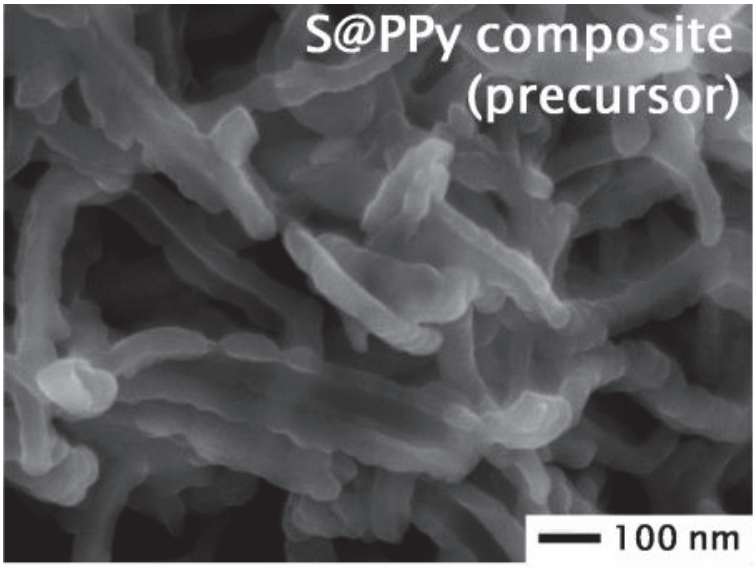

Figure 5.10 FESEM image of S@PPy composite as precursor for preparation of PPy@S@PPy composite.

To verify that the sulfur was uniformly coated on the surfaces of the split-half tubes of PPy, energy dispersive X-ray spectroscopy (EDS) mapping analysis was carried out on the S@PPy composite (Figure 5.11 (a-d)). Figure 5.11 (a) is a TEM image of the S@PPy composite. The red spots in Figure 5.11 (b) correspond to the presence of the element carbon, and the green spots in Figure 5.11 (c) correspond to the element nitrogen, in which C and N are the elements from polypyrrole. The yellow spots in Figure 5.11 (d) correspond to the element sulfur. These results show that S is distributed uniformly throughout the whole area of the S@PPy composite, which indicates that the sulfur has uniformly coated the surfaces of the split-half tubes of PPy. EDS mapping analysis was also carried on the S@PPy composite (precursor) for confirming that the sulfur was uniformly coated on the surfaces of the split-half tubes of PPy, and the results are shown in Figure 5.12. Figure (a) is the TEM image of the S@PPy composite (precursor). The red spots correspond to the presence of the element carbon (Figure 5.12 (b)), and the green spots correspond to the element nitrogen (Figure 5.12

(c)), in which C and N are elements from the polypyrrole. The yellow spots correspond to the element sulfur (Figure 5.12 (d)). The results also show that S is distributed uniformly throughout the whole area of the S@PPy composite (precursor), which indicates that the sulfur has uniformly coated the surfaces of the split-half tubes of PPy. In order to show the sulfur distribution and the structure of the PPy@S@PPy composite, TEM and EDS mapping were conducted for the PPy@S@PPy composite, and the results are shown in Figure 5.11 (e-h). Figure 5.11 (e) is the TEM image of the PPy@S@PPy composite. The red spots in Figure 5.11 (f) correspond to the presence of the element carbon, and the green spots in Figure 5.11 (g) correspond to the element nitrogen, in which C and N are the elements from polypyrrole. From Figure 5.11 (f) and (g), it is clear that the external PPy layer is very uniformly coated on the S@PPy split-half tubes. In Figure 5.11 (h), the yellow spots correspond to the element sulfur. These results show that S is distributed uniformly throughout the whole area of the PPy@S@PPy composite. Thus, the uniform distribution of sulfur and the three-layer structure of the PPy@S@PPy composite have been confirmed.

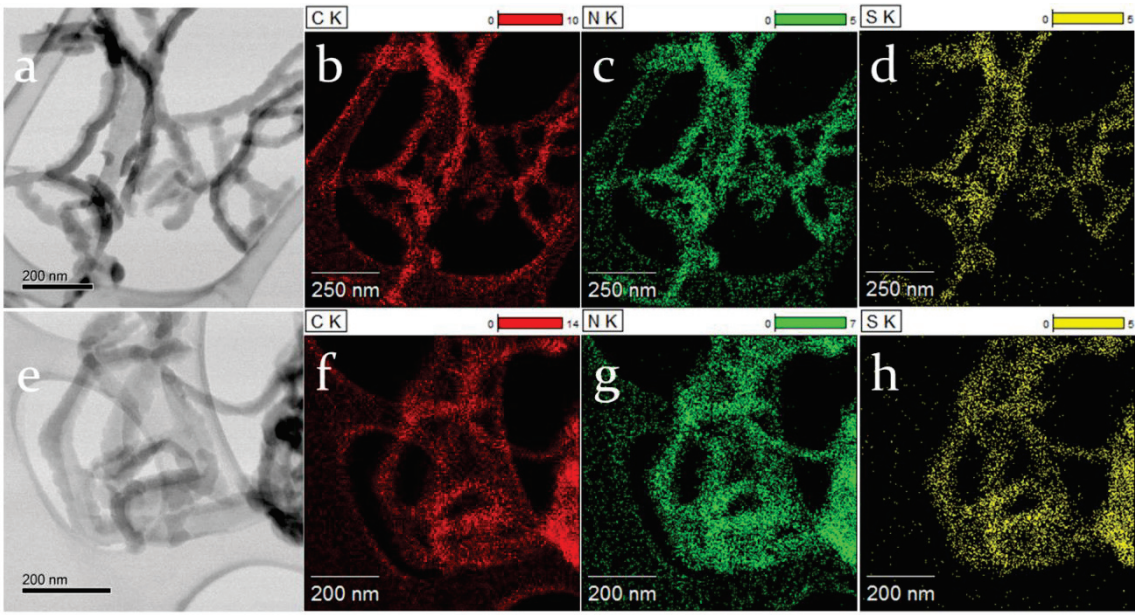

Figure 5.11 (1) S@PPy composite: (a) TEM image; (b) elemental mapping of Carbon; (c) elemental mapping of Nitrogen; (d) elemental mapping of Sulfur, (2) PPy@S@PPy

composite: (e) TEM image; (f) elemental mapping of Carbon; (g) elemental mapping of Nitrogen; (h) elemental mapping of Sulfur.

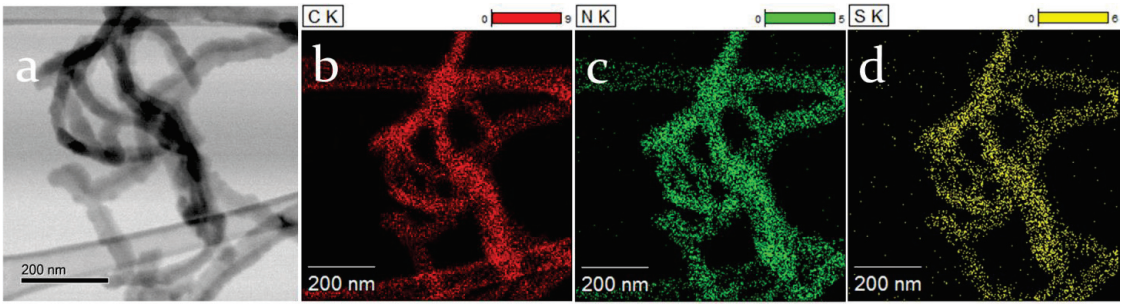

Figure 5.12 S@PPy composite (precursor): (a) TEM image; (b) elemental mapping of Carbon; (c) elemental mapping of Nitrogen; (d) elemental mapping of Sulfur

To investigate the electrochemical characteristics of the S@PPy composite and PPy@S@PPy composite, cyclic voltammetry (CV) of the initial 5 cycles in 1 M LiTFSI in PEGDME 500 with 0.1 M $LiNO_3$ additive was conducted at a scan speed of 0.1 mV s^{-1}in the potential range of 1.5-3.0 V. In Figure 5.13, S@PPy composite and PPy@S@PPy composite exhibit similar electrochemical behaviour, in which two reduction peaks are observed, which could be assigned to the multiple-step reaction mechanism of sulfur with lithium. Specifically, in the first cycle, the peak at 2.4 V is ascribed to the open ring reduction of cyclic S_8 to long chain lithium polysulfides (Li_2S_x, $4 \leq x < 8$), while the peak at 1.8 V corresponds to the further reduction of these high-order polysulfides to Li_2S_2 and Li_2S. The weak peak at 2.05 V is associated with the reduction of PPy[33]. It indicates that polypyrrole acts as not only a conducting additive, but also as an active material. From the first cycle onward, this peak becomes weaker and weaker in the CV profiles in Figure 5.13, which indicates that the lithium-storage capability of PPy has decreased. This phenomenon is in agreement with the cycling performance of PPy in Figure 5.15 (b), which shows very large irreversible capacity at the initial cycle and obvious capacity decay during the cycling. From the second cycle to the fifth cycle, there are some differences between the S@PPy composite and the

PPy@S@PPy composite. The reduction peaks of S@PPy composite are nearly at the same positions from the second cycle to the fifth cycle, while both of the reduction peaks of PPy@S@PPy composite are obviously shifted to higher voltage. This suggests that the electrochemical reactions during the first five cycles need to overcome the strong energy absorption of the conductive matrix and the outside layer of PPy[27].

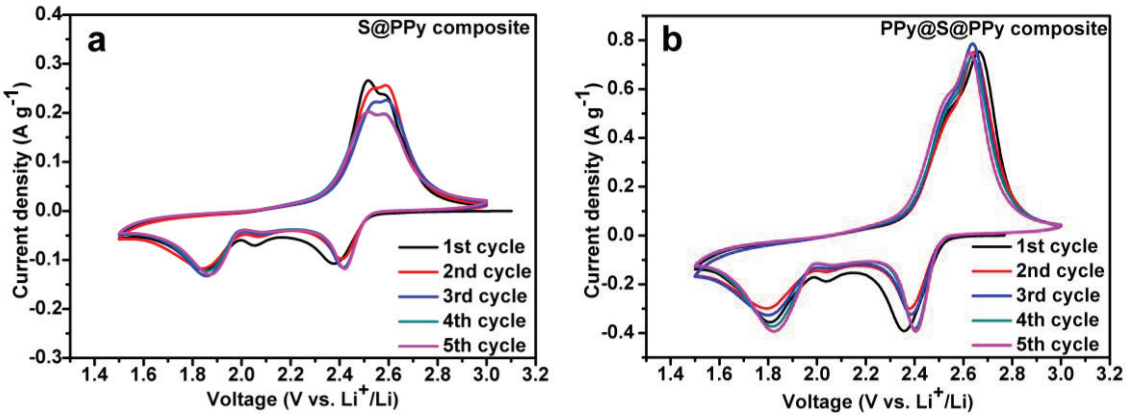

Figure 5.13 Cyclic voltammograms for the first 5 cycles of (a) S@PPy composite electrode; (b) PPy@S@PPy composite electrode.

Figure 5.14 shows representative charge and discharge voltage profiles of the 1st, 2nd, 5th, 10th, and 20th cycles of S@PPy composite and PPy@S@PPy composite electrodes in 1M LiTFSI in PEGDME 500 with 0.1 M $LiNO_3$ additive at the current density of 50 mA g^{-1}.The discharge curves present two plateaus for both cells, which are at 2.5 and 2.03 V, respectively. They are assigned to the two-step reaction of sulfur with lithium during the discharge process. Comparing Figure 5.14 (a) and (b), it is obvious that the PPy@S@PPy composite electrode shows much better reversibility than the S@PPy composite electrode. This confirms that the coating layer of PPy on the outside of the S@PPy composite can improve the cycling performance of the sulfur cathode.

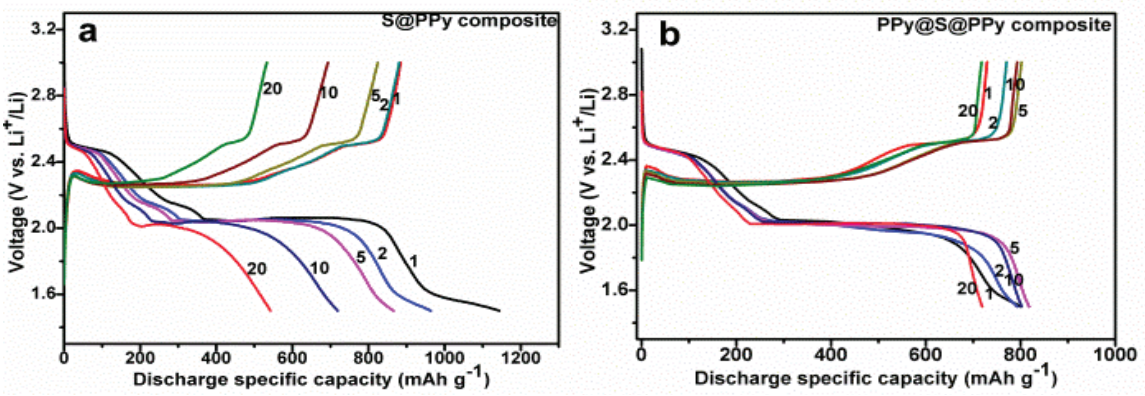

Figure 5.14 Discharge/charge curves for selected cycles of (a) S@PPy composite electrode; (b) PPy@S@PPy composite electrode.

Figure 5.15 (a) presents the discharge specific capacities of S@PPy composite and PPy@S@PPy composite cathodes in 1M LiTFSI in PEGDME 500 with 0.1 M $LiNO_3$ additive at the current density of 50mA g^{-1}. It was found that the discharge specific capacity and the reversibility of the PPy@S@PPy composite electrode are much higher than for the S@PPy composite electrode. Specifically, PPy@S@PPy composite cathode shows better cycling performance, yielding a discharge specific capacity of 554 mAh g^{-1} after 50 cycles, which is approximately 68.8% retention of the initial discharge specific capacity of about 801mAh g^{-1}, while the S@PPy composite cathode presents the discharge specific capacity of 370 mAh g^{-1} after 50 cycles, representing about 32.3% retention of the initial discharge specific capacity of about 1145mAh g^{-1}. Thus, the capacity decay of PPy@S@PPy composite electrode is as low as 0.624% per cycle during these cycles, but the capacity decay of S@PPy composite electrode is as high as 1.354% per cycle. It should be noted that the PPy@S@PPy composite cathode delivers much lower discharge specific capacity in the first five cycles compared to S@PPy composite, which could be ascribed to the incomplete utilization of the active materials during the first few cycles of the PPy@S@PPy composite electrode. The sulfur in PPy@S@PPy composite electrode is covered by another PPy external layer, which means that the sulfur cannot be completely exposed to the electrolyte during the initial cycles,

and the sulfur has to rearrange itself during the first few cycles, so that the inactive cores of sulfur are exposed to the electrolyte and then become able to be reutilized in subsequent cycles[11]. Figure 5.15 (b) shows that PPy can contribute some capacity to the lithium/sulfur battery, which can further confirm that PPy is an active material. And the discharge curve for the 1st cycle of the PPy electrode is presented in the inset figure in Figure 5.15 (b). It shows the discharge plateaus is around at 2.05 V, which agrees very well with the results in Figure 5.13 that the weak peak at 2.05 V can associated with the reduction of PPy.

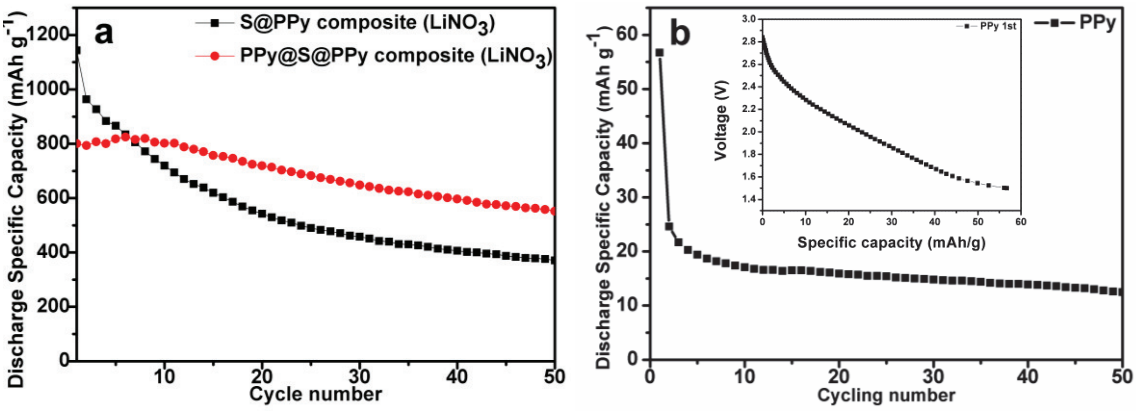

Figure 5.15 Discharge specific capacities of (a) S@PPy composite and PPy@S@PPy composite cathodes in PEGDME 500 electrolyte with 0.1 M $LiNO_3$ additive; (b) polypyrrole electrode in PEGDME 500 electrolyte with 0.1 M $LiNO_3$ additive (inset: the discharge curve for the 1st cycle of the polypyrrole electrode).

In order to compare the rate capabilities of S@PPy composite and PPy@S@PPy composite cathodes, the cells were discharged to 1.5 V at different current densities from 50 mA g^{-1} to 1600 mA g^{-1}in PEGDME 500 electrolyte with 0.1 M $LiNO_3$ additive, as shown in Figure 5.16 (a). It should be noted that the PPy@S@PPy composite delivered a higher capacity when compared to the S@PPy composite, except for the first 5 cycles at the current density of 50mA g^{-1}, the reason for which has been explained in the discussion related to Figure 5.15. In addition, the PPy@S@PPy composite also presents much better reversibility

compared to the S@PPy composite. When the current density was reduced to 50mA g^{-1}, the PPy@S@PPy composite cathode recovered 87% of its initial capacity, while S@PPy composite only recovered 42%. These improvements in the PPy@S@PPy composite are achieved by the external coating layer of PPy, which can confine the dissolved polysulfides and decrease the loss of the active sulfur. Moreover, in PPy@S@PPy composite, the sulfur is confined in a limited space between the two layers of PPy, so that the charge transfer reactions could be enhanced because of good electronic contact between the sulfur and the PPy, leading to higher rate capacities in lithium sulfur batteries[15]. It is well known that, in comparison with PEGDME 500 solvent, 1,3-dioxolane (DOL) and 1,2-dimethoxyethane (DME) have good ionic conductivity and low viscosity, which are essential to enhance the rate capabilities[53, 67]. Therefore, in order to optimize the high rate behaviour of the PPy@S@PPy composite cathode, 1 mol L^{-1} lithium bis(trifluoromethane) sulfonamide (LiTFSI) in a mixed solvent of 1,3-DOL/1,2-DME (1:1 by volume) with 0.1mol L^{-1} $LiNO_3$ as an additive was used as electrolyte to test the rate capabilities of the PPy@S@PPy composite cathode as well. As shown in Figure 5.16 (b), when the current densities are lower than 200 mA g^{-1}, there is no obvious difference between these two kinds of electrolyte. When the current density is higher than 200 mA g^{-1}, however, the PPy@S@PPy composite cathode in the electrolyte with a mixed solvent of 1,3-dioxolane(DOL)/1,2-dimethoxyethane (DME) (1:1 by volume) presents much higher capacities than in the electrolyte with PEGDME solvent. In addition, when the current density is increased, the improvement becomes more obvious. The capacity is improved to 60 mAh g^{-1} at 400 mA g^{-1}, 120 mAh g^{-1}at 800 mA g^{-1},and 160 mAh g^{-1}at 1600mA g^{-1}. This further confirms that the high-rate performance depends on the ion diffusion speed and the conductivity of the electrolyte solvent.

Based on the above discussion, the improvement of the electrochemical performance of the cell with PPy@S@PPy composite cathode could be attributed to the multiple effects of

the PPy additive and the superiority of the three-layer structure.

(1) PPy is a kind of conducting polymer, so it works as a conducting additive. (2) As shown in Figure 5.15 (b), PPy is also an active material contributing to the capacity of the electrode during cycling. This has been further confirmed by the CV measurements and the charge/discharge plateau data discussed above. (3) The internal PPy split-half-tube acts as a backbone to form the conducting network or the conducting matrix. Thereby, it can absorb the dissolved polysulfides and prevent the dissolution of polysulfides into the electrolyte to some degree, as well as improving the conductivity of the electrode at the same time. (4) The external PPy coating layer on the surface of the S@PPy composite can further improve the conductivity of the electrode. This can be confirmed by the electrochemical impedance spectroscopy (EIS) measurements in Figure 5.17. It is obvious that the impedance response exhibits a semicircular loop at high frequencies. The diameter of this semicircle gives the charge-transfer resistance, which corresponds to the charge transfer kinetics. The results show that the charge-transfer resistance of the cell with PPy@S@PPy composite electrode is lower than that of the cell made from S@PPy composite electrode, indicating that the conducting external PPy coating layer on the surface of the S@PPy composite has improved the electrochemical kinetics of the electrode in lithium/sulfur batteries. (5) In the PPy@S@PPy composite, the external PPy coating layer on the surface of the S@PPy composite also plays the role of container to trap the dissolved polysulfides, preventing them from dissolving in the electrolyte, and accommodates the volume expansion to reduce the pulverization of sulfur.

The proposed model and a cross-sectional view of the S@PPy composite are presented in Figure 5.18 (a), where it is clear that the sulfur particles are loaded on the surface of the PPy fibre without any protection on the outside. In contrast, in the PPy@S@PPy composite, there is another PPy layer coating the surface of the S@PPy composite, as shown in Figure 5.18 (b).

Figure 5.18 (c) contains a schematic diagram of the function of the external PPy coating layer on the surface of the S@PPy composite in the PPy@S@PPy composite. Without the external PPy layer protection, the dissolved polysulfides will diffuse out of the conducting matrix during charge-discharge processes. In contrast, when the external coating layer of PPy is present, polysulfides can be confined and prevented from diffusion into the electrolyte during the charge/discharge progress, so as to minimize the loss of the active materials in the cathode and improve the capacity and the cycling performance. Moreover, the containment function of the external PPy layer in PPy@S@PPy composite can be further confirmed by the coulombic efficiency results on the S@PPy composite electrode and the PPy@S@PPy composite electrode in the electrolyte with and without $LiNO_3$ additive, as shown in Figure 5.19. It is well known that the dissolution and diffusion of the polysulfides in the electrolyte can lead to a "shuttle effect", which results in low coulombic efficiency in the lithium/sulfur battery system. It is also reported that the addition of $LiNO_3$ as an additive in the electrolyte can improve the coulombic efficiency significantly[22, 31, 200]. Thus, as shown in Figure 5.19 (a), the coulombic efficiency of the S@PPy composite cathode is significantly enhanced after adding $LiNO_3$ into the electrolyte. This is because without the external PPy layer protection, quite a large amount of dissolved polysulfides diffuse to the lithium anode, which leads to a serious "shuttle effect", resulting in decreased coulombic efficiency. On adding $LiNO_3$ additive to the electrolyte, a denser and more protective passivation film is formed on the lithium surface to protect the lithium anode and reduce the loss of the active sulfur, leading to the increase in the coulombic efficiency. In contrast, Figure 5.19 (b) shows that there is no obvious improvement of the coulombic efficiency of the PPy@S@PPy composite cathode after adding $LiNO_3$ to the electrolyte. This is because in PPy@S@PPy composite, there is an external layer of PPy, so nearly all the dissolved polysulfides will be trapped. The "shuttle effect" can thus be ignored to some extent. There may be only a slight amount of dissolved

polysulfides in the lithium anode, so the coulombic efficiency will not gradually decrease, even without $LiNO_3$ additive in the electrolyte, and the effect of $LiNO_3$ is negligible on the PPy@S@PPy composite cathode. This is the most powerful evidence that the external layer of PPy can confine the dissolved polysulfides effectively. This is also the first time, to the best of my knowledge, that coulombic efficiency has been used to prove the containment function of the conducting polymer. This method is very simple and effective for test the design of the samples whether can confine the dissolved polysufides or not. Only two kinds of electrolyte are needed, one is 1M LiTFSI in DOL/DME with $LiNO_3$ additive, the other one is 1M LiTFSI in DOL/DME without $LiNO_3$ additive. Then coulombic efficiencies are tested. If the coulombic efficiency of the electrode in the electrolyte of 1M LiTFSI in DOL/DME without $LiNO_3$ additive shows no differencies between that in 1M LiTFSI in DOL/DME with $LiNO_3$ additive, it means the structure of the sample can trap the dissolved polysulfides effectively. On the contrary, if there is big difference of the coulombic efficiencies in these two kind of electrolytes, it means the structure of the sample cannot trap the dissolved polysulfides effectively.

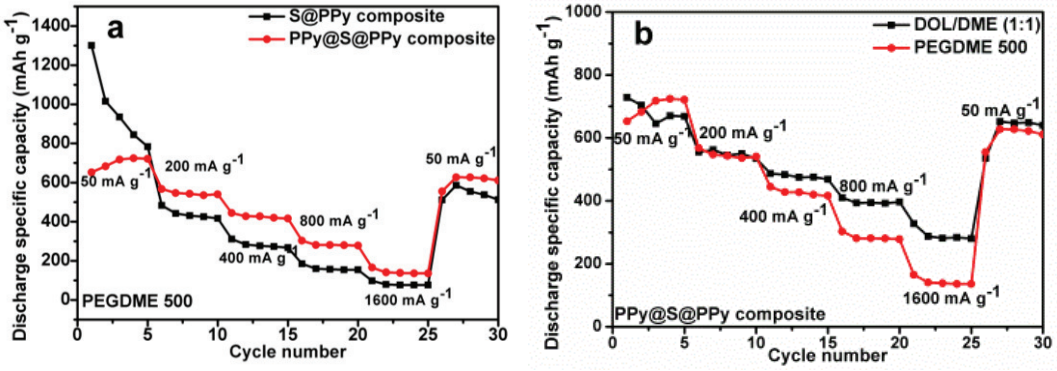

Figure 5.16 (a) Rate capabilities of S@PPy composite electrode and PPy@S@PPy composite electrode in PEGDME 500; (b) rate capabilities of PPy@S@PPy composite electrode in PEGDME 500 and DOL/DME (1/1).

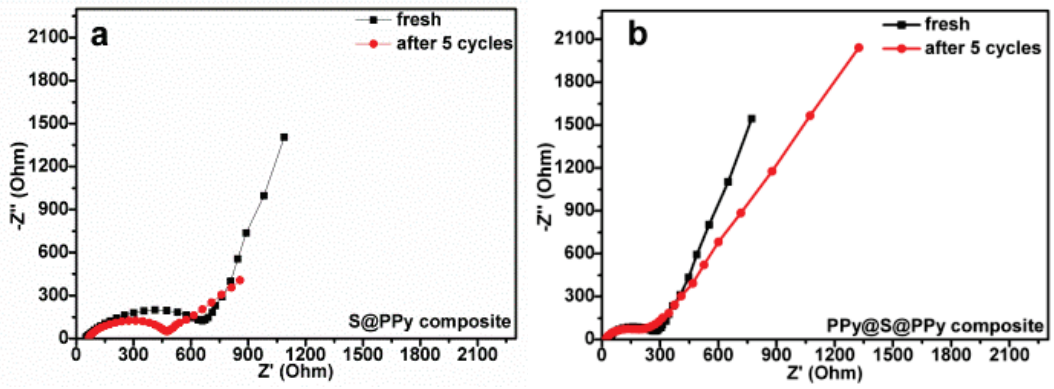

Figure 5.17 Impedance plots of (a) S@PPy composite electrode; (b) PPy@S@PPy composite electrode.

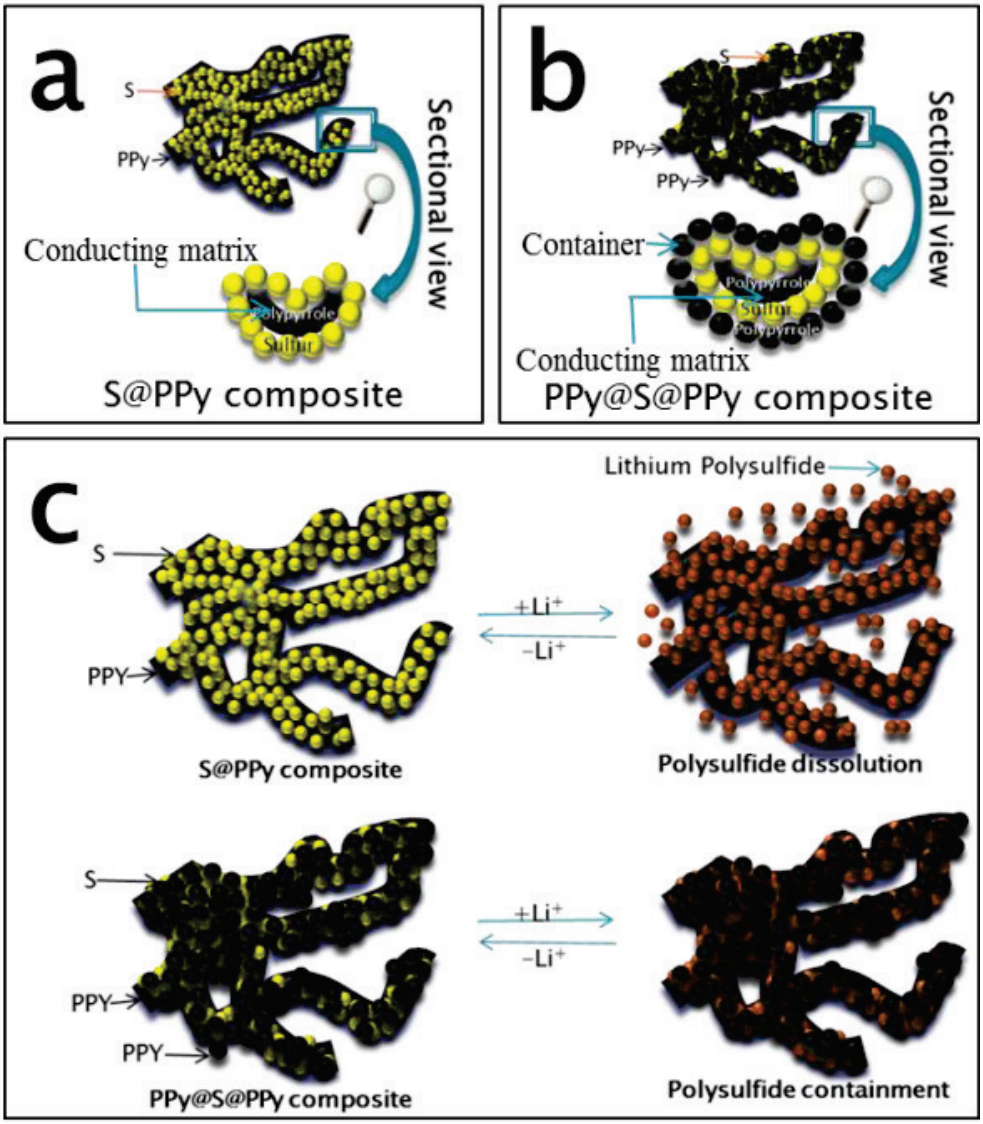

Figure 5.18 Proposed model and cross-sectional view of (a)S@PPy composite and

(b)PPy@S@PPy composite; (c) schematic diagram of the function of the external PPy layer of PPy@S@PPy composite towards trapping the dissolved polysulfides.

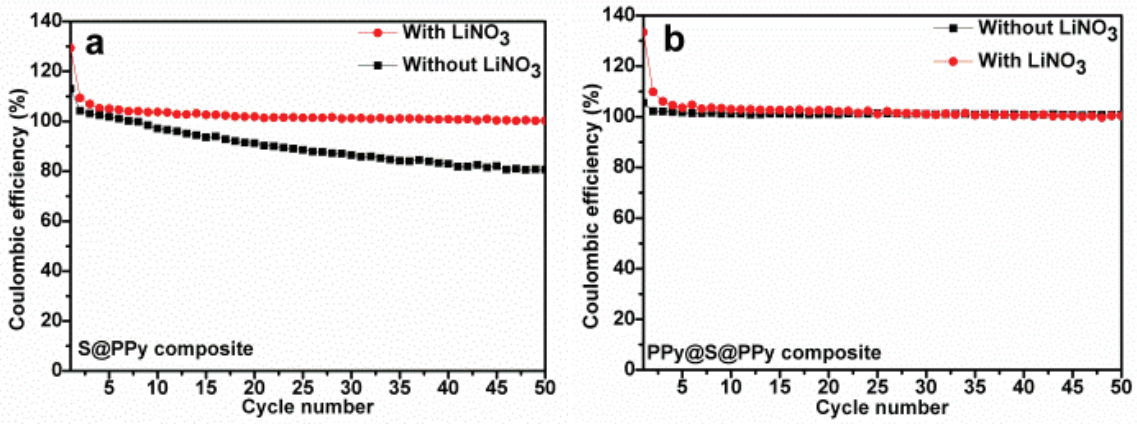

Figure 5.19 Coulombic efficiency of (a) S@PPy composite electrode, (b) PPy@S@PPy composite electrode with and without $LiNO_3$ additive in the electrolyte.

When the cells were disassembled after 100 cycles, it was clear that the PPy@S@PPy composite offered better morphological control than the S@PPy composite during cycling, as shown in Figure 5.20. Figure 5.20(a) clearly shows the agglomeration of the S@PPy composite after the cycling. During the discharge and charge processes, without the protection of the external PPy layer, the dissolved polysulfides will diffuse in the electrolyte and leave the original position of the sulfur in the S@PPy composite, so that the sulfur will agglomerate. In contrast, no agglomeration of the PPy@S@PPy composite after cycling is observed in Figure 5.20(b). In this case, the dissolved polysulfides are contained by the external PPy coating layer and will not diffuse. Due to the elastic properties of PPy, the volume expansion will be reduced as well. The better mechanical performance of the external PPy layer on the PPy@S@PPy composite and the role of the PPy external layer in confining the dissolved polysulfides are further confirmed.

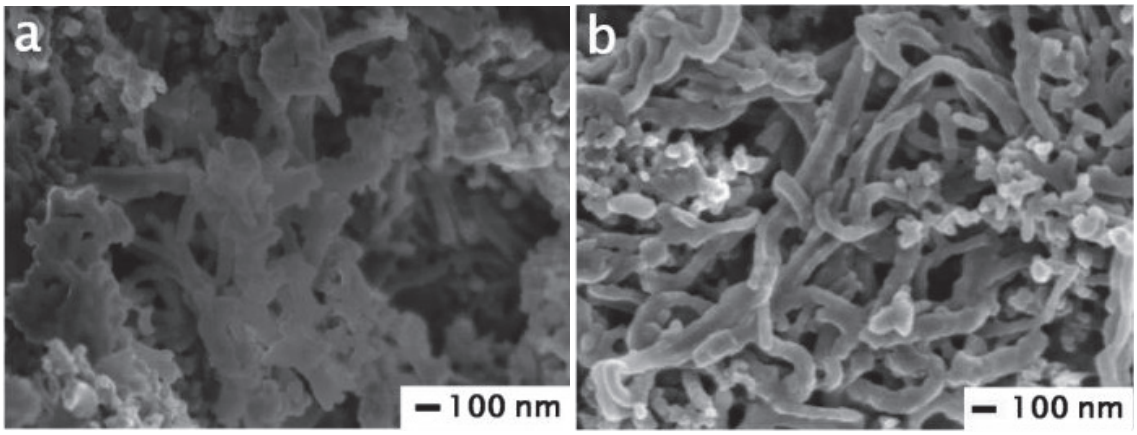

Figure 5.20 FESEM images of (a) S@PPy composite cathode after 100 cycles; (b) PPy@S@PPy composite cathode after 100 cycles.

5.4 Conclusions

A PPy@S@PPy composite with a novel three-layer-3D-structure, which consists of an external PPy coating layer, an intermediate sulfur filling layer, and an internal PPy conducting matrix layer, was synthesised by the oxidative chemical polymerization method and chemical precipitation method. The PPy@S@PPy composite has the same components with S@PPy composite except three-layer-3D-structure, which exhibits improved electrochemical performance. The discharge specific capacity of the PPy@S@PPy composite cathode is 554 mAh g^{-1} after 50 cycles, representing approximately 68.8% retention of the initial discharge specific capacity of about 801 mAh g^{-1}, while the S@PPy composite cathode demonstrates the discharge specific capacity of 370 mAh g^{-1} after 50 cycles, approximately 32.3% retention of the initial discharge specific capacity of about 1145 mAh g^{-1}. It is also found that the PPy@S@PPy composite cathode in the electrolyte with a mixed solvent of 1,3-dioxolane (DOL)/1,2-dimethoxyethane (DME) (1:1 by volume) presents much higher capacity than in the electrolyte with PEGDME solvent when the current density is higher than 200 mA g^{-1}. Moreover, the comparison experiments of $LiNO_3$ additive in the electrolyte on coulombic efficiency confirm the containment function of the external PPy layer in the

PPy@S@PPy composite and further identify the three layer structures of PPy@S@PPy composite.

Chapter 6. Ternary Porous Sulfur/Dual-Carbon Architectures for Lithium/Sulfur Batteries Obtained via an Industry-Oriented Spray-Pyrolysis/Sublimation Method

6.1. Introduction

Lithium/sulfur batteries show great potential for large-scale application in the various green energy fields[228, 239, 240], as sulfur has the highest theoretical specific capacity of 1675 mAh g^{-1} among all the solid cathode materials[26, 241-243] and a very high specific energy density[31, 32, 34, 244-246], as well as being low-cost, and non-toxic[38, 247]. Nevertheless, sulfur is an electrically insulating material, which leads to poor electrochemical accessibility and low utilization in the electrode[248-251]. The polysulfide anions that are generated during cycling are highly soluble in the organic electrolyte solvent. The diffusion of polysulfides to the lithium anode results in low active material utilization, low coulombic efficiency, and short cycle life of the sulfur electrode[9, 252-255]. In terms of making the lithium/sulfur batteries suitable for operation, carbon is the most popular conducting material to improve the performance[132, 176, 256-261].

The melt-diffusion strategy and wet chemical precipitation are currently the two major methods used to prepare carbon-sulfur composites[32, 35, 60, 87, 160, 231, 232]. Although these methods can improve the electrochemical performance of lithium/sulfur batteries, their commercialization is still unrealizable. There are two main reasons. Firstly, these methods are extremely difficult to scale up. The melt-diffusion strategy has the ability to load sulfur on carbon uniformly, but it encounters difficulty in scaling up for industrialization, as the coating would become non-uniform. Moreover, in the melt-diffusion process, a two-step heating process is required, which is time and energy consuming. In a typical melt-diffusion process, it takes at least 8 h to prepare carbon-sulfur composites not even including the time for the heating process and the

cooling process[9, 58, 60, 262]. The wet chemical precipitation method has the advantage of controlling the ratio of sulfur to carbon, but applying a uniform sulfur coating on carbon is very difficult, and washing cannot be avoided after synthesis, which again leads to the issue of scaling up. Secondly, these methods cannot produce carbon-sulfur composites continuously. They can only produce one small batch of carbon-sulfur composite at a time, which will definitely restrict the commercialization of lithium/sulfur batteries.

The spray-pyrolysis method, in which our group have established expertise[217-219], is a well-known proven industry-oriented technique, which can produce high performance cathode or anode active materials for lithium ion batteries or supercapacitors with highly developed porous structures rapidly and continuously, but without the need for any further treatments such as washing or grinding. This method has been widely and successfully used for synthesizing carbon-coated composite electrode materials for lithium ion batteries, which have shown significant improvement in their electrochemical performance[218, 220, 221]. The conventional spray-pyrolysis technique has not been explored for producing carbon-sulfur composite materials for lithium/sulfur batteries because sulfur has a low melting point (115 ºC), and it is easily oxidized to SO_2 and sublimated during the spray-pyrolysis process. Therefore, applying the spray pyrolysis method to synthesize carbon-sulfur composite seems to be a challenging task. In this study, I used the temperature range of 120-210ºC, which is higher than the melting point of sulfur, but lower than the typical operation temperature of a spray-pyrolysis method. Ultra-fast partial melting and limited sublimation of sulfur occurs at the particle surface without oxidation of S, a process which I have developed for the first time and denoted as the "spray-pyrolysis/sublimation technique".

Regarding the various types of sulfur/carbon composites, so far, many kinds have been reported, such as carbon wrapped sulfur composite[54], sulfur/multi-walled carbon nanotube (MWCNT) microspheres[69], hollow carbon nano fiber/sulfur composite[13], reduced graphene oxide (RGO)-sulfur composites[16], etc. In all these composites, the sulfur is either loaded on the surface of the carbon or is wrapped by the carbon. In the present work, ternary composites with a sulfur/dual-carbon architecture (scaffolding carbon/amorphous carbon) are designed. The scaffolding carbon works as a conducting matrix and provides an open pore structure, which can increase the contact area with the Super-P and electrolyte, decrease the transport pathways for both electrons and lithium ions, and confine the soluble lithium polysulfides, as well as providing sufficient space to accommodate sulfur volumetric expansion during charge and discharge processes. On the other hand, the amorphous carbon layer covers the surfaces of the porous sulfur particles, so that it acts as an adhesive interface to bind together the porous sulfur with the scaffolding carbon particles, further improving the conductivity. To the best of the authors' knowledge, no one has reported a similar structure before.

To obtain the above mentioned sulfur-based ternary structures, in this work, a single-step, double-suspension-based spray-pyrolysis/sublimation approach for assembly of different porous sulfur/dual-carbon architectures was reported. Only commercial low-cost materials were used, large volumes of composite materials can be produced continuously, and no harmful products were released during the synthesis. Herein, a series of experiments were carried out to find the best experimental parameters, such as temperature, solvent, and scaffolding carbon type. The as-prepared porous sulfur/dual-carbon composites were applied as the cathode in lithium/sulfur batteries, which have shown improved conductivity, capacity, reversibility, and rate

capability compared with the commercial sulfur. The reported ternary composites and method of fabrication demonstrate their great commercial potential for application in lithium/sulfur batteries with high energy density and long life

6.2. Experimental section

6.2.1. Materials

Sulfur, nano-graphite carbon, and ethanol were all purchased from Sigma Aldrich (Australia). Carbon black was bought from TIMCAL Ltd. Multi-walled carbon nanotubes (CNTs) were purchased from Shen Zhen Nanotech Port. All the chemicals were used as received without any further purification.

6.2.2. Selection of dispersion agent for sulfur

The solvent to disperse the commercial sulfur was investigated by adjusting the ratio between ethanol and distilled water. In this study, 15 mg sulfur was dispersed in three kinds of solvents: (1) 15 mL distilled water, (2) 15 mL ethanol, and (3) 5 mL ethanol mixed with10 mL distilled water. Firstly, sulfur was dispersed in each of these three solvents in an ultrasonic bath for 5 min. Then, these solutions were kept static for 5 min. Figure 6.1(a) shows many sulfur particles on the surface of the water when 15 mg sulfur was dispersed in 15 ml distilled water. Figure 6.1(b) shows that most of the sulfur has settled down at the bottom of the bottle for 15 mg sulfur in 15 ml ethanol. Figure 6.1(c) shows that the sulfur was dispersed very well in the mixture of 5 ml ethanol and 10 ml distilled water, so that it can be seen that almost all the sulfur particles were distributed throughout the whole body of the solvent. Therefore, ethanol/H_2O (1:2) was chosen as the dispersion agent for sulfur in the spray-pyrolysis/sublimation experiments. Figure 6.1(d) is a photograph of sulfur dispersed in ethanol/H_2O (1:2) for spray-pyrolysis/sublimation experiments, which further confirmed that ethanol/H_2O (1:2) is the right choice for dispersing sulfur. Therefore, the ethanol/H_2O(1:2)

solution is the best dispersion agent for sulfur, and thus the mixed solvent of ethanol/H_2O (1:2)was chosen for the spray-pyrolysis/sublimation experiments.

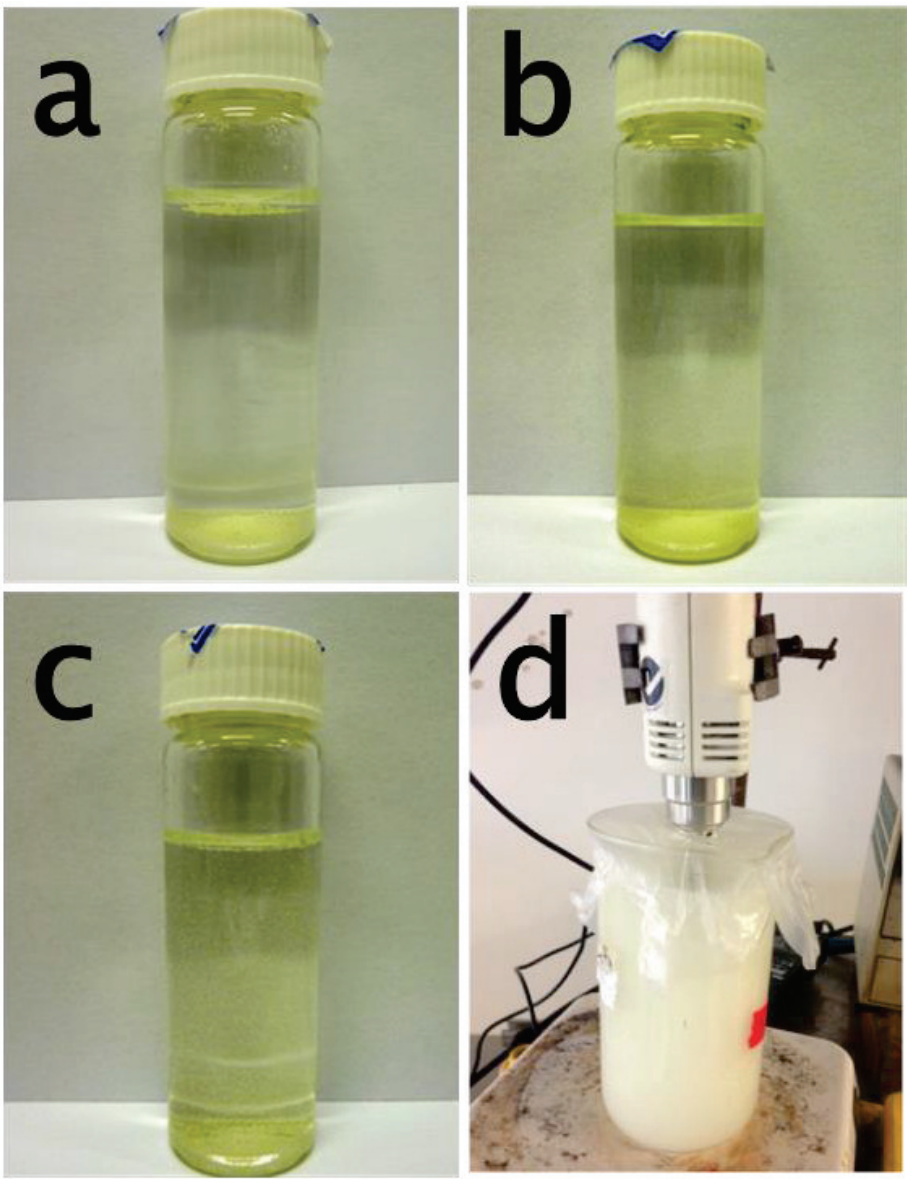

Figure 6.1 Photographs of sulfur suspension in (a) H_2O; (b) ethanol; (c) ethanol/H_2O = 1:2; (d) sulfur is suspended in ethanol/water = 1:2 during spray experiments.

6.2.3. Synthesis of samples

A schematic diagram of the spray-pyrolysis/sublimation apparatus is shown in Figure 6.2. This device includes three main parts: the solution transfer unit, the reaction unit, and the sample collection unit. During the experiments, the solution, which was kept under stirring,

was first transferred to the furnace via a nozzle by a peristaltic pump and the carrier gas. The furnace is the reaction unit, with a 2 m SiO_2 tube inside. Finally, the as-prepared samples were collected in a jar by the extractor pump.

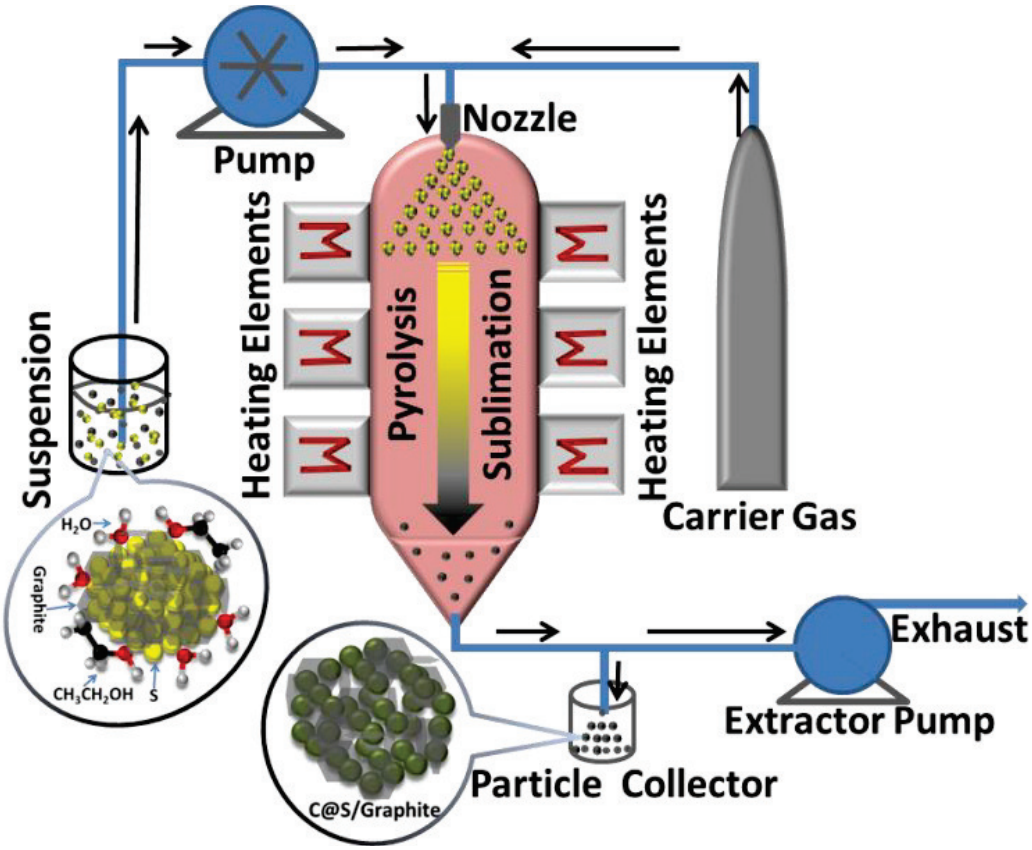

Figure 6.2 Schematic diagram of spray-pyrolysis/sublimation device.

In this experiment, a series of temperatures were set to study the influence of the operation temperature on the synthesis. 120 ºC, 140 ºC, 160 ºC, 180 ºC, and 210 ºC were applied. 120 ºC and 140 ºC were too low to obtain a dry sample. 160 ºC was not high enough for the decomposition of ethanol. At 210 ºC, most of the sulfur was sublimated and some sulfur was oxidized to SO_2, so that little sample could be collected. 180 ºC was found to be the essential temperature in this study.

6.2.3.1. Preparation of the sprayed commercial sulfur

1.2 g S was dispersed in a solvent of 200 mL ethanol and 400 mL distilled water. The mixture was ultrasonicated for 1.5 h, and subsequently stirred overnight.

After that, the mixture was sprayed at 180 ºC in air. Finally, dark green powders were collected.

6.2.3.2. Preparation of the sprayed commercial sulfur with extra carbon

Graphite, carbon black, and mixtures of carbon black and multi-walled CNTs were used as the extra carbon in the experiments. S and the extra C were dispersed in the solvent of 200 mL ethanol and 400 mL distilled water. The subsequent process is the same as for the synthesis of the sprayed commercial S. Finally, black powders were collected. The experimental details can be found in Table 6.1. As the mixture of ethanol and distilled water (volume ratio: 1:2) was shown to have the best dispersion capability for the sulfur, 200 mL ethanol and 400 mL distilled water were used for all the experiments, which also provides a fair comparison. Graphite, carbon black (CB), and multi-walled carbon nanotubes (CNTs) were used as the second carbon source. Moreover, two ratios of extra carbon were applied, which are 16% and 28%. It is concluded that carbon black and multi-walled CNTs are not suitable for the spray-pyrolysis/sublimation experiments, which as been explained in the Results and Discussion Section. Thus, the following discussion will focus on two porous sulfur/dual-carbon composites: sprayed commercial sulfur with 16% graphite and sprayed commercial sulfur with 28% graphite.

Table 6.1 Amounts of carbon, sulfur, ethanol, and distilled water in spray-pyrolysis/sublimation experiments.

Sample Name	Carbon weight (g)			Sulfur weight (g)	Ethanol (mL)	Distilled water (mL)
	Graphite	Carbon Black	Multi-walled CNT			
Sprayed commercial S				1.2	200	400

Sprayed commercial S with16% Graphite	0.2286			1.2	200	400
Sprayed commercial S with 28% Graphite	0.47			1.2	200	400
Sprayed commercial S with 16% Carbon Black		0.2286		1.2	200	400
Sprayed commercial S with 28% Carbon Black		0.47		1.2	200	400
Sprayed commercial S with 12% Carbon Black + 4% Multi-walled CNT		0.17145	0.05715	1.2	200	400
Sprayed commercial S with 8% Carbon Black + 8% Multi-walled CNT		0.1143	0.1143	1.2	200	400

6.2.2. Material characterization

The structures of the samples were characterized by X-ray diffraction (XRD) using a GBC MMA X-ray generator and diffractometer with Cu Kα radiation (λ = 1.5418 Å), employing a scanning rate of 5° min^{-1} in the 2θ range from 10° to 70°. Raman spectroscopy was conducted on a JOBIN YVON HR800 Confocal Raman system with 632.8 nm diode laser excitation on a 300 lines/mm grating at room temperature. Thermogravimetric analysis (TGA) was performed via a SETARAM Thermogravimetric Analyzer (France) in air to determine the changes in sample weight with increasing temperature and to estimate the amount of sulfur in the sample. The morphology of the samples and the mapping results were obtained with a field-

emission scanning electron microscope (FESEM; JEOL 7500, 5 kV) and a transmission electron microscope (TEM; JEM-ARM 200F).

6.2.3. Electrochemical measurements

When preparing electrodes for lithium/sulfur batteries, polyvinylidenedifluoride (PVDF) was used as the binder, Super-P as conducting agent, and N-methyl-2-pyrrolidinone (NMP) as solvent. The PVDF was added up to 10 wt%. In order to fairly compare the electrochemical performances of all the samples studied, the amount of Super-P depended on the amount of sulfur, which was maintained at 50% of the total mass of the electrode. The resultant slurries were spread onto aluminum foil substrates. The coated electrodes were dried in a vacuum oven at 50 ºC for 24 h and then pressed. Subsequently, the electrodes were cut into disks 9.5 mm in diameter. A conventional organic solvent electrolyte was used, consisting of 1 mol L^{-1} lithium bis(trifluoromethane sulfonyl) imide (LiTFSI) in 1,3-dioxolane (DOL) / 1,2-dimethoxyethane (DME) (1:1 by volume) with 0.1 mol L^{-1} $LiNO_3$ as an additive. CR 2032 type coin cells were assembled in an Ar-filled glove box. Charge-discharge testing was carried out with a LAND battery test system at a current density of 168 mA g^{-1} (0.1 C) within the voltage range of 1.5–3.0 V. Cyclic voltammetry (CV) and AC impedance measurements were performed using a Biologic VMP-3 Multichannel electrochemistry workstation at a scanning rate of 0.1 mV s^{-1} and over a frequency range of 100 kHz - 0.01 Hz, respectively.

6.3. Results and discussions

Figure 6.3 (a) and (b) shows the yellow commercial sulfur and dark green sprayed commercial sulfur, respectively. The color difference suggests that some carbon was formed. This can be further confirmed by the energy dispersive X-ray

spectroscopy (EDS) mapping analysis of the sprayed commercial sulfur in Figure 6.3 (c).The yellow spots in Figure 6.3 (c) correspond to the presence of the element sulfur, and the red spots correspond to the element carbon. These results show that a thin layer of carbon is distributed uniformly throughout the whole area of the sprayed commercial sulfur composite. As only ethanol contains the element carbon among all the reactants, the carbon that is formed can only come from the decomposition of ethanol, which can be ascribed to the attributes of the spray pyrolysis system and the presence of sulfur. The reaction unit of the spray pyrolysis device is a SiO_2 tube 2 m in length and there is a extraction pump at the end of the system. Thus, although the carrier gas is air, there is actually an anaerobic environment inside of the tube to some extent. Meanwhile, sulfur is a kind of material with reducibility, which can protect the ethanol from complete oxidation.

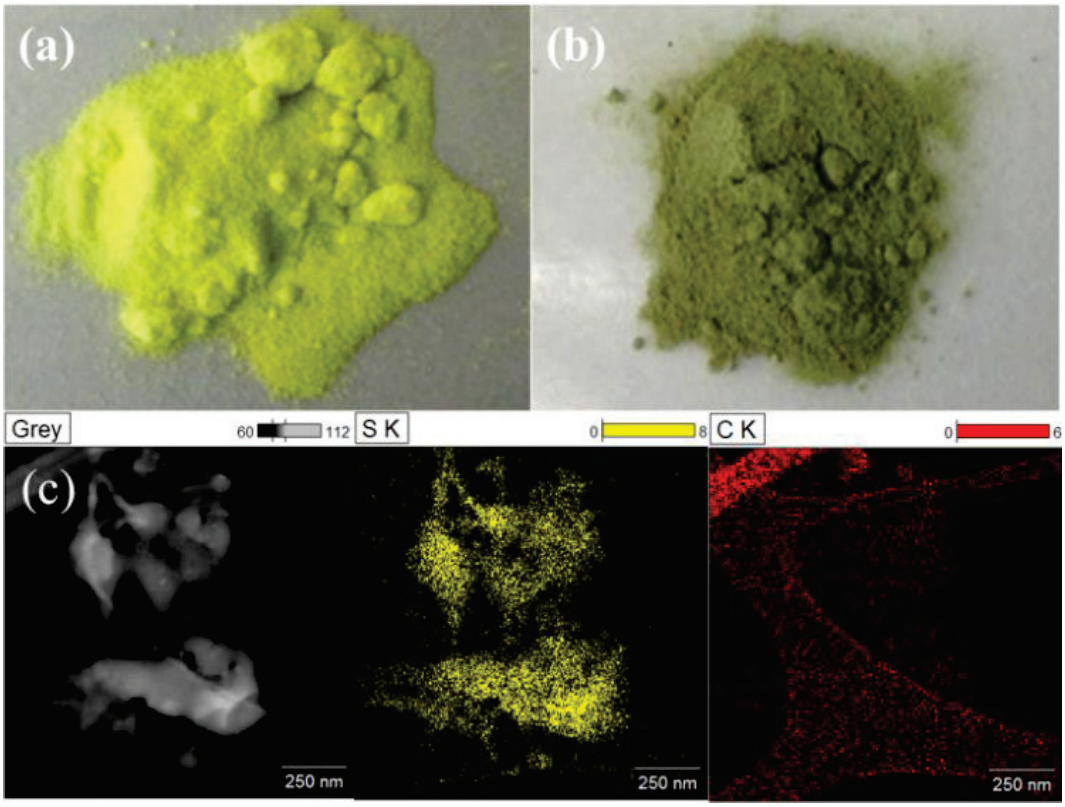

Figure 6.3 (a) Photograph of commercial S; (b) photograph of sprayed commercial S; (c) EDS mapping results for sprayed commercial S.

Figure 6.4 (a) shows the two main processes involved in the spray-pyrolysis/sublimation method for spraying commercial sulfur: (1) the evaporation/sublimation process; (2) the pyrolysis process. In the first step, some ethanol and water molecules that were adsorbed on the commercial sulfur particles are evaporated due to the heat treatment. At the same time, some sulfur molecules, especially the sulfur on the particle surfaces, will sublimate and leave pores on the surface of the sprayed commercial sulfur. In the second step, because of the presence of water, the ethanol is not as easy to evaporate as pure ethanol, so some ethanol molecules can be decomposed to form a tiny amount of amorphous carbon. A schematic diagram of the mechanism of the spray-pyrolysis/sublimation process for spraying commercial sulfur with graphite is shown in Figure 6.4 (b). It is similar to Figure 6.4 (a) for spraying commercial sulfur, but due to the presence of the graphite, the newly formed amorphous carbon can act as an adhesive interface to bind the porous sulfur and graphite together to form a conducting matrix, serve as a good electron conductor, provide interconnected open pores to reduce the diffusion paths of lithium ions, buffer the volumetric expansion of sulfur, and absorb electrolyte and polysulfides.

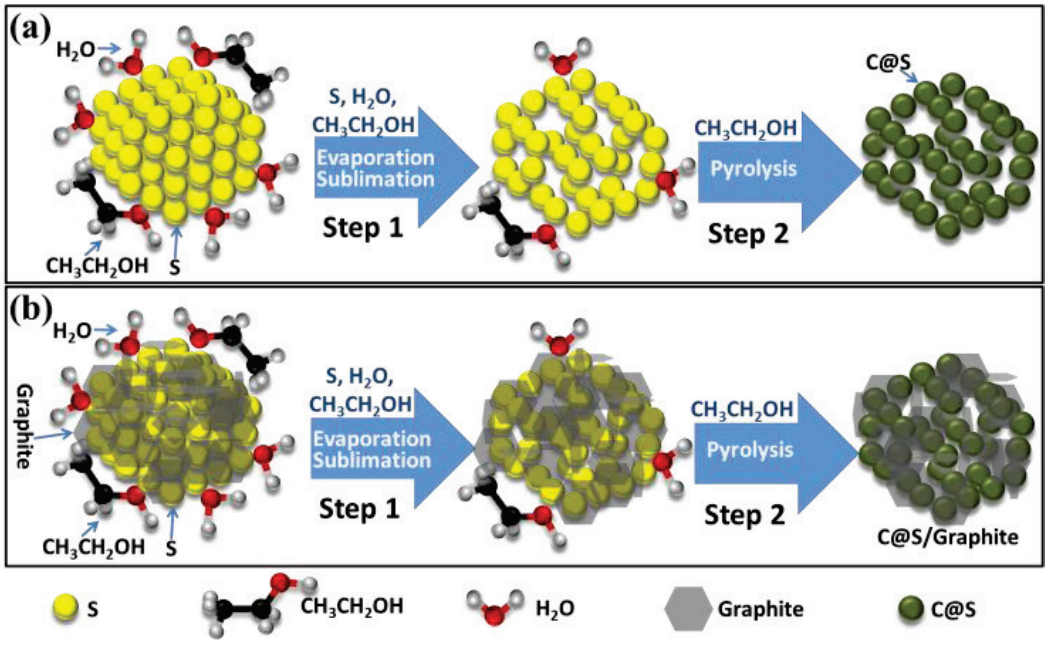

Figure 6.4 Schematic diagram of the formation of the porous structure and the

amorphous carbon during the spray-pyrolysis/sublimation process: (a) preparation of the sprayed commercial sulfur; (b) preparation of the sprayed commercial sulfur with graphite.

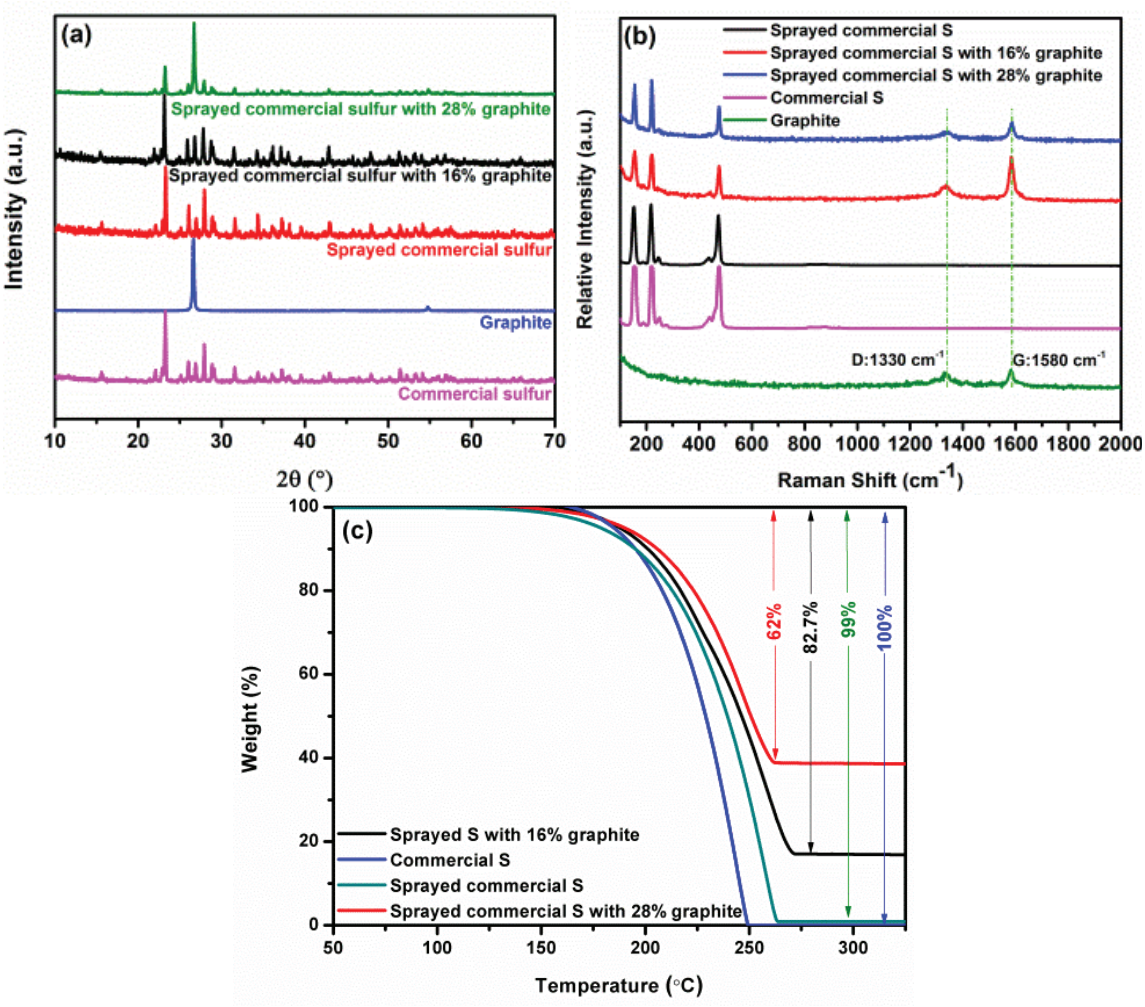

Figure 6.5 (a) X-ray diffraction patterns and (b) Raman spectra of commercial sulfur, sprayed commercial sulfur, graphite, sprayed commercial sulfur with16% graphite, and sprayed commercial sulfur with 28% graphite; (c) TGA curves of sprayed commercial sulfur; sprayed commercial sulfur with16% graphite; and sprayed commercial sulfur with 28% graphite.

Figure 6.5 (a) presents the X-ray diffraction (XRD) patterns of the samples. The diffraction peaks of the sprayed commercial sulfur, sprayed commercial sulfur with

16% graphite, and sprayed commercial sulfur with 28% graphite match very well with those of the commercial sulfur and the standard diffraction lines of sulfur (PDF card No. 00-001-0478), which can be indexed to the orthorhombic phase with space group *Fddd*. This indicates that no phase transformation of sulfur occurs during the spray-pyrolysis/sublimation process. The diffraction peaks of the sprayed commercial sulfur with 16% graphite and the sprayed commercial sulfur with 28% graphite also match the diffraction peaks of commercial graphite. The Raman spectra are shown in Figure 6.5 (b), which were obtained with 632.8 nm diode laser excitation at room temperature. The Raman spectrum of S displays three main peaks below 500 cm^{-1},[263-265] while the peaks in the Raman spectrum of carbon are located at 1330 and 1580 cm^{-1}, which are identified as the characteristic peaks of the D band and G band of carbon, respectively. From Figure 6.5 (b), it is clear that both the sprayed commercial sulfur with 16% graphite and the sprayed commercial sulfur with 28% graphite present the characteristic peaks of the D band and G band of graphite at 1330 and 1580 cm^{-1}, and the three characteristic peaks of sulfur below 500 cm^{-1} as well, while the sprayed commercial sulfur only shows the three characteristic peaks of sulfur below 500 cm^{-1}, but no obvious characteristic peaks of carbon, which can be ascribed to the limited amount of carbon in the sprayed commercial sulfur.

To quantify the amount of the sulfur in the as-prepared samples, thermogravimetric analysis (TGA) was carried out in argon, with heating from 50 ºC to 350 ºC at the rate of 5 ºC min^{-1}. As shown in Figure 6.5 (c), the commercial sulfur shows a weight loss starting at around 160 ºC, and the sulfur is gone completely at around 249 ºC, so the weight loss of all the as-prepared composites is ascribed to the sublimation of sulfur. Figure 6.5 (c) demonstrates that when pure commercial sulfur is sprayed, only 1% amorphous carbon is obtained. Moreover, graphite is important for forming amorphous carbon, as

graphite has a three-dimensional (3D) structure which can absorb much more ethanol during the sublimation of sulfur for pyrolysis. When commercial sulfur was sprayed with 16% graphite, the amorphous carbon content formed from the decomposed ethanol was 1.3%. When the graphite content was increased to 28%, the obtained amorphous carbon was up to 10%. Moreover, the thermal stability of sulfur in composites typically increases with higher carbon content due to the high affinity between carbon and sulfur. The the thermogravimetric analysis (TGA) was also carried out on the sprayed commercial sulfur with carbon black and multi-walled carbon tubes compoaites, which is demonstrated in Figure 6.6. **Figure 6.6** demonstrates that the sprayed composite of commercial sulfur with 16% CB contains 83.1% sulfur and 16.9% carbon. Similarly, the sprayed composite of commercial sulfur with 12% CB + 4% CNT contains 87.2% sulfur and 12.8% carbon, while the sprayed composite of commercial sulfur with 8% CB + 8% CNT contains 90.9% sulfur and 9.1% carbon, and the sprayed composite of commercial sulfur with 28% CB contains 79.5% sulfur and 20.5% carbon.

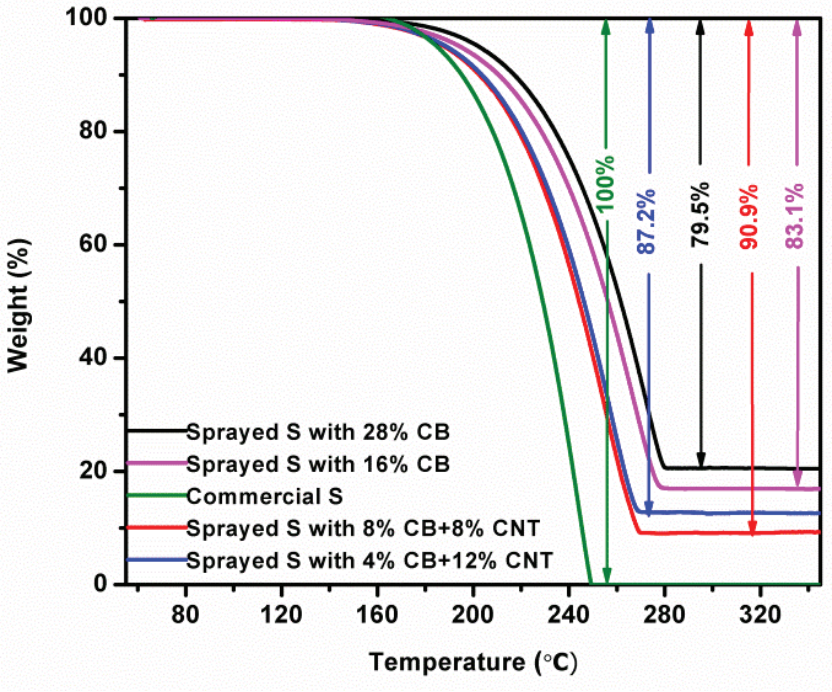

Figure 6.6 TGA curves of: sprayed commercial sulfur with 16% CB; sprayed commercial

sulfur with 12% CB + 4% CNT; sprayed commercial sulfur with 8% CB + 8% CNT; sprayed commercial sulfur with 28% CB.

All the TGA results of Figure 6.5 (c) and Figure 6.6 were summarized in Table 6.2, and it is apparent that carbon black and multi-walled CNTs are not suitable for spray-pyrolysis/sublimation experiments, especially the multi-walled CNTs. Carbon black is too light to collect and will be sucked in by the vacuum pump, while the multi-walled CNTs are too long to go through the nozzle and will be left in the beaker. Therefore, the carbon percentage in the composite with carbon black and multi-walled CNT is much lower than that of the composite with graphite added to give the same amount of carbon. In the sprayed composite of commercial sulfur with 28% graphite, the carbon percentage is 38%, while in the sprayed commercial sulfur with 28% carbon black, the carbon percentage is only 20.5%. Therefore, carbon black is worse than graphite in this study. Comparing the sprayed commercial sulfur with 16% graphite with the sprayed commercial sulfur with 16% carbon black, sprayed commercial sulfur with 12% carbon black + 4% multi-walled CNT, and the sprayed commercial sulfur with 8% carbon black + 8% multi-walled CNT, the added amount of carbon is the same, but the real carbon percentages are different. According to the TGA data, the carbon percentage in the sprayed composite of commercial sulfur with 16% graphite is 17.3%, while it is 16.9% in the sprayed composite of commercial sulfur with 16% carbon black. When using 4% multi-walled CNT to replace carbon black, the carbon percentage is reduced to 12.8%, and when 8% carbon black was replaced, the carbon percentage was only 9.1%. Thus, the multi-walled CNT is even worse than carbon black. So, among these three kinds of carbon, graphite is the best one, and the multi-walled CNT is the worst one for the spray-pyrolysis/sublimation experiments.

Table 6.2 Comparison between the designed contents and the TGA results.

Sample Name	Designed Contents		TGA results	
	C%	S%	C%	S%
Commercial S			0	100
Sprayed commercial S			1	99
Sprayed commercial S with 16% Graphite	16	84	17.3	82.7
Sprayed commercial S with 28% Graphite	28	72	38	62
Sprayed commercial S with 16% Carbon Black	16	84	16.9	83.1
Sprayed commercial S with 28% Carbon Black	28	72	20.5	79.5
Sprayed commercial S with 12% Carbon Black + 4% Multi-walled CNT	16	84	12.8	87.2
Sprayed commercial S with 8% Carbon Black + 8% Multi-walled CNT	16	84	9.1	90.9

The morphology of the samples was investigated by field emission scanning electron microscopy (FESEM) and transmission electron microscopy (TEM). Figure 6.7(a) shows that the surface of the commercial sulfur is quite smooth and without pores, while in Figure 6.7(b), the particles have become porous due to the sulfur sublimation from the surface. The inset image in Figure 6.7(b) is an enlarged image of the selected area, which clearly demonstrates the porous structure of the sprayed commercial sulfur. The TEM image of the sprayed commercial sulfur in Figure 6.8 confirms the pore formation as well. It shows the porous structure of the sprayed commercial sulfur with the pore size ranging from 10 nm to 100 nm. A FESEM image of the sprayed commercial sulfur with 16% graphite is presented in Figure 6.7 (c). It

shows that the amorphous carbon@porous-sulfur particles are uniformly embedded in the graphite, but as the amount of graphite is only 16%, it cannot cover the amorphous carbon@porous-sulfur particles very well. On the other hand, the TEM image of the sprayed commercial sulfur with 28% graphite in Figure 6.7 (d) shows that nearly all the amorphous carbon@porous-sulfur particles are set in the graphite, which can improve the confinement of the dissolved polysulfides. The inset image in Figure 6.7(d) is the fast Fourier transform (FFT) pattern of the sprayed composite of commercial sulfur with 28% graphite, which shows the diffraction spots from the graphite and the diffraction rings from the amorphous carbon, confirming the formation of amorphous carbon. Moreover, the spots are superimposed on the rings, because the spacing in graphite and that in amorphous carbon are similar. More details are explained in Figure 6.9. Figure 6.9 (a) is the FFT pattern of the sprayed commercial sulfur with 28% graphite Amorphous carbon produces a series of diffuse rings in the FFT (and diffraction pattern), while crystalline graphite produces fringes in the image and spots in the FFT and diffraction pattern. Figure 6.9 (b) is the corresponding high resolution TEM (HRTEM) image, which shows that the fringe spacing is about 3.365 Å, which closely corresponds to the *d* value of the (0 0 6) planes of graphite. The FFT (and diffraction pattern) spots can be related to particular sets of fringes in the image, because an arrow drawn from the centre of the FFT to a spot, will be perpendicular to the fringes in the image which gave rise to it. This can confirm the formation of amorphous carbon during the spray-pyrolysis/sublimation process. Figure 6.10 presents the elemental maps of sulfur and carbon in the sprayed commercial sulfur with 28% graphite. Comparing Figure 6.10 (d) with Figure 6.10 (c), it is clearly that carbon distributes very uniform through all the area. The two circles in Figure 6.10 (d) are the location of sulfur in Figure 6.10 (c). The carbon distribute uniformly in this circled area, and from Figure 6.10 (b), there is no graphite covered. Thus it

can be further confirmed that amorphous carbon was obtained during the spray-pyrolysis/sublimation progress. In the high resolution TEM image in Figure 6.11, amorphous carbon was also detected in the sprayed composite of commercial sulfur with 28% graphite. The amorphous carbon in the composite of sprayed commercial sulfur with 28% graphite can be detected as an amorphous carbon layer coating the surface of the graphite. The amorphous carbon layer on the sulfur cannot be seen because all of the sulfur will sublimate at such high magnification. Under the electron beam, sulfur particles shrink due to sublimation, despite the use of low accelerating voltage and low electron flux (at low magnification). Figure 6.11 shows that the amorphous carbon layer on graphite is very thin, being typically only several nanometres thick. In order to see equivalent layers of amorphous carbon on sulfur, very high magnification would be necessary. This would result in greatly increased electron flux and exacerbate sulfur sublimation to the point where the particles would not be sufficiently stable to image. Thus, amorphous carbon layers on sulfur were not observed.

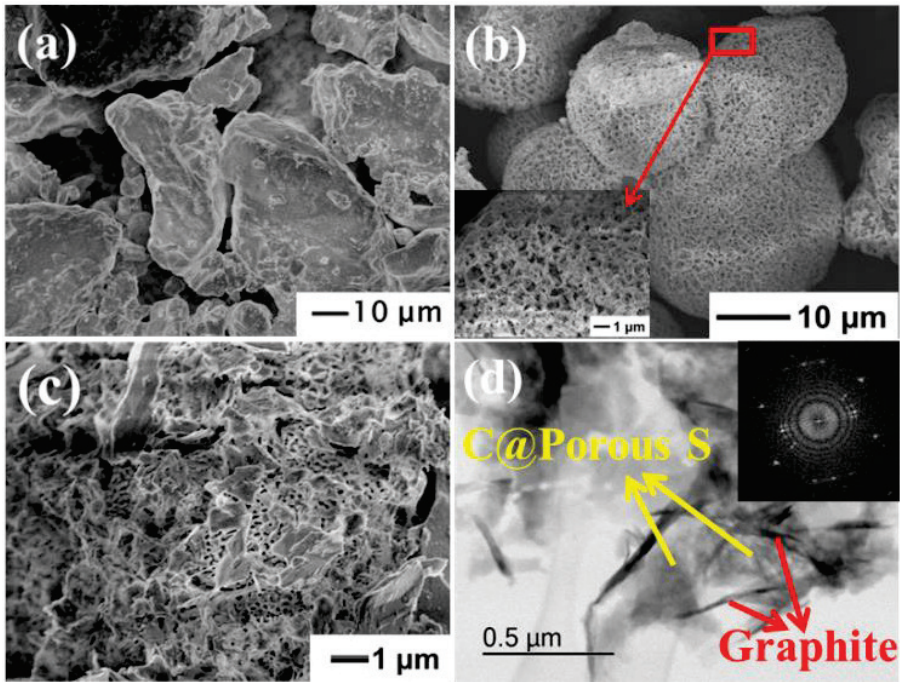

Figure 6.7 FESEM images of (a) commercial sulfur; (b) sprayed commercial sulfur

(inset: enlarged FESEM image of the selected area); (c) sprayed commercial sulfur with 16% graphite; (d) TEM image of the sprayed commercial sulfur with 28% graphite (inset: corresponding FFT pattern).

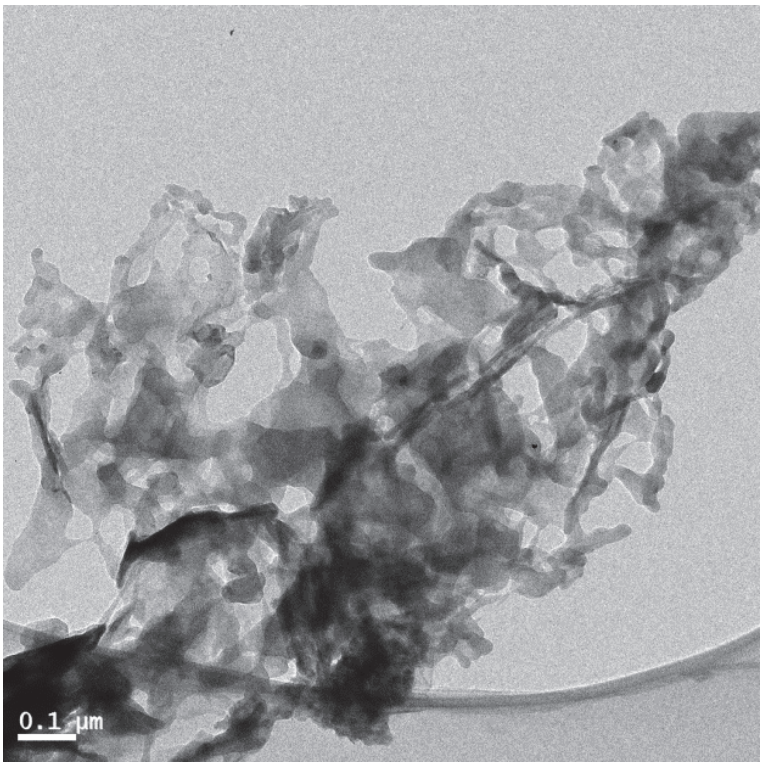

Figure 6.8 TEM image of the sprayed commercial sulfur.

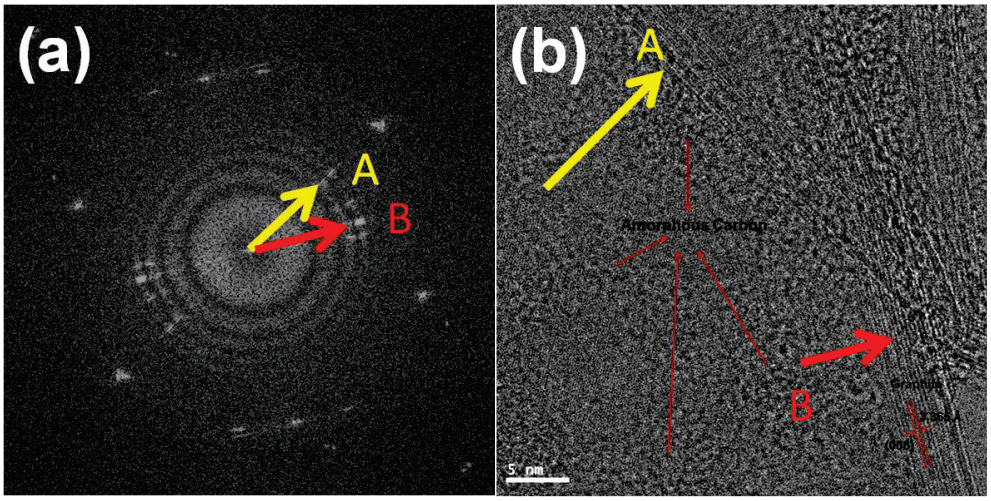

Figure 6.9 (a) The FFT pattern of the sprayed commercial sulfur with 28% graphite; (b) The related HR-TEM image of the FFT pattern in Figure 6.9(a).

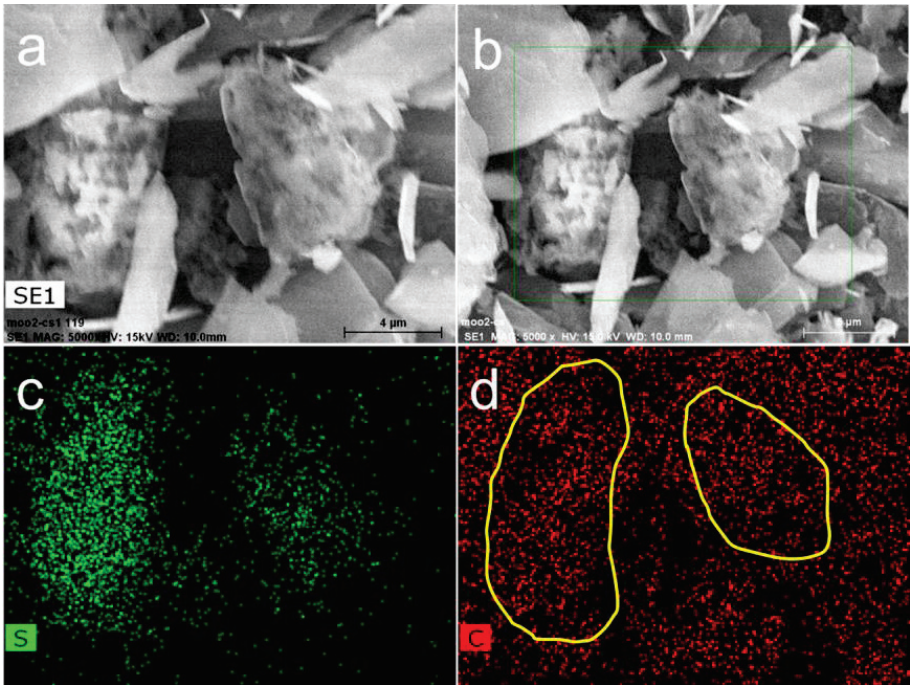

Figure 6.10 Mapping results of sprayed commercial sulfur with 28% graphite: (a) the FESEM image; (b) the selected area for mapping; (c) elemental map of sulfur; (d) elemental map of carbon.

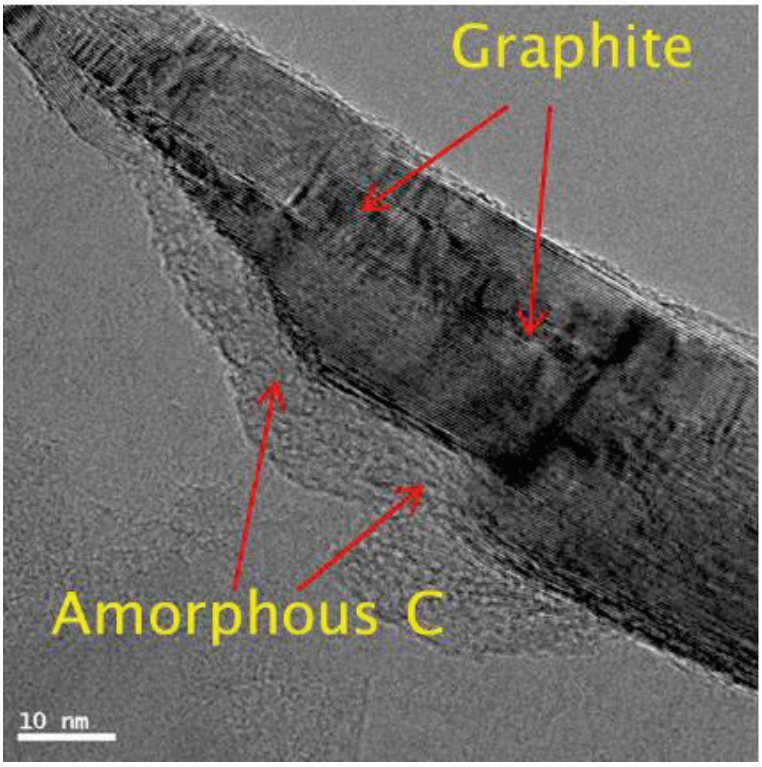

Figure 6.11 HR-TEM image of the sprayed commercial sulfur with 28% graphite.

To investigate the electrochemical characteristics of cathodes containing the sprayed commercial sulfur with 16% graphite and sprayed commercial sulfur with 28% graphite, cyclic voltammetry (CV) of the first cycle was conducted at a scan rate of 0.1 mV s^{-1} in the potential range of 1.5-3.0 V. In Figure 6.12 (a) and (b), two reduction peaks are observed, which could be assigned to the multiple-step reaction mechanism of sulfur with lithium. Specifically, the peak at 2.4 V is ascribed to the open ring reduction of cyclic S_8 to long-chain lithium polysulfides (Li_2S_x, $4 \leq x < 8$), while the peak at 2.1 V corresponds to the further reduction of these high-order polysulfides to Li_2S_2 and Li_2S.

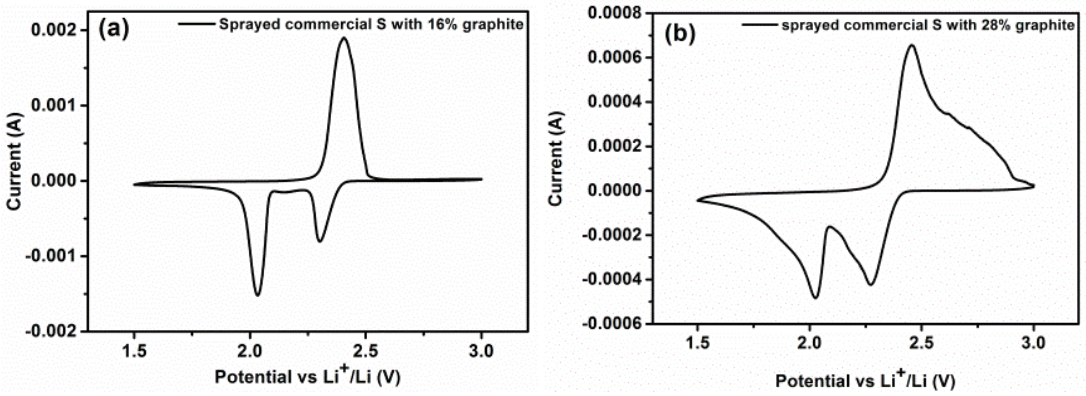

Figure 6.12. Cyclic voltammograms of:(a) electrode containing sprayed commercial sulfur with 16% graphite; (b) electrode containing sprayed commercial sulfur with 28% graphite.

Figure 6.13 (a) and (b) shows representative charge and discharge voltage profiles of the 1st, 100th, and 200th cycles for the cathode containing sprayed commercial sulfur with 16% graphite and the cathode containing sprayed commercial sulfur with 28% graphite at the current density of 0.1 C (1 C = 1680 mA g^{-1}) within a cut-off voltage window of 1.5-3 V. The discharge curves present two plateaus for both cells, which are at 2.3 and 2.05 V, respectively. They are assigned to the two-step reaction of sulfur with lithium during the discharge process. This agrees very well with

the CV results in Figure 6.12. Moreover, the electrode containing the composite of sprayed commercial sulfur with 28% graphite demonstrated much better capacity retention than that containing the composite of sprayed commercial sulfur with 16% graphite.

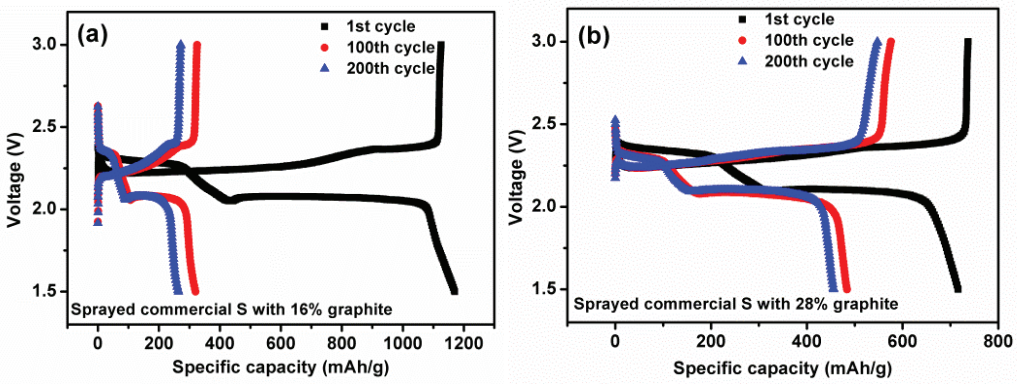

Figure 6.13 Voltage profiles of:(a) electrode containing sprayed commercial sulfur with 16% graphite; (b) electrode containing sprayed commercial sulfur with 28% graphite.

Figure 6.14 (a) presents the cycling performances of the cathodes at 0.1 C and the relevant coulombic efficiency of the two as-prepared sulfur-dual carbon composite electrodes. The discharge specific capacity and the reversibility of the electrode containing sprayed commercial S with 28% graphite are much higher than for the other three electrodes after 10 cycles. Many more details of the cycling performances of the samples are summarized in Table 6.3. The electrode containing sprayed commercial sulfur with 28% graphite shows the best cycling performance, yielding a discharge specific capacity of 480 mAh g^{-1} after 200 cycles, which is approximately 69.6% retention of the initial discharge specific capacity of about 690 mAh g^{-1}, while the electrode containing sprayed commercial sulfur with 16% graphite presents the discharge specific capacity of 290 mAh g^{-1} after 200 cycles, representing about 24.3% retention of the initial discharge specific capacity of about 1190 mAh g^{-1}, the electrode with only sprayed commercial sulfur presents

the discharge specific capacity of 200 mAh g^{-1} after 200 cycles, representing about 20.6% retention of the initial discharge specific capacity of about 970 mAh g^{-1}, and the commercial sulfur electrode presents the discharge specific capacity of 100 mAh g^{-1} after 100 cycles, representing about 9.3% retention of the initial discharge specific capacity of about 1080 mAh g^{-1}. Thus, the capacity decay of the electrode containing sprayed commercial sulfur with 28% graphite is as low as 0.152% per cycle during these cycles, but the capacity decay of the electrode containing sprayed commercial sulfur with 16% graphite is as high as 0.379% per cycle, the capacity decay of the sprayed commercial sulfur electrode is as high as 0.397% per cycle, and the capacity decay of the commercial sulfur electrode is as high as 0.907% per cycle.It should be noted that the electrode containing sprayed commercial sulfur with 28% graphite delivers much lower discharge specific capacity in the first five cycles compared to the other three electrodes, which could be ascribed to the incomplete utilization of the active materials. The sulfur in the sprayed commercial sulfur with 28% graphite is covered very well by the graphite layer, which means that the sulfur cannot be completely exposed to the electrolyte during the initial cycles, and the sulfur has to rearrange itself during the first few cycles, so that the inactive cores of the sulfur are exposed to the electrolyte and then become capable of being utilized in subsequent cycles[11]. The coulombic efficiency of the sprayed commercial sulfur with 16% graphite is as high as 97% and very stable for 200 cycles, while that of the sprayed commercial sulfur with 28% graphite cathode is not so high, which is 83% after 200 cycles. It might be ascribed to the larger amount of graphite in the sprayed commercial sulfur with 28% graphite composite. As shown in Figure 6.9 (b) and Figure 6.11, the graphite applied in this work is a kind of layered nano carbon with 5 nm to 25 nm thickness and high surface area. Thus if the percentage of graphite in composite is higher, it might lead to the formation of thicker SEI or more other side

reactions resulting in lower coulombic efficiency and worse rate capability. Figure 6.15 presents the cycling performances of the composites of sprayed commercial sulfur with 16% CB, sprayed commercial sulfur with 12% CB + 4% CNT, sprayed commercial sulfur with 8% CB + 8% CNT, and sprayed commercial sulfur with 28% CB. The cycling performance of the sulfur/dual-carbon composites is much better than these four composites with carbon black and multi-walled CNT. This is because the bridging graphite with its unique 3D layered structure can be bound with the amorphous carbon adhesive interface to form an effective conducting matrix and provide interconnected open pores to further reduce the diffusion paths of lithium ions, absorb electrolyte and polysulfides, and buffer the volumetric expansion of sulfur. The morphologies of the four composies of the sprayed commercial sulfur with carbon black and multi-walled CNT are presented in Figure 6.16. Figure 6.16 (a) and (b) are the images of sprayed commercial sulfur with 16% CB. The nano sized carbon black particles covered the sulfur particles, thus the surface of sulfur shows less porous structures than that of sprayed commercial sulfur, sprayed commercial sulfur with 16% graphite and sprayed commercial sulfur with 28% graphite. As the carbon black particles are nano size, the same amount carbon black was adding into the experiment system, but with the higher volume. Therefore these carbon black particles can prevent the porous structure of sulfur formed during the spray progress. That's why we can't see so much pores in Figure 6.16 (b). The FESEM images of sprayed commercial sulfur with 12% CB + 4% CNT are shown in Figure 6.16 (c) and (d). The multi walled CNT and the carbon black particles covered the sulfur particles very well. It is interesting that some sulfur has loaded on the surface of CNT because of the melting of the sulfur. Figure 6.16 (e) and (f) demonstrated the FESEM images of sprayed commercial sulfur with 8% CB + 8% CNT, which is similar as the that of the sprayed commercial sulfur with 12% CB + 4% CNT. But as the percentage of carbon black is higher,

the melt, evaporation or sublimation are all prevented, thus there is no significant loading sulfur on the CNT surface in Figure 6.16 (f). The FESEM images of the sprayed commercial sulfur with 28% CB are in the Figure 6.16 (g) and (h), which are also similar as that of the sprayed commercial sulfur with 16% carbon black.

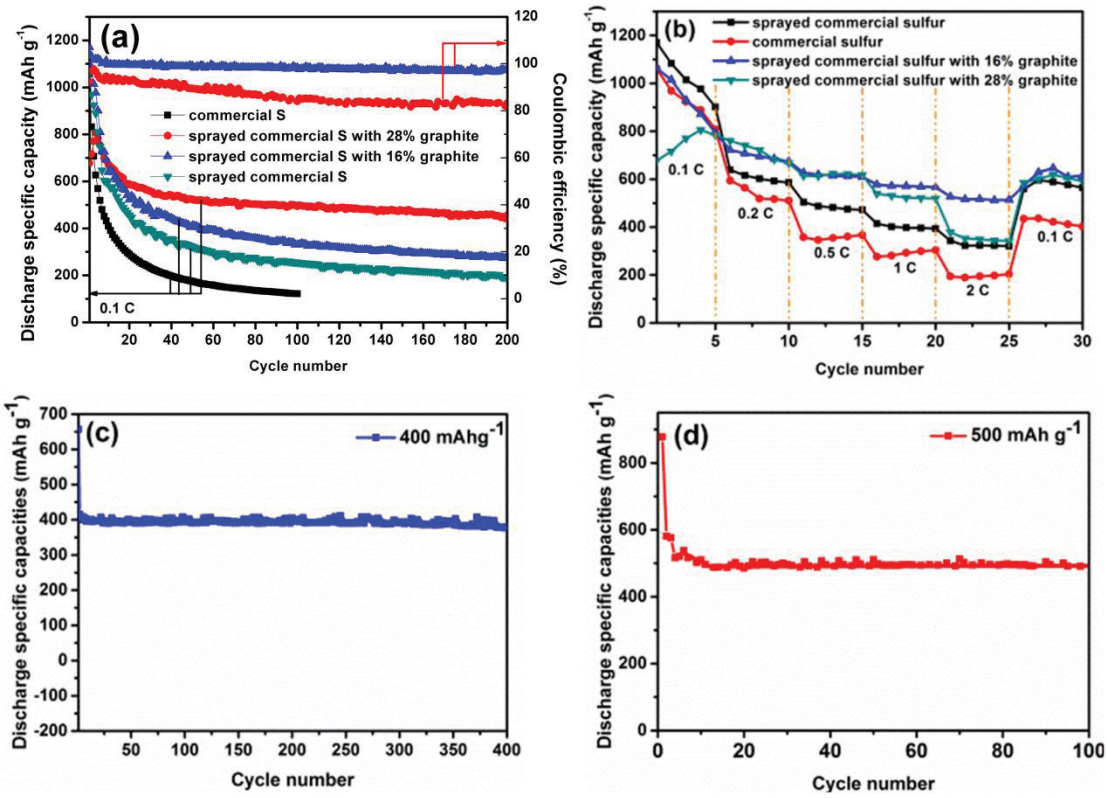

Figure 6.14 (a) Cycling performance of commercial sulfur and sprayed commercial sulfur; cycling performance and relevant coulombic efficiency of sprayed commercial sulfur with 16% graphite, sprayed commercial sulfur with 28% graphite; (b) rate capability of commercial sulfur, sprayed commercial sulfur, sprayed commercial sulfur with 16% graphite, sprayed commercial sulfur with 28% graphite. Discharge specific capacities of the sprayed commercial sulfur with 28% graphite using the new charging method: charged to (c) 400 $mAhg^{-1}$ and (d) 500 mAh g^{-1}.

In order to compare the rate capabilities, the cells were discharged to 1.5 V from 0.1 C to 2 C. In Figure 6.14 (b), the sprayed commercial S cathode delivered

higher capacity compared to the commercial sulfur electrode. This is ascribed to the carbon formed from the decomposition of ethanol, which can improve the conductivity of the electrode by increasing the conductivities of pure sulfur particles and composite particles[266]. This can be proved by the electrochemical impedance spectroscopy (EIS) results in Figure 6.17. It shows one compressed semicircle in the high to medium frequency range, which describes the charge transfer resistance (R_{ct}), since the diameter of the semicircle is related to R_{ct}. The values of R_{ct} for the electrodes containing commercial sulfur, sprayed commercial sulfur, sprayed commercial sulfur with 16% graphite, and sprayed commercial sulfur with 28% graphite were calculated to be 268 Ω, 132 Ω, 114 Ω, and 77 Ω, respectively. Obviously, the R_{ct} of the commercial sulfur electrode is much higher than those of the other three electrodes, while the R_{ct} of the electrode containing the sprayed commercial sulfur with 28% graphite shows the smallest value. Comparing the amounts of amorphous carbon in the samples with commercial sulfur, sprayed commercial sulfur, sprayed commercial sulfur with 16% graphite, and sprayed commercial sulfur with 28% graphite (0%, 1%, 1.3%, and 10% respectively), it is clear that the amorphous carbon from the decomposition of ethanol can significantly improve the conductivity and the electrochemical kinetics of the electrode in lithium/sulfur batteries, and that larger amounts of amorphous carbon are good for improving the conductivity of the electrodes. The amorphous carbon coating on the sulfur particles can improve the conductivity of pure sulfur particles and of composite particles as well. It was reported that dual-carbon-based architectures are useful for high performance energy storage materials [267]. Thus, if graphite is present, the interface coating of amorphous carbon can act as a very good soft adhesive to bind the highly porous sulfur particles with graphite to form a conductive matrix and serve as a good electron conductor to further

increase the conductivity of the composite. In addition, the cathode containing sprayed commercial sulfur with 16% graphite delivers the highest capacity at 2 C (520 mAh g^{-1}), which is even higher than that of the cathode containing sprayed commercial sulfur with 28% graphite. This is because when the current density is higher, it requires faster ion diffusion, but in the sprayed commercial sulfur with 28% graphite, graphite covers the amorphous carbon and porous sulfur composite particles very well, which can trap the dissolved polysulfides, but also can decrease the ion diffusion speed to some extent. It was reported that the cycle life of lithium/sulfur batteries can be improved by a special charging technique, in which the battery is charged to a fixed capacity to avoid the dissolution of long-chain polysulfides[23]. In this study, I have also applied this novel technique to charge the batteries. Figure 6.14 (c) and (d) shows that almost no capacity fading behavior could be observed for 400 cycles at 400 mAh g^{-1} and for 100 cycles at 500 mAh g^{-1}.

Table 6.3 Comparison of the cycling performances of the electrodes.

Electrode name	Initial discharge capacity (mAh g^{-1})	Reversible capacity (mAh g^{-1})	Capacity retention	Capacity decay rate (per cycle)
Commercial S	1080	100 (100^{th} cycle)	9.3%	0.907%
Sprayed commercial S	970	200 (200^{th} cycle)	20.6%	0.397%
Sprayed commercial S with 16% graphite	1190	290 (200^{th} cycle)	24.3%	0.379%
Sprayed commercial	690	480 (200^{th} cycle)	69.6%	0.152%

S with 28% graphite				

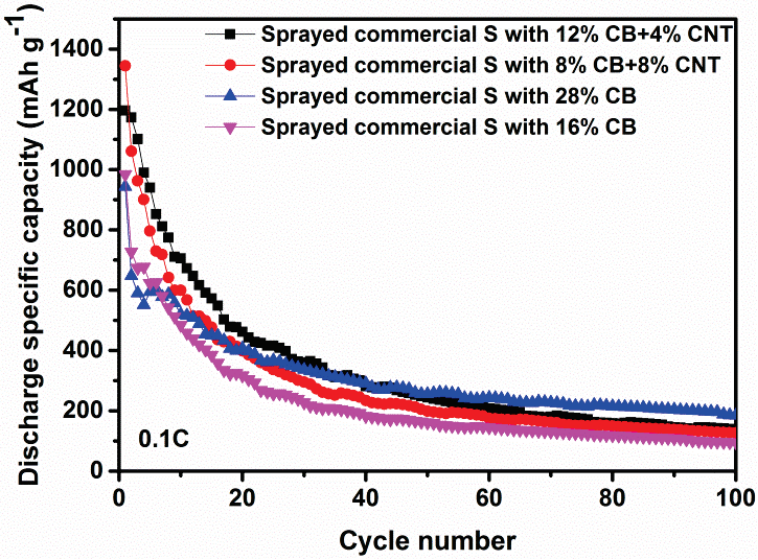

Figure 6.15 Cycling performances of sprayed commercial sulfur with 16% CB, sprayed commercial sulfur with 12% CB + 4% CNT, sprayed commercial sulfur with 8% CB + 8% CNT, sprayed commercial sulfur with 28% CB, and sprayed commercial sulphur with 16% CB.

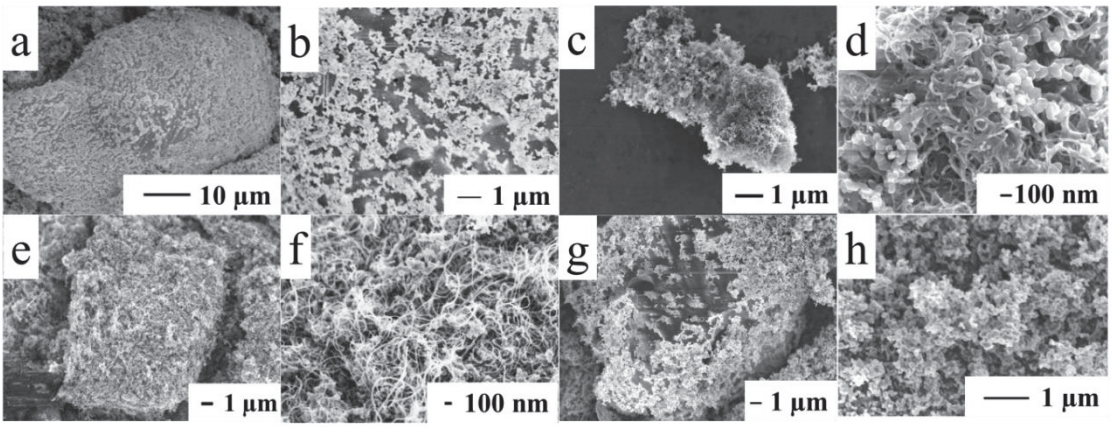

Figure 6.16 FESEM images of (a) sprayed commercial sulfur with 16% CB, (b) the enlarge image of (a), (c) sprayed commercial sulfur with 12% CB+4% CNT, (d) the enlarged image

of (c), (e) sprayed commercial sulfur with 8% CB+8% CNT, (f) the enlarged image of (e), (g) sprayed commercial sulfur with 28% CB, (h) the enlarged image of (g)

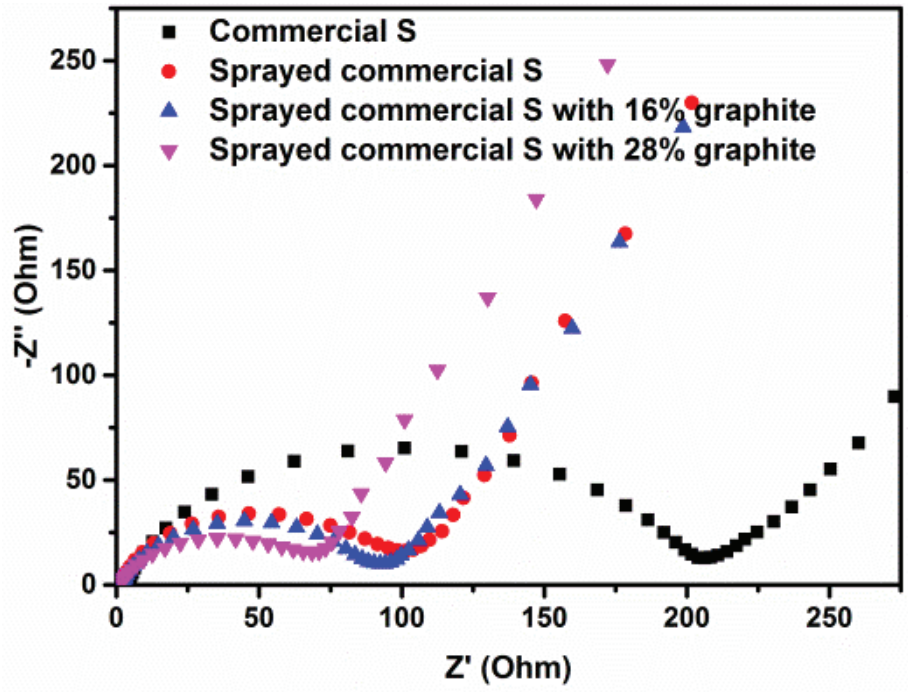

Figure 6.17 Impedance plots of fresh electrodes containing commercial sulfur; sprayed commercial sulfur; sprayed commercial sulfur with 16% graphite; and sprayed commercial sulfur with 28% graphite.

6.4. Conclusions

In summary, porous sulfur/dual-carbon ternary composite architectures using graphite, carbon black, and multi-walled CNT scaffolding particles were prepared by an advanced in-situ spray-pyrolysis/sublimation method, which is a cost-effective technique and industrially oriented approach for continuous production. In this study, the best ratio of ethanol to distilled water is confirmed to be 1:2. The influence of the operation temperature on the synthesis was investigated. 180 ºC was found to be the optimal operation temperature. Among the different types of added carbon in the forms of graphite, carbon black, and multi-walled CNT, graphite is the best form of

carbon for this spray-pyrolysis/sublimation system. The bridging graphite can be bound to porous sulfur by an adhesive interface of amorphous carbon to form an interparticle conductive matrix. Moreover, the pores on sulfur formed from sulfur sublimation and the interconnected open pores from the matrix increase the contact area with Super-P and electrolyte, decrease the transport pathways for both electrons and lithium ions, and confine the soluble lithium polysulfides, as well as providing sufficient space to accommodate sulfur volumetric expansion during charge and discharge processes. Due to this unique chemistry and structure, the porous sulfur/dual-carbon composites with graphite present attractive cycling performance of 480 mAh g^{-1} after 200 cycles, 400 mAh g^{-1} after 400 cycles and 500 mAh g^{-1} after 100 cycles with the new charging technique, and good high rate capability of 520 mAh g^{-1} at 2 C as well. The scalable and continuous-production spray-pyrolysis/sublimation method developed in this study and the novel architecture of porous sulfur/dual-carbon composites prepared for the first time in this work show great potential for the commercialization of lithium/sulfur batteries.

Chapter 7 High Performance Active-Carbon – Nano-Sulfur – Polypyrrole Composite with Host-Container Architecture for Lithium/Sulfur Batteries

7.1. Introduction

The lithium/sulfur battery has been attracting ever-increasing attention for years as the next-generation energy storage system, because it has the highest theoretical discharge specific capacity (1675 mAh g^{-1}) among all the known solid cathode materials for lithium ion batteries and very high energy density (2600 Wh kg^{-1})[26, 163, 241, 268-272]. In addition, sulfur is naturally abundant, low-cost, and environmentally friendly[263, 273-275].

It is very difficult, however, to realize the full capacity of the sulfur cathode, due to the low utilization of the active materials. Firstly, sulfur is an insulating material, whose conductivity is only 5×10^{-30} S cm^{-1} at 25 °C[276]. Thus, a high proportion of the sulfur, which isn't in contact with the carbon black and electrolyte, cannot provide any capacity. Secondly, the intermediate polysulfide ions, which are produced during the discharge and charge processes, are highly soluble in the organic electrolyte[66, 277-280]. The dissolved polysulfides will be transferred to the anode, which is called the "shuttle effect"[281]. Once there, the polysulfide ions will react with lithium metal and lithium ions, which will lead to capacity decay and a reduction in active material utilization[67, 282-285].

In order to successfully operate the lithium-sulfur battery, the sulfur powder must be well combined with electrically conductive additives and strongly adsorbent agents[286-293]. Reducing the particle size of sulfur can increase the contact area with carbon black in the electrode as well as with the electrolyte[294, 295]. There are two main approaches to obtain fine-size sulfur by a wet chemical method. [222, 223]. One involves using a surfactant such as Triton-X100, cetyl trimethyl ammonium bromide (CTAB), and sodium dodecyl benzene sulfonate (SDBS). The surfactants can effectively control the size of sulfur particles by reducing the

interfacial tension for the dispersion of a compound in a solution[296]. The problem is that these high molecular weight surfactants are expensive and not environmentally friendly. Moreover, removing the surfactant from the synthesized product is time-consuming and results in unwanted sulfur waste. Another approach is using spray precipitation method, which is a simple, single-step, and industry-oriented method. It is claimed that the atomized thiosulfate creates numerous nucleation sites to produce submicron-sized elemental sulfur particles with higher surface area compared to conventional methods. The as-prepared submicron-sized elemental sulfur particles will agglomerate, however, to form larger size sulfur particles after the washing and drying process[224]. Thus, it is necessary to add some additives to prevent the agglomeration of the as-prepared submicron-sized sulfur in the spray precipitation method. M. R. Kaiser et Al. has reported that carbon black can successfully act as a dispersion agent and conducting additive to prepare sulfur/carbon-black composite. The newly developed high-surface-area spray-precipitated carbon-sulfur composite has demonstrated superior electrochemical performance[294]. In that work, however, there is no extra layer to protect the sulfur/carbon composite. Thus the diffusion of the dissolved polysulfide species cannot be prevented effectively. Active carbon is a kind of porous material with very high surface area, which can act as a good conducting matrix in lithium/sulfur batteries, and the pores in the active carbon can absorb thiosulphate ions to form submicron-sized sulfur particles and further protect the sulfur particles from agglomeration. Thus, the small pores and the high surface area have the potential to absorb the dissolved polysulfide ions to some extent[297]. Moreover, polypyrrole (PPy) has been reported to be a very good conducting additive in sulfur cathode to improve the performance of lithium/sulfur batteries by enhancing the conductivity, providing capacity, and trapping the diffusion of the dissolved polysulfides[18, 33, 61, 64, 193, 263]. Thus, coating an external polypyrrole layer on the outside of the sulfur/active carbon is expected to further enhance the performance of lithium/sulfur batteries.

Furthermore, Manthiram's group [298], and later, other groups [299, 300] reported that inserting a free-standing layer of carbon nanotube (CNT) between the separator and the sulfur cathode as a physical barrier can help to increase the conductivity of the sulfur while preventing the diffusion of longer chain polysulfides.

In this work, there are synergetic advantages from the spray precipitation method, the unique structure of the active carbon used as host conductive agent, the polypyrrole coating layer that functions as a container, and the single-walled carbon nanotube (SWCNT) paper as interlayer. Firstly, the active-carbon – nano-sulfur – polypyrrole composite with host-container architecture was prepared, where the active carbon acts as a host to adsorb sulfur in its pore spaces and the polypyrrole layer works as a container to protect the sulfur from diffusion of the dissolved polysulfide ions in lithium/sulfur batteries. Then, the interlayer of single-walled carbon nanotube flexible film was inserted between the cathode and the separator, where it could significantly improve the rate capability of the composite cathode in lithium/sulfur batteries. As a result, the as-prepared active-carbon – nano-sulfur – polypyrrole composite was applied in lithium/sulfur batteries, which presented much better electrochemical performance than sulfur cathode and active-carbon - nano-sulfur composite cathode.

7.2 Experimental section

7.2.1 Materials

Sodium thiosulphate ($Na_2S_2O_3$), oxalic acid ($H_2C_2O_4$), activated carbon (AC), sulfur (S), nano-graphite carbon, pyrrole monomer, sodium p-toluenesulphonate (PTS Na), $FeCl_3$, Triton X-100, and ethanol were all purchased from Sigma Aldrich (Australia). All the chemicals were used as received without any further purification.

7.2.2 Material synthesis

7.2.2.1 Preparation of AC-S composite:

Firstly, 0.5 M $Na_2S_2O_3$ solution and 1 M $H_2C_2O_4$ solution were prepared. 0.6857 g AC was dispersed into 100 mL $Na_2S_2O_3$ solution. After that, the suspension of $Na_2S_2O_3$ and AC was sprayed into the $H_2C_2O_4$ solution. The precipitated solution was washed by de-ionized water and ethanol, followed by vacuum drying at 50 °C for 48 hours. The chemical reaction for sulfur precipitation is: $Na_2S_2O_3 + H_2C_2O_4 \rightarrow Na_2C_2O_4 + S\downarrow + SO_2\uparrow + H_2O$.

For investigation of the effects of the AC's position in the suspension and the spray order, an $ACS_{inverse}$ composite was prepared for comparison. A similar procedure was applied for the fabrication of $ACS_{inverse}$ composite as for the preparation of AC-S composite. The only difference is that the spray order was inverted, so that the AC was dispersed into $H_2C_2O_4$ solution rather than into $Na_2S_2O_3$ solution, and the $Na_2S_2O_3$ solution was subsequently sprayed into the suspension of $H_2C_2O_4$ and AC.

The thermogravimetric analysis (TGA) and energy dispersive spectroscopy (EDS) mapping results confirmed that the AC-S composite was much better than the $ACS_{inverse}$ composite. Therefore, the following discussion will be focused on the AC-S composite and the modification of the AC-S composite by PPy coating.

7.2.2.2 Preparation of AC-S-PPy composite:

The AC-S-PPy composite was synthesized by coating polypyrrole on the surface of the AC-S composite, which was prepared by spraying the suspension of $Na_2S_2O_3$ and AC into $H_2C_2O_4$ solution, via an optimized chemical polymerization method using pyrrole monomer, sodium p-toluenesulphonate (PTS Na) as the dopant, and $FeCl_3$ as the oxidant.

Preparation of Solution One: 115.76 mg sodium p-toluenesulfonate (PTS Na) was dispersed in 300 mL distilled water under stirring for 30 min with the temperature kept at 0-5 °C. Then

120 μL liquid pyrrole monomer was added into the above solution under stirring for 30 min with the temperature kept at 0-5 ºC as well.

Preparation of Solution Two: 870.4 mg $FeCl_3$ was dissolved in 120 mL distilled water under stirring for 30 min with the temperature kept at 0-5 ºC.

Firstly, 3.2 mL TX-100 and 320 mg AC-S composite were dispersed in Solution One and kept under stirring for 1 h, with the temperature kept at 0-5 ºC. Then, Solution Two was gradually dropped into the above mixture to initiate the polymerization. The mixture was stirred for 6 h and then aged for another 12 h. All the solutions were precooled to 0-5 ºC, and all the polymerization took place at 0-5 ºC. The resultant black aqueous solution was washed thoroughly with distilled water until free of $FeCl_3$. Finally, the black mass was dried at 45 ºC overnight under vacuum to yield AC-S-PPy composite powder.

7.2.2.3 Fabrication of SWCNT free-standing layer:

15 mg SWCNTs with 500 ml de-ionized water were poured into a beaker, and 500 mg of Triton-X100 surfactant was added. Then, the solution was probe sonicated for 1 h with a 2 s pause time, followed by vacuum filtration and washing with de-ionized water and ethanol. The polytetrafluoroethylene (PTFE) filter paper with the SWCNT layer was dried under vacuum overnight at 60 ˚C, and finally, the SWCNT layer was easily peeled off from the filter paper.

7.2.3. Materials characterization

The structures of the samples were characterized by X-ray diffraction (XRD) using a GBC MMA X-ray generator and diffractometer with Cu Kα radiation (λ = 1.5418 Å), employing a scanning rate of 5° min^{-1} in the 2θ range from 10° to 70°. Raman spectroscopy was conducted on a JOBIN YVON HR800 Confocal Raman system with 632.8 nm diode laser excitation on a 300 lines/mm grating at room temperature. Thermogravimetric analysis

(TGA) was performed via a SETARAM Thermogravimetric Analyzer (France) in air to determine the changes in sample weight with increasing temperature and to estimate the amount of sulfur in the sample. The morphology of the samples and the mapping results were obtained with a field-emission scanning electron microscope (FESEM; JEOL 7500, 5 kV) and a transmission electron microscope (TEM; JEM-ARM 200F).

7.2.4. Electrochemical measurements

When preparing electrodes for lithium/sulfur batteries, polyvinylidene fluoride (PVDF) was used as the binder and N-methyl-2-pyrrolidinone (NMP) as solvent. The weight ratio of the as-prepared composite, Super P, and PVDF in the mixture ws 80:10:10. The slurries were spread onto aluminum foil substrates. The coated electrodes were dried in a vacuum oven at 50 ^{o}C for 24 h and then pressed. Subsequently, the electrodes were cut into disks 9.5 mm in diameter. A conventional organic solvent electrolyte was used, consisting of 1 mol L^{-1} lithium bis(trifluoromethane sulfonyl) imide (LiTFSI) in 1,3-dioxolane (DOL) / 1,2-dimethoxyethane (DME) (1:1 by volume) with 0.1 mol L^{-1} $LiNO_3$ as an additive. CR 2032 type coin cells were assembled in an Ar-filled glove box. Charge-discharge testing was carried out with a LAND battery test system at a current density of 168 mA g^{-1} (0.1 C) within the voltage range of 1.5–3.0 V. Cyclic voltammetry (CV) and AC impedance measurements were performed using a Biologic VMP-3 Multichannel electrochemistry workstation at a scanning rate of 0.1 mV s^{-1} over a frequency range of 1 00 kHz - 0.01 Hz, respectively.

7.3. Results and discussions

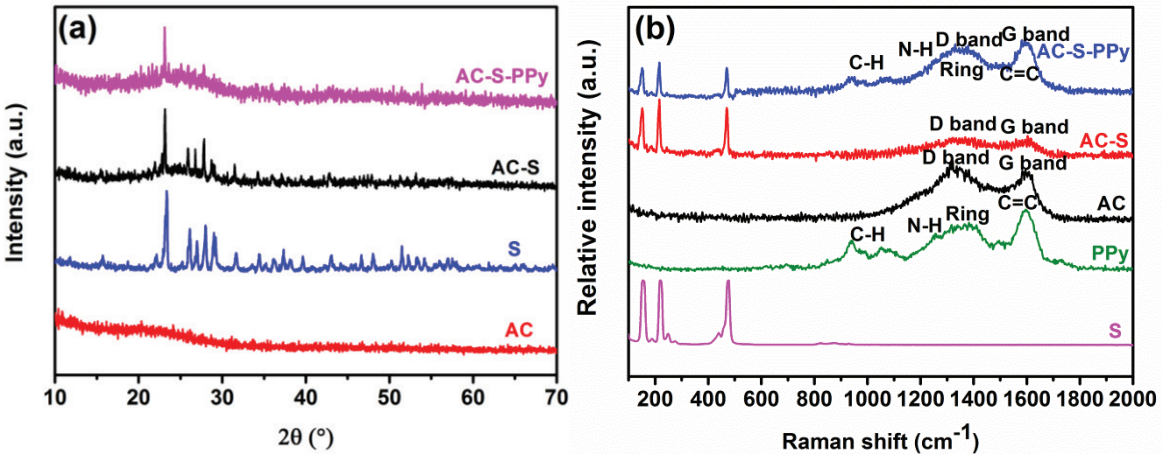

Figure 7.1 (a) X-ray diffraction patterns of AC, S, AC-S composite, and AC-S-PPy composite, (b) Raman spectra of AC, S, PPy, AC-S composite, and AC-S-PPy composite.

Figure 7.1(a) presents the X-ray diffraction (XRD) patterns of the commercial sulfur, AC, AC-S composite, and AC-S-PPy composite. The diffraction peaks of the three samples match very well with the standard diffraction lines of sulfur (PDF card No. 00-001-0478), which can be indexed to the orthorhombic phase with space group Fddd. This indicates that no phase transformation of sulfur occurs during the *in-situ* chemical polypyrrole coating process. The Raman spectra of bare S, pure PPy, AC, AC-S composite, and AC-S-PPy composite are shown in Figure 7.1(b), which were obtained with 632.8 nm diode laser excitation at room temperature. The Raman spectrum of S displays three main peaks below 500 cm^{-1}, while the peaks in the Raman spectrum of PPy are located between 800 and 1700 cm^{-1}, which are identified as the characteristic peaks of C=C backbone stretching of PPy at 1580 cm^{-1}, C-H in-plane deformation at 1050 cm^{-1} and 1080 cm^{-1}, C-H out-of-plane bending of oxidized PPy at 930 cm^{-1}, N-H in-plane bending at 1240 cm^{-1}, and the ring-stretching mode of PPy at 1320 cm^{-1} and 1380 cm^{-1}, respectively[237]. The Raman spectra of the AC-S composite and the AC-S-PPy composite show not only the three characteristic peaks of sulfur below 500 cm^{-1}, but also the typical peaks of PPy between 800 and 1700 cm^{-1}. This confirms

that the AC-S composite and AC-S-PPy composite contain both sulfur and PPy.

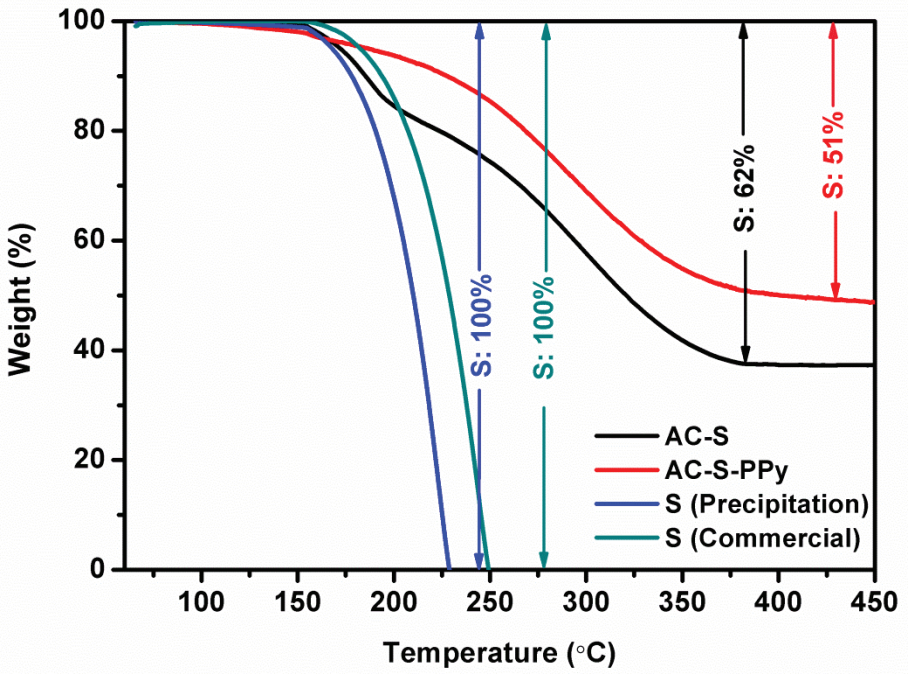

Figure 7.2 TGA curves of commercial S, precipitated S, AC-S composite, AC-S-PPy composite.

In order to quantify the amount of sulfur in the as-prepared samples, TGA was carried out in argon. The samples were heated from 60 ºC to 450 ºC at a heating rate of 5 ºC min^{-1}. In Figure 7.2, the TGA curve of the as-prepared spray-precipitated sulfur presents a different weight loss end temperature compared to the commercial sulfur, which can be ascribed to the size differences between the precipitated sulfur and the commercial sulfur. As shown in Figure 7.3, the particle size of the sulfur prepared by spray precipitation is much smaller than that of commercial sulfur. The average size of the as-prepared spray-precipitated sulfur is around 1 μm, while that of the commercial sulfur is about 50 μm. The Brunauer-Emmett-Teller (BET) surface areas of the commercial sulfur and the sulfur precipitated by the spray method are listed in Table 7.1. The BET surface area of the commercial sulfur is only 0.2023 m^2 g^{-1}, while that of the spray-precipitated sulfur is as high as 2.4815 m^2 g^{-1}.The smaller particle size leads to higher surface area and lower sublimation temperature. That is why all

the as-prepared spray-precipitated sulfur is gone at 230 ˚C, but the commercial sulfur is completely sublimated at around 250 ˚C. In Figure 7.2, the TGA curve of the AC-S composite shows two different weight loss plateaus, which can be ascribed to the presence of AC. As the morphology of AC is porous, some of the S precipitation is absorbed into the pores. Thus the S particles outside of the C evaporate much more quickly, while the S inside of the pores of the C will not be so easy to evaporate because of the capillary attraction. The quick decrease in the slope is ascribed to the loss of sulfur outside of the carbon and the slow decrease in the slope is attributed to the loss of sulfur inside of the carbon. In the AC-S composite curve, the quick weight loss is 14.7%, and the slow weight loss is 47.3%. This means that the proportion of the outside sulfur is 14.7% and that of the inside sulfur is 47.3%. The TGA curves of the CB-S and graphite-S composites only show one slope for weight decrease. As these two kinds of composites have no AC, this can further confirm that AC can adsorb precipitated sulfur during the spray process. For lithium/sulfur batteries, the dissolution of polysulfides is one of the main problems, so it is necessary to load a polypyrrole layer to prevent the dissolution of polysulfides, which has been proved to be a successful approach. [18, 33, 61, 64, 263] Thus, in this work, The PPy layer has also been coated on the as-prepared AC-S composite. The TGA curves of the AC-S-PPy composite in Figure 7.2 show only one decreasing step for the AC-S-PPy composite, which is different from the AC-S composite. This can be ascribed to the PPy coating on the sulfur, which protects the outside sulfur in a similar way to the inside sulfur. Thus, the outside sulfur and the inside sulfur sublimate at a similar rate. This can further confirm that PPy has covered the AC-S composite very well. From Figure 7.2, it can be calculated that AC-S-PPy composite contains 51.0 wt% sulfur, 27.5 wt% AC, and 21.5wt% polypyrrole.

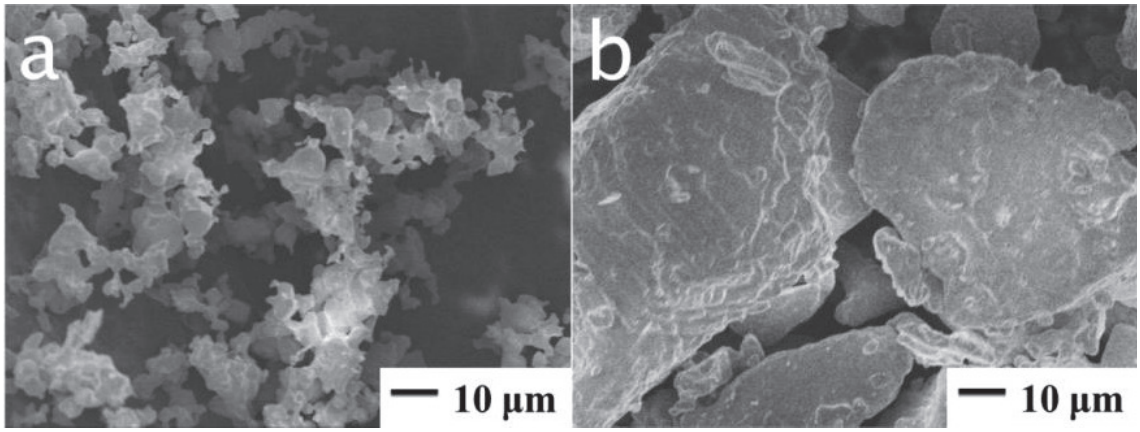

Figure 7.3 FESEM images of: (a) as-prepared sulfur by spray precipation; (b) commercial sulfur.

Table 7.1 BET surface areas of commercial S and spray-precipitated S.

Sample	Commercial S	Precipitation S by spray
BET Surface Area (m^2/g)	0.2023	2.4815

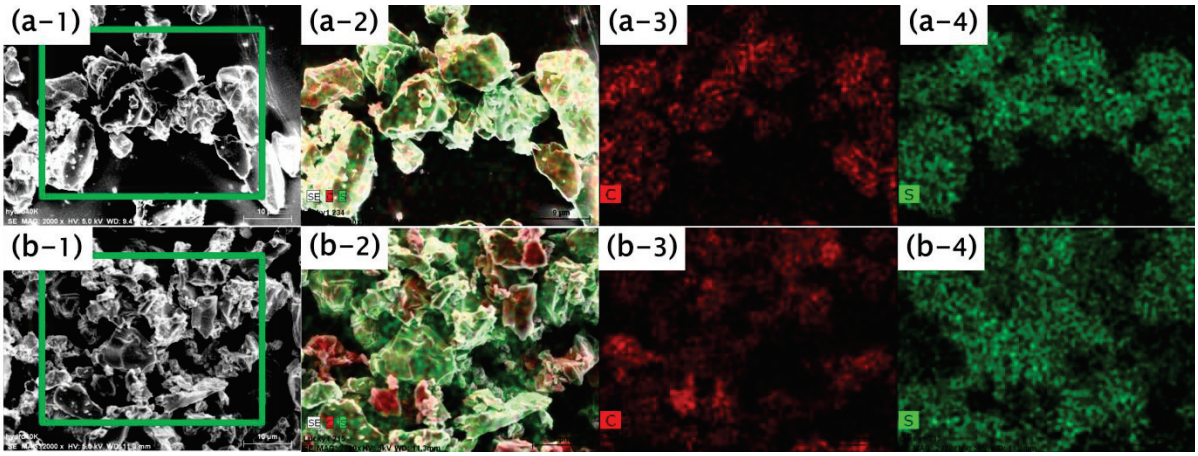

Figure 7.4 EDS mapping of (a) AC-S composite, (b) $ACS_{inverse}$ composite.

In order to compare the importance of AC's position in the suspension and the spray order, the elemental distributions of AC-S composite and $ACS_{inverse}$ composite were examined by energy dispersive X-ray spectroscopy (EDS) mapping analysis, which is shown in Figure 7.4. Figure 7.4(a-1) is the selected area of the FESEM image of the AC-S composite. The red

spots in Figure 7.4(a-3) correspond to the presence of the element carbon, and the green spots in Figure 7.4(a-4) correspond to the element sulfur. It is clear that the distributions of carbon and sulfur coincide completely, which is shown in the overall result of the EDS mapping in Figure 7.4(a-2) as well. This indicates that the sulfur was uniformly loaded throughout the carbon. EDS mapping analysis was also carried on the $ACS_{inverse}$ composite for comparison, and the results are shown in Figure 7.4(b). Figure 7.4(b-1) is the FESEM image of the detected area. Figure 7.4(b-2) gives the overall EDS mapping results, and Figure 7.4(b-3) shows the distribution of the element carbon, while Figure 7.4(b-4) shows the distribution of the element sulfur. It is clear that there is sulfur loading on most of the carbon in $ACS_{inverse}$ composite, but it is not so uniform as that of AC-S composite in Figure 7.4(a), and some carbon is not successfully coated by sulfur. The above results agree very well with the TGA results in Figure 7.5. The total weight loss of AC-S composite and $ACS_{inverse}$ composite is the same, which is 62%. But the ratio of the slow decrease slope is different. In the $ACS_{inverse}$ composite, the proportion of outside sulfur is 21.2% and that of inside sulfur is 40.8%, while in the AC-S composite, the proportion of outside sulfur is 14.7% and that of inside sulfur is 47.3%. This can be ascribed to the effect of the AC's position in the suspension and the spray order. For the synthesis of the AC-S composite, AC is dispersed in the solution of $Na_2S_2O_3$, so the $S_2O_3^{2-}$ can be plentifully adsorbed by that porous AC. Thus, when the suspension with AC and $Na_2S_2O_3$ was sprayed into the solution of $H_2C_2O_4$, the sulfur particles could be produced immediately inside of the AC. In contrast, when the $ACS_{inverse}$ composite was prepared, the AC was dispersed in the solution of $H_2C_2O_4$, and then the $Na_2S_2O_3$ solution was sprayed into the suspension of AC and $H_2C_2O_4$. As the size of $S_2O_3^{2-}$ is quite big, $S_2O_3^{2-}$ takes time to be absorbed into the AC. The precipitation of sulfur on the surface of AC will also prevent the adsorption of sulfur into the inside of the AC to some extent. Therefore, the percentage of sulfur inside the AC of $ACS_{inverse}$ composite is lower than that of AC-S

composite. It is further confirmed that the dispersion AC dispersed in $S_2O_3^{2-}$ solution, followed by spraying into the solution of $H_2C_2O_4$, is good for the preparation of AC-S composite. Therefore, the following discussion will be focused on the AC-S composite and the modification of AC-S composite by PPy coating.

In order to study the morphology of the samples, FESEM images were collected and are shown in Figure 7.6. Figure 7.6(a-1) is a FESEM image of commercial AC at lower magnification, which shows that the size of the AC particles is around 7 μm, and from the FESEM image at slightly higher magnification in Figure 7.6(a-2), it can be seen that the surface of the AC particles is very smooth. Figure 7.6(b-1) is a FESEM image of the as-prepared AC-S composite at lower magnification, which demonstrates that the size of the AC-S composite particles is still around 7 μm, with no big difference compared to that of the AC particles shown in Figure 7.6(a-1). Figure 7.6(b-2), a FESEM image of the AC-S composite at higher magnification, shows that the surface of the AC-S composite has become slightly rougher compared to that of commercial AC. Figure 7.6(c-1) shows that the size of the as-prepared AC-S-PPy composite particles is around 5 μm, which is a little smaller than that of AC-S composite, and the amount of the smaller particles has also becomes greater. This can be ascribed to the high energy ultrasonic dispersion during the PPy coating process. The biggest change is the surface, which is shown in Figure 7.6(c-2). The surface of the AC-S-PPy composite has become less smooth. Cauliflower-like structure on the surface of the AC-S composite can be seen, which is a typical PPy morphology when it is synthesized by the chemical polymerization method. [85, 263]

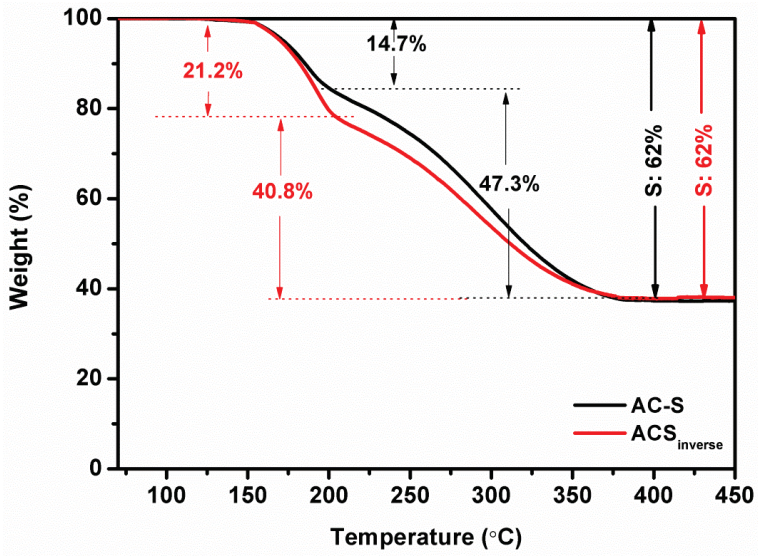

Figure 7.5 TGA curves of AC-S composite and $ACS_{inverse}$ composite.

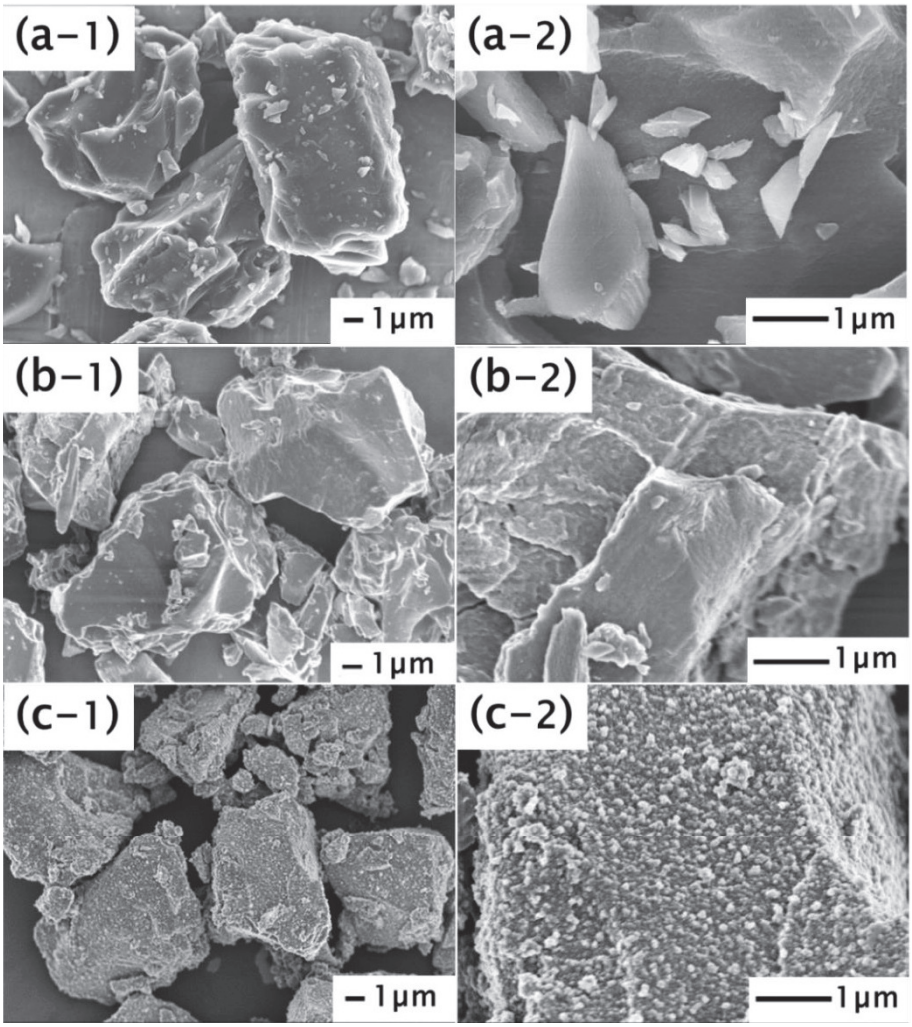

Figure 7.6 FESEM images of (a-1) AC under low magnification, (a-2) AC under high

magnification, (b-1) AC-S composite under low magnification, (b-2) AC-S composite under high magnification, (c-1) AC-S-PPy composite under low magnification, and (c-2) AC-S-PPy composite under high magnification.

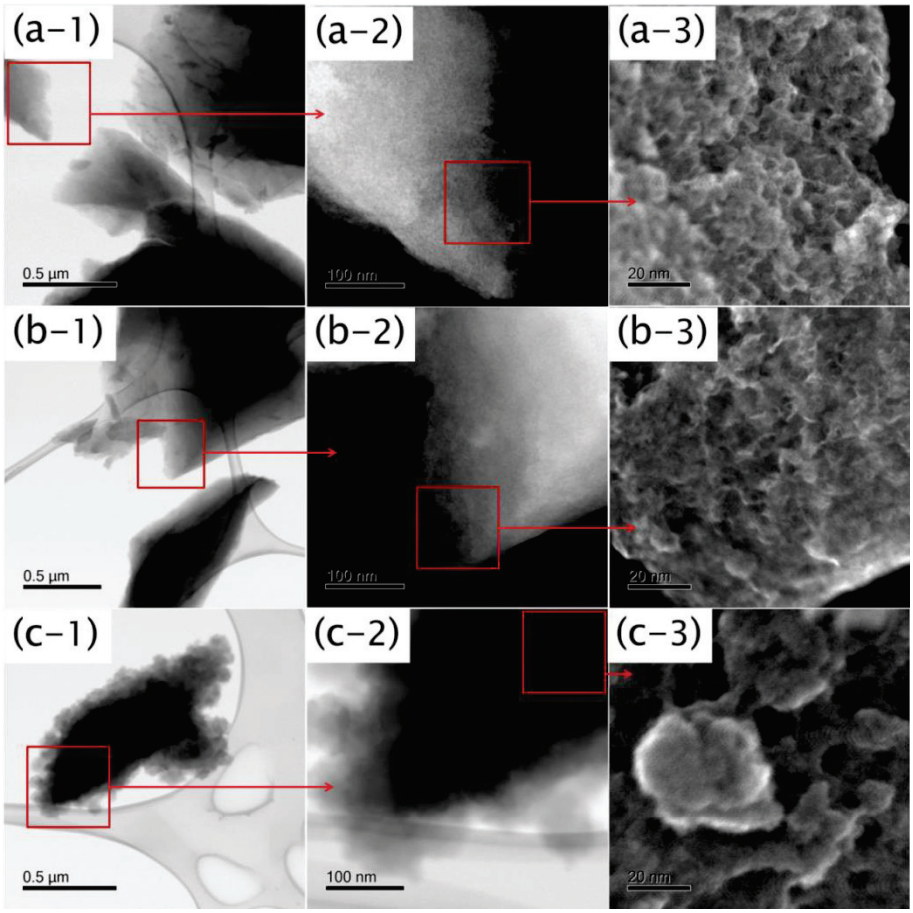

Figure 7.7 TEM and STEM images of: AC (a-1, a-2, a-3); AC-S composite (b-1, b-2, b-3); and AC-S-PPy composite (c-1, c-2, c-3).

The morphology of the samples was further investigated by transmission electron microscopy (TEM), as shown in Figure 7.7. Figure 7.7(a-1) is a bright-field TEM image of commercial AC at lower magnification. Figure 7.7(a-2) is an enlarged dark-field TEM image of the selected area in Figure 7.7(a-1). It seems that the AC has a porous structure from Figure 7.7(a-1) and Figure 7.7(a-2), but this is not very clear. In order to further confirm the surface structure of the AC, the selected area in Figure 7.7(a-2) is further enlarged and shown

in Figure 7.7(a-3), which is a scanning TEM (STEM) image of the commercial AC. It is apparent that the surface of the AC is not smooth, but very rough with pores. This is why the AC particles have a very high surface area of 2000 ± 100 m^2/g and also further confirms that AC can adsorb $S_2O_3^{2-}$ inside its pores. Figure 7.7(b-1) is a TEM image of AC-S composite at lower magnification, and Figure 7.7(b-2) is an enlarged image of the selected area in Figure 7.7(b-1), while Figure 7.7(b-3) is a further enlarged image of the selected area in Figure 7.7(b-2). Comparing Figure 7.7(a-2) and Figure 7.7(b-2), it is clear that the surface of AC-S composite has become smoother after loading sulfur. This can be seen much more clearly in Figure 7.7(b-3) and Figure 7.7(a-3). It also can confirm that the spray-precipitated sulfur is nanosize. Figure 7.7(c-1) is a TEM image of AC-S-PPy composite, Figure 7.7(c-2) is an enlarged image of the selected area in Figure 7.7(c-1). The selected area in Figure 7.7(c-2) is further enlarged and presented in Figure 7.7(c-3), where typical cauliflower structure of the PPy coating layer can be seen very clearly. This also agrees with the results presented in the FESEM images (Figure 7.6(c-1) and Figure 7.6(c-2)).

To investigate the elemental distribution in AC-S-PPy composite, EDS mapping was conducted, and the results are shown in Figure 7.8. Figure 7.8 presents the results for AC, AC-S composite, and AC-S-PPy composite. The grey image is the dark-field TEM image of AC, the red spots correspond to the element C, the yellow spots correspond to the element S, and the purple spots correspond to the element N. In respectively, Figure 7.8(a) shows the EDS mapping of AC, Figure 7.8(b) the EDS mapping of AC-S composite, and Figure 7.8(c) the EDS mapping of AC-S-PPy composite. It can be concluded that sulfur is loaded very uniformly in AC-S composite and AC-S-PPy composite, and the PPy coating on AC-S composite is also very uniform.

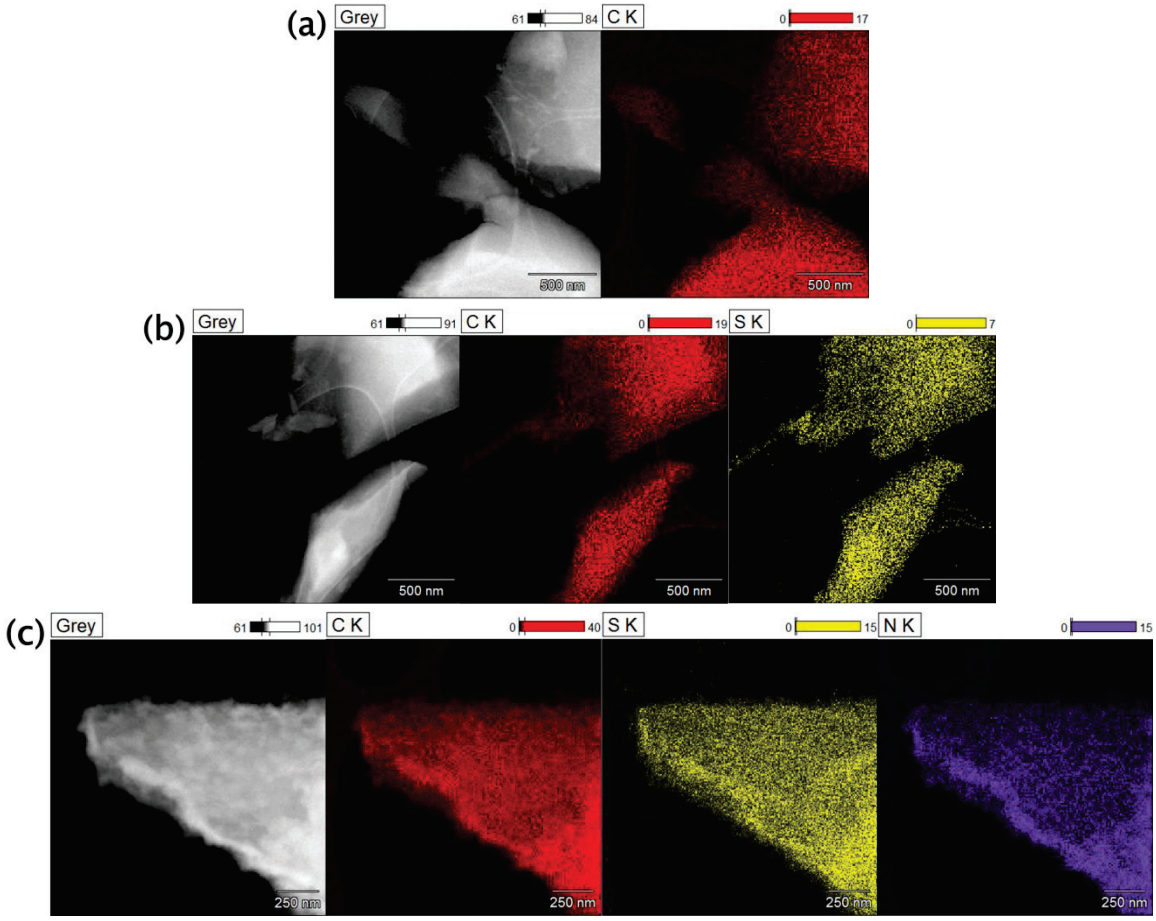

Figure 7.8 TEM image and EDS analysis of (a) AC, (b) AC-S composite, and (c) AC-S-PPy composite.

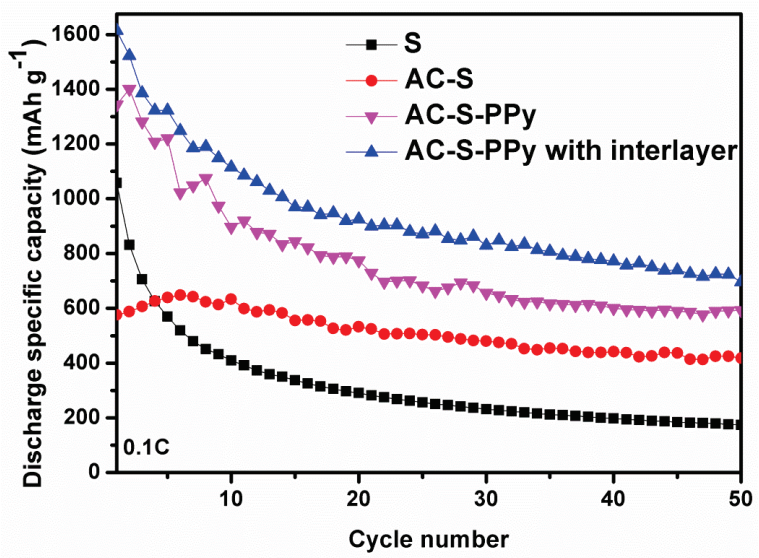

Figure 7.9 Cycling performance of commercial S, AC-S composite, AC-S-PPy composite,

and AC-S-PPy composite with SWCNT interlayer.

To investigate the electrochemical performance of the samples, commercial S, AC-S composite, and AC-S-PPy composite cathodes were cycled in 1 M LiTFSI in DOL/DME (1:1) with 0.1 M $LiNO_3$ additive at the current density of 0.1 C, and the results are shown in Figure 7.9. It was found that the discharge specific capacity of the AC-S-PPy composite electrode was the highest among the commercial sulfur electrode, the AC-S composite electrode, and the AC-S-PPy composite electrode. Specifically, the AC-S-PPy composite cathode yields a discharge specific capacity of 597.2 mAh g^{-1} after 50 cycles, while the AC-S composite cathode presents a discharge specific capacity of 420.2 mAh g^{-1} after 50 cycles, and the commercial S electrode only yields 177.9 mAh g^{-1} discharge specific capacity. It has been reported that a flexible film inserted between the separator and the cathode can improve the performance of Li/S batteries [298] [299, 300], and in this work a flexible SWCNT film was prepared as an interlayer in the Li/S batteries assembled with AC-S-PPy composite cathode. The discharge specific capacity was enhanced to 709.5 mAh g^{-1} after 50 cycles.

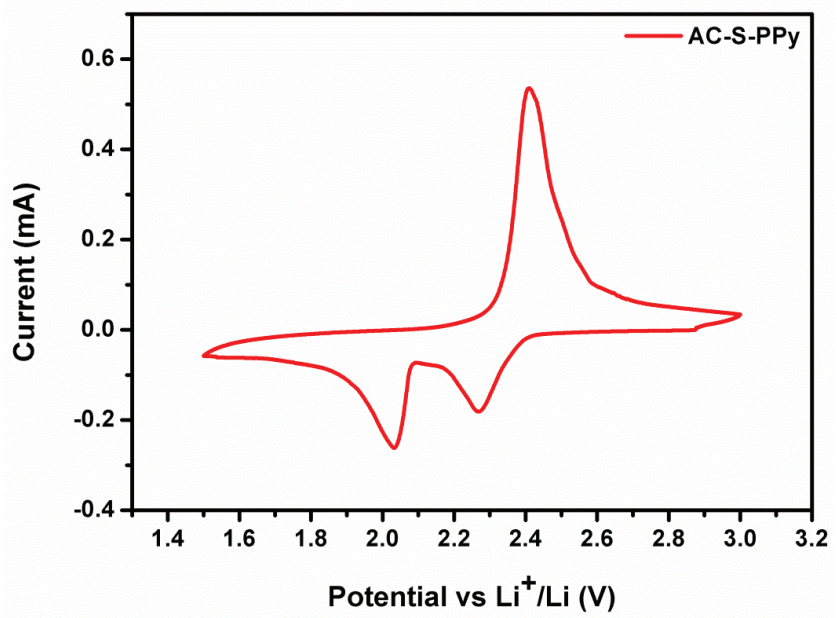

Figure 7.10 Cyclic voltammogram for the first cycle of electrode containing AC-S-PPy composite.

In Figure 7.10, cyclic voltammetry (CV) of the first cycle for the AC-S-PPy composite in 1 M LiTFSI in DOL/DME (1:1) with 0.1 M $LiNO_3$ additive was conducted at a scan speed of 0.1 mV s^{-1} in the potential range of 1.5-3.0 V. Two reduction peaks are observed, which could be assigned to the multiple-step reaction mechanism of sulfur with lithium. Specifically, in the first cycle, the peak at 2.3 V is ascribed to the open ring reduction of cyclic S_8 to long chain lithium polysulfides (Li_2S_x, $4 \leq x < 8$), while the peak at 2.0 V corresponds to the further reduction of these high-order polysulfides to Li_2S_2 and Li_2S.

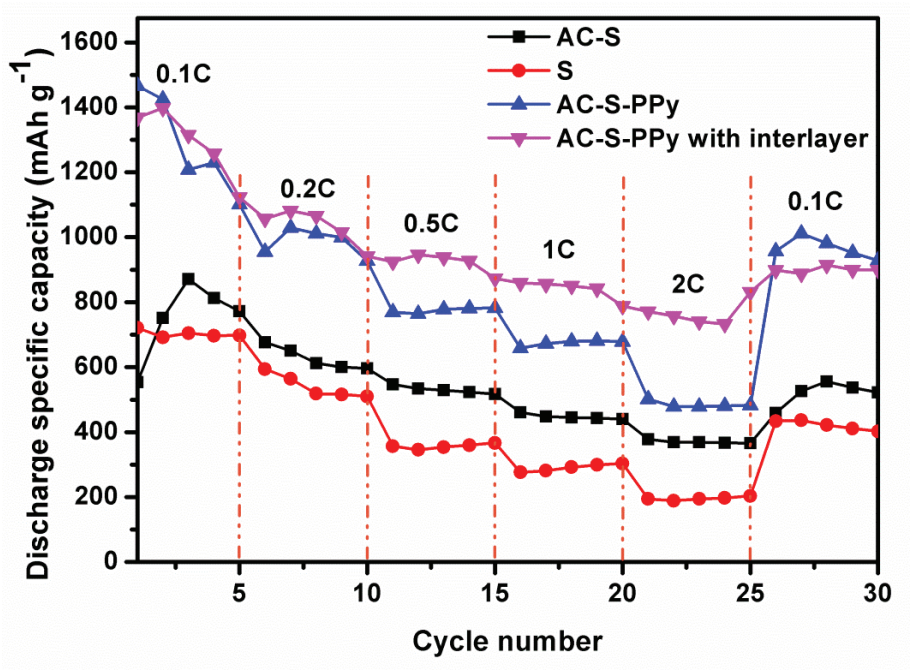

Figure 7.11 Rate capabilities of commercial S electrode, AC-S composite electrode, AC-S-PPy composite electrode, and AC-S-PPy composite electrode with interlayer.

Rate capabilities of the commercial S electrode, AC-S composite electrode, AC-S-PPy composite electrode, and the AC-S-PPy composite electrode with the interlayer were also investigated, and the cells were discharged to 1.5 V at different current densities from 0.1 C to 2 C in DOL/DME (1:1) electrolyte with 0.1 M $LiNO_3$ additive, as shown in Figure 7.11. It should be noted that the AC-S-PPy composite cathode delivered the highest discharge capacity when the SWCNT interlayer was inserted among all the tested batteries. Even at 2

C, the discharge specific capacity of the AC-S-PPy composite cathode with SWCNT interlayer was still as high as 787.9 mAh g^{-1}. The flexible SWCNT film inserted in between the separator and the cathode can help to increase the conductivity of the sulfur along with preventing the diffusion of longer chain polysulfides[298-300].

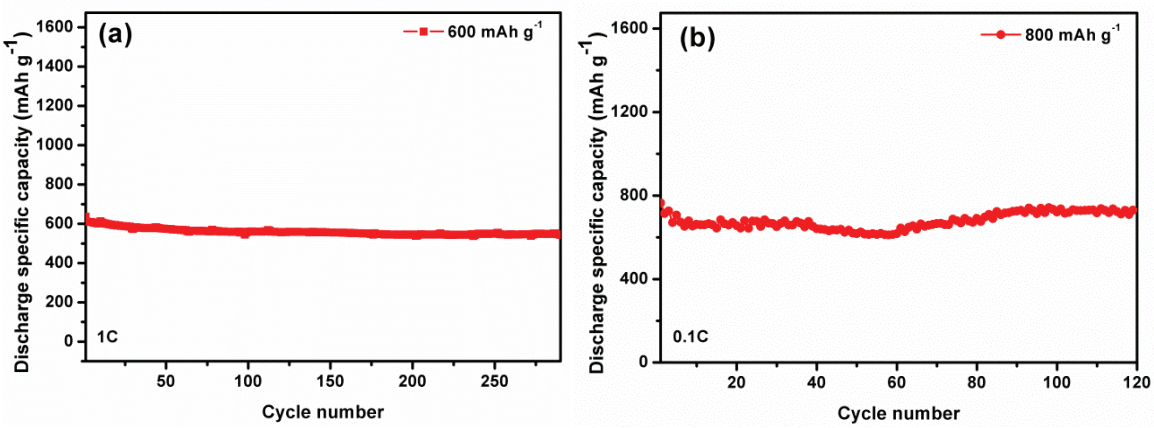

Figure 7.12 (a) Cycling performance of AC-S-PPy composite cathode with the interlayer under the new charging technique (charging to 600 mAh g^{-1} at 1 C); (b) cycling performance of AC-S-PPy composite cathode with the interlayer underthe new charging technique (charging to 800 mAh g^{-1}at 0.1 C).

It was reported that the cycle life of lithium/sulfur batteries can be improved by a special charging technique, in which the battery is charged to a fixed capacity to avoid the dissolution of long-chain polysulfides.[23] In this study, I have also applied this novel technique to charge the batteries with AC-S-PPy composite cathode with the SWCNT interlayer to 600 mAh g^{-1} at 1 C and 800 mAh g^{-1} at 0.1 C. Figure 7.12 shows that almost no capacity fading behaviour could be observed for 290 cycles at 600 mAh g^{-1} and for 120 cycles at 800 mAh g^{-1}.

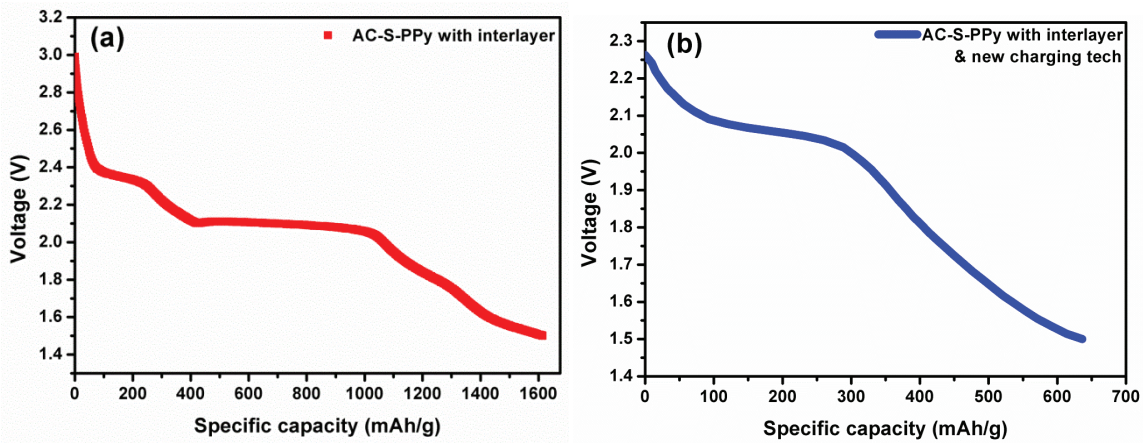

Figure 7.13 Discharge curves for 1st cycle of (a) AC-S-PPy composite electrode with interlayer; (b) AC-S-PPy composite electrode with interlayer under new charging technique.

Figure 7.13(a) shows the discharge voltage profile of the 1st cycle for AC-S-PPy composite with SWCNT interlayer in 1 M LiTFSI in DOL/DME (1:1) with 0.1 M $LiNO_3$ additive at the current density of 1 C. The discharge curve presents three plateaus, which are at 2.4 V and 2.05 V, respectively, which can be assigned to the two-step reaction of sulfur with lithium during the discharge process, which is in very good agreement with the CV results in Figure 7.10. The plateau at 2.4 V is ascribed to the open ring reduction of cyclic S_8 to long chain lithium polysulfides (Li_2S_x, $4 \leq x < 8$), while the plateau at 2.05 V corresponds to the further reduction of these high-order polysulfides to Li_2S_2 and Li_2S. Figure 13(b) presents the discharge curve of the 1st cycle of AC-S-PPy composite with SWCNT interlayer in 1 M LiTFSI in DOL/DME (1:1) with 0.1 M $LiNO_3$ additive under the new charging technique with charging to 600 mAh g^{-1} at at the current density of 1 C, and it only shows one discharge plateau at 2.05 V. No first plateau is formed, which indicates that the longer chain polysulfides have been prevented. As the longer chain polysulfides easily dissolve into the organic solvent of the electrolyte, and the longer chain polysulfides are formed in the first discharge plateau according the mechanism of the lithium/sulfur batteries, therefore, the fixed charging capacity method can prevent the diffusion of polysulfides and avoid the “shuttle

effect". I also tried to fix the charge capacity to 1000 mAh g^{-1} with discharge at 0.1 C, as is shown in Figure 7.14. The discharge specific capacity cannot reach 1000 mAh g^{-1}, but more than 800 mAh g^{-1} can be retained for 60 cycles.

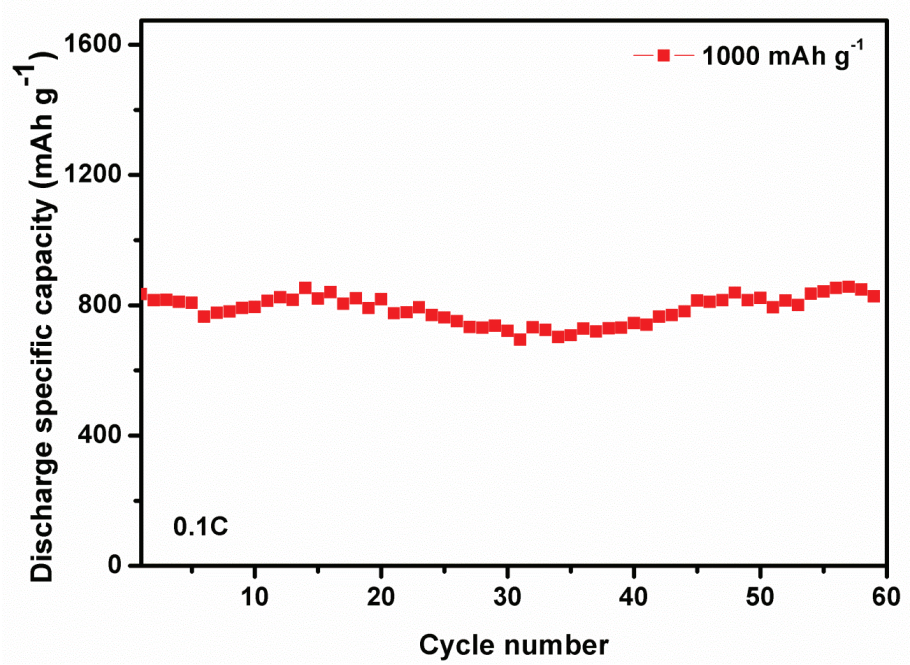

Figure 7.14 Cycling performance of commercial AC-S-PPy composite with the interlayer under the new charging technology (charging to 1000 mAh g^{-1} at 0.1 C).

7.4. Conclusions

In summary, active-carbon – nano-sulfur – polypyrrole composite with host-container architecture was prepared by the spray precipitation method followed by chemical polymerization, where the active carbon acts as a host to adsorb sulfur inside its pore spaces and the polypyrrole layer works as a container to enhance the conductivity of the electrodes, prevent polysulfide diffusion and provide additional capacity. Moreover, an interlayer consisting of a flexible film single-walled carbon nanotubes that was inserted between the cathode and separator has significantly improved the rate capability of the active-carbon – nano-sulfur – polypyrrole composite cathode in lithium/sulfur batteries. The as-prepared composite was applied in lithium/sulfur batteries, which presented much better

electrochemical performance than with sulfur cathode of active-carbon – nano-sulfur composite cathode. The AC-S-PPy composite cathode yielded a discharge specific capacity of 597.2 mAh g^{-1} after 50 cycles, while the AC-S composite cathode presented a discharge specific capacity of 420.2 mAh g^{-1} after 50 cycles, and commercial S electrode only yielded 177.9 mAh g^{-1} discharge specific capacities. When a flexible SWCNT interlayer was inserted between the cathode and separator in the assembled Li/S batteries, the discharge specific capacity with AC-S-PPy composite cathode was as high as 709.5 mAh g^{-1} at 0.1 C after 50 cycles, and could reach as high as 787.9 mAh g^{-1} at 2 C. When the novel charging technique was applied to charge the batteries with AC-S-PPy composite cathode with the SWCNT interlayer to 600 mAh g^{-1} at 1 C and 800 mAh g^{-1} at 0.1 C, almost no capacity fading behaviour could be observed for 290 cycles at 600 mAh g^{-1} and for 120 cycles at 800 mAh g^{-1}.

Chapter 8. General Conclusions and Outlook

8.1. General conclusions

The lithium sulfur battery is the most promising candidate for next-generation energy storage systems. It has the highest theoretical capacity among all the known solid cathode materials and very high energy density, as well as being low-cost and non-toxic. Although the lithium/sulfur batteries still have significant challenges to overcome, many approaches have been reported to effectively improve their electrochemical performance. There is still a long and bright way to go to exploit the potentialities of lithium/sulfur batteries. The results of this doctoral thesis work are concluded and summarized as follows:

Firstly, the conductivity of the sulfur cathode was improved by synthesis of pure sulfur particles with honeycomb-like morphology via a cooperative self-assembly process, where SDBS acts as a soft template. The as-prepared honeycomb-like sulfur cathode shows significantly improved electrochemical performance compared with the commercial sulfur powder and even the as-prepared sulfur without honeycomb-like morphology. The cells with the honeycomb-like sulfur electrode retained a reversible discharge capacity higher than 650 mAh g^{-1} for 50 cycles, while the discharge capacity of the commercial sulfur electrode was about 200 mAh g^{-1}. Moreover, the honeycomb morphology is stable and can be maintained during cycling.

Then, a conducting polymer, PPy, was applied to improve the electrochemical performance by synthesis of a PPy@S@PPy composite with a novel three-layer-3D structure, which consists of an external PPy coating layer, an intermediate sulfur filling layer, and an internal PPy conducting matrix layer. A S@PPy composite was prepared with the same components as the PPy@S@PPy composite except for the three-layer-3D-structure for

comparation. The discharge specific capacity of the PPy@S@PPy composite cathode is 554 mAh g^{-1} after 50 cycles, representing approximately 68.8% retention of the initial discharge specific capacity of about 801 mAh g^{-1}, while the S@PPy composite cathode demonstrates a discharge specific capacity of 370 mAh g^{-1} after 50 cycles, approximately 32.3% retention of the initial discharge specific capacity of about 1145 mAh g^{-1}. It is also found that the PPy@S@PPy composite cathode in the electrolyte with a mixed solvent of 1,3-dioxolane (DOL)/1,2-dimethoxyethane (DME) (1:1 by volume) presents much higher capacity than in the electrolyte with PEGDME solvent when the current density is higher than 200 mA g^{-1}. Moreover, comparative experiments with $LiNO_3$ additive in the electrolyte on coulombic efficiency confirm the containment function of the external PPy layer in the PPy@S@PPy composite and further identify the three-layer structure of PPy@S@PPy composite.

Next, an advanced *in-situ* spray-pyrolysis/sublimation method was employed to prepare a porous sulfur/dual-carbon ternary composite architecture using graphite, carbon black, and multi-walled CNT scaffolding particles. The spray-pyrolysis/sublimation method is a cost-effective and industrially oriented approach for continuous production. In this work, the best ratio of ethanol to distilled water is confirmed to be 1:2. The influence of the operation temperature on the synthesis was investigated. 180 ºC was found to be the optimal operation temperature. Among the different types of added carbon in the forms of graphite, carbon black, and multi-walled CNT, graphite was found to be the best form of carbon for this spray-pyrolysis/sublimation system. The bridging graphite can be bound to porous sulfur by an adhesive interface of amorphous carbon to form an interparticle conductive matrix. Moreover, the pores on sulfur formed from sulfur sublimation and the interconnected open pores from the matrix increase the contact area with Super-P and electrolyte, decrease the transport pathways for both electrons and lithium ions, and confine the

soluble lithium polysulfides, as well as providing sufficient space to accommodate sulfur volumetric expansion during charge and discharge processes. Due to this unique chemistry and structure, the porous sulfur/dual-carbon composites with graphite present attractive cycling performance of 480 mAh g^{-1} after 200 cycles, 400 mAh g^{-1} after 400 cycles, and 500 mAh g^{-1} after 100 cycles with the new charging technique, and good high rate capability of 520 mAh g^{-1} at 2 C as well. The scalable and continuous-production spray-pyrolysis/sublimation method developed in this study and the novel architecture of porous sulfur/dual-carbon composites prepared for the first time in this work show great potential for the commercialization of lithium/sulfur batteries.

Finally, an active-carbon – nano-sulfur – polypyrrole composite with host-container architecture was prepared by the spray precipitation method followed by chemical polymerization. In the as-prepared composite, the active carbon acts as a host matrix to adsorb sulfur inside its pore spaces and the polypyrrole layer works as a container to enhance the conductivity of the electrodes, prevent polysulfide diffusion, and provide additional capacity. Moreover, an interlayer consisting of a flexible film of single-walled carbon nanotubes inserted between cathode and separator significantly improved the rate capability of the active-carbon – nano-sulfur – polypyrrole composite cathode in lithium/sulfur batteries. The AC-S-PPy composite cathode yielded a discharge specific capacity of 597.2 mAh g^{-1} after 50 cycles, while the AC-S composite cathode presented a discharge specific capacity of 420.2 mAh g^{-1} after 50 cycles, and commercial S electrode only yielded discharge specific capacity of 177.9 mAh g^{-1}. When a flexible SWCNT interlayer was inserted during the assembly of the Li/S batteries, the discharge specific capacity with AC-S-PPy composite cathode remained as high as 709.5 mAh g^{-1} at 0.1 C after 50 cycles and could reach as high as 787.9 mAh g^{-1} at 2 C. When the novel charging technique was applied to charge the

batteries with AC-S-PPy composite cathode with SWCNT interlayer to 600 mAh g^{-1} at 1 C and 800 mAh g^{-1} at 0.1 C, almost no capacity fading behaviour could be observed for 290 cycles at 600 mAh g^{-1} and for 120 cycles at 800 mAh g^{-1}.

In summary, in this doctoral work, pure sulfur with honeycomb-like morphology, PPy@S@PPy composite, porous sulfur/dual-carbon ternary composite, and active–carbon – nano-sulfur – polypyrrole composite were successfully synthesized by the soft-template strategy, the polymerization reaction, the spray-pyrolysis/sublimation technique or the spray precipitation method. All the as-prepared samples were applied as cathode in lithium/sulfur batteries and presented significantly improved electrochemical performance. Moreover, the spray-pyrolysis/sublimation technique and the spray precipitation method are both industry-oriented methods, which show great potential for the commercialization of lithium/sulfur batteries.

8.2. Outlook

This doctoral thesis work has been mainly focused on the preparation of cathode materials, including porous sulfur, sulfur/carbon composites, sulfur/polypyrrole composites, etc. The morphology and structure of the as-prepared samples have been investigated, and the synthesis methods were studied as well. In order to satisfy the requirements for the commercialization of lithium/sulfur batteries for the EV market and the development of lithium ion batteries, many more research efforts could be undertaken, including:

(1) Increasing the sulfur ratio in the electrodes without decreasing the discharge capacity of lithium/sulfur batteries. As sulfur is an insulating material, in order to operate lithium/sulfur batteries, quite a lot of conducting agents have to be added into the sulfur cathode, which leads to the low ratio of active material (sulfur) in the electrode. Thus it is necessary for the commercialization of lithium/sulfur batteries to increase the sulfur ratio in

the whole electrode.

(2) Finding a new electrolyte system for lithium/sulfur batteries to deal with the "shuttle effect". Solid electrolyte is one possible direction.

(3) The safety issue is also a very big barrier for the commercialization of the lithium/sulfur batteries. Applying Li_2S as cathode in a full cell will be a useful approach. Much work can be done in this direction, such as preparing, studying, and developing Li_2S cathode to replace the traditional sulfur cathode in order to avoid using lithium metal, choosing and investigating suitable anode materials for the anode, and studying suitable techniques for full cell assembly and operation.

(4) Assembling and investigating lithium/sulfur pouch cells to satisfy the requirements for commercialization of lithium/sulfur batteries.

(5) Exploring extension of the synthesis methods applied in this doctoral thesis work, including the soft-template method, the chemical polymerization method, the spray-pyrolysis/sublimation technique and the spray precipitation method to the preparation other electrode materials.

References

1. W. Ahn, K. B. Kim, K. N. Jung, K. H. Shin and C. S. Jin, *J. Power Sources*, 2012, 202, 394-399.
2. S. Evers, T. Yim and L. F. Nazar, *J. Mater. Chem. C*, 2012, 116, 19653-19658.
3. P. G. Bruce, S. A. Freunberger, L. J. Hardwick and J.-M. Tarascon, *Nat Mater*, 2012, 11, 19-29.
4. X. Liang, Z. Wen, Y. Liu, H. Zhang, L. Huang and J. Jin, *J. Power Sources*, 2011, 196, 3655-3658.
5. M. Hagen, S. Doerfler, H. Althues, J. Tuebke, M. J. Hoffmann, S. Kaskel and K. Pinkwart, *J. Power Sources*, 2012, 213, 239-248.
6. J. Schuster, G. He, B. Mandlmeier, T. Yim, K. T. Lee, T. Bein and L. F. Nazar, *Angew. Chem. Int. Ed.*, 2012, 51, 3591-3595.
7. C. Liang, N. J. Dudney and J. Y. Howe, *Chem. Mater.*, 2009, 21, 4724-4730.
8. C. Zhang, H. B. Wu, C. Yuan, Z. Guo and X. W. Lou, *Angew. Chem. Int. Ed.*, 2012, 51, 9592-9595.
9. B. Zhang, X. Qin, G. R. Li and X. P. Gao, *Energy Environ. Sci.*, 2010, 3, 1531-1537.
10. G. Zhou, D. W. Wang, F. Li, P. X. Hou, L. Yin, C. Liu, G. Q. Lu, I. R. Gentle and H. M. Cheng, *Energy Environ. Sci.*, 2012, 5, 8901-8906.
11. Y. S. Su, Y. Fu and A. Manthiram, *Phys. Chem. Chem. Phys.*, 2012, 14, 14495-14499.
12. G. Zheng, Y. Yang, J. J. Cha, S. S. Hong and Y. Cui, *Nano Lett.*, 2011, 11, 4462-4467.
13. G. Zheng, Q. Zhang, J. J. Cha, Y. Yang, W. Li, Z. W. Seh and Y. Cui, *Nano Lett.*, 2013, 13, 1265-1270.
14. N. W. Li, M. B. Zheng, H. L. Lu, Z. B. Hu, C. F. Shen, X. F. Chang, G. B. Ji, J. M. Cao and Y. Shi, *Chem. Commun.*, 2012, 48, 4106-4108.
15. M. S. Park, J. S. Yu, K. J. Kim, G. Jeong, J. H. Kim, Y. N. Jo, U. Hwang, S. Kang, T.

Woo and Y. J. Kim, *Phys. Chem. Chem. Phys.*, 2012, 14, 6796-6804.

16. B. Ding, C. Yuan, L. Shen, G. Xu, P. Nie, Q. Lai and X. Zhang, *J. Mater. Chem. A*, 2013, 1, 1096-1101.

17. Z. Wei Seh, W. Li, J. J. Cha, G. Zheng, Y. Yang, M. T. McDowell, P. C. Hsu and Y. Cui, *Nat. Commun.*, 2013, 4, 1331-1331.

18. Y. Fu and A. Manthiram, *J. Phys. Chem. C*, 2012, 116, 8910-8915.

19. Y. Yang, G. H. Yu, J. J. Cha, H. Wu, M. Vosgueritchian, Y. Yao, Z. A. Bao and Y. Cui, *ACS Nano*, 2011, 5, 9187-9193.

20. L. Xiao, Y. Cao, J. Xiao, B. Schwenzer, M. H. Engelhard, L. V. Saraf, Z. Nie, G. J. Exarhos and J. Liu, *Adv. Mater.*, 2012, 24, 1176-1181.

21. C. Huang, J. Xiao, Y. Shao, J. Zheng, W. D. Bennett, D. Lu, S. V. Laxmikant, M. Engelhard, L. Ji and J. Zhang, *Nat Commun*, 2014, 5.

22. Y. S. Su and A. Manthiram, *Chem. Commun.*, 2012, 48, 8817-8819.

23. Y. S. Su, Y. Fu, T. Cochell and A. Manthiram, *Nat Commun*, 2013, 4.

24. G. Du, Nanostructured anode materials for lithium-ion batteries， University of Wollongong, Thesis Collection, 2011.

25. S. S. Zhang, *J. Power Sources*, 2013, 231, 153-162.

26. X. B. Cheng, J. Q. Huang, Q. Zhang, H. J. Peng, M. Q. Zhao and F. Wei, *Nano Energy*, 2014, 4, 65-72.

27. X. Liang, Z. Wen, Y. Liu, H. Zhang, J. Jin, M. Wu and X. Wu, *J. Power Sources*, 2012, 206, 409-413.

28. L. Chen and L. L. Shaw, *J. Power Sources*, 2014, 267, 770-783.

29. M. J. Lacey, F. Jeschull, K. Edstrom and D. Brandell, *Journal of physical chemistry. C*, 2014, 118, 25890-25898.

30. L. Miao, W. Wang, K. Yuan, Y. Yang and A. Wang, *Chem. Commun.*, 2014, 50,

13231-13234.

31. L. Yin, J. Wang, X. Yu, C. W. Monroe, Y. NuLi and J. Yang, *Chem. Commun.*, 2012, 48, 7868-7870.

32. X. L. Ji, K. T. Lee and L. F. Nazar, *Nat. Mater.*, 2009, 8, 500-506.

33. J. Wang, J. Chen, K. Konstantinov, L. Zhao, S. H. Ng, G. X. Wang, Z. P. Guo and H. K. Liu, *Electrochim. Acta*, 2006, 51, 4634-4638.

34. H. Wang, Y. Yang, Y. Liang, J. T. Robinson, Y. Li, A. Jackson, Y. Cui and H. Dai, *Nano Lett.*, 2011, 11, 2644-2647.

35. L. Ji, M. Rao, S. Aloni, L. Wang, E. J. Cairns and Y. Zhang, *Energy Environ. Sci.*, 2011, 4, 5053-5059.

36. H. Nagata and Y. Chikusa, *J. Power Sources*, 2014, 264, 206-210.

37. Y. Zhang, Y. Zhao, Z. Bakenov, M. Tuiyebayeva, A. Konarov and P. Chen, *Electrochim. Acta*, 2014, 143, 49-55.

38. M. S. Song, S. C. Han, H. S. Kim, J. H. Kim, K. T. Kim, Y. M. Kang, H. J. Ahn, S. X. Dou and J. Y. Lee, *J. Electrochem. Soc.*, 2004, 151, A791-A795.

39. Q. Li, Z. Zhang, Z. Guo, Y. Lai, K. Zhang and J. Li, *Carbon*, 2014, 78, 1-9.

40. Z. Yuan, H. J. Peng, J. Q. Huang, X. Y. Liu, D. W. Wang, X. B. Cheng and Q. Zhang, *Adv. Funct. Mater.*, 2014, 24, 6105-6112.

41. H. J. Peng, J. Liang, L. Zhu, J. Q. Huang and X. B. Cheng, *ACS Nano*, 2014, 8, 11280-11289.

42. J. Wang, Y. Wu, Z. Shi and C. Wu, *Electrochim. Acta*, 2014, 144, 307-314.

43. M. Nagao, A. Hayashi and M. Tatsumisago, *Electrochim. Acta*, 2011, 56, 6055-6059.

44. H. Wei, J. Ma, B. Li, Y. Zuo and D. Xia, *ACS Applied Materials & Interfaces*, 2014, 6, 20276-20281.

45. X. Pu, G. Yang and C. Yu, *Advanced materials*, 2014, 26, 7456-7461.

46. S. H. Chung and A. Manthiram, *Advanced materials*, 2014, 26, 7352-7357.

47. S. Zheng, Y. Wen, Y. Zhu, Z. Han, J. Wang, J. Yang and C. Wang, *Adv. Ener. Mater.*, 2014, 4, 1400482.

48. M. Depardieu, R. Janot, C. Sanchez, A. Bentaleb, R. Demir-Cakan, C. Gervais, M. Birot, M. Morcrette and R. Backov, *J. Mater. Chem. A*, 2014, 2, 18047-18057.

49. W. Cai, J. Li, Y. Zhang, G. Xu and H. Cheng, *ChemElectroChem*, 2014, 1, 1662-1666.

50. W. Yuan, D. Xie, Z. Dong, Q. Su, J. Zhang, G. Du and B. Xu, *Mater. Lett.*, 2013, 97, 129-132.

51. M. Rao, X. Song and E. J. Cairns, *J. Power Sources*, 2012, 205, 474-478.

52. M. Rao, X. Song, H. Liao and E. J. Cairns, *Electrochim. Acta*, 2012, 65, 228-233.

53. G. He, X. Ji and L. Nazar, *Energy Environ. Sci.*, 2011, 4, 2878-2883.

54. Y. S. Su and A. Manthiram, *Electrochim. Acta*, 2012, 77, 272-278.

55. J. Schuster, G. He, B. Mandlmeier, T. Yim, K. T. Lee, T. Bein and L. F. Nazar, *Angew. Chem. Int. Ed.*, 2012, 51, 3591-3595.

56. C. Wang, W. Wan, J. T. Chen, H. H. Zhou, X. X. Zhang, L. X. Yuan and Y. H. Huang, *J. Mater. Chem. A*, 2013, 1, 1716-1723.

57. S. Evers and L. F. Nazar, *Chem. Commun.*, 2012, 48, 1233-1235.

58. M. Q. Zhao, X. F. Liu, Q. Zhang, G. L. Tian, J. Q. Huang, W. Zhu and F. Wei, *ACS Nano*, 2012, 6, 10759-10769.

59. J. Z. Wang, L. Lu, M. Choucair, J. A. Stride, X. Xu and H. K. Liu, *J. Power Sources*, 2011, 196, 7030-7034.

60. Y. X. Wang, L. Huang, L. C. Sun, S. Y. Xie, G. L. Xu, S. R. Chen, Y. F. Xu, J. T. Li, S. L. Chou, S. X. Dou and S. G. Sun, *J. Mater. Chem.*, 2012, 22, 4744-4750.

61. Y. Zhang, Z. Bakenov, Y. Zhao, A. Konarov, T. N. L. Doan, M. Malik, T. Paron and P. Chen, *J. Power Sources*, 2012, 208, 1-8.

62. Y. Fu and A. Manthiram, *Chem. Mater.*, 2012, 24, 3081-3087.

63. L. Qiu, S. Zhang, L. Zhang, M. Sun and W. Wang, *Electrochim. Acta*, 2010, 55, 4632-4636.

64. J. Wang, L. Lu, D. Shi, R. Tandiono, Z. Wang, K. Konstantinov and H. Liu, *ChemPlusChem*, 2013, 78, 318-324.

65. X. L. Ji and L. F. Nazar, *J. Mater. Chem.*, 2010, 20, 9821-9826.

66. V. S. Kolosnitsyn and E. V. Karaseva, *Russ. J. Electrochem.*, 2008, 44, 506-509.

67. Y. Yang, G. Zheng and Y. Cui, *Chem. Soc. Rev.*, 2013, 42, 3018-3032.

68. C. Barchasz, J. C. Lepretre, F. Alloin and S. Patoux, *J. Power Sources*, 2012, 199, 322-330.

69. J. J. Chen, Q. Zhang, Y. N. Shi, L. L. Qin, Y. Cao, M. S. Zheng and Q. F Dong, *Phys. Chem. Chem. Phys.*, 2012, 14, 5376-5382.

70. J. Kim, D. J. Lee, H. G. Jung, Y. K. Sun, J. Hassoun and B. Scrosati, *Adv. Funct. Mater.*, 2013, 23, 1076-1080.

71. C. Barchasz, F. Mesguich, J. Dijon, J. C. Lepretre, S. Patoux and F. Alloin, *J. Power Sources*, 2012, 211, 19-26.

72. S. Niu, W. Lv, C. Zhang, Y. Shi, J. Zhao, B. Li, Q.-H. Yang and F. Kang, *J. Power Sources*, 2015, 295, 182-189.

73. Q. Zeng, F. Li, I. R. Gentle, H.-M. Cheng and D.-W. Wang, *Carbon*, 2015, 93, 161-168.

74. F. Wu, Q. Zhu, R. Chen, N. Chen, Y. Chen, Y. Ye, J. Qian and L. Li, *J. Power Sources*, 2015, 296, 10-17.

75. A. Jozwiuk, H. Sommer, J. Janek and T. Brezesinski, *J. Power Sources*, 2015, 296, 454-461.

76. S. Moon, Y. H. Jung and D. K. Kim, *J. Power Sources*, 2015, 294, 386-392.

77. Y. Jiang, M. Lu, X. Ling, Z. Jiao, L. Chen, L. Chen, P. Hu and B. Zhao, *Journal of Alloys and Compounds*, 2015, 645, 509-516.

78. Z. Zhang, Y. Lai, Z. Zhang and J. Li, *Solid State Ionics*, 2015, 278, 166-171.

79. G. C. Yang, S. Q. Shi, J. H. Yang and Y. M. Ma, *J. Mater. Chem. A*, 2015, 3, 8865-8869.

80. G. Xu, B. Ding, J. Pan, P. Nie, L. Shen and X. Zhang, *J. Mater. Chem. A*, 2014, 2, 12662-12676.

81. E. S. Shin, K. Kim, S. H. Oh and W. Il Cho, *Chem. Commun.*, 2013, 49, 2004-2006.

82. C. Erhardt, Ş. Sörgel, S. Meinhard and T. Sörgel, *J. Power Sources*, 2015, 296, 70-77.

83. F. Wu, J. Li, Y. Tian, Y. Su, J. Wang, W. Yang, N. Li, S. Chen and L. Bao, *Scientific Reports*, 2015, 5, 13340.

84. Y. Xu, Y. Wen, Y. Zhu, K. Gaskell, K. A. Cychosz, B. Eichhorn, K. Xu and C. Wang, *Adv. Funct. Mater.*, 2015, 25, 4312-4320.

85. Q. Zhang, Y. Wang, Z. W. Seh, Z. Fu, R. Zhang and Y. Cui, *Nano Lett.*, 2015, 15, 3780-3786.

86. C. Sun, L. Shi, C. Fan, X. Fu, Z. Ren, G. Qian and Z. Wang, *RSC Adv.*, 2015, 5, 28832-28835.

87. K. Xi, S. Cao, X. Peng, C. Ducati, R. V. Kumar and A. K. Cheetham, *Chem. Commun.*, 2013, 49, 2192-2194.

88. W. Wei, J. Wang, L. Zhou, J. Yang, B. Schumann and Y. NuLi, *Electrochem. Commun.*, 2011, 13, 399-402.

89. Y. Li, H. Zhan, S. Liu, K. Huang and Y. Zhou, *J. Power Sources*, 2010, 195, 2945-2949.

90. G. Li, W. Cai, B. Liu and Z. Li, *J. Power Sources*, 2015, 294, 187-192.

91. Z. Li, Y. Huang, L. Yuan, Z. Hao and Y. Huang, *Carbon*, 2015, 92, 41-63.

92. L. Ma, K. E. Hendrickson, S. Wei and L. A. Archer, *Nano Today*, 2015, 10, 315-338.

93. J. Yan, X. Liu, M. Yao, X. Wang, T. K. Wafle and B. Li, *Chem. Mater.*, 2015, 27, 5080-5087.

94. Z. Cao, C. Ma, Y. Jia, Z. Sun, H. Yue, Y. Yin and S. Yang, *RSC Adv.*, 2015, 5, 28349-28353.

95. Z. Zhang, H.-K. Jing, S. Liu, G. R. Li and X. P. Gao, *J. Mater. Chem. A*, 2015, 3, 6827-6834.

96. Z. Lin, C. Nan, Y. Ye, J. Guo, J. Zhu and E. J. Cairns, *Nano Energy*, 2014, 9, 408-416.

97. A. Manthiram, Y. Fu, S.-H. Chung, C. Zu and Y.-S. Su, *Chemical reviews*, 2014, 114, 11751-11787.

98. Q. Zeng, X. Leng, K. H. Wu, I. R. Gentle and D. W. Wang, *Carbon*, 2015, 93, 611-619.

99. J. L. Shi, H. J. Peng, L. Zhu, W. Zhu and Q. Zhang, *Carbon*, 2015, 92, 96-105.

100. C. Y. Fan, H. H. Li, L. L. Zhang, H. Z. Sun, X. L. Wu, H. M. Xie and J. P. Zhang, *Phys. Chem. Chem. Phys.*, 2015, 17, 23481-23488.

101. G. M. Zhou, L. Li, C. Q. Ma, S. G. Wang, Y. Shi, N. Koratkar, W. C. Ren, F. Li and H. M. Cheng, *Nano Energy*, 2015, 11, 356-365.

102. J. W. Zhou, X. S. Yu, X. X. Fan, X. J. Wang, H. W. Li, Y. Y. Zhang, W. Li, J. Zheng, B. Wang and X. G. Li, *J. Mater. Chem. A*, 2015, 3, 8272-8275.

103. N. Ding, S. W. Chien, T. S. A. Hor, Z. Liu and Y. Zong, *J. Power Sources*, 2014, 269, 111-116.

104. H. Chen, C. Wang, Y. Dai, S. Qiu, J. Yang, W. Lu and L. Chen, *Nano Lett.*, 2015, 15, 5443-5448.

105. Q. Zhao, X. F. Hu, K. Zhang, N. Zhang, Y. X. Hu and J. Chen, *Nano Lett.*, 2015, 15, 721-726.

106. J. Brückner, S. Thieme, H. T. Grossmann, S. Dörfler, H. Althues and S. Kaskel, *J. Power Sources*, 2014, 268, 82-87.

107. X. Li, A. Lushington, J. Liu, R. Li and X. Sun, *Chem. Commun.*, 2014, 50, 9757-9760.

108. X. Q. Yu, H. L. Pan, Y. N. Zhou, P. Northrup, J. Xiao, S. Bak, M. Z. Liu, K. W. Nam, D. Y. Qu, J. Liu, T. P. Wu and X. Q. Yang, *Adv. Ener. Mater.*, 2015, 5, 1500072.

109. S. H. Yeon, W. Ahn, K. H. Shin, C. S. Jin, K. N. Jung, J. D. Jeon, S. Lim and Y. Kim, *Korean J Chem Eng*, 2015, 32, 867-873.

110. H. Shao, C. Li, N. Liu, W. Wang, H. Zhang, X. Zhao and Y. Huang, *RSC Adv.*, 2015, 5, 47757-47761.

111. Z. Zhang, Q. Li, K. Zhang, W. Chen, Y. Lai and J. Li, *J. Power Sources*, 2015, 290, 159-167.

112. Q. Sun, X. Fang, W. Weng, J. Deng, P. Chen, J. Ren, G. Guan, M. Wang and H. Peng, *Angew. Chem. Int. Ed.*, 2015, 54, 10539-10544.

113. Q. Sun, B. He, X. Q. Zhang and A. H. Lu, *ACS Nano*, 2015, 9, 8504-8513.

114. J. Liu, W. Li, L. Duan, X. Li, L. Ji, Z. Geng, K. Huang, L. Lu, L. Zhou, Z. Liu, W. Chen, L. Liu, S. Feng and Y. Zhang, *Nano Lett.*, 2015, 15, 5137-5142.

115. M. Agostini, S. Xiong, A. Matic and J. Hassoun, *Chem. Mater.*, 2015, 27, 4604-4611.

116. L. Zeng, Y. Jiang, J. Xu, M. Wang, W. Li and Y. Yu, *Nanoscale*, 2015, 7, 10940-10949.

117. B. Ding, Z. Chang, G. Xu, P. Nie, J. Wang, J. Pan, H. Dou and X. Zhang, *ACS Applied Materials & Interfaces*, 2015, 7, 11165-11171.

118. A. Manthiram, S.-H. Chung and C. Zu, *Adv. Mater.*, 2015, 27, 1980-2006.

119. N. Yan, X. F. Yang, W. Zhou, H. Z. Zhang, X. F. Li and H. M. Zhang, *RSC Adv.*, 2015, 5, 26273-26280.

120. G. M. Zhou, Y. B. Zhao and A. Manthiram, *Adv. Ener. Mater.*, 2015, 5.

121. X. Gu, C. Lai, F. Liu, W. Yang, Y. Hou and S. Zhang, *J. Mater. Chem. A*, 2015, 3, 9502-9509.

122. C. N. Lin, W. C. Chen, Y. F. Song, C. C. Wang, L. D. Tsai and N. L. Wu, *J. Power Sources*, 2014, 263, 98-103.

123. H. Yao, K. Yan, W. Li, G. Zheng, D. Kong, Z. W. Seh, V. K. Narasimhan, Z. Liang and Y. Cui, *Energy Environ. Sci.*, 2014, 7, 3381-3390.

124. J. Xu, J. Shui, J. Wang, M. Wang and H. K. Liu, *ACS Nano*, 2014, 8, 10920-10930.

125. B. Wang, S. M. Alhassan and S. T. Pantelides, *Physical review applied*, 2014, 2.

126. S. H. Chung and A. Manthiram, *Adv. Funct. Mater.*, 2014, 24, 5299-5306.

127. Q. Pang, D. Kundu, M. Cuisinier and L. F. Nazar, *Nat Commun*, 2014, 5.

128. S. Risse, S. Angioletti-Uberti, J. Dzubiella and M. Ballauff, *J. Power Sources*, 2014, 267, 648-654.

129. Y. J. Choi, B. S. Jung, D. J. Lee, J. H. Jeong, K. W. Kim, H. J. Ahn, K. K. Cho and H. B. Gu, *Phys. Scr.*, 2007, T129, 62-65.

130. C. Zu, Y.-S. Su, Y. Fu and A. Manthiram, *Phys. Chem. Chem. Phys.*, 2013, 15, 2291-2297.

131. R. Younesi, G. M. Veith, P. Johansson, K. Edstrom and T. Vegge, *Energy Environ. Sci.*, 2015, 8, 1905-1922.

132. T. Lin, Y. Tang, Y. Wang, H. Bi, Z. Liu, F. Huang, X. Xie and M. Jiang, *Energy Environ. Sci.*, 2013, 6, 1283-1290.

133. J. Wang, S. Y. Chew, Z. W. Zhao, S. Ashraf, D. Wexler, J. Chen, S. H. Ng, S. L. Chou and H. K. Liu, *Carbon*, 2008, 46, 229-235.

134. L. Wang, X. He, J. Li, J. Gao, J. Guo, C. Jiang and C. Wan, *J. Mater. Chem.*, 2012, 22, 22077-22081.

135. G. C. Li, G. R. Li, S. H. Ye and X. P. Gao, *Adv. Ener. Mater.*, 2012, 2, 1238-1245.

136. Y. G. Zhang, Y. Zhao, A. Konarov, Z. Li and P. Chen, *Journal of Alloys and Compounds*, 2015, 619, 298-302.

137. C. Zhang, D. H. Liu, W. Lv, D. W. Wang, W. Wei, G. M. Zhou, S. G. Wang, F. Li, B. H. Li, F. Y. Kang and Q. H. Yang, *Nanoscale*, 2015, 7, 5592-5597.

138. Q. C. Zeng, F. Li, I. R. Gentle, H. M. Cheng and D. W. Wang, *Carbon*, 2015, 93, 161-168.

139. S. Zhang, N. Li, H. Lu, J. Zheng, R. Zang and J. Cao, *RSC Adv.*, 2015, 5, 50983-50988.

140. G. Babu and L. M. Reddy Arava, *RSC Adv.*, 2015, 5, 47621-47627.

141. Y. Li, L. Yuan, Z. Li, Y. Qi, C. Wu, J. Liu and Y. Huang, *RSC Adv.*, 2015, 5, 44160-44164.

142. H. Wang, C. Zhang, Z. Chen, H. K. Liu and Z. Guo, *Carbon*, 2015, 81, 782-787.

143. X. Duan, Y. Han, L. Huang, Y. Li and Y. Chen, *J. Mater. Chem. A*, 2015, 3, 8015-8021.

144. G. He, S. Evers, X. Liang, M. Cuisinier, A. Garsuch and L. F. Nazar, *ACS Nano*, 2013, 7, 10920-10930.

145. D. Li, F. Han, S. Wang, F. Cheng, Q. Sun and W.-C. Li, *ACS Applied Materials & Interfaces*, 2013, 5, 2208-2213.

146. B. Ding, C. Yuan, L. Shen, G. Xu, P. Nie and X. Zhang, *Chemistry – A European Journal*, 2013, 19, 1013-1019.

147. Z. Ma, Q. Liu and S. Wang, *RSC Adv.*, 2015, 5, 2096-2099.

148. Y. S. Su and A. Manthiram, *J. Power Sources*, 2014, 270, 101-105.

149. W. Zhou, X. Xiao, M. Cai and L. Yang, *Nano Lett.*, 2014, 14, 5250-5256.

150. X. Li, X. Li, M. N. Banis, B. Wang, A. Lushington, X. Cui, R. Li, T.-K. Sham and X. Sun, *J. Mater. Chem. A*, 2014, 2, 12866-12872.

151. Q. Zhang, X. B. Cheng, J. Q. Huang, H. J. Peng and F. Wei, *New Carbon Materials*, 2014, 29, 241-264.

152. F. F. Li, W. Lu, S. Z. Niu and B. H. Li, *New Carbon Materials*, 2014, 29, 309-315.

153. Q. T. Qu, T. Gao, H. Y. Zheng, Y. Wang, X. Y. Li, X. X. Li, J. M. Chen, Y. Y. Han, J. Shao and H. H. Zheng, *Adv Mater Interfaces*, 2015, 2.

154. J. Ma, Z. Fang, Y. Yan, Z. Z. Yang, L. Gu, Y. S. Hu, H. Li, Z. X. Wang and X. J. Huang, *Adv. Ener. Mater.*, 2015, 5.

155. H. K. Jing, L. L. Kong, S. Liu, G. R. Li and X. P. Gao, *J. Mater. Chem. A*, 2015, 3, 12213-12219.

156. C. Zhao, C. Shen, F. Xin, Z. Sun and W. Han, *Mater. Lett.*, 2014, 137, 52-55.

157. X. Tao, J. Wang, Z. Ying, Q. Cai, G. Zheng, Y. Gan, H. Huang, Y. Xia, C. Liang, W. Zhang and Y. Cui, *Nano Lett.*, 2014, 14, 5288-5294.

158. F. Wu, J. Qian, R. Chen, J. Lu and L. Li, *ACS Applied Materials & Interfaces*, 2014, 6, 15542-15549.

159. A. Unemoto, S. Yasaku, G. Nogami, M. Tazawa, M. Taniguchi, M. Matsuo, T. Ikeshoji and S.-i. Orimo, *Applied Physics Letters*, 2014, 105, 083901.

160. M. Rao, W. Li and E. J. Cairns, *Electrochem. Commun.*, 2012, 17, 1-5.

161. W. Weng, V. G. Pol and K. Amine, *Adv. Mater.*, 2013, 25, 1608-1615.

162. G. Li, H. Jing, H. Li, L. Liu, Y. Wang, C. Yuan, H. Jiang and L. Chen, *Ionics*, 2015, 21, 2161-2170.

163. Z. Peng, W. Fang, H. Zhao, J. Fang, H. Cheng, T. N. L. Doan, J. Xu and P. Chen, *J. Power Sources*, 2015, 282, 70-78.

164. J. Yan, X. Liu, X. Wang and B. Li, *J. Mater. Chem. A*, 2015, 3, 10127-10133.

165. C. Zhang, W. Wang, A. Wang, K. Yuan, Y. Yang and Y. Lu, *J. Electrochem. Soc.*, 2015, 162, A1067-A1071.

166. Y. Hao, Z. Shi, J. Wang and Q. Xu, *RSC Adv.*, 2015, 5, 31629-31636.

167. J. J. Cheng, Y. Pan, J. A. Pan, H. J. Song and Z. S. Ma, *RSC Adv.*, 2015, 5, 68-74.

168. C. Hoffmann, S. Thieme, J. Brueckner, M. Oschatz and T. Biemelt, *ACS Nano*, 2014, 8, 12130-12140.

169. H. J. Peng, T. Z. Hou, Q. Zhang, J. Q. Huang and X. B. Cheng, *Adv Mater Interfaces*, 2014, 1, 1400227.

170. Y. Wu, M. Gao, X. Li, Y. Liu and H. Pan, *Journal of Alloys and Compounds*, 2014, 608, 220-228.

171. X. Chen, Z. Xiao, X. Ning, Z. Liu, Z. Yang, C. Zou, S. Wang, X. Chen, Y. Chen and S. Huang, *Adv. Ener. Mater.*, 2014, 4, 1301988.

172. C. Tang, Q. Zhang, M. Q. Zhao, J. Q. Huang and X.-B. Cheng, *Advanced materials (Weinheim)*, 2014, 26, 6100-6105.

173. B. Zhang, M. Xiao, S. Wang, D. Han, S. Song, G. Chen and Y. Meng, *ACS Applied Materials & Interfaces*, 2014, 6, 13174-13182.

174. Y. Zhao, W. Wu, J. Li, Z. Xu and L. Guan, *Advanced materials*, 2014, 26, 5113-5118.

175. D. S. Jung, T. H. Hwang, J. H. Lee, H. Y. Koo, R. A. Shakoor, R. Kahraman, Y. N. Jo, M. S. Park and J. W. Choi, *Nano Lett.*, 2014, 14, 4418-4425.

176. Y. Liu, H. Zhan and Y. Zhou, *Electrochim. Acta*, 2012, 70, 241-247.

177. L. Zhou, T. Huang and A. Yu, *ACS sustainable chemistry & engineering*, 2014, 2, 2442-2447.

178. Z. Li, Y. Jiang, L. Yuan, Z. Yi and C. Wu, *ACS Nano*, 2014, 8, 9295-9303.

179. M. Agrawal, S. Choudhury, K. Gruber, F. Simon, D. Fischer, V. Albrecht, M. Göbel, S. Koller, M. Stamm and L. Ionov, *J. Power Sources*, 2014, 261, 363-370.

180. N. Moreno, A. Caballero, L. Hernan, J. Morales and J. Canales-Vazquez, *Phys. Chem. Chem. Phys.*, 2014, 16, 17332-17340.

181. L. Zeng, F. Pan, W. Li, Y. Jiang, X. Zhong and Y. Yu, *Nanoscale*, 2014, 6, 9579-9587.

182. X. B. Cheng, H. J. Peng, J. Q. Huang, L. Zhu, S. H. Yang, Y. Liu, H. W. Zhang, W. Zhu, F. Wei and Q. Zhang, *J. Power Sources*, 2014, 261, 264-270.

183. D. A. C. Brownson, D. K. Kampouris and C. E. Banks, *J. Power Sources*, 2011.

184. L. Ji, M. Rao, H. Zheng, L. Zhang, Y. Li, W. Duan, J. Guo, E. J. Cairns and Y. Zhang, *J. Am. Chem. Soc.*, 2011, 133, 18522-18525.

185. F. Zhang, Y. Dong, Y. Huang, G. Huang, X. Zhang, L. Wang and Iop, in *4th International Symposium on Functional Materials*, 2012, vol. 339.

186. Y. You, W. C. Zeng, Y. X. Yin, J. Zhang, C. P. Yang, Y. W. Zhu and Y. G. Guo, *J. Mater. Chem. A*, 2015, 3, 4799-4802.

187. Z. Wang, Y. Dong, H. Li, Z. Zhao, H. Bin Wu, C. Hao, S. Liu, J. Qiu and X. W. Lou, *Nat Commun*, 2014, 5.

188. K. Han, J. Shen, S. Hao, H. Ye and C. Wolverton, *Chemsuschem*, 2014, 7, 2545-2553.

189. H. Kim, J. Lee, H. Ahn, O. Kim and M. J. Park, *Nat Commun*, 2015, 6.

190. X. Li, M. Rao, D. Chen, H. Lin, Y. Liu, Y. Liao, L. Xing and W. Li, *Electrochim. Acta*, 2015, 166, 93-99.

191. J. Ye, F. He, J. Nie, Y. Cao, H. Yang and X. Ai, *J. Mater. Chem. A*, 2015, 3, 7406-7412.

192. J. Lee and W. Choi, *J. Electrochem. Soc.*, 2015, 162, A935-A939.

193. G. Yuan and H. Wang, *J Energy Chem*, 2014, 23, 657-661.

194. M. Sun, S. Zhang, T. Jiang, L. Zhang and J. Yu, *Electrochem. Commun.*, 2008, 10, 1819-1822.

195. L. Yin, J. Wang, F. Lin, J. Yang and Y. Nuli, *Energy Environ. Sci.*, 2012, 5, 6966-6972.

196. H. Hu, H. Cheng, Z. Liu, G. Li, Q. Zhu and Y. Yu, *Nano Lett.*, 2015, 15, 5116-5123.

197. S. Xiong, J. Scheers, L. Aguilera, D. H. Lim, K. Xie, P. Jacobsson and A. Matic, *RSC Adv.*, 2015, 5, 2122-2128.

198. L. W. Ji, M. M. Rao, H. M. Zheng, L. Zhang, Y. C. Li, W. H. Duan, J. H. Guo, E. J. Cairns and Y. G. Zhang, *J. Am. Chem. Soc.*, 2011, 133, 18522-18525.

199. S. S. Zhang, *Electrochim. Acta*, 2012, 70, 344-348.

200. S. S. Zhang and J. A. Read, *J. Power Sources*, 2012, 200, 77-82.

201. X. Liang, Z. Wen, Y. Liu, M. Wu, J. Jin, H. Zhang and X. Wu, *J. Power Sources*, 2011, 196, 9839-9843.

202. R. Cao, W. Xu, D. Lv, J. Xiao and J. G. Zhang, *Adv. Ener. Mater.*, 2015, 5, n/a-n/a.

203. X. Zhang, W. Wang, A. Wang, Y. Huang, K. Yuan, Z. Yu, J. Qiu and Y. Yang, *J. Mater. Chem. A*, 2014, 2, 11660-11665.

204. C. L. Lee and I. D. Kim, *Nanoscale*, 2015, 7, 10362-10367.

205. J. Wang, Y. Yang and F. Kang, *Electrochim. Acta*, 2015, 168, 271-276.

206. Z. Yunbo, M. Lixiao, N. Jing, X. Zhichang, H. Long, W. Bin and Z. Linjie, *2D Materials*, 2015, 2, 024013.

207. W. Cai, G. Li, F. He, L. Jin, B. Liu and Z. Li, *J. Power Sources*, 2015, 283, 524-529.

208. W. Ahn, S. N. Lim, D. U. Lee, K. B. Kim, Z. Chen and S. H. Yeon, *J. Mater. Chem. A*, 2015, 3, 9461-9467.

209. G. Ma, Z. Wen, Q. Wang, C. Shen, P. Peng, J. Jin and X. Wu, *J. Power Sources*, 2015, 273, 511-516.

210. G. Ma, Z. Wen, J. Jin, M. Wu, X. Wu and J. Zhang, *J. Power Sources*, 2014, 267, 542-546.

211. Y. S. Su and A. Manthiram, *Nat Commun*, 2012, 3, 1166.

212. Y. S. Su, Y. Z. Fu, T. Cochell and A. Manthiram, *Nat Commun*, 2013, 4.

213. N. Pal and A. Bhaumik, *Adv.Colloid and Interface Sci.*, 2013, 189, 21-41.

214. J. M. G. Cowie, *Polymers: Chemistry and Physics of Modern Materials*, Chapman and Hall, 1991.

215. E. Vivaldo-Lima, P. E. Wood, A. E. Hamielec and A. Penlidis, *Industrial & engineering chemistry research*, 1997, 36, 939-965.

216. J. Clayden, N. Greeves and S. Warren, *Organic chemistry*, Oxford University Press, 2000.

217. S. H. Ng, J. Wang, D. Wexler, K. Konstantinov, Z. P. Guo and H. K. Liu, *Angew. Chem. Int. Ed.*, 2006, 45, 6896-6899.

218. S. A. Needham, G. Wang, K. Konstantinov, Y. Tournayre, Z. Lao and H. K. Liu, *Electrochemical and solid-state letters*, 2006, 9, A315-A319.

219. A. Chidembo, S. H. Aboutalebi, K. Konstantinov, M. Salari, B. Winton, S. A. Yamini, I. P. Nevirkovets and H. K. Liu, *Energy Environ. Sci.*, 2012, 5, 5236-5240.

220. S. H. Ng, J. Wang, D. Wexler, K. Konstantinov, Z. P. Guo and H. K. Liu, *Angew. Chem. Int. Ed.*, 2006, 45, 6896-6899.

221. S. H. Ng, J. Wang, K. Konstantinov, D. Wexler, S. Y. Chew, Z. P. Guo and H. K. Liu, *J. Power Sources*, 2007, 174, 823–827.

222. M. Trautz, *Zeitschrift für anorganische und allgemeine Chemie*, 1916, 96, 1-28.

223. D. Cardillo, M. Tehei, M. Lerch, S. Corde, A. Rosenfeld and K. Konstantinov, *Mater Lett*, 2014, 117, 279-282.

224. N. N. Jason, R. G. Chaudhuri and S. Paria, *Soft Matter*, 2012, 8, 3771-3780.

225. A. W. Coats and J. P. Redfern, *Analyst*, 1963, 88, 906-924.

226. N. B. Colthup, L. H. Daly and S. E. Wiberley, *Introduction to infrared and Raman spectroscopy*, Academic press, 1990.

227. S. Brunauer, P. H. Emmett and E. Teller, *J Am Chem Soc*, 1938, 60, 309-319.

228. Y. Deng, Z. Li, Z. Shi, H. Xu, F. Peng and G. Chen, *RSC Adv.*, 2012, 2, 4645-4647.

229. H. L. Wang, Y. Yang, Y. Y. Liang, J. T. Robinson, Y. G. Li, A. Jackson, Y. Cui and H. J. Dai, *Nano Lett.*, 2011, 11, 2644-2647.

230. X. Ji, K. T. Lee and L. F. Nazar, *Nat Mater*, 2009, 8, 500-506.

231. N. Jayaprakash, J. Shen, S. S. Moganty, A. Corona and L. A. Archer, *Angew. Chem. Int. Ed.*, 2011, 123, 6026-6030.

232. C. Lai, X. P. Gao, B. Zhang, T. Y. Yan and Z. Zhou, *J. Phys. Chem. C*, 2009, 113, 4712-4716.

233. Y. M. Guo, J. Z. Zhao, S. F. Yang, Z. C. Wang and H. B. Zhang, *Powder Technol.*, 2006, 162, 83-86.

234. F. Wu, J. Chen, R. Chen, S. Wu, L. Li, S. Chen and T. Zhao, *J. Phys. Chem. C*, 2011, 115, 6057-6063.

235. J. Wang, J. Yang, C. Wan, K. Du, J. Xie and N. Xu, *Adv. Funct. Mater.*, 2003, 13, 487-492.

236. S. C. Zhang, L. Zhang, W. K. Wang and W. J. Xue, *Synthetic Metals*, 2010, 160, 2041-2044.

237. I. Sultana, M. M. Rahman, S. Li, J. Wang, C. Wang, G. G. Wallace and H.-K. Liu, *Electrochim. Acta*, 2012, 60, 201-205.

238. X. Liang, Y. Liu, Z. Wen, L. Huang, X. Wang and H. Zhang, *J. Power Sources*, 2011, 196, 6951-6955.

239. J. Wang, Y. S. He and J. Yang, *Adv. Mater.*, 2015, 27, 569-575.

240. X. Yu and A. Manthiram, *Phys. Chem. Chem. Phys.*, 2015, 17, 2127-2136.

241. X. Liang, M. Kaiser, K. Konstantinov, R. Tandiono, Z. Wang, H. K. Liu, S. X. Dou and J. Wang, *RSC Adv.*, 2014, 4, 36513-36516.

242. X. Wang, Z. Zhang, X. Yan, Y. Qu, Y. Lai and J. Li, *Electrochim. Acta*, 2015, 155,

54-60.

243. C. Xu, Y. Wu, X. Zhao, X. Wang, G. Du, J. Zhang and J. Tu, *J. Power Sources*, 2015, 275, 22-25.

244. M. R. Kaiser, J. Wang, X. Liang, H. K. Liu and S. X. Dou, *J. Power Sources*, 2015, 279, 231-237.

245. S. Lim, R. Lilly Thankamony, T. Yim, H. Chu, Y. J. Kim, J. Mun and T. H. Kim, *ACS Applied Materials & Interfaces*, 2015, 7, 1401-1405.

246. G. Zhou, L. Li, D. W. Wang, X. Y. Shan, S. Pei, F. Li and H. M. Cheng, *Adv. Mater.*, 2015, 27, 641-647.

247. C. J. Hart, M. Cuisinier, X. Liang, D. Kundu, A. Garsuch and L. F. Nazar, *Chem. Commun.*, 2015, 51, 2308-2311.

248. W. Hu, H. Zhang, Y. Zhang, M. Wang, C. Qu and J. Yi, *Chem. Commun.*, 2015, 51, 1085-1088.

249. V. S. Kolosnitsyn, E. V. Kuzmina and E. V. Karaseva, *J. Power Sources*, 2015, 274, 203-210.

250. Q. Zhao, X. Hu, K. Zhang, N. Zhang, Y. Hu and J. Chen, *Nano Lett.*, 2015, 15, 721-726.

251. X. Yang, N. Yan, W. Zhou, H. Zhang, X. Li and H. Zhang, *J. Mater. Chem. A*, 2015, 3, 15314-15323.

252. X. Liu, Z. Shan, K. Zhu, J. Du, Q. Tang and J. Tian, *J. Power Sources*, 2015, 274, 85-93.

253. Q. Li, Z. Zhang, Z. Guo, K. Zhang, Y. Lai and J. Li, *J. Power Sources*, 2015, 274, 338-344.

254. X. Li, M. Rao, H. Lin, D. Chen, Y. Liu, S. Liu, Y. Liao, L. Xing, M. Xu and W. Li, *J. Mater. Chem. A*, 2015, 3, 18098-18104.

255. K. Park, J. H. Cho, J. H. Jang, B. C. Yu, A. T. De La Hoz, K. M. Miller, C. J. Ellison and J. B. Goodenough, *Energy Environ. Sci.*, 2015, 8, 2389-2395.

256. Y. Zhang, Y. Zhao, A. Konarov, Z. Li and P. Chen, *Journal of Alloys and Compounds*, 2015, 619, 298-302.

257. P. Strubel, S. Thieme, T. Biemelt, A. Helmer, M. Oschatz, J. Brückner, H. Althues and S. Kaskel, *Adv. Funct. Mater.*, 2015, 25, 287-297.

258. Z. Zhang, Q. Li, S. Jiang, K. Zhang, Y. Lai and J. Li, *Chemistry – A European Journal*, 2015, 21, 1343-1349.

259. J. He, Y. Chen, P. Li, F. Fu, Z. Wang and W. Zhang, *J. Mater. Chem. A*, 2015, 3, 18605-18610.

260. X. Gu, C. J. Tong, C. Lai, J. Qiu, X. Huang, W. Yang, B. Wen, L. M. Liu, Y. Hou and S. Zhang, *J. Mater. Chem. A*, 2015, 3, 16670-16678.

261. G. Li, W. Zhao, L. Liu and L. Chen, *RSC Adv.*, 2015, 5, 54293-54300.

262. X. Zhou, J. Xie, J. Yang, Y. Zou, J. Tang, S. Wang, L. Ma and Q. Liao, *J. Power Sources*, 2013, 243, 993-1000.

263. X. Liang, M. Zhang, M. R. Kaiser, X. Gao, K. Konstantinov, R. Tandiono, Z. Wang, H. K. Liu, S. X. Dou and J. Wang, *Nano Energy*, 2015, 11, 587-599.

264. M. S. Dresselhaus, G. Dresselhaus, R. Saito and A. Jorio, *Physics Reports*, 2005, 409, 47-99.

265. A. Ferrari and J. Robertson, *Physical review B*, 2000, 61, 14095.

266. Y. Shi, S. L. Chou, J. Z. Wang, D. Wexler, H. J. Li, H. K. Liu and Y. Wu, *J. Mater. Chem.*, 2012, 22, 16465-16470.

267. S. H. Aboutalebi, A. T. Chidembo, M. Salari, K. Konstantinov, D. Wexler, H. K. Liu and S. X. Dou, *Energy Environ. Sci.*, 2011, 4, 1855-1865.

268. L. Sun, W. Kong, Y. Jiang, H. Wu, K. Jiang, J. Wang and S. Fan, *J. Mater. Chem. A*,

2015, 3, 5305-5312.

269. Y. Chen, S. Lu, X. Wu and J. Liu, *J. Phys. Chem. C*, 2015, 119, 10288-10294.

270. J. Xiao, J. Z. Hu, H. Chen, M. Vijayakumar, J. Zheng, H. Pan, E. D. Walter, M. Hu, X. Deng, J. Feng, B. Y. Liaw, M. Gu, Z. D. Deng, D. Lu, S. Xu, C. Wang and J. Liu, *Nano Lett.*, 2015, 15, 3309-3316.

271. J. G. Werner, S. S. Johnson, V. Vijay and U. Wiesner, *Chem. Mater.*, 2015, 27, 3349-3357.

272. G. Zhou, Y. Zhao and A. Manthiram, *Adv. Ener. Mater.*, 2015, 5, 1402263.

273. L. Wang, J. Liu, S. Haller, Y. Wang and Y. Xia, *Chem. Commun.*, 2015, 51, 6996-6999.

274. L. Qie and A. Manthiram, *Adv. Mater.*, 2015, 27, 1694-1700.

275. Y. Sun, S. Wang, H. Cheng, Y. Dai, J. Yu and J. Wu, *Electrochim. Acta*, 2015, 158, 143-151.

276. D. W. Wang, Q. Zeng, G. Zhou, L. Yin, F. Li, H. M. Cheng, I. R. Gentle and G. Q. M. Lu, *Journal of Materials Chemistry A*, 2013, 1, 9382-9394.

277. X. Zhao, H.-J. Ahn, K.-W. Kim, K.-K. Cho and J.-H. Ahn, *J. Phys. Chem. C*, 2015, 119, 7996-8003.

278. G. Babu, K. Ababtain, K. Y. S. Ng and L. M. R. Arava, *Scientific Reports*, 2015, 5, 8763.

279. J. Chen, D. Wu, E. Walter, M. Engelhard, P. Bhattacharya, H. Pan, Y. Shao, F. Gao, J. Xiao and J. Liu, *Nano Energy*, 2015, 13, 267-274.

280. Z. Lyu, D. Xu, L. Yang, R. Che, R. Feng, J. Zhao, Y. Li, Q. Wu, X. Wang and Z. Hu, *Nano Energy*, 2015, 12, 657-665.

281. G. Zhou, Y. Zhao, C. Zu and A. Manthiram, *Nano Energy*, 2015, 12, 240-249.

282. M. Yu, A. Wang, F. Tian, H. Song, Y. Wang, C. Li, J. D. Hong and G. Shi,

Nanoscale, 2015, 7, 5292-5298.

283. H. Li, X. Yang, X. Wang, M. Liu, F. Ye, J. Wang, Y. Qiu, W. Li and Y. Zhang, *Nano Energy*, 2015, 12, 468-475.

284. X. Wang, Y. Gao, J. Wang, Z. Wang and L. Chen, *Nano Energy*, 2015, 12, 810-815.

285. J. Q. Huang, T. Z. Zhuang, Q. Zhang, H. J. Peng, C. M. Chen and F. Wei, *ACS Nano*, 2015, 9, 3002-3011.

286. G. Yuan, G. Wang, H. Wang and J. Bai, *J Solid State Electr*, 2015, 19, 1143-1149.

287. Y. Qu, Z. Zhang, X. Zhang, G. Ren, Y. Lai, Y. Liu and J. Li, *Carbon*, 2015, 84, 399-408.

288. J. Balach, T. Jaumann, M. Klose, S. Oswald, J. Eckert and L. Giebeler, *J. Phys. Chem. C*, 2015, 119, 4580-4587.

289. K. Xi, B. Chen, H. Li, R. Xie, C. Gao, C. Zhang, R. V. Kumar and J. Robertson, *Nano Energy*, 2015, 12, 538-546.

290. F. Wu, J. Qian, R. Chen, T. Zhao, R. Xu, Y. Ye, W. Li, L. Li, J. Lu and K. Amine, *Nano Energy*, 2015, 12, 742-749.

291. K. Yang, Q. Gao, Y. Tan, W. Tian, L. Zhu and C. Yang, *Microporous and Mesoporous Materials*, 2015, 204, 235-241.

292. M. Wang, H. Zhang, Q. Wang, C. Qu, X. Li and H. Zhang, *ACS Applied Materials & Interfaces*, 2015, 7, 3590-3599.

293. X. B. Yang, W. Zhu, K. Qin and H. Y. Wang, *Electrochim. Acta*, 2014, 143, 374-382.

294. M. R. Kaiser, X. Liang, K. Konstantinov, H. K. Liu, S. X. Dou and J. Z. Wang, *Chemistry – A European Journal*, 2015, 21, 10061-10069.

295. H. Chen, C. Wang, W. Dong, W. Lu, Z. Du and L. Chen, *Nano Lett.*, 2015, 15, 798-802.

296. Y. Zhang, Y. Zhao and Z. Bakenov, *Ionics*, 2014, 20, 1047-1050.

297. Z. Li and L. Yin, *ACS Applied Materials & Interfaces*, 2015, 7, 4029-4038.

298. Y. S. Su and A. Manthiram, *Chem Commun*, 2012, 48, 8817-8819.

299. X. F. Wang, Z. X. Wang and L. Q. Chen, *J Power Sources*, 2013, 242, 65-69.

300. T. G. Jeong, Y. H. Moon, H. H. Chun, H. S. Kim, B. W. Cho and Y. T. Kim, *Chem Commun*, 2013, 49, 11107-11109.

Appendix

Appendix A Awards (2012.3-2015.9)

1. 2012-2015 University Postgraduate Award, University of Wollongong
2. 2012-2015 International Postgraduate Tuition Award, University of Wollongong
3. 2015 ISEM Postgraduate Student Merit Award, University of Wollongong.
4. 2014 AIIM HDR Student Conference and International Travel Grants, University of Wollongong
5. Poster Award at the International Symposium of Young Scientists on Next-Generation Batteries 2015, Changsha, July 31 – August 2, 2015 (ISYSNGB 2015).

Appendix B

1. Publications (2012.3-2015.9)

(1) **Xin Liang**, Mingang Zhang, Mohammad Rejaul Kaiser, Xuanwen Gao, Konstantin Konstantinov, Richard Tandiono, Zhaoxiang Wang, Hua-Kun Liu, Shi-Xue Dou, Jiazhao Wang, Split-half-tubular polypyrrole@sulfur@polypyrrole composite with a novel three-layer-3D structure as cathode for lithium/sulfur batteries, **Nano Energy**, 2015, 11, 587-599.

(2) **Xin Liang**, Mohammad Kaiser, Konstantin Konstantinov, Richard Tandiono, Zhaoxiang Wang, Hua-Kun Liu, Shi-Xue Dou and Jiazhao Wang, High performance pure sulfur honeycomb-like architectures synthesized by a cooperative self-assembly strategy for lithium–sulfur batteries, **RSC Adv.**, 2014, 4, 36513–36516.

(3) **Xin Liang**, Mohammad Rejaul Kaiser, Konstantin Konstantinov,* Richard Tandiono, Zhaoxiang Wang, Chunhua Chen, Hua-Kun Liu, Shi-Xue Dou, Jiazhao Wang, One–Step and Continuous Industry-Oriented Spray-Pyrolysis/Sublimation Method to Synthesize Porous Sulfur/ Dual-Carbon Architectures for Lithium/Sulfur Batteries. (**Journal of**

Power Sources , under revision)

(4) Mohammad Rejaul Kaiser, **Xin Liang**, Konstantin Konstantinov, Hua-Kun Liu, Shi-Xue Dou, and Jiazhao Wang, A Facile Synthesis of High Surface Area Sulfur-Carbon Composite for Li/S Batteries, **Chemistry -A European Journal**, **2015,** 21, 10061-10069. **(Back Page Cover & Hot Paper)**

(5) Jingfa Li, Jiazhao Wang,* **Xin Liang**, Zhijia Zhang, Huakun Liu, Yitai Qian, Shenglin Xiong, Hollow $MnCo_2O_4$ Submicrospheres with Multilevel Interiors: From Mesoporous to Core-in-Double-Shell Structures, **ACS Applied Materials & Interfaces,** *2014,* 6, 24-30.

(6) Mohammad Rejaul Kaiser, Jiazhao Wang*, **Xin Liang**, Hua-Kun Liu, Shi-Xue Dou, A systematic approach to high and stable discharge capacity for scaling up the lithium–sulfur battery, **Journal of Power Sources**, 2015, 279, 231-237

(7) Xiaowei Li, Shenglin Xiong*, Jingfa Li, **Xin Liang**, Jiazhao Wang, Jing Bai, Yitai Qian, Constructed Functional Systems from Mn_2O_3 Nanowires to MnO@Carbon Core-Shell Nanowires as Stable High-Performance Anodes for Lithium-Ion Batteries, **Chemistry -A European Journal**, 2013, 19, 11310-11319.

(8) Bang-Kun Zou, Yan-Yu Zhang, Jia-Yi Wang, **Xin Liang**, Xiao-Hang Ma, Chun-Hua Chen, Hydrothermally enhanced MnO/reduced graphite oxide composite anode materials for high performance lithium-ion batteries, **Electrochimica Acta,** 2015, 167, 25-31**.**

(9) Xiao-Hang Ma, Shuang-Shuang Zeng, Bang-Kun Zou, **Xin Liang,** Jia-Ying Liao, Chun-Hua Chen, Synthesis of different CuO nanostructures by new catalytic template method as anode materials for lithium-ion batteries, **RSC Adv.,** 2015, 5, 57300-57308.

(10) **Xin Liang**, Mohammad Rejaul Kaiser, Jun Wang, Konstantin Konstantinov, Richard Tandiono, Chunhua Chen, Hua-Kun Liu, Shi-Xue Dou, Jiazhao Wang, High Performance of Active Carbon- Nano Sulfur-Polypyrrole Composite with Host-Container Architecture for

Lithium/Sulfur Batteries. (To be submitted)

2. Intellectual Property:

Mass production synthesis of nanocrystalline sulphur via spray assisted co-precipitation technique for Li-Sulphur batteries. (Under application)

3. Conferences:

(1) The 17th International Meeting on Lithium Batteries, Como, Italy, Jun 10-14, 2014.

(2) The International Symposium of Young Scientists on Next-Generation Batteries 2015 (ISYSNGB 2015), Changsha, July 31-August 2, 2015

4. Other activities:

(1) 3 Minutes Competition in AIIM, Wollongong, Australia, Jun. 5, 2013.

(2) Professional Development Short Course on Improving Energy Efficiency in Manufacturing and Industrial Processes, Wollongong, Australia, Nov. 22, 2012.